Energy generation from mixing salt water and fresh water

Smart flow strategies for reverse electrodialysis

David A. Vermaas

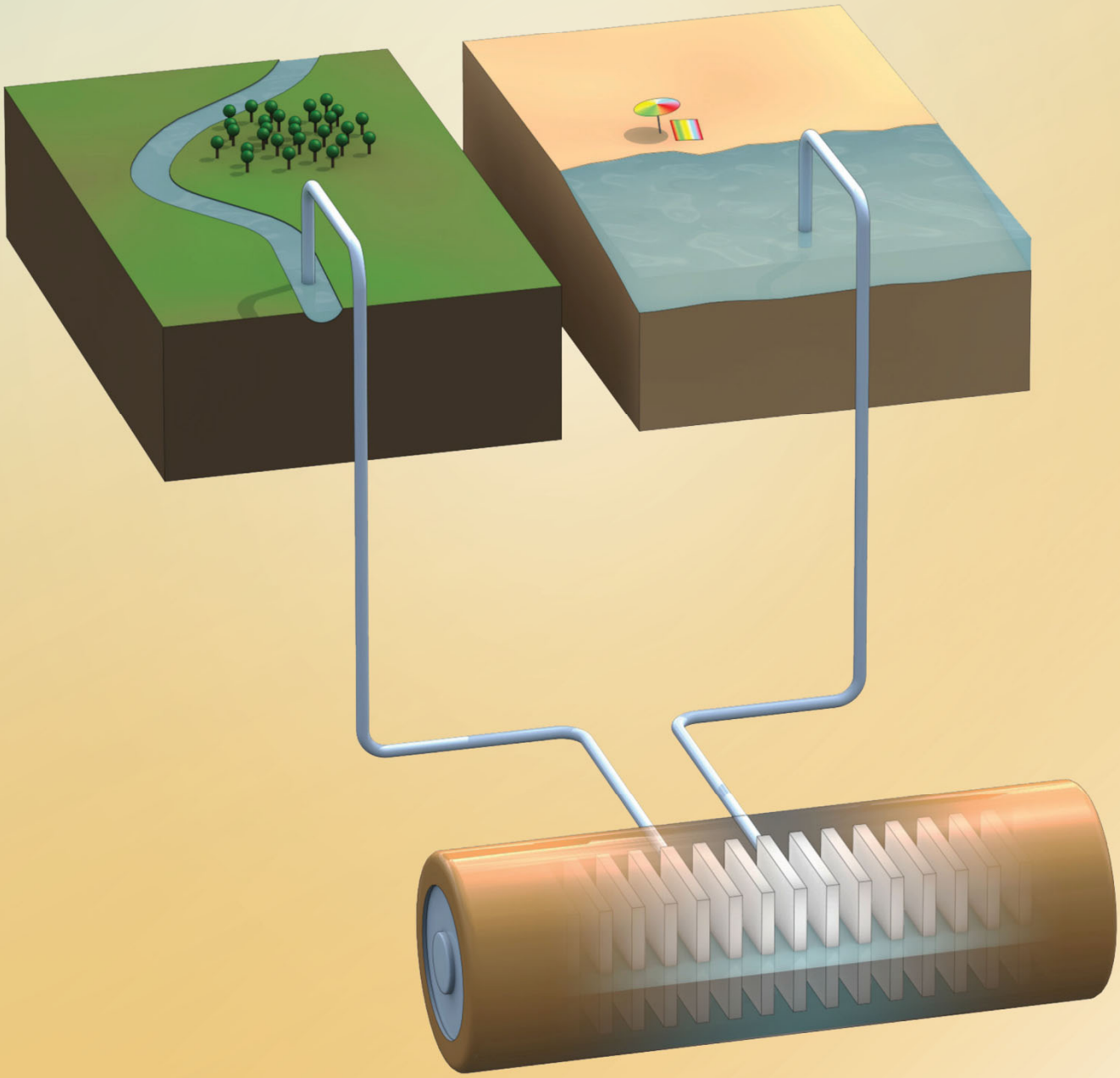

ENERGY GENERATION FROM MIXING SALT WATER AND FRESH WATER

SMART FLOW STRATEGIES FOR REVERSE ELECTRODIALYSIS

David A. Vermaas

ISBN 978-90-365-3573-1
DOI: 10.3990/1.9789036535731

Energy generation from mixing salt water and fresh water
PhD thesis, University of Twente, The Netherlands
With references, with summaries in English and Dutch
254 pages

Cover images: Jos Blomsma

Lay-out: David Vermaas

Printed by: Gildeprint Drukkerijen, The Netherlands

ENERGY GENERATION FROM MIXING SALT WATER AND FRESH WATER

SMART FLOW STRATEGIES FOR REVERSE ELECTRODIALYSIS

PROEFSCHRIFT

ter verkrijging van
de graad van doctor aan de Universiteit Twente,
op gezag van de rector magnificus,
prof.dr. H. Brinksma,
volgens besluit van het College voor Promoties,
in het openbaar te verdedigen
op vrijdag 17 januari 2014 om 12.45 uur

door

David Arie Vermaas
geboren op 6 oktober 1983
te Hoogeveen

Dit proefschrift is goedgekeurd door de promotor:
Prof. Dr. Ir. D.C. (Kitty) Nijmeijer
Professor Membrane Science & Technology
Faculty of Science and Technology
University of Twente

Promotion committee

Prof. Dr. G. van der Steenhoven (chairman)	University of Twente, The Netherlands
Prof. Dr. Ir. D.C. Nijmeijer (promotor)	University of Twente, The Netherlands
Prof. Dr. Ir. A. van den Berg	University of Twente, The Netherlands
Prof. Dr. Ir. L. Lefferts	University of Twente, The Netherlands
Dr. Ir. H.V.M. Hamelers	Wetsus, The Netherlands
Prof. Dr. J.G. Crespo	University of Lisbon, Portugal
Prof. Dr. M. Elimelech	Yale University, United States

Contents

Summary

S

Energy generation from mixing salt water and fresh water

Smart flow strategies for reverse electrodialysis

Reverse electrodialysis (RED) is a technology to capture renewable energy from mixing water with different salinities, for example from mixing seawater and river water (chapter 1). The salinity difference between seawater and river water induces a potential difference when both waters are separated by an ion exchange membrane, selective for cations (cation exchange membrane, CEM) or anions (anion exchange membrane, AEM). In a RED stack of alternating CEMs and AEMs, with seawater and river water in compartments between these membranes, the voltage over each membrane is accumulated and this voltage can be used as a power source, using e.g. electrodes and a (reversible) redox reaction that convert the ionic current into an electrical current.

Capacitive reverse electrodialysis (CRED), which uses capacitive electrodes instead of redox reactions, is a novel alternative for energy generation from salinity gradients (chapter 6). The storage of ions in the capacitive electrodes enables the conversion of the ionic current into an electrical current. The performance of such device is only slightly lower than that of RED with conventional a reversible redox reaction, but much higher compared to capacitive mixing technologies (CAPMIX). As an additional benefit, CRED can operate without the circulation of electrode rinse solution as no redox reactions are required, which simplifies the system and saves pumping costs.

The power density (i.e., the power per membrane area) of a RED stack fed by seawater and river water is limited by the electrical resistance of the river water compartment (chapter 2). The highest gross power density is obtained using compartments as thin as 100 μm. This power density (2.2 W/m^2) is, to the best of my knowledge, the highest experimentally obtained power for RED at this scale using seawater and river water.

The energy efficiency, which is the ratio of the actually obtained energy and the theoretically available energy, is another important output parameter of RED. The theoretical energy efficiency for RED using a single electrode pair is 40 - 95%, depending on the fraction of seawater with respect to river water and the flow orientation (chapter 5). This dependency is due to the interaction between the ion transport from the seawater compartments to the river water compartments and the corresponding electromotive force

and electrical resistance. Higher energy efficiencies are obtained when multiple stages are considered, e.g., using segmented electrodes.

A trade-off between energy efficiency and power density exists, as the energy efficiency is generally highest at low feedwater flow rates, while the power density benefits from higher feedwater flows (chapter 11). Thinner compartments improve both the power density and energy efficiency (chapter 2), but at the expense of a higher power consumption for pumping.

Profiled membranes, i.e., membranes with ion conductive ridges that create flow channels for feedwater, make the use of spacers obsolete and reduce the pumping power by a factor 4 - 8 (chapter 3 and 4). This would allow smaller intermembrane distances, leading to high (gross and net) power densities for micro-designs (chapter 11). The ion conductive ridges of the profiled membranes further reduce the ohmic resistance, compared to RED stacks with spacers. However, the non-ohmic resistance, due to concentration changes in the boundary layer and along the feedwater channels, is higher.

The diffusive boundary layer and the associated non-ohmic resistance can be decreased significantly when the feedwater is uniformly distributed over its compartments. Additional mixing promoters, such as twisted spacer structures or profiled membranes with 50 μm sub-corrugations, did not further decrease the boundary layer resistance at typical Reynolds numbers for RED ($Re < 100$) (chapter 4). The necessity for uniform feedwater distribution emphasizes the importance of prevention of colloidal fouling, which can make part of the feedwater compartments inaccessible, i.e., create preferential channeling (chapter 9 and 10).

Preferential channeling causes a serious decrease in performance, e.g., a 20% decrease in net power density when only 10% of the feedwater channels is inaccessible (chapter 9). The most sensitive indicator for preferential channeling is the response time of the voltage in chronopotentiometric measurements, as ion transport in feedwater channels that are inaccessible for flow is mainly dependent on diffusive transport.

Fouling of RED stacks using natural seawater and river water for a long period is mostly inorganic colloidal fouling (clay minerals, diatom shells) and in lesser degree scaling and biofouling (chapter 7). Stacks with spacers are much more sensitive to this colloidal fouling than stacks with profiled membranes. AEMs attract more colloidal fouling than CEMs, while non-conductive plastic sheets show no significant fouling at all. The use of air sparging effectively removes the majority of the colloidal fouling, which finally results in a significantly higher power density and lower pressure drop (chapter 10).

Multivalent ions (e.g., Mg^{2+} and SO_4^{2-}) that are present in natural feed waters cause a dramatic decrease in obtainable power density (chapter 8). The difference in ion valence and the associated difference in membrane potential induce transport of multivalent ions against the concentration gradient in exchange for monovalent ions. In addition, the apparent membrane permselectivity decreases when mixtures of monovalent and multivalent ions are present. The voltage response after a change in feedwater composition is in the order of hours (chapter 8), which is in agreement with observations using natural feed waters (chapter 10). Reversal of the electrical current direction, as imposed by switching the feed waters, results in higher power densities in the short term, and hence this approach can be applied as anti fouling strategy.

An ongoing challenge for RED is fouling prevention and dealing with multivalent ions. Although the current anti fouling strategies already temper the effects of fouling, they cannot prevent that the power density is roughly halved when using natural feedwater instead of artificial NaCl solutions. The economical perspective strongly depends on the practically obtained (net) power density and costs for fouling control (chapter 11). The financial feasibility can be estimated from the current state of the art, assuming the use of monovalent ions, optimization of the current design (resulting in a net power density of 2.7 W/m^2) and estimated costs for fouling control (1850 €/kW plus operational costs for pre-filtration with mesh sizes of tens of μm). Assuming these parameters can be met for large scale operation, RED can be competitive with other renewable energy sources at a membrane price of approximately 4 € per m^2 of membrane area.

Samenvatting

Energieopwekking door het mengen van zoet en zout water

Inventieve waterstroming in omgekeerde elektrodialyse

Omgekeerde elektrodialyse (*reverse electrodialysis*, RED) is een technologie om energie op te wekken uit het mengen van watertypen met verschillende zoutgehaltes, bijvoorbeeld zeewater en rivierwater (hoofdstuk 1). Het concentratieverschil tussen zee- en rivierwater zorgt voor een potentiaalverschil als deze vloeistoffen gescheiden zijn door een ionen-wisselend membraan dat selectief is voor kationen (CEM) of anionen (AEM). In een serie van afwisselend kation- en anionselectieve membranen met daartussen steeds zeewater of rivierwater kunnen deze individuele potentiaalverschillen bij elkaar worden opgeteld. Met behulp van elektroden en bijvoorbeeld een (reversibele) redox-reactie om de ionenstroom om te zetten in een elektrische stroom, kan deze spanning (de som van alle potentiaalverschillen over de membranen) worden gebruikt als een elektrische energiebron.

Capacitieve omgekeerde elektrodialyse (*capacitive reverse electrodialysis*, CRED) is een nieuwe wijze om energie uit verschillen in zoutconcentraties om te zetten in elektriciteit. Hier wordt gebruik gemaakt van capacitieve elektroden in plaats van redox-reacties (hoofdstuk 6). De opslag van ionen in de capacitieve elektroden zorgt voor de omzetting van de ionenstroom in een elektrische stroom. De prestaties van deze technologie zijn slechts marginaal lager dan die van RED met reversibele redox-reacties, maar veel hoger dan die van andere capacitieve technieken om energie op te wekken uit zoet en zout water (CAPMIX). Daarentegen hoeft er bij CRED geen elektrodevloeistof te worden rondgepompt, hetgeen het systeem eenvoudiger maakt en pompkosten reduceert.

De vermogensdichtheid (ofwel het vermogen per membraanoppervlak) van een RED-opstelling op basis van zee- en rivierwater wordt met name beperkt door de elektrische weerstand van de rivierwatercompartimenten (hoofdstuk 2). De hoogste bruto vermogensdichtheid is behaald wanneer deze compartimenten slechts 100 μm dik zijn. Deze vermogensdichtheid (2.2 W/m^2) is, voor zover bekend, de hoogst behaalde experimentele waarde voor RED op deze schaal met zeewater en rivierwater.

De energie-efficiëntie, die de verhouding weergeeft tussen de daadwerkelijk verkregen energie en de theoretisch beschikbare energie, is een andere belangrijke parameter voor RED. De theoretische energie-efficiëntie voor een RED-opstelling met een enkele set elektroden is 40 - 95%, afhankelijk van de verhouding tussen zee- en rivierwater en de

stroomrichting van het water (hoofdstuk 5). Deze factoren spelen een rol vanwege de interactie tussen het iontransport van de zeewatercompartimenten naar de rivierwatercompartimenten en de bijbehorende elektrische spanning en weerstand. Hogere energie-efficiënties zijn mogelijk als het proces in meerdere stappen wordt uitgevoerd, bijvoorbeeld door het gebruik van gesegmenteerde elektroden.

Een balans tussen vermogensdichtheid en energie-efficiëntie is nodig, omdat de energie-efficiëntie maximaal is bij lage watertoevoer en de vermogensdichtheid juist maximaal is bij hoge watertoevoer (hoofdstuk 11). Dunne compartimenten verhogen zowel de vermogensdichtheid als de energie-efficiëntie (hoofdstuk 2), maar gaan ten koste van het benodigde pompvermogen.

Geprofileerde membranen, ofwel membranen met iongeleidende richels en tussenliggende kanalen voor waterstroming, maken het gebruik van spacers overbodig en verminderen het benodigde pompvermogen met een factor 4 - 8 (hoofdstuk 3 en 4). Dit concept maakt het mogelijk om dunnere compartimenten te gebruiken, wat leidt tot hogere (bruto en netto) vermogensdichtheden voor micro-ontwerpen (hoofdstuk 11). De iongeleidende richels van het geprofileerde membraan verlagen tevens de ohmse weerstand in vergelijking met een vergelijkbaar systeem met spacers. Daarentegen is de niet-ohmse weerstand hoger voor deze geprofileerde membranen als gevolg van limiteringen in iontransport in de grenslagen en compartimenten en de bijbehorende concentratieveranderingen.

De diffusiegrenslaag in de watercompartimenten, nabij de membranen, en de bijbehorende niet-ohmse weerstand kan sterk worden gereduceerd door het water homogeen te verdelen over de compartimenten. Verdere maatregelen om menging te stimuleren, zoals spiraalvormige spacerstructuren of geprofileerde membranen met sub-corrugaties, geven geen significante verlaging van de grenslaagweerstand voor gebruikelijke Reynoldsgetallen ($Re < 100$) (hoofdstuk 4). De vereiste gelijkmatige waterverdeling maakt het extra belangrijk om colloïdale vervuiling en dien ten gevolge verstopping van een deel van de waterkanalen (preferente kanaalvorming) te voorkomen.

Preferente kanaalvorming geeft een sterke afname in prestatie; de vermogensdichtheid daalt met 20% zodra slechts 10% van de waterkanaaltjes verstopt is (hoofdstuk 9). De meest gevoelige indicator voor preferente stroomkanalen is de responstijd van de spanning, bij een verandering van de stroomsterkte, daar het iontransport in de verstopte kanaaltjes voornamelijk afhankelijk is van diffusie.

Vervuiling van RED-opstellingen, zoals dat optreedt bij langdurig gebruik van daadwerkelijk zee- en rivierwater, bestaat voornamelijk uit anorganische colloïden

(kleiplaatjes en diatomeeresten) en in mindere mate uit aanslag en biologische vervuiling (hoofdstuk 7). Opstellingen met spacers zijn veel gevoeliger voor colloïdale vervuiling dan opstellingen met geprofileerde membranen. Anionwisselende membranen trekken meer colloïdale vervuiling aan dan kationwisselende membranen, terwijl ongeladen plastic folie nauwelijks vervuilt. De meeste colloïdale vervuiling kan effectief worden verwijderd door perslucht door de opstelling te blazen, wat een significant hogere vermogensdichtheid geeft (hoofdstuk 10).

Multivalente ionen (zoals Mg^{2+} en SO_4^{2-}), die van nature aanwezig zijn in zee- en rivierwater, veroorzaken een drastische afname van de vermogensdichtheid (hoofdstuk 8). Het verschil in valentie tussen eenwaardige ionen (Na^+ en Cl^-) en deze meerwaardige ionen, en de daaraan gekoppelde membraanpotentiaal, geeft transport van multivalente ionen in een richting tegengesteld aan de concentratiegradiënt. Dit gaat ten koste van de concentratiegradiënt van monovalente ionen en resulteert daardoor in een aanzienlijk lagere vermogensdichtheid en efficiëntie. Daarnaast leidt het gebruik van mengsels van monovalente en multivalente ionen tot een verlaging van de permselectiviteit van de membranen. De respons van de membraanspanning, zodra de watersamenstelling wordt gewijzigd, is in de orde van uren (hoofdstuk 8), wat overeenkomt met de observaties bij gebruik van echt zee- en rivierwater (hoofdstuk 10). Het omdraaien van de elektrische stroomrichting, wat kan worden bereikt door zee- en rivierwater om te wisselen, geeft een hogere vermogensdichtheid op de korte termijn, en kan dus worden gebruikt als strategie om membraanvervuiling tegen te gaan.

Huidige uitdagingen voor RED zijn het tegengaan van vervuiling en het reduceren van de effecten van multivalente ionen (zoals Mg^{2+} en SO_4^{2-}). Hoewel de huidige strategieën de effecten van vervuiling kunnen beperken, kan nog niet worden voorkomen dat de vermogensdichtheid grofweg wordt gehalveerd zodra echt zee- en rivierwater worden gebruikt in plaats van synthetische oplossingen van NaCl. Het economische vooruitzicht van RED is sterk afhankelijk van de daadwerkelijk verkregen netto vermogensdichtheid en de kosten voor de beheersing van vervuiling (hoofdstuk 11). De financiële haalbaarheid kan worden geschat op basis van de *state of the art*, verkregen met monovalente ionen, een optimaal ontwerp (met een netto vermogensdichtheid van 2.7 W/m^2) en geschatte kosten voor beheersing van vervuiling (1850 €/kW plus operationele kosten). Op basis van deze gegevens is RED concurrerend met andere duurzame energiebronnen bij een membraanprijs van ongeveer €4,- per m^2 membraan.

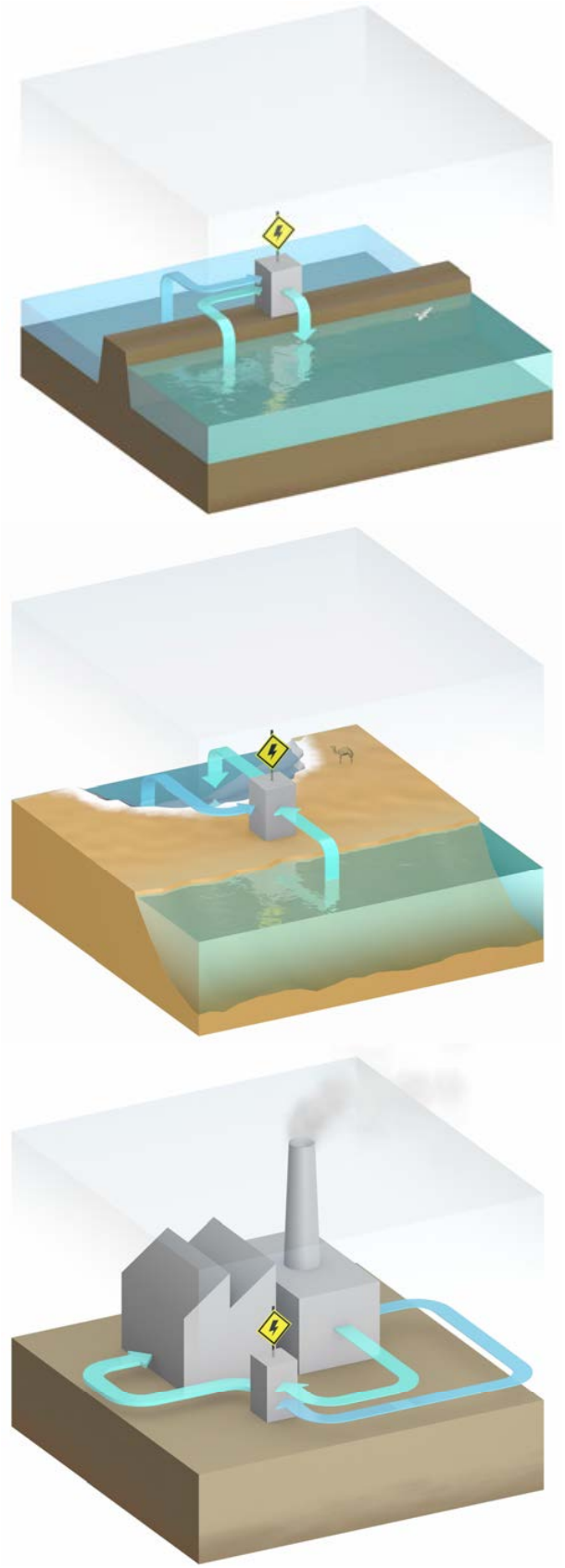

Chapter 1

Introduction

1.1 Background

Renewable energy can be captured when mixing salt water and fresh water, e.g., seawater and river water. This relatively unknown source of energy was recognized already in the '50s, when Pattle presented his first experiments on the ‘hydroelectric pile’ [1], which is nowadays known as reverse electrodialysis (RED). The potential for energy generation from mixing salt and fresh water is huge; the amount of energy that can be captured theoretically when mixing the global river water runoff with seawater meets the present worldwide electricity demand [2, 3]. In addition, energy can be generated from closed loop systems and industrial water streams (as discussed later), which leads to an even bigger potential for energy generation from salinity gradients.

Despite the large potential for RED, its first publication [1] drew only minor attention, as indicated by the low number of citations after 20 years (7 according to Google Scholar; 4 according to Web of Science). New research on power generation from salinity gradients (salinity gradient power, SGP) was performed in the late seventies and early eighties [4-8] and the last decade [9-19]. In these same periods, attention was also brought to other technologies to generate salinity gradient power, for example using pressure retarded osmosis (PRO) [20-25]. These peaks in attention for salinity gradient power are driven by the increasing price of fossil fuels and discussions on pollution and hence an increased demand for renewable energy sources.

In the meantime, other renewable energy sources such as wind, solar and hydropower have developed much faster and are well established within the present energy mix. These renewable energy sources have an even larger potential in terms of theoretical capacity compared to salinity gradient power. However, as the contribution of solar and wind energy to the electrical grid grows, the unpredictable fluctuations in power production of these sources, dependent on local sunshine and wind, become an increasing problem. In contrast, salinity gradient power can be better predicted, and in case of a fresh water lake, even regulated to compensate the fluctuating production of other renewable energy sources. In addition to the large potential for SGP, established renewable energy sources create an extra reason to develop large scale production of salinity gradient power.

1.2 Principle

Energy can be captured from mixing salt water and fresh water in reverse electrodialysis (RED) using ion exchange membranes, as illustrated in Figure 1.1. The cell comprises a number of alternating cation exchange membranes (CEMs) and anion exchange membranes (AEMs) separated by spacers to provide a flow compartment for the feed waters. The ion exchange membranes are only selective for cations (CEM) or anions (AEM). When salt water is at one side of such membrane and fresh water at the other side, a voltage is created over each ion selective membrane, due to the Donnan potentials at the membrane-water interfaces. In fact, the voltage over the membrane balances the selective diffusion of cations or anions when no current is generated. The voltage over each membrane accumulates when CEMs and AEMs are stacked alternately, with salt water and fresh water supplied in between the membranes. This voltage can be used to power an electrical device, using electrodes and e.g. a redox reaction to convert the ionic current into electrical current. As an alternative for the redox reactions, capacitive electrodes can be used [26].

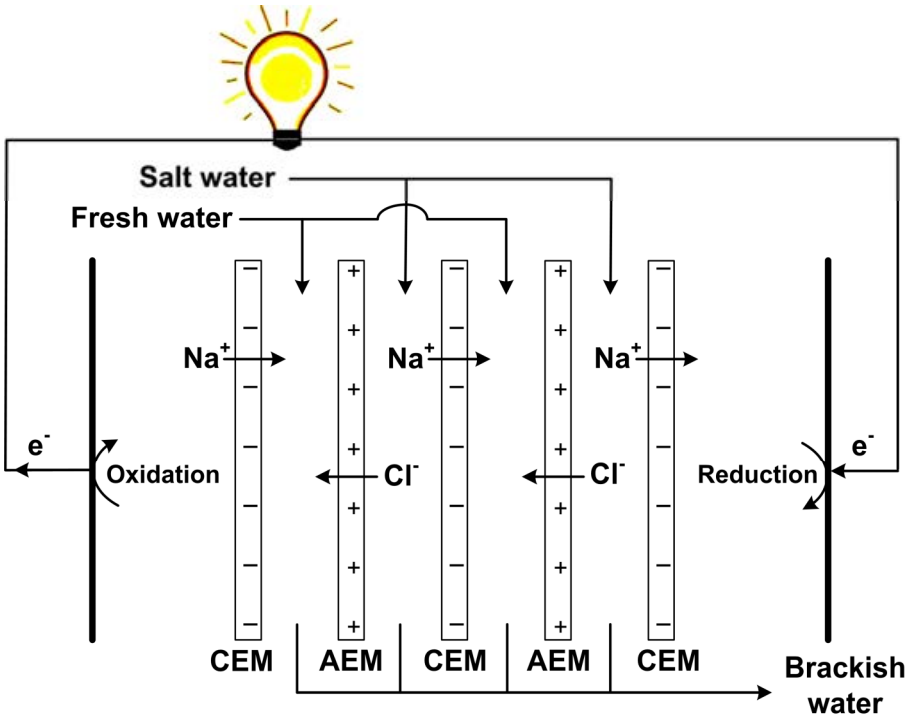

Figure 1.1: Principle of RED. In this case, a reversible redox reaction converts the ionic current into an electrical current.

1.3 Hydrological cycle

To understand that salinity gradient power is a renewable energy source, the hydrological cycle can be considered. The energy generated with salinity gradient energy originates from the increase in entropy when water streams with different salinity mix. To establish a continuous supply of salinity gradient energy, a continuous source separating salt water and fresh water is required. In case of mixing seawater and river water, salt and fresh water are provided when fresh water evaporates from the sea, as illustrated in the hydrological cycle (Figure 1.2).

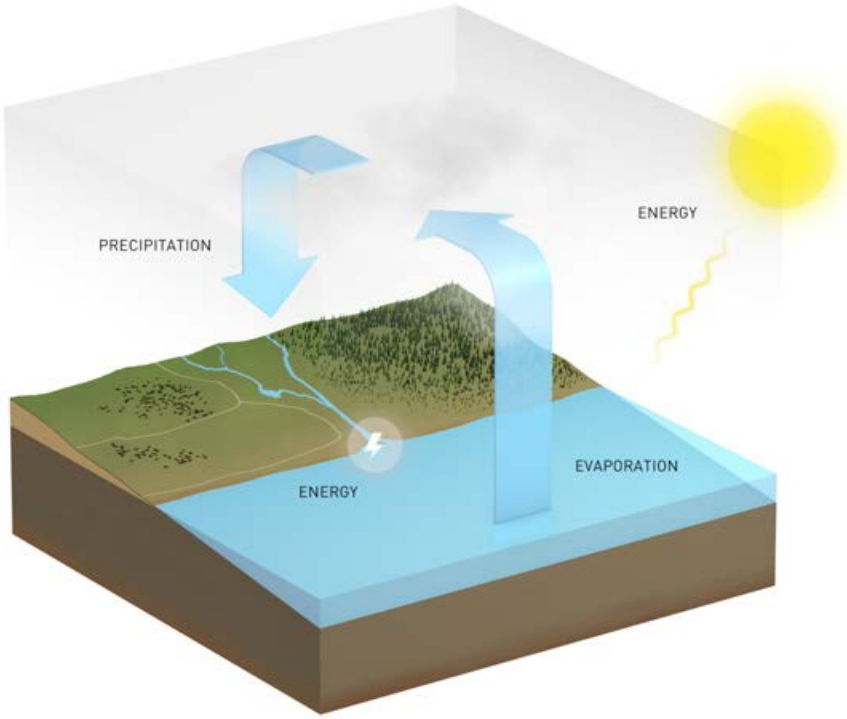

Figure 1.2: Hydrological cycle. Salinity gradient energy can be captured continuously because of the energy that enters the system when separating water and salt during the evaporation of seawater.

Evaporation of seawater requires slightly more energy than evaporating fresh water. Figure 1.2 illustrates that heat (provided by the sun) is used for this additionally required energy. The evaporated water condensates in clouds and subsequently precipitates as rain or snow. This water is collected into rivers and transported to the sea. When river water is discharged into the sea, the energy that was required to separate salt water and fresh water can be converted into electrical energy. This closed hydrological cycle ensures that salinity gradient energy, when using seawater and river water, is indeed renewable.

1.4 Applications

Electricity can be generated from different sources as long as there exists a salinity gradient. This section will discuss the application of RED using seawater and river water (Figure 1.3), using brine and seawater or river water (Figure 1.4), and using closed systems (Figure 1.5).

1.4.1 Seawater and river water

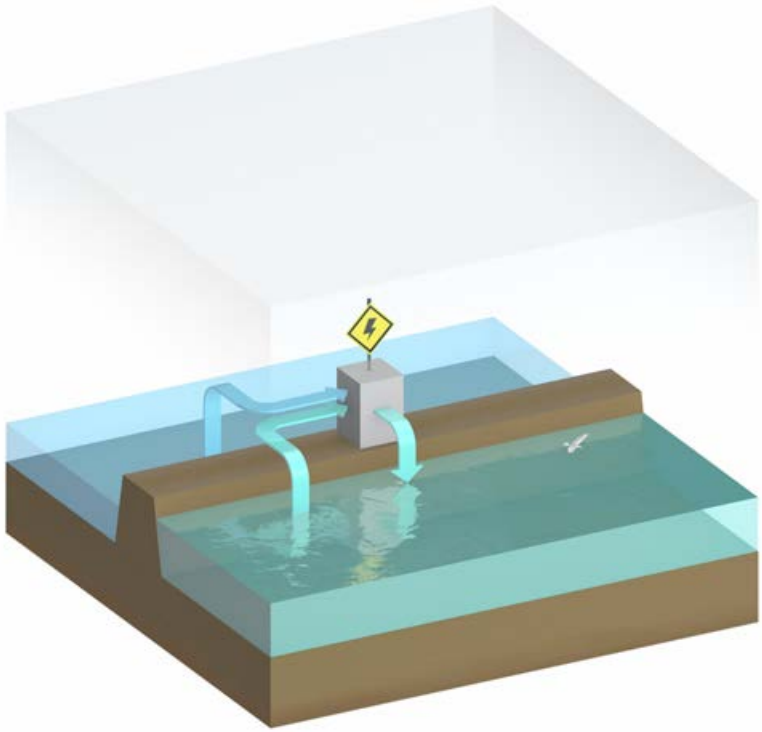

Figure 1.3: Illustration of reverse electrodialysis plant mixing seawater and river water.

The energy that can be obtained when mixing 1 m^3 seawater (containing 30 gram of NaCl per liter) and 1 m^3 river water (containing 1 gram of NaCl per liter) is 1.39 MJ, equivalent to 0.386 kWh, as given by the increase in Gibbs free energy of mixing [13, 25]. This energy density is low compared to the energy density of fossil fuels, which is typically 32000 MJ per m^3 [27]. However, when comparing the energy density of salinity gradient energy to other technologies that capture energy from water, it is revealed that this value is actually high. The energy that can be obtained from mixing 1 m^3 seawater and 1 m^3 river water (1.39 MJ) equals the potential energy when 1 m^3 water falls down for 142 meter. In other words, the energy density in salinity gradient energy is much larger than using tidal or wave energy, which have typical water level amplitudes of only a few meter, and comparable to that of hydropower.

Since the volume of seawater is virtually infinite, it could be tempting to use excess sea water. In fact, when mixing river water with an excess of seawater, the theoretically obtained energy per m^3 river water is even increasing to 2.1 MJ. However, this larger amount of energy cannot be used as efficient as mixing equal quantities in practical applications of RED, as explained in chapter 5 of this thesis. Therefore, the energy density is often limited by the availability of river water.

The potential for power generation from mixing seawater and river water is listed for several rivers in Table 1.1. Although the rivers with the largest discharge (e.g., Amazon) have the largest theoretical potential, the practical potential is smaller for these rivers due to the diffuse salinity gradient in its estuary [28]. Moreover, these tropical rivers generally convey a large amount of sediment and have a high biological activity, which enhances the fouling potential of RED. Rivers in moderate climates, such as the Rhine, Mississippi and Yangtze, benefit additionally from the available infrastructure and strong demand for renewable energy sources in those areas [16]. Therefore, these locations are regarded as the best potential locations to harvest salinity gradient energy.

Table 1.1: Theoretical and technical potentials for applications of RED using seawater and river water. The theoretical potential is calculated from the discharge multiplied with the theoretical energy that comes available when mixing the feed waters. The technical potential is derived from the minimum monthly energy densities, using constant river water salinity and seawater salinities as from the National Oceanic Atmospheric Administration (NOAA) database, and assuming a energy efficiency of 70% [28].

River	Discharge (m^3/s)	Theoretical potential (calculated from discharge) (GW)	Technical potential (GW)
Global runoff	1100000 [29]	1529	983 [28]
Amazon river	200000 [29]	278	8.3 [30]
Congo river	57000 [29]	79	57.3 [30]
Mississippi river	18000 [29]	25	17.8 [30]
Yangtze river	13800 [16]	19	11.5 [16]
Rhine	1846 [30]	2.6	2.0 [30]

1.4.2 Brine and seawater or river water

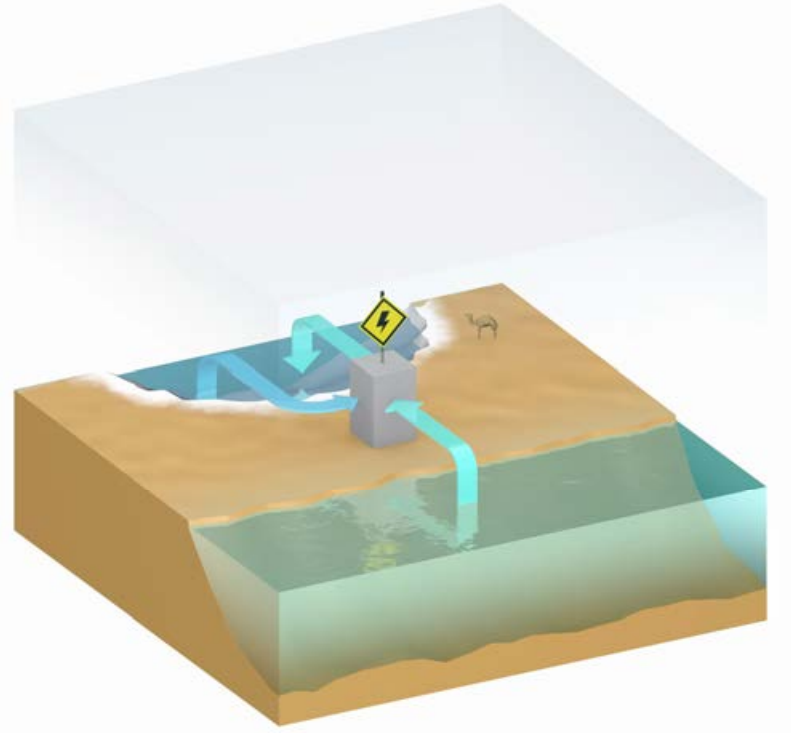

Figure 1.4: Illustration of reverse electrodialysis plant mixing seawater and brine.

The energy density increases rapidly when using feedwater streams that are more saline than seawater, i.e., brine. In the extreme case, when mixing 1 m^3 saturated NaCl brine (5.4 M NaCl) and 1 m^3 river water, approximately 17 MJ can be obtained. Also the salinity difference between brine and seawater can be used to generate energy, in which seawater is used as a diluted feedwater stream (Figure 1.4). A European sponsored consortium, named REAPower (www.reapower.eu), investigates the possibilities for energy generation from brine and seawater using RED.

The practical potential for such cases can be found in hypersaline lakes, such as the Dead Sea and the Great Salt Lake [31], using brine from waste streams [32] or using brine from salt mining [27, 33]. In all cases, the brine stream can be mixed with an inflowing river as diluted feed. In case of the Dead Sea, mixing with seawater may be even an option, as an old idea to connect the Dead Sea to the Red Sea has revived in 2013 [34]. The potentials for these options are estimated in Table 1.2.

The use of brine in RED benefits from its high available energy density and high feedwater conductivity. Consequently, the power density is significantly higher than obtained when using seawater and river water [35]. Moreover, brine streams have a low biofouling

potential, as the large salinity differences between brine and diluted streams create a large osmotic shock [36].

On the other hand, the feedwater streams when using brine and diluted water are often very limited in volumetric flow. Moreover, the energy efficiency in RED generally decreases when the salinity of the feedwater increases, which further limits the total capacity of power plants using brine as feedwater [35]. The energy efficiency can be larger when using pressure retarded osmosis for brine streams [9]. Therefore, only relatively small power plants seem to be possible when using brine as a feed in RED.

Table 1.2: Theoretical and technical potentials for applications of RED using brines or closed loop systems. The theoretical potential is calculated from the discharge multiplied with the theoretical energy that comes available when mixing the feed waters.

Application	Sources	Flux of water or CO_2	Theoretical potential (calculated from discharge, heat or CO_2 emission) (GW)
Brine vs. fresh	Great Salt Lake and rivers	125 m^3/s [29]	1.8
Brine vs. sea	Dead Sea and Red Sea	25 m^3/s	0.3
Closed loop (thermolytic solution)	Waste heat	-	3993 [3]
Closed loop	CO_2 in exhaust and CO_2 in air	23 Gton CO_2 per year [37]	179 [37]

1.4.3 Closed loop systems

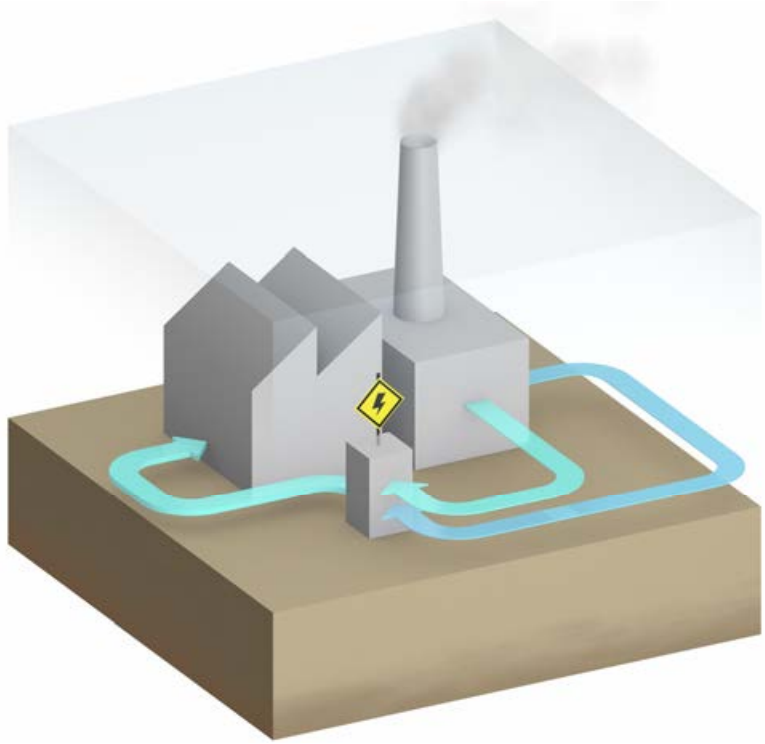

Figure 1.5: Illustration of reverse electrodialysis plant mixing concentrated and diluted streams (e.g., using waste heat) from industry.

A third alternative is to re-use the feedwater in RED and re-generate the salinity difference in a closed loop system (Figure 1.5). The most obvious system in this category is the evaporation of (salt) water in solar ponds and collection of evaporated water [32], to create brine and condensate, which can be used to generate electricity in RED, as explained in the previous section.

In addition, many other possibilities for closed systems can be developed, as closed systems are not limited by the salts that are present in natural waters. For example, thermolytic solutions (e.g., ammonium bicarbonate) can be used to create a salinity difference using waste heat in a distillation column and subsequently this concentration difference can be used to feed a RED stack [38-41]. As approximately 2/3 of the energy in conventional power plants is spent as waste heat, the theoretical potential can be roughly estimated (Table 1.2). Although the potential of this application is enormous and larger than for all other applications, the technical potential may be reduced due to the poor thermal efficiency when converting heat into salinity gradients [41]. Another recent example is dissolving high concentrations of CO_2 in water, creating carbonic acid, which can be used to generate

electricity when mixed with water and low concentrated CO_2 (e.g., from air) [37]. These technologies use salinity gradients to convert virtually low-quality energy (waste heat or CO_2 in the latter cases) into useful electricity.

As most of these systems are invented recently, these technologies are not yet optimized and consequently accompany low power densities. However, when operational parameters are tuned and these technologies will develop further, higher power densities are envisaged. Moreover, because of the industrial origin of the feedwater, the fouling potential is very low and the concentrations in closed systems can be controlled better than when using natural feedwater.

1.5 Challenges

This thesis focuses on the generation of electricity from mixing seawater and river water, as this case has most certainly potential for power generation at large scale. Nevertheless, most improvements for RED using seawater and river water can be translated to other applications of RED as well, as all mentioned applications of RED are closely related and share to a large extend the same challenges.

Previous research showed that a high energy efficiency, up to 80%, can be obtained in reverse electrodialysis [13]. However, the earlier reported power densities were regarded too low for commercial application [10, 42, 43]. A major limitation is the electrical resistance of the stack. This stack resistance comprises an ohmic component, which can be subdivided into the membrane resistance and the feedwater resistance, and a non-ohmic component, due to the concentration changes in the boundary layer and along the flow channel. Reduction of these resistances has a direct impact on the power output obtainable in RED [44].

The feedwater resistance and the non-ohmic resistance are strongly dependent on the dimensions, geometry and type of the feedwater compartments. For example, previous research indicated that when the non-conductive spacer, which is traditionally in between the membranes, is replaced for an ion-conductive spacer, the power density increases with a factor 3 to 4 [45]. For ion-conductive spacers, the non-ohmic resistance was identified as a major component for the stack resistance. The large influence on the power density and the large contribution of the non-ohmic resistance, due to a single change in type of feedwater compartment, reveals opportunities for further improving the power density by altering the dimensions, geometry and type of the feedwater compartments.

In particular, RED systems without the use of (non-conductive) spacers are of interest, as previous research also pointed out that spacerless systems are insensitive for biological fouling [36]. Because fouling – composed of scaling, biological or colloidal in nature – is an extensive problem in many membrane processes [46-48], improving the power density and reducing fouling at the same would be a valuable combination.

1.6 Aim

The aim of this research is to understand how the obtained power density for sustainable energy generation from mixing seawater and river water in reverse electrodialysis can be improved, while focusing on the water flow behavior in a RED stack. This includes the power density under laboratory conditions as well as effects such as fouling under natural conditions.

1.7 Outline

This thesis can be divided into two major parts. The first part, chapter 2 – 6, concerns the investigation of the limiting factors in the present operation of RED and presents new strategies that improve the obtained power density in RED. The second part, chapter 7 – 10, investigates the occurrence and influence of fouling in RED and proposes strategies to detect, reduce and control the effects of fouling.

Chapter 2 evaluates the contribution of the individual stack elements in the RED stack to the total electrical resistance and demonstrates the importance of the intermembrane distance. Improvements in this field doubled the power density with respect to the state of the art at that moment.

Chapter 3 introduces a novel RED design with profiled (i.e., corrugated) membranes that integrate the membrane and spacer functionality. This first prototype already achieved a higher power density compared to a traditional design with spacers, although the results indicate that further improvement is possible when reducing the non-ohmic resistance, e.g., reducing the concentration boundary layer.

Chapter 4 focuses on enhanced mixing in the concentration boundary layer, using mixing promoters in stacks with spacers and stacks with profiled membranes. The influence of these mixing promoters on the stack performance is elaborated in detail.

Chapter 5 evaluates the theoretical maximum in energy efficiency, and the dependency of the feedwater flow direction and electrode segmentation. This research helps understanding where energy is lost in an idealized system, sets directions for further improvements and gives insight in interior phenomena occurring in a RED stack.

Chapter 6 presents a novel concept, i.e., capacitive reverse electrodialysis (CRED), based on RED and capacitive mixing (CAPMIX). It uses capacitive electrodes to generate electricity from salinity gradients. This research demonstrates that high power densities can be obtained while redox reactions and the corresponding chemicals are no longer required.

Chapter 7 maps the effect of fouling in RED for designs with spacers and profiled membranes. This research shows that the degree and type of fouling is strongly dependent on the membrane charge, which disables to use the knowledge from fouling in filtration and osmosis membrane technologies.

Chapter 8 demonstrates the individual influence of mixtures with multivalent cations (Mg^{2+}) and/or anions (SO_4^{2-}) and NaCl on the electrical performance of different RED stacks. This research explains the unexpectedly large influence of multivalent ions and emphasizes the differences between heterogeneous and homogeneous membranes.

Chapter 9 imitates the occurrence of preferential channeling, i.e., when a part of the feedwater compartment is inaccessible for water flow, to detect and understand these effects individually. A method for early detection of preferential channeling is developed.

Chapter 10 provides a first step to reduce the effects of fouling in RED by analyzing the effectiveness of two anti fouling strategies: periodic feedwater switch and air sparging. The significant effects of these anti fouling strategies on the obtained power density show the importance of using and further developing anti fouling strategies for RED.

Chapter 11 finally gives a discussion on which parameters in the present RED technology can be tuned to improve the performance. Furthermore, this chapter indicates the financial feasibility of RED in the current and future state.

References

1. Pattle, R. E., Production of Electric Power by mixing Fresh and Salt Water in the Hydroelectric Pile. *Nature* **1954,** *174*, (4431), 660-660.

2. Jones, A. T.; Finley, W., Recent Developments in Salinity Gradient Power. In *Oceans 2003*, **2003**; Vol. 4, pp 2284-2287.

3. EIA, *International energy outlook 2011*. U.S. Department of Energy: Washington D.C., **2011**; 301 p.

4. Clampitt, B. H.; Kiviat, F. E., Energy Recovery from Saline Water by Means of Electrochemical Cells. *Science* **1976,** *194*, 719-720.

5. Weinstein, J. N.; Leitz, F. B., Electric Power from Differences in Salinity: The Dialytic Battery. *Science* **1976,** *191*, (4227), 557-559.

6. Lacey, R. E., Energy by Reverse Electrodialysis. *Ocean Engineering* **1980,** *7*, (1), 1-47.

7. Forgacs, C., Recent developments in the utilization of salinity power. *Desalination* **1982,** *40*, (1-2), 191-195.

8. Audinos, R., Electrodialyse inverse. Etude de l'energie electrique obtenue a partir de deux solutions de salinites differentes. *Journal of Power Sources* **1983,** *10*, (3), 203-217.

9. Post, J. W.; Veerman, J.; Hamelers, H. V. M.; Euverink, G. J. W.; Metz, S. J.; Nijmeijer, K.; Buisman, C. J. N., Salinity-gradient power: Evaluation of pressure-retarded osmosis and reverse electrodialysis. *Journal of Membrane Science* **2007,** *288*, (1-2), 218-230.

10. Turek, M.; Bandura, B., Renewable energy by reverse electrodialysis. *Desalination* **2007,** *205*, 67-74.

11. Długołęcki, P. E.; Nijmeijer, K.; Metz, S. J.; Wessling, M., Current status of ion exchange membranes for power generation from salinity gradients. *Journal of Membrane Science* **2008,** *319*, (1-2), 214-222.

12. Veerman, J.; Post, J. W.; Saakes, M.; Metz, S. J.; Harmsen, G. J., Reducing power losses caused by ionic shortcut currents in reverse electrodialysis stacks by a validated model. *Journal of Membrane Science* **2008,** *310*, (1-2), 418-430.

13. Post, J. W.; Hamelers, H. V. M.; Buisman, C. J. N., Energy Recovery from Controlled Mixing Salt and Fresh Water with a Reverse Electrodialysis System. *Environmental Science & Technology* **2008,** *42*, (15), 5785-5790.

14. Brauns, E., Salinity gradient power by reverse electrodialysis: effect of model parameters on electrical power output. *Desalination* **2009,** *237*, 378–391.

15. Długołęcki, P. E.; Gambier, A.; Nijmeijer, K.; Wessling, M., Practical Potential of Reverse Electrodialysis As Process for Sustainable Energy Generation. *Environmental Science & Technology* **2009,** *43*, (17), 6888-6894.

16. Gao, X.; Kroeze, C., The effects of blue energy on future emissions of greenhouse gases and other atmospheric pollutants in China. *Journal of Integrative Environmental Sciences* **2012,** *9*, (sup1), 177-190.

17. Veerman, J.; Saakes, M.; Metz, S. J.; Harmsen, G. J., Electrical Power from Sea and River Water by Reverse Electrodialysis: A First Step from the Laboratory to a Real Power Plant. *Environmental Science & Technology* **2010,** *44*, (23), 9207-9212.

18. Burheim, O. S.; Seland, F.; Pharoah, J. G.; Kjelstrup, S., Improved electrode systems for reverse electro-dialysis and electro-dialysis. *Desalination* **2012,** *285*, (0), 147–152.

19. Guler, E.; Zhang, Y.; Saakes, M.; Nijmeijer, K., Tailor-Made Anion-Exchange Membranes for Salinity Gradient Power Generation Using Reverse Electrodialysis. *ChemSusChem* **2012,** *5*, (11), 2262-2270.

20. Loeb, S., Osmotic Power Plants (comments on paper of R.S. Norman). *Science* **1975,** *189*, (4203), 654-655.

21. Gerstandt, K.; Peinemann, K. V.; Skilhagen, S. E.; Thorsen, T.; Holt, T., Membrane processes in energy supply for an osmotic power plant. *Desalination* **2008,** *224*, 64-70.

22. Achilli, A.; Childress, A. E., Pressure retarded osmosis: From the vision of Sidney Loeb to the first prototype installation — Review. *Desalination* **2010,** *261*, 205-211.

23. She, Q.; Jin, X.; Tang, C. Y., Osmotic power production from salinity gradient resource by pressure retarded osmosis: Effects of operating conditions and reverse solute diffusion. *Journal of Membrane Science* **2012,** *401-402*, (0), 262-273.

24. Yip, N. Y.; Tiraferri, A.; Phillip, W. A.; Schiffman, J. D.; Hoover, L. A.; Kim, Y. C.; Elimelech, M., Thin-Film Composite Pressure Retarded Osmosis Membranes for Sustainable Power Generation from Salinity Gradients. *Environmental Science & Technology* **2011,** *45*, (10), 4360-4369.

25. Yip, N. Y.; Elimelech, M., Thermodynamic and Energy Efficiency Analysis of Power Generation from Natural Salinity Gradients by Pressure Retarded Osmosis. *Environmental Science & Technology* **2012,** *46*, (9), 5230-5239.

26. Vermaas, D. A.; Bajracharya, S.; Sales, B. B.; Saakes, M.; Hamelers, B.; Nijmeijer, K., Clean energy generation using capacitive electrodes in reverse electrodialysis. *Energy & Environmental Science* **2013,** *6*, (2), 643-651.

27. Wick, G. L.; Isaacs, J. D., Salt Domes: Is There More Energy Available from Their Salt than from Their Oil? *Science* **1978,** *199*, (4336), 1436-1437.

28. Kuleszo, J.; Kroeze, C.; Post, J. W.; Fekete, B. M., The potential of blue energy for reducing emissions of CO2 and non-CO2 greenhouse gases. *Journal of Integrative Environmental Sciences* **2010,** *7*, (S1), 89-96.

29. Wick, G. L., Power from salinity gradients. *Energy* **1978,** *3*, (1), 95-100.

30. Kuleszo, J. The global and regional potential of salinity-gradient power. MSc thesis Wageningen University, **2008**.

31. Loeb, S., Energy production at the Dead Sea by pressure-retarded osmosis: challenge or chimera? *Desalination* **1998,** *120*, (3), 247-262.

32. Brauns, E., Towards a worldwide sustainable and simultaneous large-scale production of renewable energy and potable water through salinity gradient power by combining reversed electrodialysis and solar power? *Desalination* **2008,** *219*, 312–323.

33. Williams, W. G.; Wick, G. L.; Isaacs, J. D., Mineral Salt: A Source of Costly Energy? *Science* **1979,** *203*, (4378), 376-377.

34. Al-Ghazawy, O., World Bank backs Red-Dead Sea canal. *Nature Middle East* **2013**.

35. Daniilidis, A.; Vermaas, D. A.; Herber, R.; Nijmeijer, K., Effect of salinity gradient on power output in reverse electrodialysis. *Renewable energy* **2013**, (submitted).

36. Post, J. W. Blue Energy: electricity production from salinity gradients by reverse electrodialysis. PhD thesis Wageningen University, **2009**.

37. Hamelers, H. V. M.; Schaetzle, O.; Paz-Garcia, J. M.; Biesheuvel, P. M.; Buisman, C. J. N., Harvesting Energy from CO2 Emissions. *Environmental Science & Technology Letters* **2013**.

38. Luo, X.; Cao, X.; Mo, Y.; Xiao, K.; Zhang, X.; Liang, P.; Huang, X., Power generation by coupling reverse electrodialysis and ammonium bicarbonate: Implication for recovery of waste heat. *Electrochemistry Communications* **2012,** *19*, (0), 25-28.

39. Cusick, R. D.; Kim, Y.; Logan, B. E., Energy Capture from Thermolytic Solutions in Microbial Reverse-Electrodialysis Cells. *Science* **2012,** *335*, (6075), 1474-1477.

40. Hatzell, M. C.; Logan, B. E., Evaluation of Flow Fields on Bubble Removal and System Performance in an Ammonium Bicarbonate Reverse Electrodialysis Stack. *Journal of Membrane Science* **2013**, (in press).

41. McGinnis, R. L.; McCutcheon, J. R.; Elimelech, M., A novel ammonia–carbon dioxide osmotic heat engine for power generation. *Journal of Membrane Science* **2007,** *305*, (1), 13-19.

42. Post, J. W.; Goeting, C. H.; Valk, J.; Goinga, S.; Veerman, J.; Hack, P. J. F. M., Towards implementation of reverse electrodialysis for power generation from salinity gradients. *Desalination and water treatment* **2010,** *16*, 182-193.

43. Daniilidis, A.; Herber, R.; Vermaas, D. A., Upscale potential and financial feasibility of a reverse electrodialysis (RED) power plant. *Applied Energy* **2013**, (submitted).

44. Vermaas, D. A.; Saakes, M.; Nijmeijer, K., Double Power Densities from Salinity Gradients at Reduced Intermembrane Distance. *Environmental Science & Technology* **2011,** *45*, (16), 7089-7095.

45. Długołęcki, P. E.; Dąbrowska, J.; Nijmeijer, K.; Wessling, M., Ion conductive spacers for increased power generation in reverse electrodialysis *Journal of Membrane Science* **2010,** *347*, (1-2), 101-107.

46. Vrouwenvelder, J. S.; Schulenburg, D. A. G. v. d.; Kruithof, J. C.; Johns, M. L.; Loosdrecht, M. C. M. v., Biofouling of spiral-wound nanofiltration and reverse osmosis membranes: A feed spacer problem. *Water Research* **2009,** *43*, (3), 583-594.

47. Fane, A. G.; Fell, C. J. D., A review of fouling and fouling control in ultrafiltration. *Desalination* **1987,** *62*, 117-136.

48. Allison, R. P., Electrodialysis reversal in water reuse applications. *Desalination* **1995,** *103*, (1-2), 11-18.

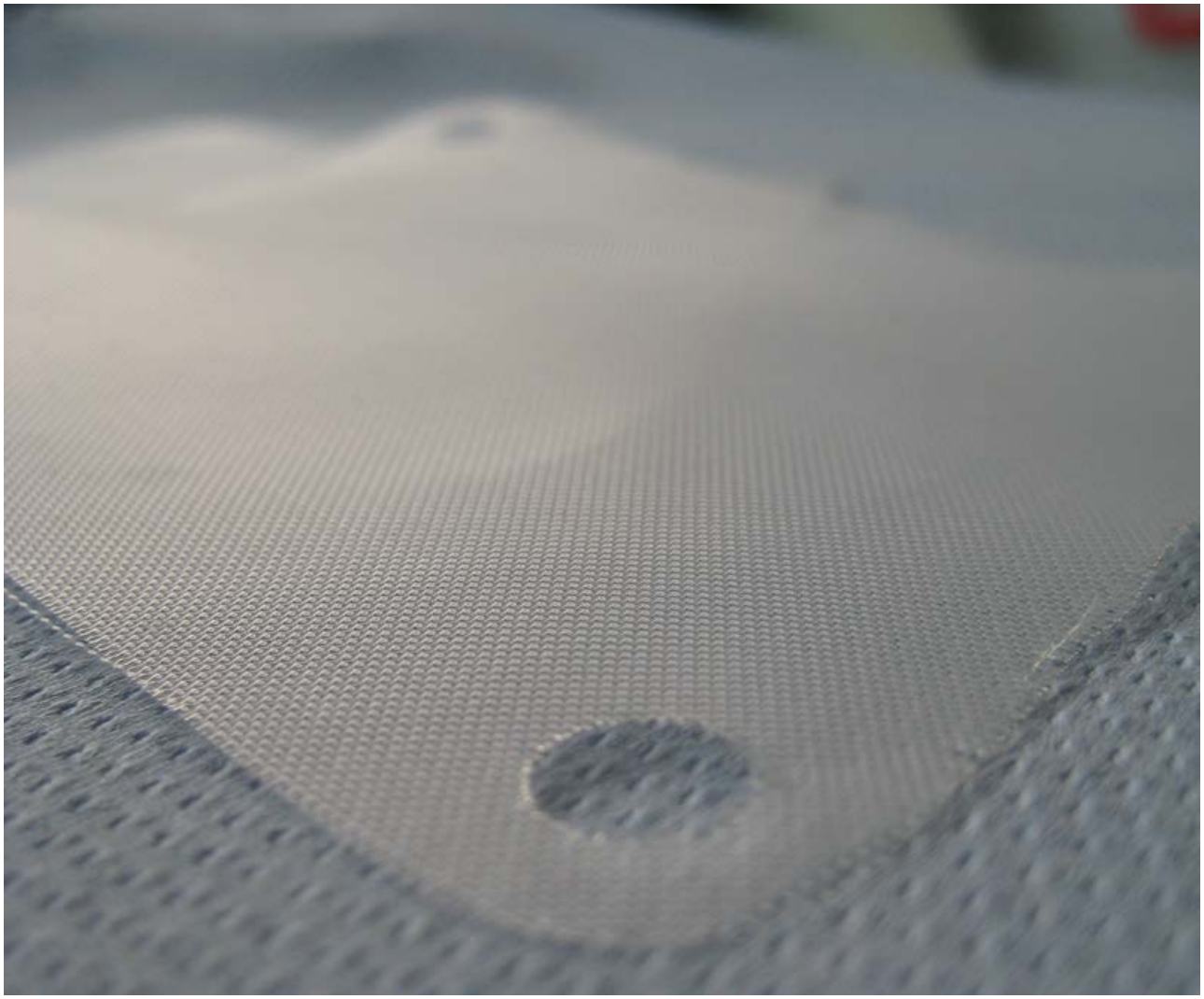

Chapter 2

Doubled power density from salinity gradients at reduced intermembrane distance

Abstract

The mixing of sea and river water can be used as a renewable energy source. The Gibbs free energy that is released when salt and fresh water mix can be captured in a process called reverse electrodialysis (RED). This research investigates the effect of the intermembrane distance and the feedwater flow rate in RED as a route to double the power density output. Intermembrane distances of 60, 100, 200, and 485 μm were experimentally investigated, using spacers to impose the intermembrane distance. The generated (gross) power densities (i.e., generated power per membrane area) are larger for smaller intermembrane distances. A maximum value of 2.2 W/m^2 is achieved, which is almost double the maximum power density reported in previous work. In addition, the energy efficiency is significantly higher for smaller intermembrane distances. New improvements need to focus on reducing the pressure drop required to pump the feedwater through the RED device using a spacerless design. In that case power outputs of more than 4 W per m^2 of membrane area at small intermembrane distances are envisaged.

This chapter has been published as

David A. Vermaas, Michel Saakes, Kitty Nijmeijer, Doubled Power Density from Salinity Gradients at Reduced Intermembrane Distance, *Environmental Science & Technology* **2011,** *45*, (16), 7089-7095

2.1 Introduction

The salinity difference between salt water and fresh water can be used to generate renewable energy. This salinity gradient power is available from the change in Gibbs energy when fresh and salt water mix to a brackish solution; for example at locations where river water flows into the sea. The global runoff of river water into the sea has a potential to generate 2.4 TW [1] of salinity gradient power. This huge amount of power exceeds the prospected global electricity demand for 2011, which is 2.3 TW [2].

Several techniques are proposed to capture salinity gradient power [1, 3-7]. Reverse electrodialysis (RED) [1, 3, 4, 8] and pressure retarded osmosis (PRO) [5, 6] are most cited in literature. RED facilitates the transport of positive and negative ions present in the water through selective ion exchange membranes. PRO uses membranes that allow only water to pass, creating a pressure difference that can be converted into electrical energy. Although the theoretical potential is equal for both technologies, Post *et al.* [9] concluded that RED is more favorable for power generation from sea and river water, because the power density (i.e., generated power per membrane area) was expected to be higher for RED in that case and this technology was considered less sensitive to fouling of the membranes. Although power densities reported in literature are currently higher for PRO [5], RED is considered as a viable candidate to generate energy from salinity gradients. Modeling data show that much higher power densities in RED are possible [8, 10, 11] by optimizing the flow rates and intermembrane distance. The present research focuses on power generation from sea water and river water using RED to test this hypothesis.

A RED device consists of an alternating series of cation exchange membranes (CEMs) and anion exchange membranes (AEMs), stacked with alternately salt water and fresh water flowing between these membranes. The salinity difference on either side of the membrane generates ion transport through the ion exchange membranes, resulting in a net charge transport. At the electrodes this ionic charge transport is converted into electrical energy by a reversible redox reaction. To save electrode area in a large-scale application, a sequence of multiple CEMs and AEMs can be stacked between two electrodes (i.e., anode and cathode).

To make RED a commercially attractive renewable energy source, the gross power density should reach a value of at least 2.2 W/m^2 [12]. The highest reported gross power density so far is 1.2 W/m^2 [13]. The design of the RED stack as used in previous experiments is predominantly based on its reverse application, electrodialysis (ED), where an electric

current is applied to desalinate water or recover dissolved salts. Because ED has a different aim, its optimal design is significantly different than the design preferred in RED. For example, high flow velocities, which require a thick feedwater compartment, are desired in ED to reduce salt depletion in the boundary layers adjacent to the membranes. In RED, where ions move in the direction of the concentration gradient, depletion of salt is not an issue and the optimal thickness of the water compartments will be smaller. Consequently, power densities obtainable in RED can be significantly increased by tuning and improving the design of the RED stack towards the specific application.

The feedwater compartments, and more specifically the river water compartments with their low salt concentrations, have a large contribution to the internal resistance of the RED system [3, 4, 14]. Thinner compartments, i.e., smaller intermembrane distances, will reduce this resistance and consequently increase the obtained power densities. Previous work shows that a RED stack with an intermembrane distance of 200 μm generates more than twice the power density obtainable from the same stack with an intermembrane distance of 500 μm [3, 4]. Model calculations for intermembrane distances smaller than 200 μm indicate that higher power densities are possible [10, 11, 14].

A disadvantage of small intermembrane distances is the large hydraulic friction of the feedwater in the compartments and extra pretreatment to avoid fouling. The energy spent on pretreatment to prevent fouling is considered relatively small for intermembrane distances in previous research (<10% of the generated power) [12]. The required pretreatment for smaller intermembrane distances might be more significant, but is beyond the scope of the present work. The loss for pumping the feedwater is accounted for in the net power density, which is the generated power density minus the power density spent on pumping. Modeling work [10] predicts that, using non-ideal membranes, the maximal net power density is obtained with a RED stack at a river water compartment thickness of 96 μm. Using (hypothetical) ideal membranes, a river water compartment thickness of only 48 μm is preferred for the highest net power density, which resulted in a power density as high as 11.6 W/m^2. The best experimental value obtained for the net power density so far is approximately 0.7 W/m^2, using an intermembrane distance of 200 μm [15]. However the effect of an intermembrane distance smaller than 200 μm on the power density has, to the best of our knowledge, never been investigated experimentally, although theoretical calculations show the importance of this issue.

In the present work, we investigate experimentally the influence of the intermembrane distance on the power output obtainable in a RED system. It includes smaller intermembrane distances than previously reported, resulting in significantly higher practical power densities.

2.2 Experimental setup

2.2.1 Reverse electrodialysis stack

The RED stack comprised five cells, each consisting of a CEM and an AEM, with alternately river water and sea water flowing in between. Additionally, at the end of the stack next to the electrode, one additional CEM was used as shielding membrane to close the last compartment. Two Ti mesh 1.0 electrodes coated with Ir/Ru and an area of 10x10 cm^2 (Magneto Special Anodes BV, The Netherlands) were used as the anode and the cathode. Details of the experimental stack are described in the supporting information (appendix A). All measurements were performed in duplicate. The mean values of these duplicates and the standard deviations of the sample means were calculated and are presented.

Special homogenous ion exchange membranes (Fumatech, Germany) were used; FKS as CEM and FAS as AEM. These membranes were made on demand and had a thickness of only 30-40 μm (dry form), to obtain an average area resistance of < 1 $\Omega \cdot cm^2$ (in 0.5 M NaCl) and an average permselectivity of 97.5% (in 0.1 M and 0.5 M KCl). These membranes have a very low resistance and high permselectivity compared to other commercial ion exchange membranes [14]. Especially the low resistance is an important membrane characteristic for this experiment, since the membrane resistance should be relatively small compared to that of the feedwater compartments.

The intermembrane distance was fixed by using woven fabric spacers (Sefar, Switserland). Four different spacers were used. The thickness, open area, porosity and mesh size are listed in Table 2.1. The open area, porosity and ratio mesh size / wire diameter are chosen to be similar for all spacers. The spacer thickness was measured using a digital thickness meter (Mitutoyo 547-401, Japan) and found to be slightly different than specified. In the remainder of this paper, stacks will be referred to according to the spacer thickness specified (60, 100, 200 and 485 μm) in Table 2.1.

Table 2.1: Characteristics of spacers as used in this research.

Type	Thickness specified (μm)	Thickness measured (μm)	Ratio mesh size / wire diameter	Open area (%)	Porosity (%)
Sefar 03-90/49	60	61 ± 1	2.31	49	71
Sefar 03-160/53	100	101 ± 1	2.62	53	70
Sefar 03-300/51	200	209 ± 2	2.46	51	67
Sefar 06-700/53	485	455 ± 6	2.64	53	75

2.2.2 Feedwater

The artificial sea water had a concentration of 0.507 M (30.0 g NaCl per kg water) and artificial river water had a concentration of 0.017 M (1.00 g NaCl per kg water). The feed waters were pumped through the stack at 10 different flow rates between 0.017 and 4.17 cm^3/s. For the thinnest spacers (60 and 100 μm), the flow rate was limited by the large pressure drop.

The conditions for the river water compartments (thickness and flow rate) were set equal to those for the sea water compartments. Although the optimal conditions for a maximum net power density could be further tuned by choosing the thickness of the river water compartment independent to that of the sea water compartment [10], the equal condition enable to switch the feed waters (for example to prevent biofouling) and prevent a pressure imbalance over the membrane.

2.2.3 Electrochemical Measurements

The internal resistance of the RED stack was measured at the electrodes by using chronopotentiometry. Current density steps of 0, 2.5, 5 … 65 A/m^2 were applied for at least 60 s until a constant value was reached by using a potentiostat (Ivium Technologies, The Netherlands). The current was interrupted between every step (see the supporting information for an example). The sudden jump in voltage when the current is interrupted reveals the ohmic resistance, R_{ohmic}, attributed to the ionic transport through the individual components (CEM, AEM, river water compartment, sea water compartment) [16]. The subsequent, time-dependent, voltage change is referred to as the non-ohmic resistance [3]. This latter is caused by the transport of ions, which induces a decrease in the concentration

gradient between the sea water and river water over time, and consequently result in a decrease in the electromotive force (i.e., the generated voltage, disregarding ohmic losses). This voltage decrease, divided by the electrical current, can be interpreted as a resistance, the non-ohmic resistance.

The non-ohmic resistance can be further specified into a boundary layer resistance, R_{BL}, often referred to as concentration polarization, and a resistance due to the reduced electromotive force as a consequence of the change in the concentration of the bulk solution, here referred to as $R_{\Delta C}$. R_{BL} is dependent on the geometry of the membrane surface [17] and the flow velocity [4], while $R_{\Delta C}$ is inherent to the ion transport from sea to river water.

The contribution of $R_{\Delta C}$ can be estimated from a theoretical calculation. As elaborated in the supporting information (appendix B), $R_{\Delta C}$ can be approximated by:

$$R_{\Delta C} = \frac{\alpha \cdot R \cdot T}{F \cdot j} \cdot \ln\left(\frac{\Delta a_r}{\Delta a_s}\right) \qquad \text{(eq. 2.1)}$$

In which $R_{\Delta C}$ is expressed in $\Omega \cdot m^2$ per cell, α is the average apparent membrane permselectivity (-), R is the universal gas constant (8.314 J/(mol·K)), T is the temperature (K), F is the Faraday constant (96485 C/mol), j is the current density (A/m^2), $\Delta a_r = 1 + \frac{j \cdot L}{F \cdot q_r \cdot c_r}$, $\Delta a_s = 1 - \frac{j \cdot L}{F \cdot q_s \cdot c_s}$ (both dimensionless), L is the cell length (m), q is the flow rate of the feedwater per cell divided by the width of the flow compartment (m^2/s) and c is the concentration (mol/m^3). The subscripts s and r refer to sea water and river water, respectively.

Thus, the internal area resistance R_i per cell ($\Omega \cdot m^2$ per cell) is composed of three parts:

$$R_i = R_{ohmic} + R_{\Delta c} + R_{BL} \qquad \text{(eq. 2.2)}$$

The resistance of the electrodes and its corresponding compartments are neglected here as this resistance will be negligible in a large-scale application where a large number of membrane pairs is stacked.

Because R_i and R_{ohmic} are determined experimentally and $R_{\Delta C}$ is estimated from eq. 2.1, R_{BL} can obtained from eq. 2.2.

Hence, the gross power density (i.e., power density without correction for pumping losses) was calculated by [18]:

$$P_{gross} = \frac{OCV^2}{4 \cdot R_{stack} \cdot N_m} \qquad \text{(eq. 2.3)}$$

In which P_{gross} is the gross power density (in W/m^2), OCV is the open circuit voltage, i.e., the stack voltage measured at zero current (V), R_{stack} is the internal resistance of all cells in the RED stack ($\Omega \cdot m^2$) and N_m is the number of membranes contributing to the voltage (-). The maximum power density is obtained at an external resistance equal to the internal resistance [1, 18]. The internal resistance might be slightly dependent on the current density. The presented values for the resistance correspond to the current density at which the maximum gross power density was obtained. This optimal current density was between 15 A/m^2 (485 μm) and 45 A/m^2 (60 μm) for high flow rates, whereas the optimal current density was as low as to 5 A/m^2 for the lowest flow rate.

2.3 Results

2.3.1 Internal Resistance

The internal area resistance per cell, split in R_{ohmic}, R_{BL} and $R_{\Delta C}$, is plotted against the flow and Re in Figure 2.1a, b, c and d. The Reynolds number (Re) is calculated for a wide, empty slit, i.e., twice q divided by the kinematic viscosity of water.

The ohmic resistance increases slowly to an asymptotic value as the flow rate increases, and grows to the largest contribution in R_i for intermembrane distances of 100 μm and higher. R_{ohmic} is extrapolated to this asymptotic value at infinitely high flow rates and is subdivided in the individual components in Figure 2.1e, as calculated from the specifications of the membranes and the conductivity of the feed waters. The remaining part of the ohmic resistance is attributed to the effect of the spacer. Figure 2.1e reveals that the ohmic resistance is dominated by the resistance of the river water compartment, which is proportional to the intermembrane distance. The ohmic resistance for an intermembrane distance of 485 μm is roughly 5 times higher than for the 60 μm distance, 4 times higher than for 100 μm distance and 2 times higher than for 200 μm distance, at the same flow rate. Small intermembrane distances give a serious decrease in ohmic resistance and consequently also in the total internal resistance.

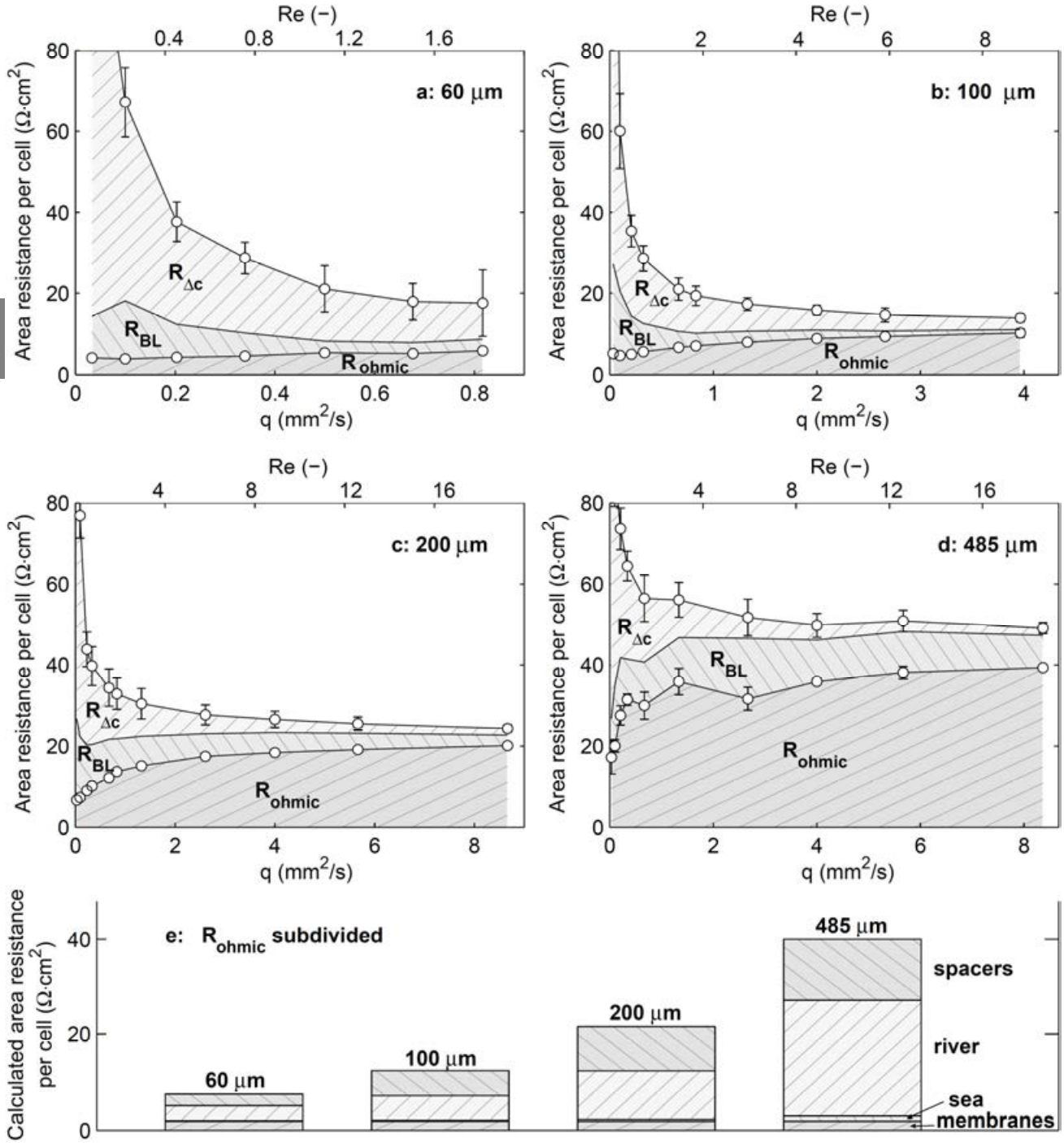

Figure 2.1: a, b, c and d: Internal area resistance per cell (R_i) as a function of the flow per cell per unit width (q) for different intermembrane distances. The differences between two lines indicate the individual components (R_{ohmic}, R_{BL} and $R_{\Delta C}$). The sum of all components equals R_i. Mind the difference in scale of the x-axes for 60 and 100 μm spacers distances. e: The component R_{ohmic} subdivided in a resistance originating from the spacers, river water, sea water and membranes.

The dominance of the river water compartment in the ohmic resistance also explains the influence of the flow rate on R_{ohmic}. The conductivity of the river water increases when ions move from the sea water to the river water compartment. At high flow rates, the river water is refreshed more rapidly, limiting changes in concentration due to ion transport, thus increasing R_{ohmic}.

The boundary layer resistance, R_{BL}, decreases with increasing q, thus with increasing flow velocity (in mm/s), because mixing is more effective at higher velocities [4]. Smaller intermembrane distances reduce R_{BL}, when comparing equal q as well when comparing equal flow velocity. A small intermembrane distance, combined with a finer spacer mesh, restricts the boundary layer thickness, which reduces R_{BL} [19]. The unknown relation between intermembrane distance and boundary layer thickness disables to examine whether this effect resolves all differences in R_{BL}. Probably, subtle changes in other parameters, such as the ratio between spacer filament size to mesh opening size and spacer mesh angles, have its resemblance in the mixing rate [20] and thus influence R_{BL}.

The contribution of $R_{\Delta C}$ is dominant at very low flow rates, whereas it diminishes at high flow rates. The decrease in $R_{\Delta C}$ with increasing flow was already indicated by eq. 2.1. The concentration gradient over the membrane is restored by flushing the feed waters and hence lowers $R_{\Delta C}$. $R_{\Delta C}$ is very similar for each intermembrane distance at the same flow rates.

2.3.2 Gross Power Density

The open circuit voltages (OCV) as generated by all RED stacks was 93-98% of the theoretical values derived from the Nernst equation (e.g., ref [1]) at flows larger than 0.5 mm^2/s, for all intermembrane distances. This is close to the expected values based on the specified perm-selectivity. The OCV and resistance yield the gross power density by using eq. 2.3. The gross power density is shown in Figure 2.2 as a function of the flow, q, and intermembrane distance.

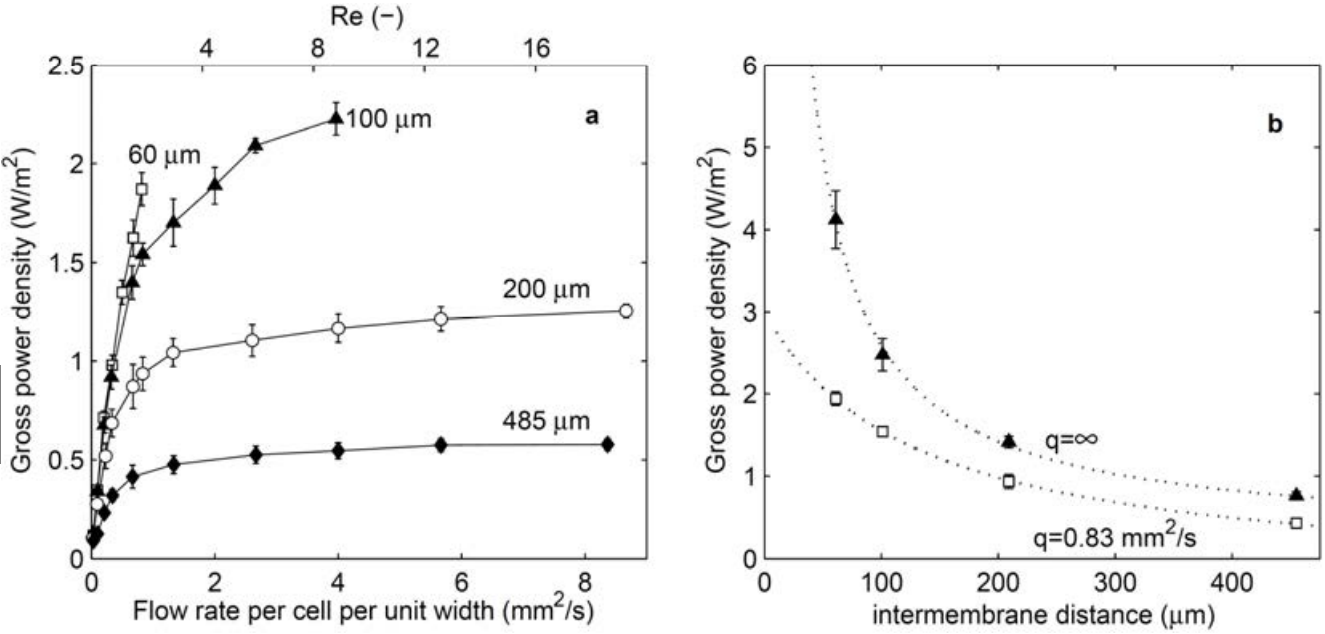

Figure 2.2: Gross power density (a) as a function of flow rate per cell per unit width (i.e., q) and Re and (b) as a function of the intermembrane distance at a flow rate of 0.83 mm^2/s (measured) and for an infinitely high flow rate (extrapolated). Dotted trend lines are added to guide the eye.

P_{gross} increases strongly with decreasing intermembrane distance, due to the lower internal resistances. P_{gross} reaches certain asymptotic values at high flow rates (Figure 2.2a) for each intermembrane distance, which is apparently not reached yet for the smaller intermembrane distances. Although measurements at higher flow rates were not yet possible for an intermembrane distance of 60 and 100 µm, due to the large pressure drops, still the highest power densities were obtained at these smaller intermembrane distances. The highest power density measured experimentally was as high as 2.2 W/m^2, which is almost double the highest power density reported in literature so far (1.2 W/m^2 [13]).

The power density obtained at an intermembrane distance of 60 and 100 µm was limited by the absence of measurements at high flow rates. To predict the maximum power densities at infinitely high flow rates, the non-ohmic resistances (R_{BL} and $R_{\Delta C}$) are neglected in that case because they approach a value of 0 at infinitely high flow rates (Figure 2.1 and eq. 2.1). Using only the ohmic resistance (Figure 2.1e), the power density for q=∞ can be estimated. Figure 2.2b shows that a power density of more than 4 W/m^2 can be obtained at an intermembrane distance of 60 µm at high flow rates.

2.3.3 Energy Efficiency

Next to the much higher power densities, a small intermembrane distance has another important advantage. A high power density at relatively low flow rate yields high energy efficiency. This energy efficiency is the extracted energy in the practical application compared to the theoretical amount of energy that is released during mixing of the same amount of water:

$$\eta = \frac{P_{gross} \cdot 2L}{\Delta G_{mix} \cdot q} \cdot 100\% \qquad \text{(eq. 2.4)}$$

In which η is the energy efficiency (-) and ΔG_{mix} is the Gibbs energy of mixing (J) per m^3 water (1.4 MJ for 1 m^3 river water and 1 m^3 sea water). The factor 2L originates from the membrane area, which was included in the gross power density. Previous work showed that the energy efficiency has its maximum at relatively low flow rates and low current densities, whereas the gross power density generally increases with increasing flow rate [15]. When sea water and river water only pass the RED stack once, the energy efficiency is theoretically at maximum 50% when operated at maximum P_{gross}. The remaining 50% is lost to internal resistance, independent of the internal resistance itself [18]. Higher energy efficiencies (up to 80%) can be achieved when the feed waters are recycled (multiple pass) and a lower current density is applied [3]. In this research, where the gross power density is maximized, such high energy efficiencies cannot be obtained.

Figure 2.3a reveals that in our system 50% energy efficiency is reached at low flow rates, whereas the efficiency drops for higher flow rates.

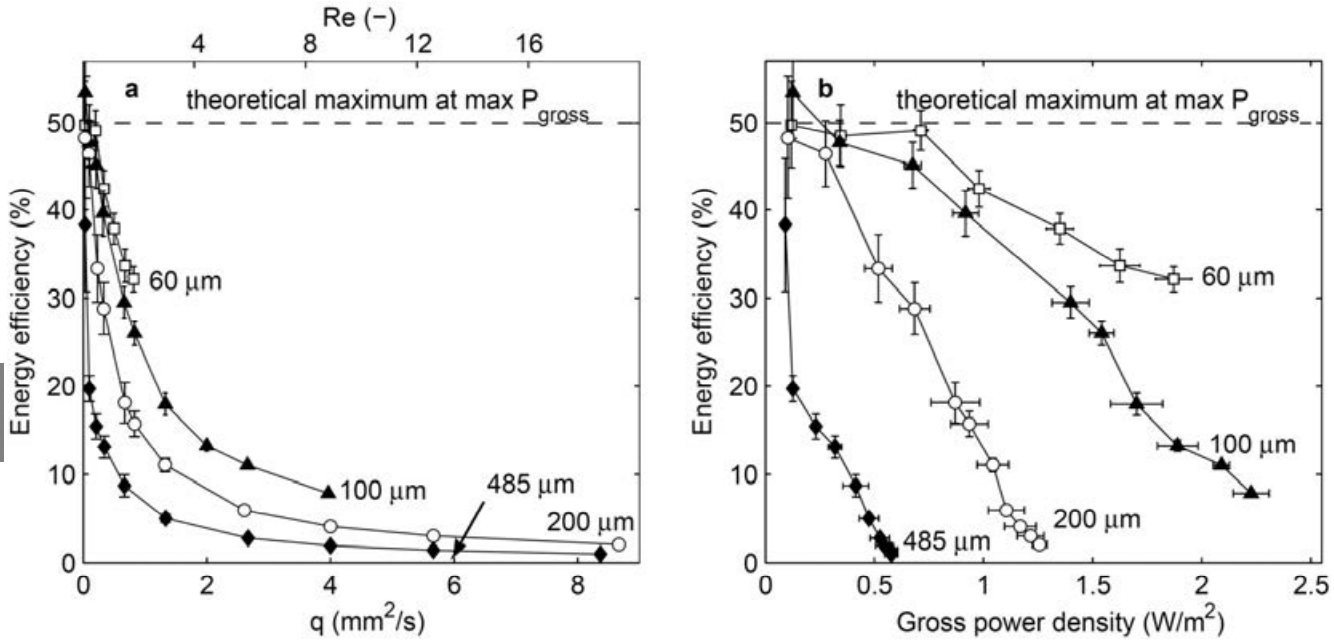

Figure 2.3: Energy efficiency plotted against the (a) flow rate and (b) gross power density, at different intermembrane distances.

At higher flow rates, there is not sufficient time to complete the ion transport and consequently not all energy available from the mixing of the two feed waters is captured. Stacks with smaller intermembrane distances use the water much more efficient than stacks with larger intermembrane distances. As demonstrated in Figure 2.3b, a power density of almost 2 W/m^2 can be combined at a energy efficiency of more than 30% at an intermembrane distance of 60 µm. Large intermembrane distances give a much lower gross power density at the same energy efficiency.

At the same flow rate, the gross power density and efficiency are improved by more than a factor 2 when the intermembrane distance is reduced from 200 to 60 µm. Considering even smaller intermembrane distances, P_{gross} and η can be further improved, although not to an unlimited extent. Apart from practical limitations, the amount of energy available from mixing is limited. At a flow rate of 0.42 cm^3/s (which was the maximum for an intermembrane distance of 60 µm) and assuming an energy efficiency of 50%, the maximum power available from mixing is 0.29 W, which corresponds to 2.9 W/m^2 for the current stack dimensions. Higher power densities require a higher flow rate per cell per area.

2.3.4 Pressure Drop

Figure 2.2b and the limitation in efficiency as stated above indicate that a combination of a small intermembrane distance and a high flow rate results into the highest power density. The hydraulic resistance of the feedwater is currently limiting the flow rates for small intermembrane distances. The hydraulic resistance is expressed in a pressure drop over the inflow and outflow of the feedwater compartments. The theoretical pressure drop in uniform, laminar flow between two infinitely wide flat plates (e.g., ref [21]) is given by:

$$\Delta p = \frac{12\mu \cdot L \cdot q}{d^3} \qquad \text{(eq. 2.5)}$$

In which Δp is the pressure drop (Pa) and μ is the dynamic viscosity of water (Pa·s). So theoretically the pressure drop linearly depends on the flow rate and depends on the intermembrane distance to the power -3.

Figure 2.4 presents the experimentally determined dependence of the pressure drop on the flow rate (Figure 2.4a) and the intermembrane distance (Figure 2.4b). The theoretical pressure drop for uniform flows as calculated from eq. 2.5 at q=0.83 mm^2/s is added to Figure 2.4b as well.

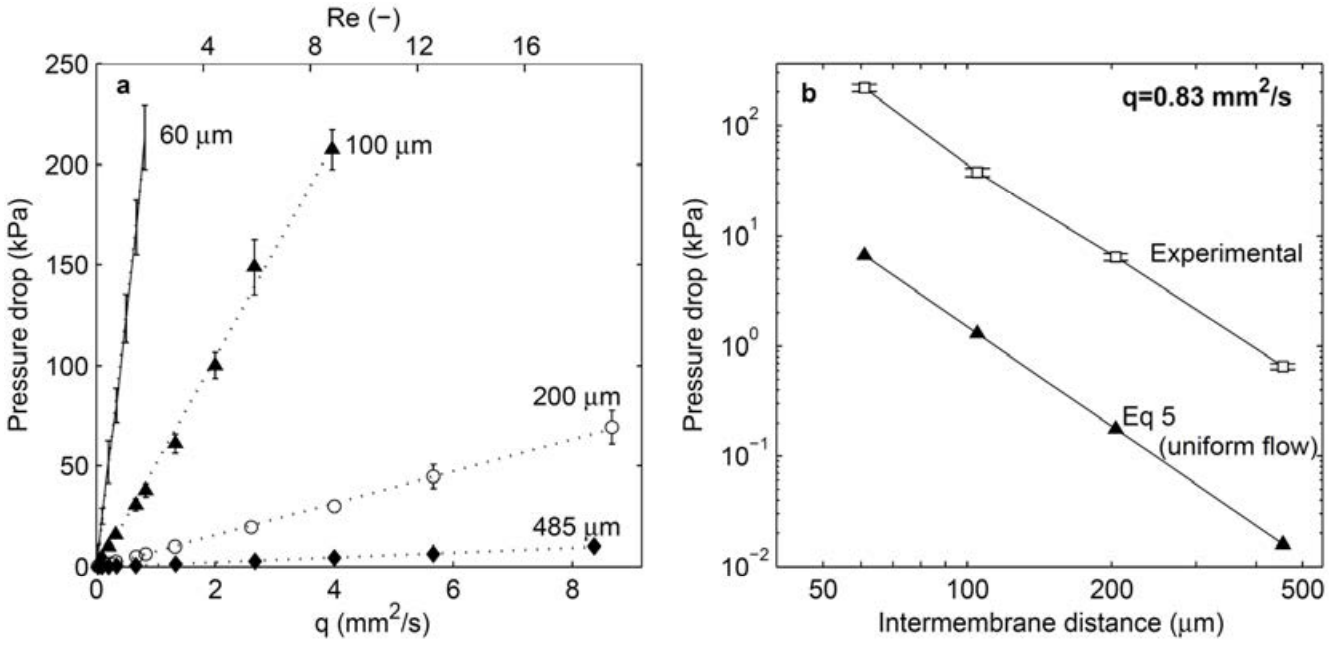

Figure 2.4: Average pressure drop over the feedwater compartments, versus (a) the flow rate and (b) the intermembrane distance for a flow rate per cell per unit width of 0.83 mm^2/s. The right panel has logarithmic axes.

Both Figures 2.4a and 2.4b show that the pressure drop is strongly dependent on the intermembrane distance. The theoretical pressure drop has the same relation with the intermembrane distance as the experimental results ($\Delta p \propto q$ and $\Delta p \propto d^{-3}$), but the experimental values are more than one order of magnitude higher than the theoretical equivalents for uniform flow. Similar results were found in previous work [10]. Obviously, the theory for uniform flow cannot be applied directly for this flow through a spacer as the presence of spacer filaments prevents uniform flow. The spacer filaments enforce a tortuous flow, which is known to increase the pressure drops (e.g., ref [21]). Second, at the position of a spacer filament, the water is funneled through the opening between the spacer filament and the membrane, which is a much smaller distance than the intermembrane distance, and thus leads to an increase in pressure drop [22].

2.3.5 Net Power Density

The power density consumed for pumping the feed waters (P_{pump}, in W/m^2) is determined from the pressure drop over the inlet and outlet (Δp, Figure 2.4a) and the flow rate per cell per unit width (q) per unit length (L):

$$P_{pump} = \frac{\Delta p \cdot q}{L} \qquad \text{(eq. 2.6)}$$

The net power density (P_{net}, in W/m^2) that is generated by a RED stack is subsequently calculated as the difference between the gross power density and the power density consumed for pumping of both feed waters:

$$P_{net} = \frac{OCV^2}{4 \cdot R_{stack} \cdot N_m} - \frac{\Delta p \cdot q}{L} \qquad \text{(eq. 2.7)}$$

As a consequence of the high pressure drop, the power loss due to pumping the feedwater has a significant effect on the net power density obtainable in RED. The net power densities experimentally obtained in the present work are shown in Figure 2.5.

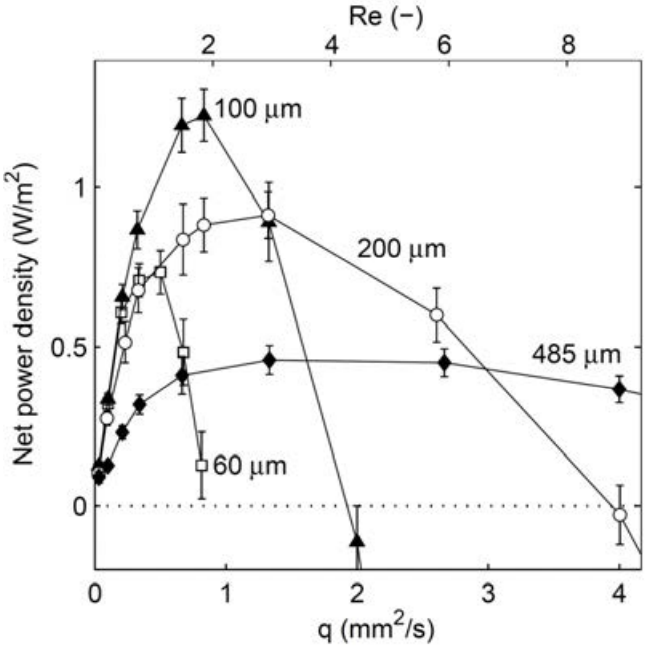

Figure 2.5: Net power density, experimentally obtained, as a function of the flow rate per cell per unit width, q.

The net power density is highest for an intermembrane distance of 100 µm, and a value of 1.2 W/m^2 can be reached. This is easily exceeding the previously reported values for the net power density (at maximum 0.7 W/m^2 [15]).

The RED stack with the smallest intermembrane distance, 60 µm, cannot reach higher power densities, due to the high power consumed on pumping the feed waters. These results emphasize the need for a RED design that features lower pumping losses. When the pressure drop can be reduced to an equivalent of the theoretical pressure drop, much higher net power densities will be obtained. The net power density will benefit from this in two ways. The lower pressure drops will directly lower the power spent for pumping and thus increase the net power density. When the pressure drop can approach the theoretical equivalents for uniform flow, the power density consumed for pumping is small compared to the gross power density for the current flow rates. At the same time, a lower pressure drop will enable higher flow rates at small intermembrane distances (60 µm or less), which will enhance the gross power density as well. In other words, the graphs in Figure 2.5 will not only amplify, but the maximum will also shift to higher flow rates.

2.4 Outlook

A design that features uniform flow conditions cannot include a spacer. An alternative for a spacer is a so called profiled membrane, i.e., a membrane with ridges that keep the next membrane distant. The design of such ridges can have a geometry that enables a uniform flow. Such profiled membranes are already applied in electrodialysis [23], mostly because profiled membranes also decrease the internal (ohmic) resistance. Profiled membranes will benefit extra in RED because the hydraulic resistance will be reduced and the vulnerability to fouling is expected to be lower for profiled membranes [12]. Profiled membranes can solve the currently largest limitations in RED, by further reducing the internal resistance and reducing the hydraulic resistance experienced on the feed waters.

References

1. Weinstein, J. N.; Leitz, F. B., Electric Power from Differences in Salinity: The Dialytic Battery. *Science* **1976,** *191*, (4227), 557-559.
2. EIA, *International energy outlook 2010*. U.S. Department of Energy: Washington D.C., **2010**; 328 p.
3. Post, J. W.; Hamelers, H. V. M.; Buisman, C. J. N., Energy Recovery from Controlled Mixing Salt and Fresh Water with a Reverse Electrodialysis System. *Environmental Science & Technology* **2008,** *42*, (15), 5785-5790.
4. Długołęcki, P. E.; Gambier, A.; Nijmeijer, K.; Wessling, M., Practical Potential of Reverse Electrodialysis As Process for Sustainable Energy Generation. *Environmental Science & Technology* **2009,** *43*, (17), 6888-6894.
5. Thorsen, T.; Holt, T., The potential for power production from salinity gradients by pressure retarded osmosis. *Journal of Membrane Science* **2009,** *335*, (1-2), 103-110.
6. Achilli, A.; Cath, T. Y.; Childress, A. E., Power generation with pressure retarded osmosis: An experimental and theoretical investigation. *Journal of Membrane Science* **2009,** *343*, (1-2), 42-52.
7. Sales, B. B.; Saakes, M.; Post, J. W.; Buisman, C. J. N.; Biesheuvel, P. M.; Hamelers, H. V. M., Direct Power Production from a Water Salinity Difference in a Membrane-Modified Supercapacitor Flow Cell. *Environmental Science & Technology* **2010,** *44*, (14), 5661–5665.
8. Lacey, R. E., Energy by Reverse Electrodialysis. *Ocean Engineering* **1980,** *7*, (1), 1-47.
9. Post, J. W.; Veerman, J.; Hamelers, H. V. M.; Euverink, G. J. W.; Metz, S. J.; Nijmeijer, K.; Buisman, C. J. N., Salinity-gradient power: Evaluation of pressure-retarded osmosis and reverse electrodialysis. *Journal of Membrane Science* **2007,** *288*, (1-2), 218-230.
10. Veerman, J.; Saakes, M.; Metz, S. J.; Harmsen, G. J., Reverse electrodialysis:A validated process model for design and optimization. *Chemical Engineering Journal* **2011,** *166*, (1), 256–268.
11. Brauns, E., Salinity gradient power by reverse electrodialysis: effect of model parameters on electrical power output. *Desalination* **2009,** *237*, 378–391.
12. Post, J. W.; Goeting, C. H.; Valk, J.; Goinga, S.; Veerman, J.; Hack, P. J. F. M., Towards implementation of reverse electrodialysis for power generation from salinity gradients. *Desalination and water treatment* **2010,** *16*, 182-193.
13. Veerman, J.; Jong, R. M. D.; Saakes, M.; Metz, S. J.; Harmsen, G. J., Reverse electrodialysis: Comparison of six commercial membrane pairs on the thermodynamic efficiency and power density. *Journal of Membrane Science* **2009,** *343*, (1-2), 7-15.

14. Długołęcki, P. E.; Nijmeijer, K.; Metz, S. J.; Wessling, M., Current status of ion exchange membranes for power generation from salinity gradients. *Journal of Membrane Science* **2008,** *319*, (1-2), 214-222.

15. Veerman, J.; Saakes, M.; Metz, S. J.; Harmsen, G. J., Electrical Power from Sea and River Water by Reverse Electrodialysis: A First Step from the Laboratory to a Real Power Plant. *Environmental Science & Technology* **2010,** *44*, (23), 9207-9212.

16. Sistat, P.; Pourcelly, G., Chronopotentiometric response of an ion-exchange membrane in the underlimiting current-range. Transport phenomena within the diffusion layers. *Journal of Membrane Science* **1997,** *123*, (1), 121-131.

17. Balster, J.; Yildirim, M. H.; Stamatialis, D. F.; Ibanez, R.; Lammertink, R. G. H.; Jordan, V.; Wessling, M., Morphology and Microtopology of Cation-Exchange Polymers and the Origin of the Overlimiting Current. *J. Phys. Chem. B* **2007,** *111*, (9), 2152-2165.

18. Veerman, J.; Post, J. W.; Saakes, M.; Metz, S. J.; Harmsen, G. J., Reducing power losses caused by ionic shortcut currents in reverse electrodialysis stacks by a validated model. *Journal of Membrane Science* **2008,** *310*, (1-2), 418-430.

19. Spiegler, K. S., Polarization at ion exchange membrane-solution interfaces. *Desalination* **1971,** *9*, (4), 367-385.

20. Li, F.; Meindersma, G. W.; Haan, A. B. D.; Reith, T., Optimization of commercial net spacers in spiral wound membrane modules. *Journal of Membrane Science* **2002,** *208*, (1-2), 289-302.

21. Batchelor, G. K., *An introduction to fluid dynamics*. Cambridge University Press: New York, **2000**; 615 p.

22. Schock, G.; Miquel, A., Mass transfer and pressure loss in spiral wound modules. *Desalination* **1987,** *64*, 339-352.

23. Strathmann, H., Electrodialysis, a mature technology with a multitude of new applications. *Desalination* **2010,** *264*, (3), 268-288.

Supporting information

Appendix A: Experimental setup

The RED stack comprised 5 CEMs and 5 AEMs. Additionally, at the end of the stack next the electrode, one additional CEM was used as shielding membrane to close the last compartment. Two Ti mesh 1.0 electrodes coated with Ir/Ru and an area of 10x10 cm^2 (MAGNETO Special Anodes B.V., The Netherlands) were used as the anode and the cathode. Figure S2.1 shows the configuration of the RED stack. The resistance of the electrodes, its corresponding compartments and the last shielding membrane was measured and used a correction for all measurements.

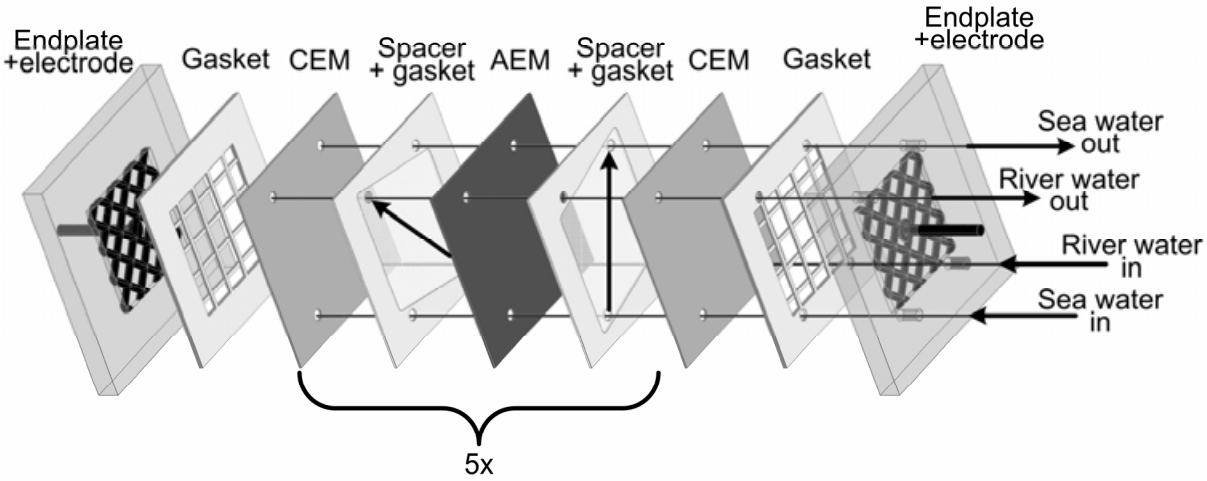

Figure S2.1: Configuration of the RED stack.

The river water and sea water compartments were fed by inlets at the right bottom and left bottom respectively. A drawing of the compartment shape is given in previous work [3]. A gasket made of silicone rubber (Special Silicone Fabricators, USA), with a thickness equivalent to the spacer thickness, was used to seal all compartments. The stack was closed with plates of PMMA (poly(methyl methacrylate)) and 8 bolts, all tightened with a torque key at 2 N·m.

Artificial sea and river water was prepared by dissolving NaCl (technical grade, 99.5% purity, ESCO, The Netherlands) in demineralized water. The concentration NaCl in the sea water was 0.507 M (30.0 g NaCl per kg water) and the concentration NaCl in the river water was 0.017 M (1.00 g NaCl per kg water). The water was stored at 25 (±1) ºC.

The feed waters were pumped through the stack by using peristaltic pumps (Cole-Parmer, Masterflex L/S Digital drive, USA) at 10 different flow rates between 0.017 and 4.17 cm^3/s. The pressure drop between inflow and outflow of both feed waters was measured by a differential pressure meter

(Endress+Hauser Deltabar S, Germany). A pressure meter with a range of 0-500 mbar was used for the intermembrane distance of 200 and 485 μm, whereas a pressure meter with a range of 0-3000 mbar was used for the intermembrane distance of 60 and 100 μm.

The electrode rinse solution was made from 0.025 M $K_3Fe(CN)_6$, 0.025 M $K_4Fe(CN)_6$ and 0.25 M NaCl in demineralized water. This solution was circulated at ca. 2 cm/s along the electrodes and stored in a bottle at 25 (±0.1) ºC. The RED stack was located in an isolated chamber (Friocell, Germany), which was kept at 25 (±0.1) ºC.

The internal resistance (R_i) and the ohmic resistance (R_{ohmic}) of the RED stack were determined using chronopotentiometry. A fixed current density was set, in steps of 0, 2.5, 5 … 65 A/m^2, and applied for at least 60 s until a constant value was reached by using a potentiostat (Ivium Technologies, The Netherlands). The sampling interval time was 4 ms. For low flow rates, it took up to 1200 s for the voltage to equilibrate. In between every step, the current was interrupted. The sudden jump in voltage when the current is interrupted reveals the ohmic resistance, whereas the remaining change in voltage is attributed to the non-ohmic resistances. Figure S2.2 shows a typical example of such a measurement series. Because R_i and R_{ohmic} can be determined from the chronopotentiometric measurements, and $R_{\Delta C}$ can be calculated, the remaining contribution can be attributed to R_{BL}.

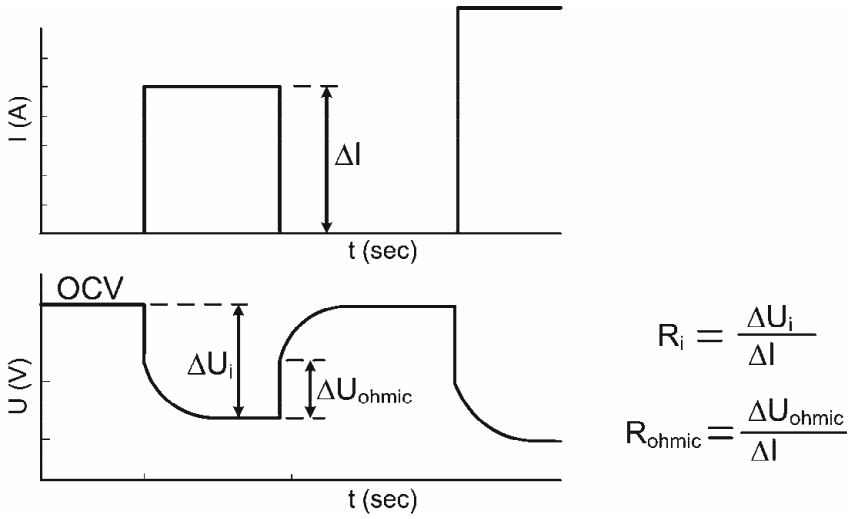

Figure S2.2: Typical example of chronopotentiometric measurement series, showing the current in the upper graph and the corresponding voltage obtained from the stack in the lower graph as a function of the measurement time.

Appendix B: Derivation of $R_{\Delta C}$

The contribution of $R_{\Delta C}$ can be estimated from theory. The derivation of eq. 2.1 as given in the research paper is presented here.

The salt concentrations at the inflow of sea water and river water are defined as c_s and c_r, respectively. The concentration at the outflow, when ions are exchanged under influence of a direct current

(assuming no leakage), can be calculated by:

$$c_{s,out} = c_s - \frac{j \cdot L}{F \cdot q_s} \qquad \text{(eq. S2.1a)}$$

$$c_{r,out} = c_r + \frac{j \cdot L}{F \cdot q_r} \qquad \text{(eq. S2.1b)}$$

In which j is the current density (A/m^2), L is the cell length (m), F is the Faraday constant (96485 C/mol), c is the concentration (mol/m^3) and q is the flow rate per cell per unit width (m^2/s).

The theoretical value for the electromotive force is dependent on the concentrations on either side of the membrane, as described by the Nernst equation. Considering membranes with an average apparent permselectivity α (-), and using monovalent ion species, the electromotive force E per cell can be calculated by:

$$E = 2 \cdot \frac{\alpha \cdot R \cdot T}{F} \cdot \ln\left(\frac{c_s \cdot \gamma_s}{c_r \cdot \gamma_r}\right) \qquad \text{(eq. S2.2)}$$

In which R is the universal gas constant (8.314 J/(mol·K)), T is the temperature (K), and γ represents the activity coefficient (-). The feedwater in the stack has a concentration in between the extreme concentrations at the inflow and outflow. Hence the local electromotive force over the membranes varies spatially. The effective electromotive force is an average value of this spatially varying field. The highest value for the electromotive force is based on the inflow concentrations. If the outflow concentrations from eq. S2.1a and eq. S2.1b are considered, the electromotive force is lower. As a rough estimate, the average electromotive force is approximated by the average of these two extreme values. This average electromotive force per cell is given by:

$$E_{average} = 2\frac{\alpha \cdot R \cdot T}{F} \cdot \frac{1}{2} \cdot \left[\ln\left(\frac{\gamma_s \cdot c_s}{\gamma_r \cdot c_r}\right) + \ln\left(\frac{\gamma_s}{\gamma_r} \cdot \frac{c_s - \frac{j \cdot L}{F \cdot q_s}}{c_r + \frac{j \cdot L}{F \cdot q_r}}\right) \right]$$

$$= 2\frac{\alpha \cdot R \cdot T}{F} \cdot \frac{1}{2} \cdot \ln\left(\frac{{\gamma_s}^2 \cdot {c_s}^2}{{\gamma_r}^2 \cdot {c_r}^2} \cdot \frac{1 - \frac{j \cdot L}{F \cdot q_s \cdot c_s}}{1 + \frac{j \cdot L}{F \cdot q_r \cdot c_r}}\right)$$

$$= 2\frac{\alpha \cdot R \cdot T}{F} \cdot \ln\left(\frac{\gamma_s \cdot c_s}{\gamma_r \cdot c_r} \cdot \frac{\sqrt{1 - \frac{j \cdot L}{F \cdot q_s \cdot c_s}}}{\sqrt{1 + \frac{j \cdot L}{F \cdot q_r \cdot c_r}}}\right) \qquad \text{(eq. S2.3)}$$

This approach neglects changes in the activity coefficient within a compartment and assumes a linear decrease in electromotive force from the inflow to outflow of feed waters. These assumptions are reasonable for small changes in concentration between the inflow and outflow.

The area resistance ($\Omega \cdot m^2$) per cell due to the change in bulk concentrations can be calculated according to:

$$R_{\Delta C} = \frac{E - E_{average}}{j} \qquad \text{(eq. S2.4)}$$

Substitution of eq. S2.2 and eq. S2.3 in eq. S2.4 subsequently yields:

$$R_{\Delta C} = 2\frac{\alpha \cdot R \cdot T}{F \cdot j} \cdot \left[\ln\left(\frac{\gamma_s \cdot c_s}{\gamma_r \cdot c_r}\right) - \ln\left(\frac{\gamma_s \cdot c_s}{\gamma_r \cdot c_r} \cdot \frac{\sqrt{1 - \frac{j \cdot L}{F \cdot q_s \cdot c_s}}}{\sqrt{1 + \frac{j \cdot L}{F \cdot q_r \cdot c_r}}} \right) \right]$$

$$= 2\frac{\alpha \cdot R \cdot T}{F \cdot j} \cdot \ln\left(\sqrt{\frac{1 + \frac{j \cdot L}{F \cdot q_r \cdot c_r}}{1 - \frac{j \cdot L}{F \cdot q_s \cdot c_s}}} \right) \qquad \text{(eq. S2.5)}$$

$$= \frac{\alpha \cdot R \cdot T}{F \cdot j} \cdot \ln\left(\frac{1 + \frac{j \cdot L}{F \cdot q_r \cdot c_r}}{1 - \frac{j \cdot L}{F \cdot q_s \cdot c_s}} \right)$$

Or, in short:

$$R_{\Delta C} = \frac{\alpha \cdot R \cdot T}{F \cdot j} \cdot \ln\left(\frac{\Delta a_r}{\Delta a_s}\right) \qquad \text{(eq. S2.6)}$$

In which $\Delta a_r = 1 + \frac{j \cdot L}{F \cdot q_r \cdot c_r}$ and $\Delta a_s = 1 - \frac{j \cdot L}{F \cdot q_s \cdot c_s}$

This first order approach should be considered only as a rough estimate due to the assumptions made. For the current research, in which $R_{\Delta C}$ is estimated only as a rough indication and where no information is available about the local concentration gradients, this model satisfies.

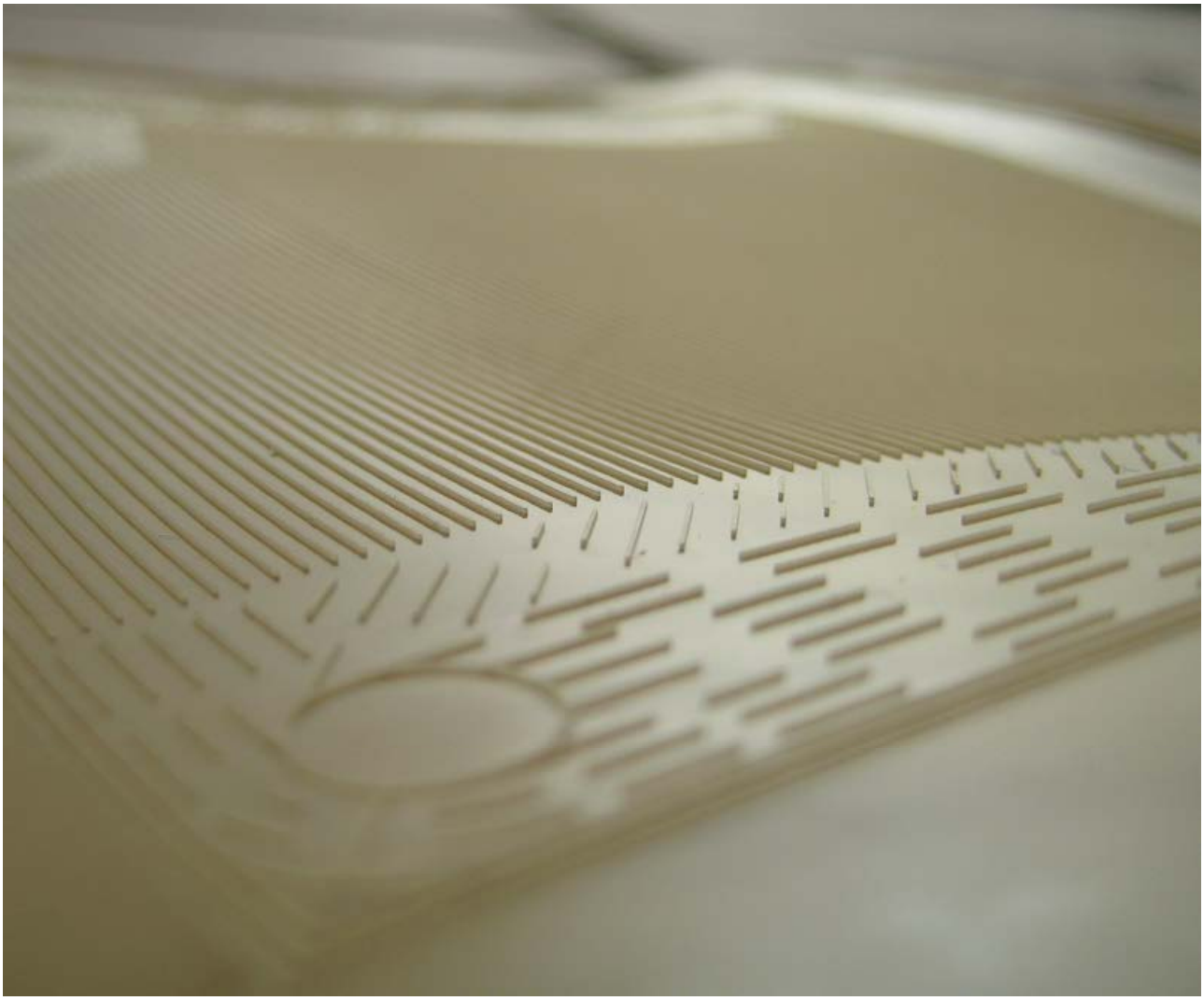

Chapter 3

Power generation using profiled membranes in a spacerless reverse electrodialysis system

Abstract

Reverse electrodialysis (RED) is a technology to obtain energy from the salinity difference between salt water and fresh water. Traditionally, ion exchange membranes, separated by non-conductive spacers, are used in this technology. As an alternative for these non-conductive spacers, in this work, heterogeneous ion exchange membranes were hot pressed in the dry state to create a profiled membrane comprising 230-245 μm ridges (in wet state) on one side of the membrane. Stacking such profiled membranes creates channels for the feedwater, thus make the use of spacers obsolete. The performance of a RED stack with such profiled membranes was compared for the first time with a RED stack with traditional, non-conductive spacers. The ohmic resistance was significantly lower for the stack with profiled membranes compared to that with spacers, whereas the boundary layer resistance was higher. This resulted in slightly higher power densities for the stack with profiled membranes. Despite this only small improvement, profiled membranes have a strong future development potential. Experimental data show that the hydraulic friction is much lower for the stack with profiled membranes and hence higher Reynolds numbers are possible than in a stack with spacers. Furthermore, profiling membranes allows much freedom to create new profile geometries where a hydrodynamic flow can be combined with efficient mixing in the boundary layers.

This chapter has been published as

David A. Vermaas, Michel Saakes, Kitty Nijmeijer, Power generation using profiled membranes in reverse electrodialysis, *Journal of Membrane Science*, **2011**, *385-386*, 234-242

3.1 Introduction

Reverse electrodialysis (RED) is a renewable energy source that uses the energy from the mixing of salt and fresh water. This Gibbs free energy of mixing is available when concentrated and diluted salt solutions mix and RED captures this salinity gradient energy using ion exchange membranes.

The principle of RED has been described by several authors [1-3]. A RED stack comprises an alternating series of cation exchange membranes (CEM) and anion exchange membranes (AEM). When alternating concentrated and diluted salt solutions flow in between the ion exchange membranes, ions are transported from the concentrated to the diluted compartment, forced by the salinity gradient. Since the ion exchange membranes ideally only allow either positive or negative ions to pass, cations are transported to one side and anions to the other side. The resulting potential difference over the membranes can be used to power an electrical device.

To make RED an economically attractive technology to extract energy from the mixing of sea and river water, the net power to be generated per membrane area (i.e., net power density) is estimated to be 2 W/m^2 at a fuel efficiency of 70% [4]. Previous research already showed that 80% fuel efficiency is possible [2]. The net power density in RED was recently increased to 1.2 W/m^2 [5]. Although this was almost twice the highest value reported previously, it is still considerably lower than the aimed 2 W/m^2. A high power density will reduce the price because the membrane costs are dominant compared to the other costs in a large scale RED power plant [4]. The fuel efficiency is of minor importance for a first plant, as water flows are not limiting yet.

To achieve a high net power density, the internal resistance of the system and the hydraulic friction of the feed waters in the compartments should be low. A low internal resistance minimizes the electrical loss in the stack and a low hydraulic friction of the feed waters minimizes the pumping power. The non-conducting spacers, which are traditionally used to keep the membranes separated, significantly increase the internal resistance and the hydraulic friction of the feed waters.

A non-conductive spacer made from materials such as PET (polyethylene terephthalate), covers a part of the membrane and reduces the membrane area available for ion conduction. This is known as the spacer shadow effect [6]. Furthermore, the ionic current through the spacer grid is tortuous, which lengthens the current streamlines and thus increases the electrical resistance. Due to the presence of non-conductive spacers, the internal resistance in

previous experiments was more than twice the value expected based on the conductivity of the individual components [6, 7].

In addition, the knits of the spacers (where the spacer filaments cross) are a major source of hydraulic friction of the feed waters; experimental values exceed the theoretical equivalents for uniform laminar flow by more than an order of magnitude [5, 8]. Consequently, the power spent on pumping of the feed waters is significant compared to the actual power generated. In addition, spacers are vulnerable to biofouling, which increases the hydraulic friction even more. Biofouling is recognized as a spacer problem rather than a membrane problem [9, 10].

Ion-conductive spacers reduce the internal resistance (e.g., ref [6, 11]), but do not reduce the hydraulic friction. Profiled membranes on the other hand, i.e., membranes with a relief on their surface integrating the spacer and membrane functionality, make the use of separate spacers obsolete since the profile keeps the membranes separated while providing channels for the feed waters. Such profiled membranes (sometimes referred to as corrugated membranes) can combine a low internal resistance due to their ion-conducting ridges with a low hydraulic friction.

Profiled membranes have been used incidentally in electrodialysis (ED) [12-14]. The internal resistance in these experiments was approximately 1.6 times lower for a stack with double sided profiled membranes when compared to a system with non-conductive spacers [14]. At higher feedwater concentrations, the difference with non-conductive spacers became less pronounced. Higher limiting currents were found for devices with profiled membranes [14] due to the increase in available area for ion exchange. Profiled membranes show also a lower hydraulic friction in ED when compared to a device with spacers [13].

So far, profiled membranes have not been used in reverse electrodialysis and the results found in ED cannot be adopted a priori in RED, because the inter-membrane distance and the Reynolds numbers in RED are significantly smaller than in ED; Reynolds numbers in RED are usually an order of magnitude smaller than those in ED. Moreover, phenomena such as the overlimiting current and water splitting are absent in RED.

Here we investigate for the first time the operation of a RED stack with profiled membranes, and compare its performance to that of a RED stack with non-conductive spacers. The open circuit voltage, internal resistance and hydraulic friction of the feed waters are experimentally determined for both stacks, which enables comparing both stacks in terms of (net) power density and fuel efficiency.

3.2 Theory

The gross power density that can be obtained from a RED stack is related to the electromotive force E (V) that follows from the concentration difference over the membrane, the current density j (A/m^2) and the ohmic area resistance R_{ohmic} ($\Omega \cdot m^2$), according to:

$$P_{gross} = \frac{E \cdot j - R_{ohmic} \cdot j^2}{N_m} \qquad \text{(eq. 3.1)}$$

In which P_{gross} is the gross power density (in W/m^2 membrane) and N_m is the number of membranes (-). The electromotive force is given by the Nernst equation (as a theoretical voltage over the membranes due to different ion activities at either side of a membrane) and corrected for the membrane permselectivity and the number of membranes [15].

When no current is applied, the electromotive force can be estimated based on the inflow concentrations of the feed waters. This yields the open circuit voltage (E_{OCV}). When a current is applied, ions exchange from the salt water to the fresh water, and the concentrations at the membrane surface will be different than the concentration at the feedwater inflow. Due to the process of ion exchange, the concentrations of the feedwater compartments will approach each other. Hence, the electromotive force will be lower than the E_{OCV}. We can subdivide this potential reduction into a part due to the concentration change in the (concentration) boundary layer, E_{BL}, and a part due to the concentration change in the bulk solution, $E_{\Delta C}$. The equation for the gross power density can thus be written as:

$$P_{gross} = \frac{\left(E_{OCV} - E_{BL} - E_{\Delta C}\right) \cdot j - R_{ohmic} \cdot j^2}{N_m} \qquad \text{(eq. 3.2)}$$

In which E_{OCV}, E_{BL} and $E_{\Delta C}$ are in Volt. The impact of E_{BL} and $E_{\Delta C}$ can be compared to the ohmic resistance if E_{BL} and $E_{\Delta C}$ are divided by the current density. The reduction in electromotive force, divided by the current density, is than interpreted as a (non-ohmic) resistance:

$$P_{gross} = \frac{E_{OCV} \cdot j - R_i \cdot j^2}{N_m} \qquad \text{(eq. 3.3)}$$

With

$$R_i = R_{ohmic} + R_{\Delta C} + R_{BL} \qquad \text{(eq. 3.4)}$$

In which R_i is the total internal area resistance ($\Omega \cdot m^2$), $R_{\Delta C}$ is the contribution to the resistance due to the concentration change in the bulk solution ($\Omega \cdot m^2$) and R_{BL} is the

boundary layer resistance ($\Omega \cdot m^2$). The boundary layer resistance, R_{BL}, is associated with concentration polarization [6, 16]. The contribution of $R_{\Delta C}$ was often not recognized in previous research (e.g., ref [2, 6]), but is significant in RED [5].

The values of R_i and R_{ohmic} can be determined experimentally from chrono-potentiometric experiments [5, 16]. The total internal resistance, R_i, is derived from the (stationary) voltage when a stable current is applied. The sudden jump in voltage when the current is released reveals the contribution of the ohmic resistance. The latter time dependent voltage change is due to R_{BL} and $R_{\Delta C}$.

The contribution of $R_{\Delta C}$ can be estimated from [5]:

$$R_{\Delta C} = \frac{N_m}{2} \cdot \frac{\alpha \cdot R \cdot T}{F \cdot j} \cdot \ln\left(\frac{\Delta a_r}{\Delta a_s}\right) \qquad \text{(eq. 3.5)}$$

In which $\Delta a_r = 1 + \frac{j \cdot A}{F \cdot \Phi_r \cdot c_r}$ and $\Delta a_s = 1 - \frac{j \cdot A}{F \cdot \Phi_s \cdot c_s}$, α is the apparent permselectivity (as defined in e.g. ref [15]), R is the universal gas constant (8.314 J/mol/K), T is the absolute temperature (K), F is the Faraday constant (96485 C/mol), A is the electrode area (m^2), Φ is the discharge of the feedwater per compartment (m^3/sec), c is the inflow concentration of the feed waters (mol/m^3) and the subscripts r and s refer to river water and seawater, respectively. The last contribution, the boundary layer resistance (R_{BL}), can subsequently be derived as the remaining contribution in eq. 3.4.

Next to the power generated by the RED stack, power is consumed to pump the feedwater through the stack. The pumping power per membrane area, P_{pump} (W/m^2 membrane), can be calculated as [17]:

$$P_{pump} = \frac{\Delta p_r \cdot \Phi_r + \Delta p_s \cdot \Phi_s}{2A} \qquad \text{(eq. 3.6)}$$

In which Δp is the pressure drop in the feedwater over the RED stack (Pa). The factor 2A originates from the membrane area of cation and anion exchange membranes together. The pressure drop for a fully developed, uniform and laminar flow in an infinite wide channel can be calculated by using a momentum balance containing the pressure gradient and the wall friction. This theoretical pressure drop is given by [5]:

$$\Delta p = \frac{12\mu \cdot L \cdot \Phi}{b \cdot d^3} \qquad \text{(eq. 3.7)}$$

In which μ is the viscosity of water (Pa·s), L is the length of the flow path (m), b is the width of the flow path (m) and d is the height of the flow path (m). Under experimental conditions

and especially in spacer filled channels, the pressure drop can be significantly higher than this theoretical value [5]. Consequently, this theoretical value is considered as a minimum value, corresponding to optimum (uniform, infinite wide) circumstances.

The net power density is the difference between the maximum value from eq. 3.3 (gross power density) and eq. 3.6 (power losses by pumping):

$$P_{net} = \frac{E_{OCV}{}^2}{4N_m \cdot R_i} - \frac{\Delta p_r \cdot \Phi_r + \Delta p_s \cdot \Phi_s}{2A} \qquad \text{(eq. 3.8)}$$

Profiled membranes are expected to lower the ohmic resistance, and thus the total resistance R_i, by providing ion conducting pathways in stead of a spacer shadow when using non-conductive spacers. Furthermore the pressure drop, Δp, is expected to be lower using profiled membranes compared to stacks with flat membranes and spacers, due to the absence of spacer filaments disturbing the flow. Therefore, the net power density is expected to be higher for a stack with profiled membranes when compared to a stack with flat membranes and spacers.

3.3 Experimental setup

3.3.1 Membranes

Commercial heterogeneous membranes, types Ralex CMH and AMH (Mega a.s., Czech Republic) were used. These membranes are composed of a polyethene (PE) substrate with ion exchange resins and polyethersulfone (PES) re-inforcement incorporated. Although the resistance of these membranes is relatively high compared to that of homogeneous ion exchange membranes [15], these membranes were selected because of their relatively low melting temperature of approximately 115ºC. This offers the possibility to apply a profile in the membrane in dry form using hot pressing at relatively low temperatures.

The resistance and permselectivity of the membranes were measured before and after hot pressing of the membranes. The membrane resistance was measured in 0.5 M NaCl. The permselectivity was measured using 0.1 M NaCl and 0.5 M NaCl. The experimental setup for membrane resistance and permselectivity determination is described elsewhere [15].

3.3.2 Membrane profiling

To create the one-sided profiled membranes, the dry membranes were cut in pieces of 160x160 mm^2 and sandwiched between two aluminum moulds. One of these moulds had a profile comprising of channels of 200 μm in depth and 200 μm in width, as shown in Figure 3.1. The other mould had a chamber with a flat bed of 164x164 mm in size and 220 μm in depth.

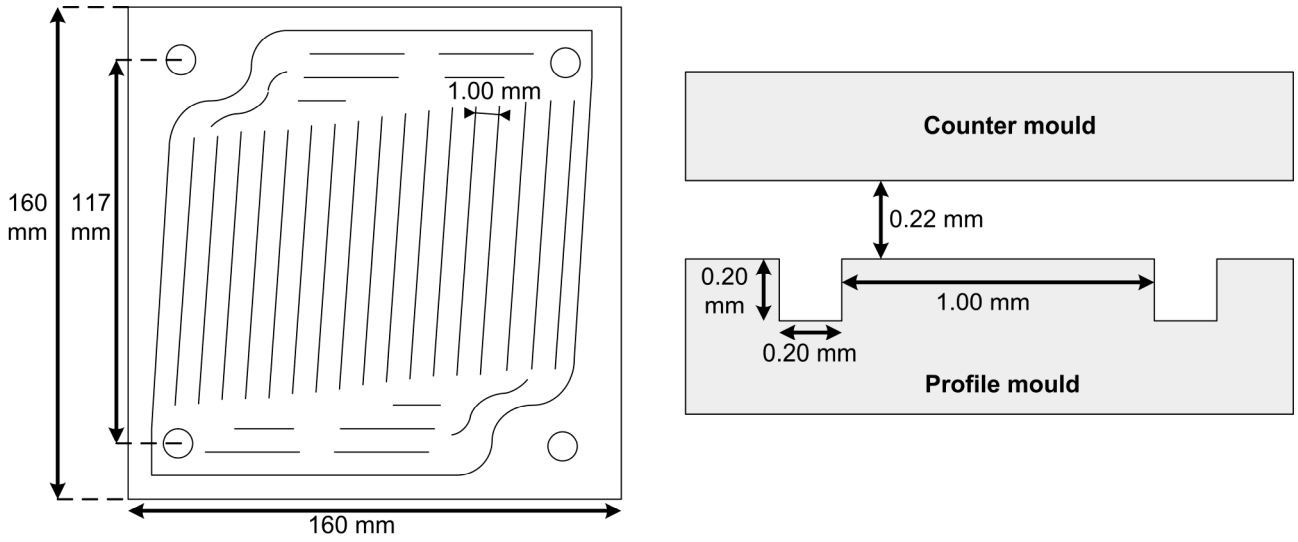

Figure 3.1: Drawing of moulds. Left: top view of profile mould (not on scale). The black lines indicate the grooves in the mould. Right: cross section at the middle of the moulds.

A release agent (EWO 7902, KVS, Germany) was sprayed on the membranes to facilitate release of the membranes from the moulds after hot pressing. The moulds and membranes were placed in a thermal press (Vogt Maschinenbau, Germany), which was preheated to 140ºC. The moulds were heated for two minutes, and subsequently pressed for ten minutes at 53 tons. The pressure on the total area of 160x160 mm^2 was 210 bars. Finally, the moulds were cooled to 40ºC and removed from the press.

The use of a thermal press to apply the profile on the membranes could alter the characteristics of the membrane [18]. To exclude this effect, also the membranes used in the stack with spacers were hot pressed according to the same procedure. In this case, the same mould with a 220 μm deep chamber was used on one side, while the other side was covered by a flat aluminum plate.

The pressed membranes were immersed in demineralized water, ultrasonically treated in approximately 0.25 M NH_3 to remove the release agent, rinsed in demineralized water, immersed in 3 M NaCl to exchange the counter ions in the membranes towards Na^+ or Cl^-, and finally immersed in 0.25 M NaCl to equal conditions in the stack. The final, wet membranes have ridges with a height of 245 ± 5 μm for the CEMs and 230 ± 5 μm for the AEMs.

3.3.3 Stack

A schematic picture of the stack with profiled membranes and that with spacers is given in Figure 3.2.

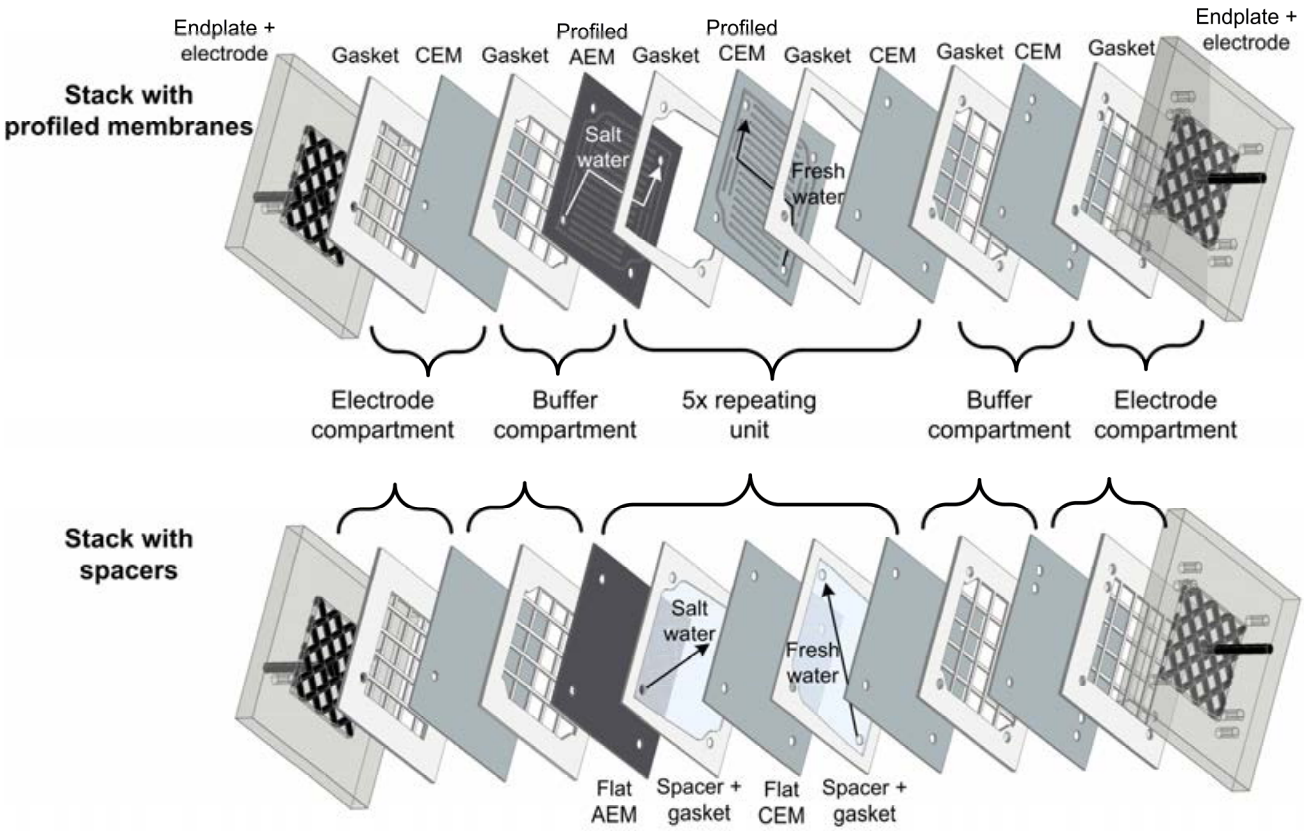

Figure 3.2: Illustration of stack setup with profiled membranes (upper part) and that with spacers (bottom part).

Both stacks contained 2 Ti electrodes (mesh 1.0, 10x10 cm^2) coated with Ir/Ru (Magneto Special Anodes B.V., The Netherlands), two CEMs (Neosepta, CMX) shielding the

electrode compartments, and two buffer compartments (Figure 3.2) to prevent leakage of the electrolyte towards the feed waters and vice versa.

The stack with the profiled membranes contained 5 profiled CEMs and 5 profiled AEMs, alternately stacked. A silicone film of 100 μm (Specialty Silicone Fabricators, USA), that fits around the profiled area, was used to seal the water compartments in the stack with profiled membranes. In case of the stack with spacers, 5 flat (pressed) CEMs and 5 flat (pressed) AEMs were alternately stacked. A woven fabric, non-conductive spacer (Sefar Nitex 07-300/46, Switzerland), was cut in the same shape (Figure 3.2) as the profiled area of the profiled membranes. The thickness of this spacer was 240 ± 5 μm as measured using a thickness gage (Mutitoyo 547-401, Japan). According to the specifications of the manufacturer, the open area of the spacer was 46% and its porosity was 72%. A silicone film (Specialty Silicone Fabricators, USA) of approximately 250 μm thick was used to seal the water compartments.

3.3.4 Feed waters

Synthetic feed waters representative for seawater and river water with a concentration of 0.507 M (i.e., 3.00 %) and 0.017 M (i.e., 0.10 %) NaCl, respectively, were prepared by dissolving NaCl (technical grade, ESCO, The Netherlands) in demineralized water. The feed solutions were kept at 25 ± 0.5 ºC by a heater (Tetratec HT300, Germany) and a pump.

The artificial sea and riverwater solutions were pumped through the stack by two adjustable peristaltic pumps (Cole-Parmer, Masterflex L/S Digital drive, USA). Measurements were performed at 0.8, 1.5, 3, 5, 8, 15, 30, 60, 100, 150, 200 and 250 ml/min. A 1 μm cartridge filter was placed in a two liter container just before the stack, not only for filtering, but rather to dampen the pressure pulse created by the peristaltic pumps.

For each flow rate, the Reynolds number was calculated being defined as the Reynolds number for a wide slit:

$$\mathrm{Re} = \frac{\bar{u} \cdot D_h}{\nu} = \frac{\bar{u} \cdot 2d}{\nu} = \frac{2\Phi}{b \cdot \nu} \qquad \text{(eq. 3.9)}$$

Where $\bar{u}$ is the average flow velocity, D_h is the hydraulic diameter and ν is the kinematic viscosity of water ($8.9 \cdot 10^{-7}$ m^2/s at 25 ºC).

The pressure drop between the inflow and outflow of the feed waters was measured using a differential pressure meter (Endress+Hauser Deltabar S, Germany) with an accuracy of 0.1 kPa ± 1%.

3.3.5 Electrode and buffer compartments

The electrode rinse solution was composed of 0.05 M $K_3Fe(CN)_6$, 0.05 M $K_4Fe(CN)_6$ and 0.5 M NaCl, and circulated at 400 ml/min from one electrode compartment to the other electrode compartment and back to its storage vessel.

The buffer compartments were fed with 0.5 M NaCl circulating at 80 ml/min and kept at 1 bar by a pressure control valve. In this way, the pressure outside of the membranes is always higher than that in the interior, ensuring that the membranes remain closely packed.

The electrode rinse solution and buffer solution were kept at 25 ± 0.2 ºC using a water bath (Haake DC10, Germany). The complete stack, including the filters for the feedwater, was placed in a thermostatic chamber (MMM Friocell 222, Germany) to maintain the temperature at 25.0 ± 0.1ºC during operation.

3.3.6 Electrical characterization

Chronopotentiometry was performed on both stacks. At least 4 current steps were applied for every flow rate using a galvanostat (Ivium Technologies, The Netherlands). The level and duration of the current steps were different for all flow rates to ensure that equilibrium was reached. At the lowest flow rate, 0.8 ml/min, the current steps ranged from 2.5 to 10 A/m^2 and each level was imposed for 7200 s. At the highest flow rate of 250 ml/min, the current steps ranged from 5 to 30 A/m^2 and lasted 50 s each, which was already sufficient to reach equilibrium at this flow rate.

A part of the internal resistance of the system is due to the resistance of the electrodes and buffer compartments. These resistances are not of interest for a full-scale application, where many more membrane pairs can be stacked and the contribution of the electrodes and corresponding compartments is small compared to that of the other resistances. However, in a lab-scale stack these resistances do play a role and should be taken into account. As such, the total internal area resistance of the system is corrected for the resistance of the electrodes and buffer compartments. The resistance of the electrodes and buffer compartments was measured using an ‘empty’ stack, consisting of two electrodes, two electrode compartments and two buffer compartments only. Chronopotentiometry was conducted on this empty stack under the same conditions as for the RED stacks.

Figure 3.3 shows a typical example of the experimental data obtained for the resistance and the corresponding gross power density, as a function of the current density.

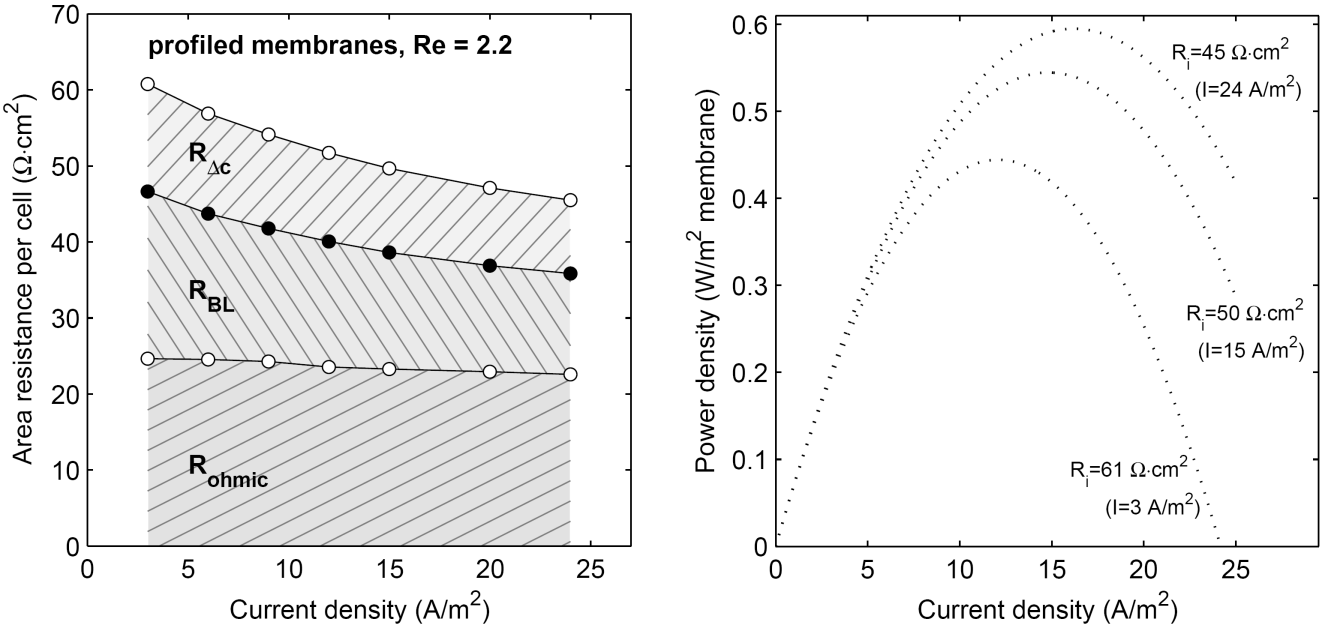

Figure 3.3: Typical example of area resistance and gross power density as a function of the current density, for a stack with profiled membranes, at a Reynolds number of 2.2.

The total area resistance is often assumed to be independent of the current density, which would result in a single parabolic graph for the gross power density when plotted against the current density (eq. 3.3) [19-21]. However, Figure 3.3 shows that the resistance is not constant for different current densities, and thus the estimated maximum gross power density is differs, depending on the current density used to measure the resistance. All components of the resistance decrease if the current density increases, with a most significant decrease in R_{BL}. The decrease in resistance is due to ion transport and the corresponding increase in conductivity of the fresh water. The resistance has a stronger dependency on the current density at lower Reynolds numbers or flow rates, whereas the resistance is hardly influenced by the current density at higher flow rates when the feed waters are rapidly renewed. For a typical Reynolds number in RED, as in Figure 3.3, the maximum power density can be estimated 10% lower or higher when the resistance is measured at a suboptimal current density. Consequently, the representative resistance is measured at a current density corresponding to the maximum power density.

Using the open circuit voltage and the resistances as determined experimentally, the maximum power density output can be calculated using eq. 3.3. Subtracting the pumping power losses, the net power density can be calculated using eq. 3.8.

All measurements were performed in duplicate, i.e., on two individual stacks with profiled membranes and two stacks with spacers. The average values are presented, with error bars at one standard deviation to indicate the fluctuations. Some error bars are smaller than the symbol size and therefore not visible.

3.4 Results

3.4.1 Profiled membrane characteristics

Table 3.1 shows the specifications of the manufacturer and the measured permselectivity and resistance of the membranes, before and after hot pressing. The permselectivity and resistance do change after hot pressing, most drastically in the case of the AEMs (AMH). The differences between the profiled membranes and the corresponding flat pressed membranes are nevertheless small. This emphasizes that a RED stack with profiled membranes needs to be compared to a RED stack with flat pressed membranes only.

Table 3.1: Properties of Ralex CMH and AMH

Membrane	Area resistance ($\Omega \cdot cm^2$)	Permselectivity (%)	Wet thickness (μm)	Conductivity (mS/cm)
CMH-PES				
Specification	< 10	> 92	< 700	> 6.3
Measured, unpressed	7.0 ± 0.3	97 ± 2	650 ± 15	9.3 ± 0.3
Measured, flat pressed	5.8 ± 0.3	95 ± 1	570 ± 25	9.8 ± 0.4
Measured, profiled	5.4 ± 0.3	95 ± 1	510 ± 15 [a]	9.3 ± 0.5
AMH-PES				
Specification	< 7.5	> 90	< 750	> 8.3
Measured, unpressed	7.3 ± 0.3	89 ± 1	670 ± 15	9.1 ± 0.3
Measured, flat pressed	3.5 ± 0.3	87 ± 1	485 ± 15	13.9 ± 0.6
Measured, profiled	2.7 ± 0.1	87 ± 1	475 ± 10 [a]	17.7 ± 0.6

[a]: thickness of membrane excluding ridges. The ridges were 245 ± 5 μm (CEM) and 230 ± 5 μm (AEM) high.

The changes occurring in the membranes due to hot pressing are not the main focus of this research and will not be discussed in detail. Hot pressing is not the only method available for

profiled membrane production and other methods, e.g., casting [22, 23], could be used as well. Nevertheless, some explanations for the observations in Table 3.1 can be suggested. The reduced membrane resistance after hot pressing is mainly caused by the lower thickness of the membranes. For AMHs, the specific conductivity increased after pressing, while the permselectivity decreased. Previous research showed that the membrane surface area covered by ion exchange resin particles was reduced after hot pressing of heterogeneous ion exchange membranes [18]. This suggests a lower surface charge and hence a lower permselectivity. To obey continuity of mass, ion exchange particles will become more closely packed in the cross sectional direction, which may explain a slightly higher specific conductivity.

Figure 3.4 shows scanning electron microscope (SEM) images of dry profiled cation and anion exchange membranes.

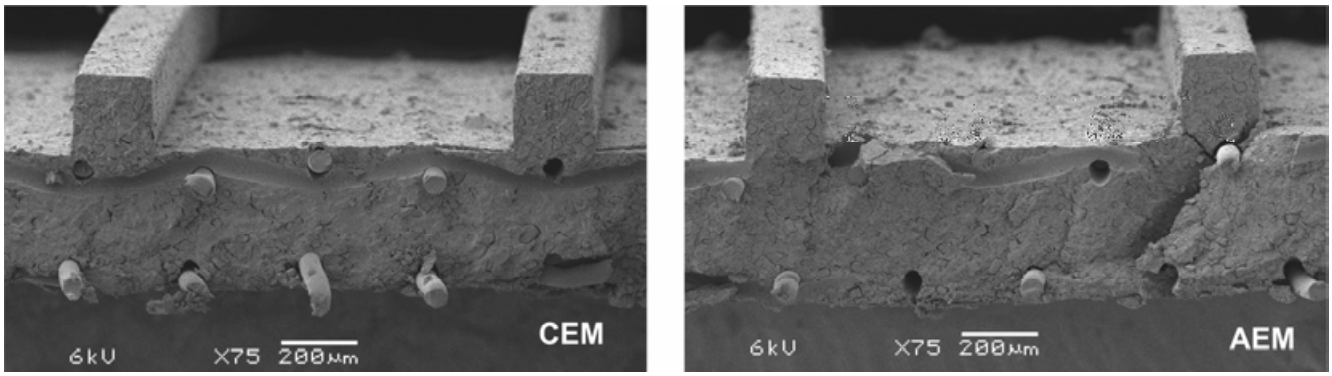

Figure 3.4: Representative SEM-image of cross-section of the profiled CEM (CMH) left and AEM (AMH) right. The protruding fibers and black holes are remnants of the reinforcement (PES) in the membrane. The small crack in the AEM is due to cutting of the membrane.

The ridges of the dry profiled membrane are as expected 200 (± 5) μm in height, corresponding to the mould grooves. The width of the ridges is slightly more than 200 μm, especially at the ridge foot. The ridges expand in wet state to a height of 245 ± 5 μm for the CEMs and 230 ± 5 μm for the AEMs.

3.4.2 Power density

Figure 3.5 shows the gross power density of the stacks with profiled membranes and that with spacers as a function of the Reynolds number and the fuel efficiency (i.e., the actual generated energy per liter feedwater compared to the theoretical equivalent).

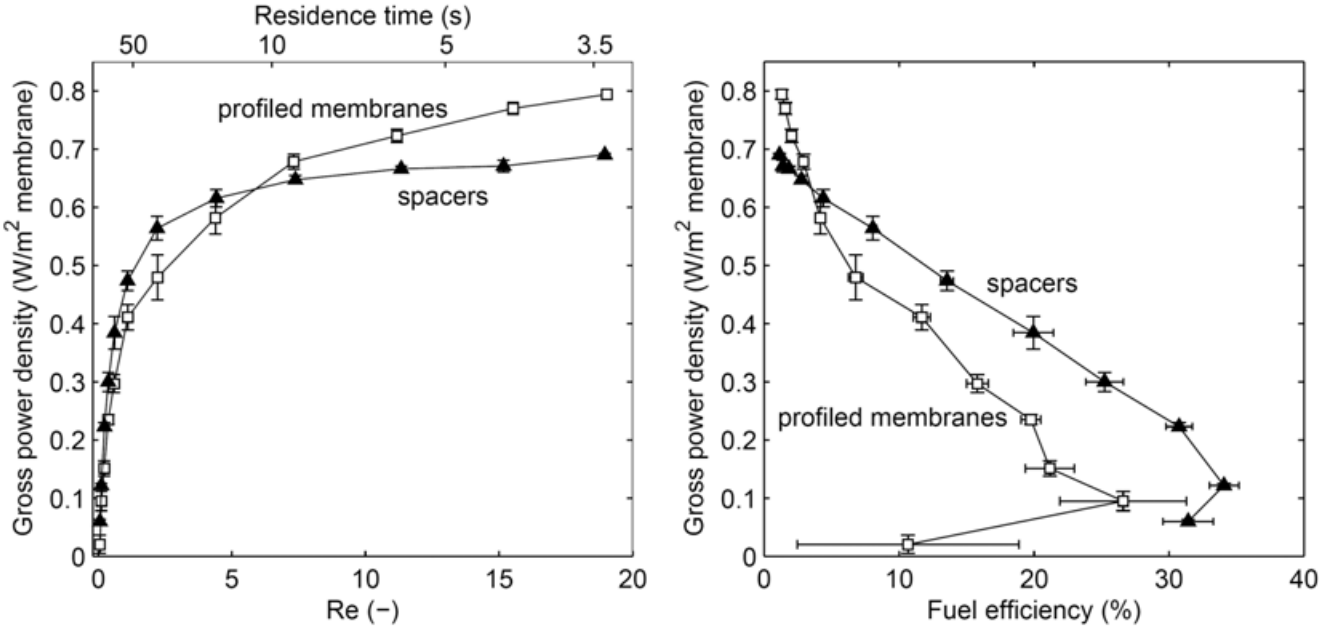

Figure 3.5: Power density as a function of the Reynolds number and fuel efficiency, for a stack with profiled membranes and a stack with spacers.

The gross power density increases with increasing Reynolds number because the internal resistance decreases with increasing Reynolds number. At higher Reynolds numbers, the power density of the stack with profiled membranes is higher than that obtained for the stack with spacers, whereas the stack with spacers gives the highest power densities at lower Reynolds numbers. The power density for the stack with spacers only increases slightly for residence times smaller than 10 s, which is in agreement with previous observations [15, 17]. The stack with profiled membranes on the other hand shows a much steeper increase in gross power density at lower residence times. This shows that the power density of a RED stack with profiled membranes can exceed the power density for a stack with spacers even more at higher Reynolds numbers (i.e., very high flow rates and lower residence times).

This observation is reflected in the fuel efficiency as well. At high flow rates, the stack with profiled membranes generates higher power densities at the expense of the fuel efficiency compared to the stack with spacers. At high fuel efficiencies (low flow rates), the stack with spacers yields a higher power density. The maximum fuel efficiency was found for the one but lowest flow rate. At the lowest flow rate, losses due to co-ion transport and osmosis reduce the fuel efficiency again, as was demonstrated previously [17].

For a small-scale power plant, where not the amount of water but the price of the plant limit the process, low fuel efficiencies are acceptable to generate high power densities. Profiled

membranes give a higher gross power density in that range. When the supply of water becomes limiting, higher fuel efficiencies are desired.

3.4.3 Open circuit voltage

To explain the differences in gross power density for the stack with profiled membranes and that with spacers, the open circuit voltage (OCV) and the resistance of both stacks are examined. Figure 3.6 shows the OCV for the stack with profiled membranes and that with spacers.

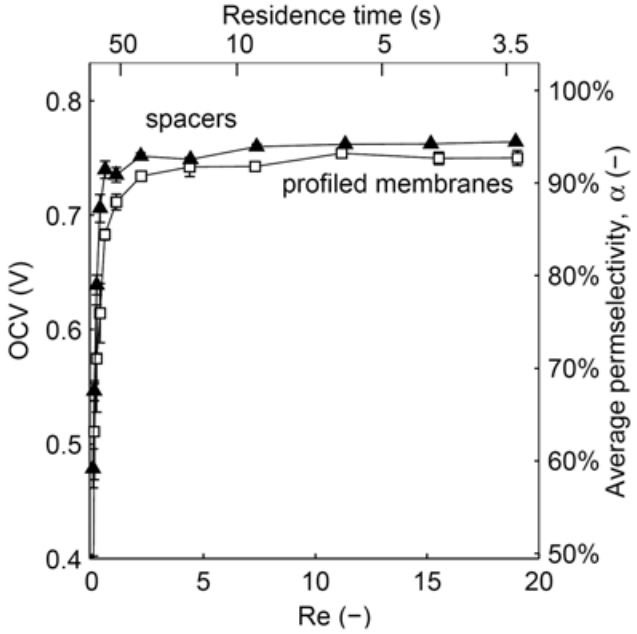

Figure 3.6: Open circuit voltage (OCV) as a function of the Reynolds number, for a stack with profiled membranes and one with spacers.

At high Reynolds numbers, the values found for the OCV are approximately 92-94% of the theoretical value as derived from the Nernst equation, whereas significantly lower values are measured at low flow velocities. Długołęcki et al [20] reported similar behavior. They explained the low OCV at low flow velocities by referring to concentration polarization. Although this term is somewhat ambiguous for open circuit conditions (no net charge transport), the OCV is indeed limited by changes in concentration in the vicinity of the membranes, which is most pronounced at low flow velocities. The non-perfect membranes allow small fluxes of water from the river water compartments to the seawater compartments and salt transport (co-ion and counter-ion) from the seawater to the river water compartment are apparent as well. This transport is assumed to be confined in a relatively small layer

adjacent to the membranes, as the outflow concentrations at open circuit conditions are not significantly different from those at the inflow. At higher flow velocities, mixing of the boundary layers is improved and the measured OCV approaches the theoretical value. This in contrast to the mixing at very low flow rates (i.e., very low Reynolds numbers).

The stack with spacers has a slightly higher OCV compared to the stack with profiled membranes, although not as significant at all Reynolds numbers. Based on the permselectivity of the individual membranes (Table 3.1), the OCV could be expected to be the same for both stacks. The small differences are probably due to the better mixing in the stack with spacers. The same is observed for the resistance, as will be discussed later. Poor mixing introduces the same effects (osmosis and co-ion transport) as low Reynolds numbers do.

3.4.4 Resistance

Figure 3.7 shows the area resistances for the stack with profiled membranes and the stack with spacers, divided in R_{ohmic}, $R_{\Delta C}$ and R_{BL}, as function of the Reynolds number.

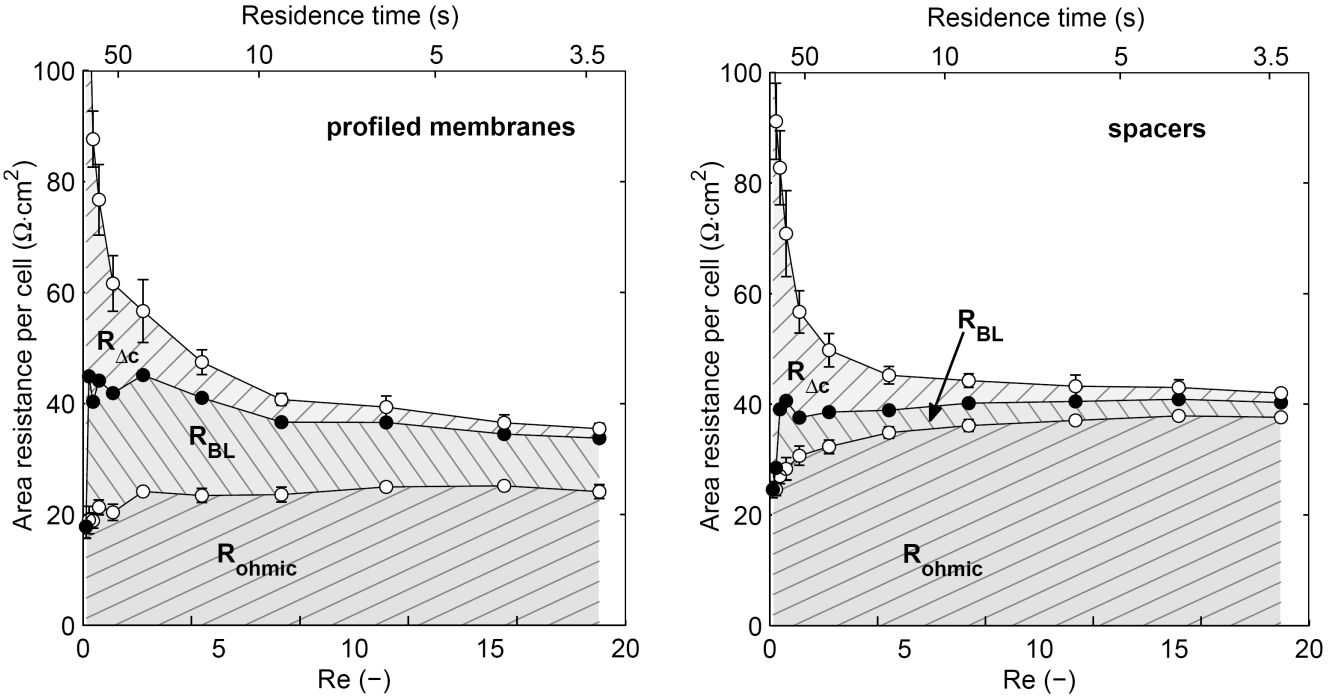

Figure 3.7: Area resistance as a function of the Reynolds number, for a stack with profiled membranes and a stack with spacers.

Figure 3.7 shows that R_{ohmic} increases, while $R_{\Delta C}$ and R_{BL} decrease with increasing Reynolds number for both stacks. The decrease of R_{BL} was observed before [5], and is a direct effect of the higher mixing rate at high flow velocities (and thus at high Reynolds numbers). $R_{\Delta C}$ is significant at low Reynolds numbers (even dominant at the lowest Reynolds number), whereas $R_{\Delta C}$ has the smallest contribution at the highest Reynolds number. The decrease of $R_{\Delta C}$ at higher Reynolds numbers is a consequence of the faster re-supply of feedwater and can be derived from eq. 3.5. Compared to the stack with spacers, the stack with profiled membranes has a significantly lower ohmic resistance, but a distinctively higher boundary layer resistance.

The lower ohmic resistance in case of the profiled membranes was expected, as the profiles provide an ion conductive path, i.e., the spacer shadow effect is eliminated. The ohmic resistance was reduced by approximately 30% compared to the stack with spacers. Although this is a major improvement, the ohmic resistance was even more dramatically reduced when ion conductive spacers were used [6]. This can be due to the relatively high area resistance of the heterogeneous membranes (Table 3.1; 2.7-5.8 $\Omega \cdot cm^2$) as used in this experiment, while the experiment with ion conductive spacers in previous research used homogeneous membranes with an area resistance of only 2-3 $\Omega \cdot cm^2$ [6]. It is expected that profiled membranes with a lower area resistance (for example homogeneous membranes) would result in a more distinct difference when compared to non-conductive spacers is expected.

The boundary layer resistance in the stack with profiled membranes is significantly higher than that in the stack with spacers. This obviously reveals the much better promotion of mixing in the case of the spacers compared to that in the stack with profiled membranes. The spacer filaments act as an obstacle forcing the flow to follow a tortuous path and thus generating additional mixing in the boundary layer. This process is absent when membranes with the current profile are used, leading to an increased R_{BL}.

Overall, the area resistance of the stack with profiled membranes is slightly higher at low Reynolds numbers and slightly lower at high Reynolds numbers than that of the stack with spacers.

3.4.5 Hydraulic losses

The flow channels as provided by the profiled membranes differ from a hydrodynamic point of view from those provided by the spacers. Spacers are known to cause a large pressure

drop over the inflow and outflow of the feedwater, indicating large hydraulic friction. The flow along the straight ridges of the profiled membranes is expected to feature less hydraulic friction. Figure 3.8 shows the pressure drop over the inflow and outflow of the feedwater.

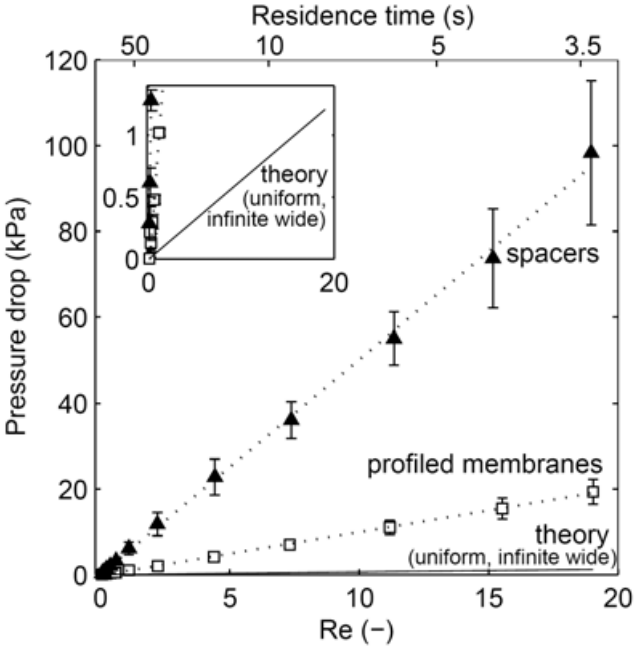

Figure 3.8: Pressure drop as a function of the Reynolds number, for a stack with profiled membranes, a stack with spacers and the theoretical pressure drop assuming uniform flow in an infinite wide channel (eq. 3.7). The small axis at the left top shows a zoom for small pressure drops (0-1.5 kPa).

The pressure drop is approximately 4 times lower for the stack with profiled membranes, i.e., the profiled membranes induce significantly less hydraulic friction than the spacers. Still, the pressure drop in the stack with profiled membranes is almost twenty times the theoretical value as calculated for uniform laminar flow as described by eq. 3.7. A minor part of this excess can be explained by the finite width of the profiled channels. If the actual geometries of the profiled membranes are considered, in stead of an infinite wide channel, the theoretical pressure drop is still approximately 13 times lower than the measured values for the profiled membranes. The latter excess in hydraulic friction is caused at the inflow and outflow of each compartment, where the flow is subject to sharp corners and narrow channels, and thus cannot be considered uniform.

The power spent on pumping the feed waters increases with the square of the flow rate (eq. 3.7 and 3.6). Subtraction of the power losses for pumping from the gross power density gives the net power density (Figure 3.9).

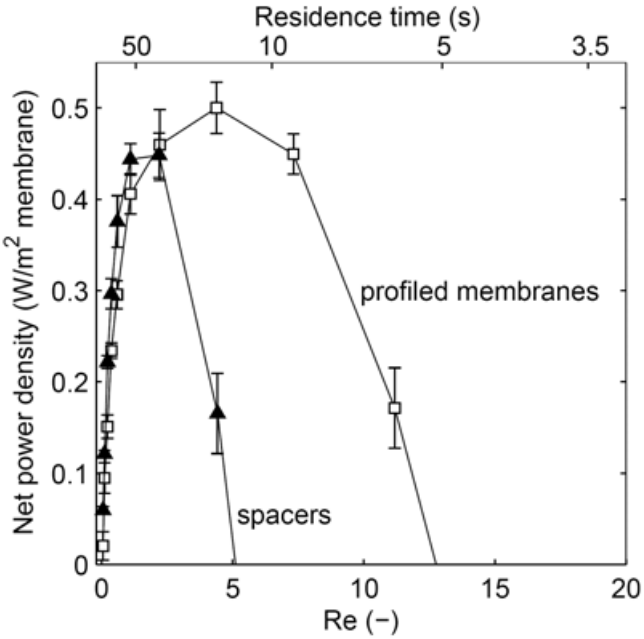

Figure 3.9: Net power density as a function of the Reynolds number, for a stack with profiled membranes and a stack with spacers.

The maximum net power density is approximately 10% higher for the stack with profiled membranes (in the current design) than for the stack with spacers. More important however, is the observation that the peak in net power density shifts towards higher Reynolds numbers for the stack with profiled membranes compared to the stack with spacers, due to the lower hydraulic friction. If the gross power density at this flow rate would increase due to future developments, and thus the efficiency approaches its maximum value (50% for the stacks in this setup), higher flow rates (so higher Reynolds numbers) are inevitable to further improve the power density. The four times lower hydraulic friction for the profiled membranes allows a wider range in Reynolds number. Therefore the profiled membranes have a much better perspective for further improvement in (net) power density.

The relatively low hydraulic friction also allows new flow geometries that improve the gross power density. For example, a smaller intermembrane distance, i.e., thinner profiled ridges, will significantly enhance the gross power density [5]. Furthermore, new geometries can be designed that induce better mixing than the traditional spacers. Profiling membranes offers a

higher degree of freedom to create new profile geometries where a hydrodynamic flow can be combined with efficient mixing in the boundary layers.

3.5 Conclusions

In this work we show the performance of a reverse electrodialysis (RED) stack using profiled membranes instead of traditionally used non-conductive spacers in between the ion exchange membranes. Hot pressing of commercially available membranes is used to create profiled membranes, which resulted in a slight reduction in permselectivity and significant decrease in resistance. The stack with profiled membranes shows a 30% lower ohmic resistance compared to that with spacers, but the boundary layer resistance is significantly higher. The maximum gross power density of the stack with profiled membranes is slightly higher than that in the stack with spacers. In combination with a lower hydraulic friction, this resulted in a net power density that is 10% higher for the stack with profiled membranes. Even more important is the scope for future development of profiled membranes. The low hydraulic friction enables higher Reynolds numbers than in a stack with spacers. Furthermore, profiling membranes offers a high degree of freedom to create new profile geometries where a hydrodynamic flow can be combined with efficient mixing in the boundary layers.

References

1. Pattle, R. E., Production of Electric Power by mixing Fresh and Salt Water in the Hydroelectric Pile. *Nature* **1954,** *174*, (4431), 660-660.
2. Post, J. W.; Hamelers, H. V. M.; Buisman, C. J. N., Energy Recovery from Controlled Mixing Salt and Fresh Water with a Reverse Electrodialysis System. *Environmental Science & Technology* **2008,** *42*, (15), 5785-5790.
3. Veerman, J.; Saakes, M.; Metz, S. J.; Harmsen, G. J., Reverse electrodialysis: Performance of a stack with 50 cells on the mixing of sea and river water. *Journal of Membrane Science* **2009,** *327*, 136-144.
4. Post, J. W.; Goeting, C. H.; Valk, J.; Goinga, S.; Veerman, J.; Hack, P. J. F. M., Towards implementation of reverse electrodialysis for power generation from salinity gradients. *Desalination and water treatment* **2010,** *16*, 182-193.
5. Vermaas, D. A.; Saakes, M.; Nijmeijer, K., Double Power Densities from Salinity Gradients at Reduced Intermembrane Distance. *Environmental Science & Technology* **2011,** *45*, (16), 7089-7095.
6. Długołęcki, P. E.; Dąbrowska, J.; Nijmeijer, K.; Wessling, M., Ion conductive spacers for increased power generation in reverse electrodialysis *Journal of Membrane Science* **2010,** *347*, (1-2), 101-107.
7. Veerman, J.; Post, J. W.; Saakes, M.; Metz, S. J.; Harmsen, G. J., Reducing power losses caused by ionic shortcut currents in reverse electrodialysis stacks by a validated model. *Journal of Membrane Science* **2008,** *310*, (1-2), 418-430.
8. Veerman, J.; Saakes, M.; Metz, S. J.; Harmsen, G. J., Reverse electrodialysis:A validated process model for design and optimization. *Chemical Engineering Journal* **2011,** *166*, (1), 256–268.

9. Vrouwenvelder, J. S.; Schulenburg, D. A. G. v. d.; Kruithof, J. C.; Johns, M. L.; Loosdrecht, M. C. M. v., Biofouling of spiral-wound nanofiltration and reverse osmosis membranes: A feed spacer problem. *Water Research* **2009,** *43*, (3), 583-594.

10. Post, J. W. Blue Energy: electricity production from salinity gradients by reverse electrodialysis. PhD thesis Wageningen University, **2009**.

11. Kedem, O., Reduction of polarization in Electrodialysis by ion-conducting spacers. *Desalination* **1975,** *16*, 105-118.

12. Nikonenko, V. V.; Pismenskaya, N. D.; Istoshin, A. G.; Zabolotsky, V. I.; Shudrenko, A. A., Description of mass transfer characteristics of ED and EDI apparatuses by using the similarity theory and compartmentation method. *Chemical Engineering and Processing* **2008,** *47*, 1118-1127.

13. Larchet, C.; Zabolotsky, V. I.; Pismenskaya, N.; Nikonenko, V. V.; Tskhay, A.; Tastanov, K.; Pourcelly, G., Comparison of different ED stack conceptions when applied for drinking water production from brackish waters. *Desalination* **2008,** *222*, 489-496.

14. Strathmann, H., Electrodialysis, a mature technology with a multitude of new applications. *Desalination* **2010,** *264*, (3), 268-288.

15. Długołęcki, P. E.; Nijmeijer, K.; Metz, S. J.; Wessling, M., Current status of ion exchange membranes for power generation from salinity gradients. *Journal of Membrane Science* **2008,** *319*, (1-2), 214-222.

16. Sistat, P.; Pourcelly, G., Chronopotentiometric response of an ion-exchange membrane in the underlimiting current-range. Transport phenomena within the diffusion layers. *Journal of Membrane Science* **1997,** *123*, (1), 121-131.

17. Veerman, J.; Saakes, M.; Metz, S. J.; Harmsen, G. J., Electrical Power from Sea and River Water by Reverse Electrodialysis: A First Step from the Laboratory to a Real Power Plant. *Environmental Science & Technology* **2010,** *44*, (23), 9207-9212.

18. Zabolotsky, V. I.; Loza, S. A.; Sharafan, M. V., Physicochemical Properties of Profiled Heterogeneous Ion-Exchange Membranes. *Russian Journal of Electrochemistry* **2005,** *41*, (10), 1053–1060.

19. Weinstein, J. N.; Leitz, F. B., Electric Power from Differences in Salinity: The Dialytic Battery. *Science* **1976,** *191*, (4227), 557-559.

20. Długołęcki, P. E.; Gambier, A.; Nijmeijer, K.; Wessling, M., Practical Potential of Reverse Electrodialysis As Process for Sustainable Energy Generation. *Environmental Science & Technology* **2009,** *43*, (17), 6888-6894.

21. Veerman, J.; Jong, R. M. D.; Saakes, M.; Metz, S. J.; Harmsen, G. J., Reverse electrodialysis: Comparison of six commercial membrane pairs on the thermodynamic efficiency and power density. *Journal of Membrane Science* **2009,** *343*, (1-2), 7-15.

22. Balster, J.; Yildirim, M. H.; Stamatialis, D. F.; Ibanez, R.; Lammertink, R. G. H.; Jordan, V.; Wessling, M., Morphology and Microtopology of Cation-Exchange Polymers and the Origin of the Overlimiting Current. *J. Phys. Chem. B* **2007,** *111*, (9), 2152-2165.

23. Balster, J.; Stamatialis, D. F.; Wessling, M., Membrane with integrated spacer. *Journal of Membrane Science* **2010,** *360*, (1-2), 185-189.

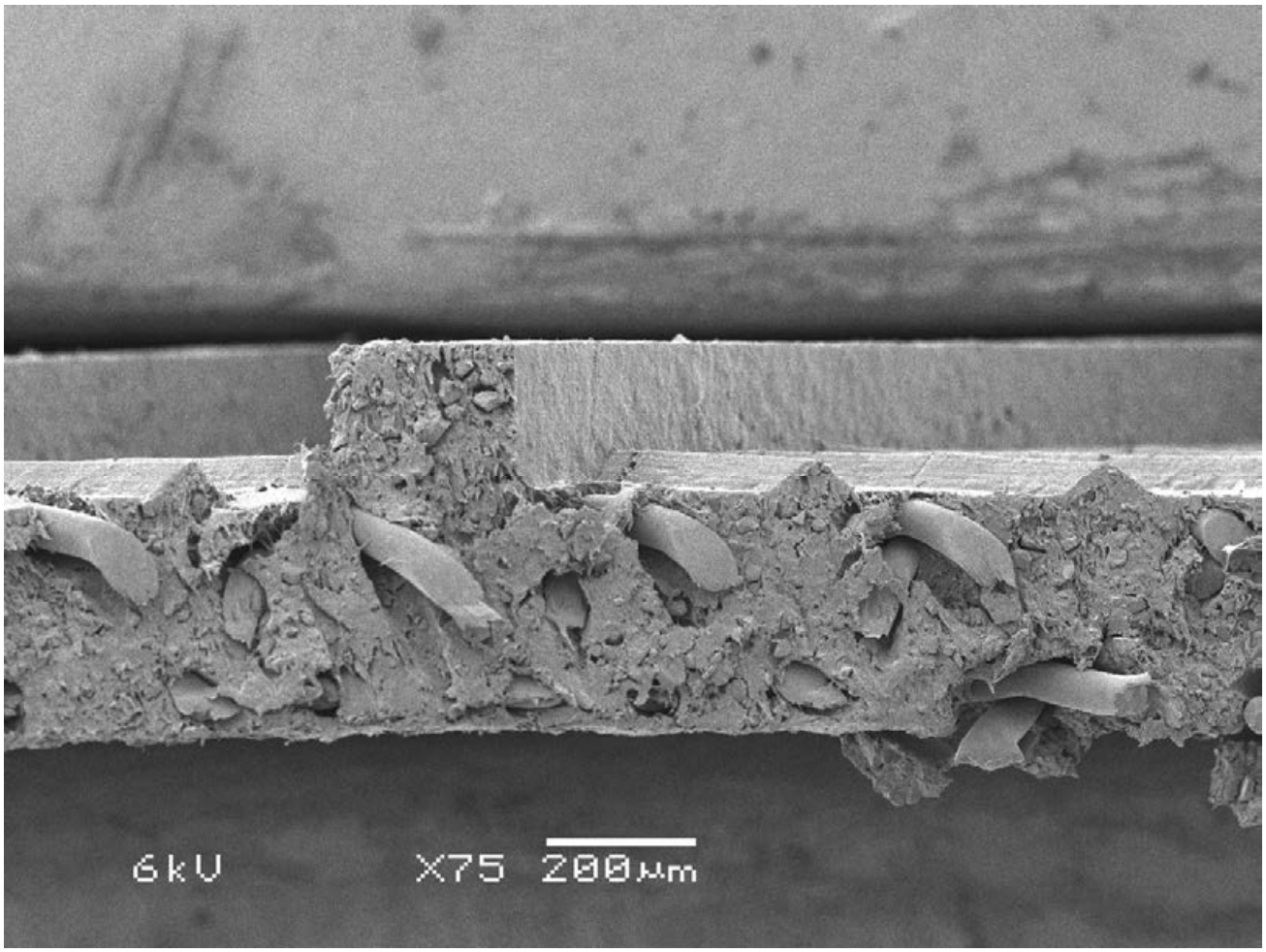
6kV
X75 200µm

Chapter 4

Enhanced mixing in the diffusive boundary layer for profiled membranes and spacer filled channels

Abstract

Renewable energy can be obtained from mixing waters with different salinity using reverse electrodialysis (RED). To obtain a high power per membrane area, combined with a low power consumption for pumping the feedwater, RED is preferably operated using small intermembrane distances and low flow rates. However, the diffusive boundary layer near the membranes induces a significant (non-ohmic) resistance at lower flow rates. This is even more pronounced when a spacerless design, with profiled membranes, is used. This research presents how the non-ohmic resistance in RED can be reduced, and consequently the obtained power can be increased, without compromising the power consumed for pumping. Experiments were conducted using several designs, with and without mixing promoters such as twisted spacers and additional sub-corrugations on the membrane, to investigate the effect of additional mixing in the diffusive boundary layer on the obtainable power in RED. The results show that these mixing promoters are not effective at the low Reynolds numbers typically used in RED. The distribution of the feedwater inflow, however, has a major impact on the non-ohmic resistance. The design with profiled membranes without sub-corrugations has the best performance, which is almost twice the net power density obtained with a design with normal spacers.

This chapter will be published as

David A. Vermaas, Michel Saakes, Kitty Nijmeijer, Enhanced mixing in the diffusive boundary layer for energy generation in reverse electrodialysis, *Journal of Membrane Science*, **2014**, *453*, 312-319

4.1 Introduction

Reverse electrodialysis (RED) is a technology to capture the available energy when waters with different salinity mix, for example where river water is discharged into the sea. This source for renewable energy is unused at the moment, while the theoretical potential is huge. In theory, the global discharge of river water into the sea can generate sufficient electricity to cover the worldwide electricity consumption [1, 2]. The relatively low obtained power per membrane area (i.e., power density) so far inhibited commercial application of this technology, although pilot plants to capture salinity gradient energy have been built or are planned [3, 4].

The principle of reverse electrodialysis relies on ion exchange membranes, which are selective for either cations (cation exchange membrane, CEM) or anions (anion exchange membrane, AEM). When waters with different salinity are on either side of such a selective ion exchange membrane, a Donnan potential is created over the membrane. When these membranes are stacked alternately, with compartments for seawater or river water in between, the Donnan potentials over each membrane cumulate to a voltage that can be used for electricity generation. The electrodes at both ends of the stack convert the ionic flux into an electrical current, using a (reversible) redox reaction [5, 6] or using ion storage in capacitive electrodes [7].

In traditional designs for RED, the power density is limited mainly by the weakly conductive river water compartments [1, 8] and the non-conductive spacers in the compartments [9]. The electrical resistance of the river water compartments can be minimized using very thin feedwater compartments, at the cost of higher power consumption for pumping the feedwater [1, 10]. The pumping power is further increased due to the presence of spacers, which create a tortuous flow [1, 11, 12]. The spacers (often non-conductive polymeric fabrics) are used between the ion exchange membranes to create a constant intermembrane distance and create extra mixing of the flow within the feedwater compartments. However, the non-conductive material of the spacers partly covers the membrane area (and the feedwater compartment) and disables that area for ion exchange. This is referred to as the spacer shadow effect [9].

A design without spacers can be created using membranes with a corrugation, i.e., profiled membranes [12, 13]. Experiments showed that these profiled membranes have a lower ohmic resistance (i.e., AC resistance) and a four times lower pumping power consumption, compared to a similar design with flat membranes and spacers [12]. However, the non-ohmic

resistance, sometimes referred as concentration polarization, was higher in the case of profiled membranes. This non-ohmic resistance is due to concentration changes in the feed water compartments, which are most pronounced in the diffusive boundary layer near the membrane surface, when an electrical current is allowed. When the non-ohmic resistance of the design with profiled membranes would decrease to the level as for the design with spacers, the net power density would almost double [12].

The high non-ohmic resistance in the absence of spacers was attributed to reduced mixing near the membrane-water interface [12]. The slow refreshment of the feed waters near the membranes lowers the concentration difference over the membrane and therefore decreases the electromotive force. This results in a non-ohmic resistance. Previous research for other applications showed that additional mixing can be obtained using spacers with a twisted (i.e., helical) structure [14-17] or other static mixing spacers [18]. Also spacerless systems can be equipped with mixing promoters, by adding micro-corrugations such as herringbone structures, on the membrane surface [19, 20]. This suggests that with such flow geometry a decrease of the non-ohmic resistance in RED could be obtained.

Alternatively or additionally, a poor water distribution within each feedwater compartment causes a higher non-ohmic resistance. In a design with spacers, the feedwater is homogeneously distributed in all directions in each feedwater compartment, while the profiled membranes guide the water through narrow channels. When a local blockage occurs somewhere in a profiled channel (e.g., due to an air bubble or a locally thicker membrane), the whole channel is unavailable, while using a design with spacers the water can re-distribute in case of a local blockage.

To distinguish the cause of the high non-ohmic resistance of profiled membranes, and to improve the obtained power density in RED, this research investigates two novel designs with mixing promoters. One of the mixing promoters includes spacers while the other type of mixing promoter can be used in a spacerless system. These two novel designs are compared with designs with traditional (straight, non-conductive) spacers and traditional profiled membranes. The performance is evaluated by electrical measurements as well as experimental flow visualization for one of the novel designs with mixing promoters. This research reveals the individual effects of different types of mixing promoters, for designs with spacers as well as for designs with profiled membranes. Consequently, this research shows how the (non-ohmic) resistance can be reduced and a significantly higher (net) power density can be obtained in RED.

4.2 Experimental setup

4.2.1 RED designs

Four different RED stacks were built, from which two designs comprised flat membranes with a spacer between the membranes and two designs comprised profiled membranes. The stacks contained several cells, each composed of a CEM, an AEM, a compartment for river water and a compartment for seawater. All designs used commercial Ralex membranes (MEGA, Czech Republic); type CMH-PES was used as CEM and type AMH-PES was used as AEM. Both stacks with spacers were composed of 5 cells and both stacks with profiled membranes were composed of 6 cells. For a fair (scale independent) comparison, the effect of the electrodes was subtracted using a blank measurement with zero cells (i.e., only electrodes, electrode compartments and one CEM that separates the final cell from the electrodes).

The designs with spacers had either symmetrical spacers composed of filaments of 143 μm in both directions (Figure 4.1A) or asymmetrical spacers composed of single wires of 64 μm as a weft and two twisted wires of 64 μm as a warp (Figure 4.1B). The twisted structure of this warp creates a helical structure. Each feedwater compartment contained two layers of this twisted spacers, to obtain a similar thickness as the normal spacers (Table 4.1). The spacer type, porosity and open area of both spacers are given in Table 4.1. Both spacer types were not ion-conductive.

Both designs with profiled membranes included straight ridges in the direction of the feed water flow on one side of the membrane. When the membranes were stacked, these ridges created straight channels of 230 μm high and 1 mm in width. These channels were straight and uniform for one design (Figure 4.1C), while the other design had additional, smaller, corrugations in a triangular shape with a height of 50 μm, perpendicular to the flow through the channel (Figure 4.1D). These sub-corrugations were added to disturb the uniform flow and create extra mixing in the concentration boundary layer near the membrane surface. To ensure that the sub-corrugations were aligned with the channels created by the larger profiles, the sub-corrugations were only added at one side of the profiled membrane. Both types of profiled membranes (with and without sub-corrugations) were prepared by hot pressing the membranes into a mould, at 140 ºC and 200 bar, as explained in more detail in previous research [12]. The membranes were conditioned in 0.5 M NaCl afterwards and the thickness of the membranes and corrugations was measured (Mitutoyo 547-401, Japan); see Table 4.1.

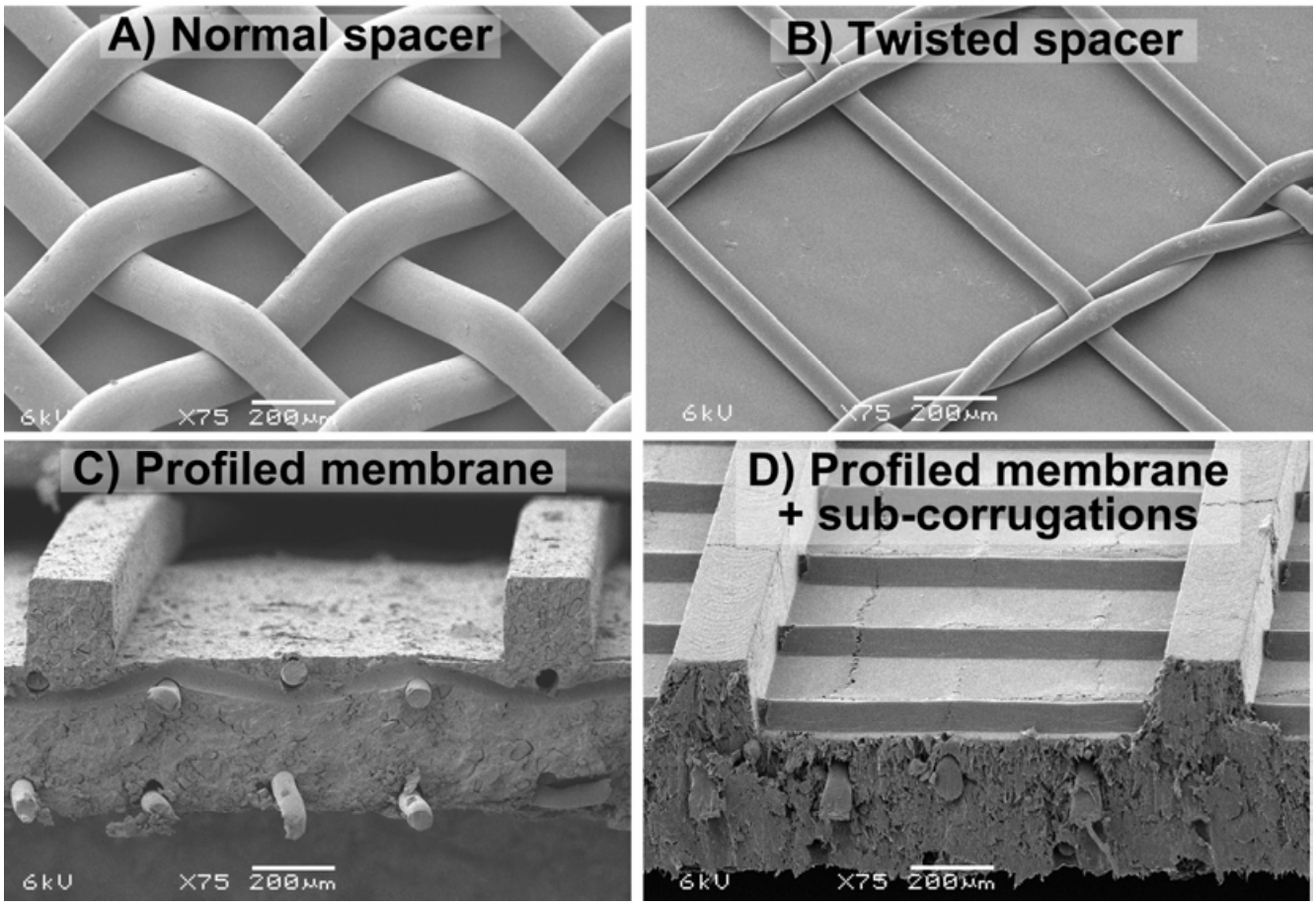

Figure 4.1: Images obtained from a scanning electron microscope (SEM, magnification: 75x), for normal spacers, twisted spacers and profiled membranes without or with sub-corrugations.

Table 4.1: Specifications for spacers and membrane profiles.

	Normal spacer	Twisted spacers	Profiled membrane	Profiled membrane + sub-corrugations
Type of spacer	1 layer of Sefar 07-300/46	2 layers of Sefar IEM 07-750/83	No spacer	No spacer
Membrane thickness (wet)	580 ± 25 µm	580 ± 25 µm	475 ± 15 µm (excluding profiles)	520 ± 20 µm (excluding profiles and sub-corrugations)
Compartment thickness (wet)	245 ± 5 µm	223 ± 7 µm	230 ± 11 µm	230 ± 10 µm
Open area	46%	83%	83%	83%
Porosity	72%	88%	83%	81%

4.2.2 Feedwater

An artificial solution of 0.508 M NaCl (technical grade, ESCO, The Netherlands) was used as seawater and 0.017 M NaCl was used as river water. These feed waters were supplied through a manifold and such that the flow directions of the feed waters were oriented 90º with respect to each other (i.e., cross-flow), as shown in Figure 4.2.

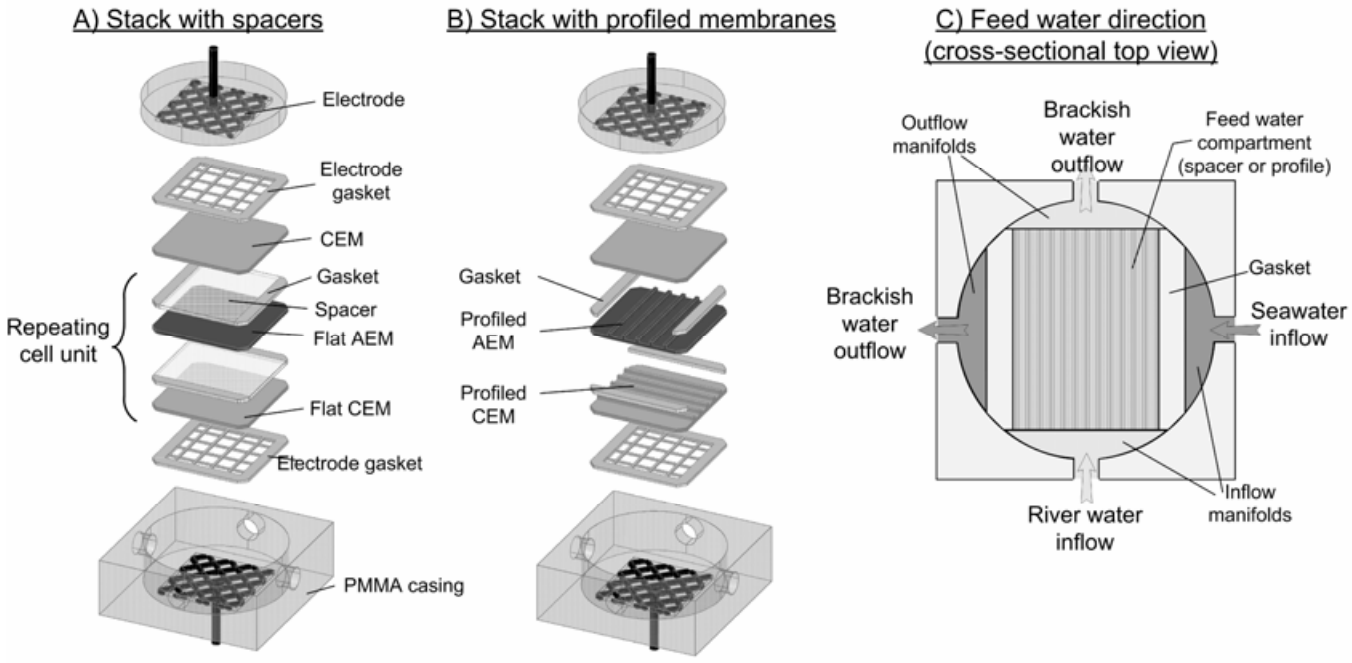

Figure 4.2: Composition of RED stacks in case of A) spacers and B) profiled membranes (for clarity both stacks are drawn here with only 1 repeating cell unit). C) represents a cross-sectional top view showing the manifolds and one feedwater compartment; in this case a river water compartment. The seawater compartment is oriented perpendicular to the river water compartment.

The inflows as depicted in Figure 4.2 allowed the feedwater to redistribute in the wide manifold and ensured uniform pressure over the full width of the feedwater compartments.

The membranes had a dimension of approximately 7 cm by 7 cm. A gasket of 1 cm was used at both sides to prevent river water entering the seawater compartments and vice versa (Figure 4.2A and 4.2B). Hence, the effective area for ion exchange was 5 cm by 5 cm. All membrane stacks, either with spacers or profiled membranes, were packed between a Ti/Pt mesh electrode of 5 cm by 5 cm (MAGNETO Special Anodes B.V., The Netherlands) and a poly(methyl methacrylate) (PMMA) casing (STT Products, The Netherlands).

The measurements were performed at several flow rates, between 0.5 and 100 ml/min per cell, which are equivalent to Reynolds numbers between 0.5 and 100. The Reynolds number

based on half the channel height, Re_h (-), for a wide channel and corrected for the volume filled by spacer or membrane profile (i.e., including porosity) is defined as

$$\mathrm{Re}_h = \frac{\bar{u} \cdot D_h \cdot \rho}{\mu} \approx \frac{2\Phi \cdot \rho}{b \cdot \varepsilon \cdot \mu} \qquad \text{(eq. 4.1)}$$

In which $\bar{u}$ is the average flow velocity (m/s), D_h is the hydraulic diameter (m), ρ is the density of water (kg/m^3), μ is the (dynamic) viscosity of water (kg/(m·s)), Φ is the flow rate per feedwater compartment (m^3/s), b is the width of the feedwater compartment (m) and ε is the compartment porosity (-).

4.2.3 Electrical measurements

To benchmark the obtained power density obtained in each RED stack, chronopotentiometry was applied. A galvanostat (Ivium Technologies, The Netherlands) was used to measure the voltage at a 0.1 s sample rate for current densities of 4, 8, 12, 16, 20, 24 and 28 A/m^2, each for a duration of at least 4 times the residence time of the feedwater, to ensure a stable voltage. Each stage in current density was preceded and followed by a stage with open circuit (open circuit voltage, OCV). The stack resistance (R_{stack}, in Ω·cm^2) is then determined from the difference between the stable voltage at each current density and the OCV. The total electrical resistance of the stack can be divided into an ohmic (R_{ohmic}) and a non-ohmic resistance ($R_{non\text{-}ohmic}$), both in Ω·cm^2:

$$R_{stack} = R_{ohmic} + R_{non-ohmic} \qquad \text{(eq. 4.2)}$$

The ohmic resistance originates from the membrane resistance and the limited conductivity of the feedwater. The non-ohmic resistance is due to concentration changes within each compartment, which are oriented perpendicular to the membrane (due to a concentration boundary layer) as well as along the feedwater flow (due to a slowly changing bulk concentration). As the ions are transported from the seawater compartment to the river water compartment, the concentration difference over the membranes decreases, which slowly decreases the electromotive force. This decrease in voltage, divided by the current density, determines the non-ohmic resistance.

The ohmic resistance is determined from the sudden jump in voltage when an electrical current is interrupted. The remaining, time-dependent voltage change during the current interrupt is due to the non-ohmic resistance [1].

The obtained gross power density P_{gross} (W/m^2 of membrane area) is calculated from the open circuit voltage (OCV, in V) and the stack resistance:

$$P_{gross} = \frac{OCV^2}{4 \cdot N_m \cdot R_{stack}} \qquad \text{(eq. 4.3)}$$

In which N_m represents the number of membranes (-). This paper focuses on the obtained power density rather than the energy efficiency, as the non-ohmic resistance influences the power density unambiguous while the energy efficiency can still be high with significant non-ohmic resistance when using multiple stages [21]. For large scale applications, high energy efficiency can be obtained without compromising the power density when using multiple (small) stages, e.g., using segmented electrodes [22].

All measurements are duplicated, from which the average values and the standard errors are shown.

4.2.4 Flow visualization

In addition to the electrical measurements in a stack, a cell with a single flow compartment was used to visualize the flow through the channels with sub-corrugations. The flow compartment contained one membrane with sub-corrugations only (approximately 60 μm in height), both at the bottom and top side, glued to a PMMA casing. These membranes only contained the sub-corrugations without the larger corrugations, such that the flow compartment could be visualized from the side (Figure 4.3). A glass window was installed at one side of the cell, to ensure a good optical path. The flow compartment was 4 cm in width, 24 cm in length, and approximately 300 μm in height. A solution with 0.25 M NaCl and polystyrene particles with a diameter of 5 μm (Dantec Dynamics, Denmark) was pumped through the flow compartment.

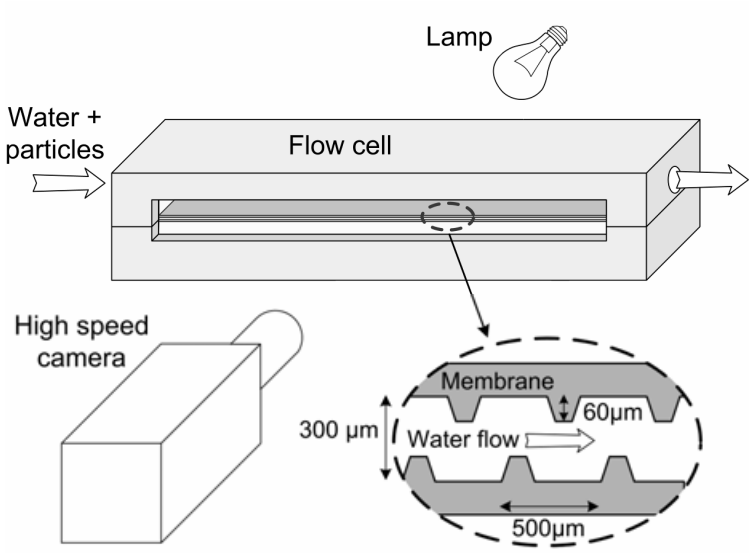

Figure 4.3: Experimental setup for flow visualization.

A light source was installed at one side of the flow compartment, while a high-speed camera (Photron Fastcam SA1.1, United States) was installed at the other side. Images were recorded using a resolution of 1024x1024 pixels, corresponding to an image size of approximately 1.5 mm. Frame rates of 250 fps (Re_h = 10) and 2000 fps (Re_h = 100) were used. The movement of the micro-particles in two subsequent images was used to calculate the local flow velocity, using a technique known as particle tracking velocimetry (PTV). Approximately 5000 subsequent images were processed to obtain an average flow field. The images were processed in Matlab (Mathworks, v2010b), searching for cross-correlation peaks of tracked particles, with an interrogation window of 64 pixels. A time-average vector field was created by distributing the vectors over a regular grid of 80x80, which corresponds to a final resolution of 19 µm.

4.3. Results

4.3.1 Power density

The experimentally obtained gross power density is shown in Figure 4.4 as a function of the Reynolds number for all four designs.

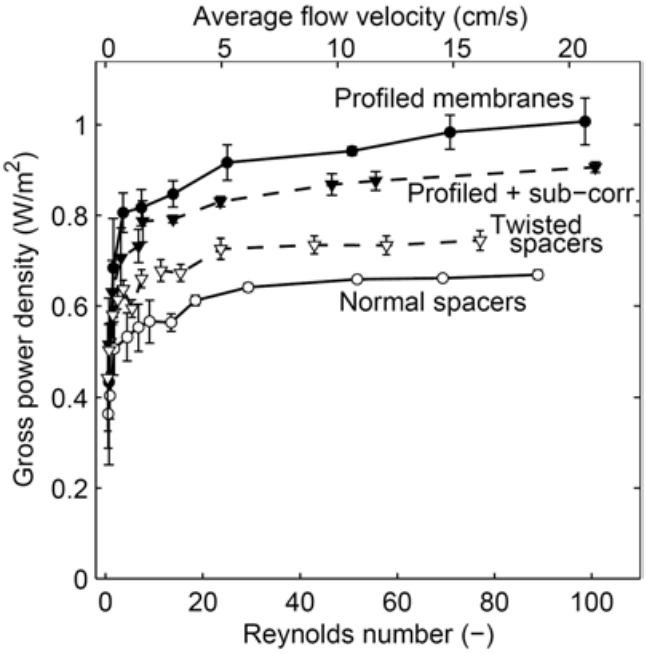

Figure 4.4: Gross power density for RED stacks with normal spacers, twisted spacers, profiled membranes and profiled membranes with additional sub-corrugations as function of the Reynolds number.

As expected, the gross power density increases with increasing Reynolds number (Figure 4.4). The concentration difference over each membrane remains highest when seawater and river water are rapidly refreshed (i.e., high Re_h). For lower Reynolds numbers, thus lower flow rates, the ion transport from seawater compartments to river water compartments lowers the salinity difference over the membrane and therefore lowers the gross power density. In other words, the non-ohmic resistance decreases when the Reynolds number increases, and hence the power density increases.

The stack with twisted spacers has a significantly higher power density than the stack with normal spacers. However, the stack with profiled membranes with sub-corrugations obtains a slightly lower power density than when profiled membranes without sub-corrugations are used. Although both twisted spacers and sub-corrugations were expected to generate more

mixing, i.e., a lower non-ohmic resistance, and thus a higher power density, the effect of these mixing promoters on the power density is contradictive. To investigate this in more detail, the ohmic and non-ohmic resistance are analyzed and discussed in more detail hereafter.

4.3.2 Ohmic resistance

The total electrical resistance of the stack is decomposed into an ohmic and a non-ohmic resistance, according to eq. 4.2. The ohmic resistance, due to the membrane resistance and the ohmic resistance in the feedwater compartments, is shown as a function of Re_h for all designs in Figure 4.5.

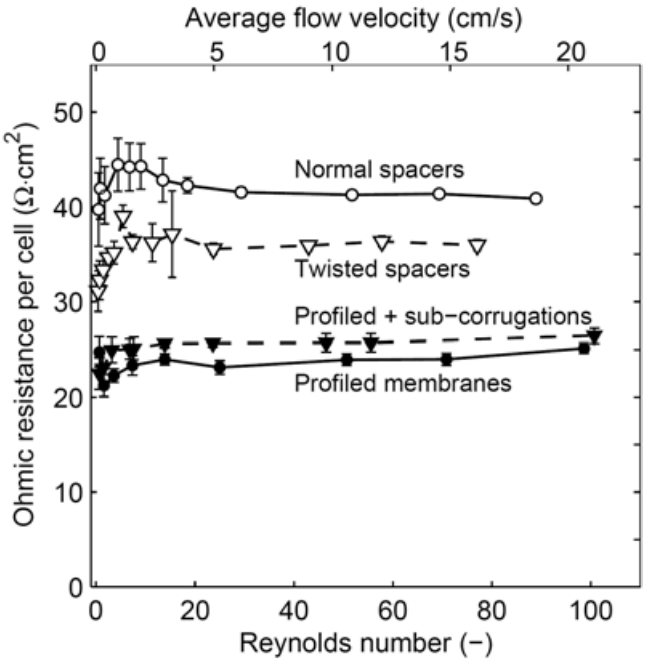

Figure 4.5: Ohmic resistance per cell for RED stacks with normal spacers, twisted spacers, profiled membranes and profiled membranes with additional sub-corrugations as function of the Reynolds number.

Figure 4.5 shows that the ohmic resistance is rather independent of the Reynolds number, as was demonstrated also in previous research [9, 12]. The ohmic resistance is only slightly lower for very low Reynolds numbers, which is caused by the higher conductivity of the river water compartments. This effect is strongest for low Reynolds numbers, because lower flow rates imply larger residence times, which result in accumulated transport of ions from the seawater into the river water compartments. Because the low conductive river water

compartment contributes more to the ohmic resistance than the seawater compartment, the ohmic resistance slightly decreases at low Reynolds numbers.

The stack with twisted spacers shows a significantly lower ohmic resistance than the stack with normal spacers. This is due to the more open structure of the twisted spacer, which can be quantified by the higher open area and porosity, compared to the normal spacers (Table 4.1). The more open structure of the twisted spacers reduces the spacer shadow effect. Therefore, the ohmic resistance is lower for the stack with twisted spacers in comparison to that with normal spacers. In addition, the twisted spacers are slightly thinner than the normal spacers, which would give a little lower resistance for the compartments filled with twisted spacers than those with normal spacers [1]. Based on previous research [10], the difference in spacer thickness decreases R_{ohmic} by approximately 5%, and consequently the difference in open area and porosity are responsible for the latter 15% decrease in R_{ohmic} for the stack with twisted spacers, relative to stack with normal spacers.

Both designs with profiled membranes have a lower ohmic resistance than both designs with spacers (Figure 4.5). This is due to the absence of the spacer shadow effect in stacks with profiled membranes, as the use of (non-conductive) spacers is obsolete in the designs with profiled membranes. The difference in ohmic resistance between the stacks with profiled membranes and the stack with normal spacers is even more pronounced than demonstrated in previous research [12], which is caused by the slightly thicker membranes (i.e., higher resistance) for the stack with spacers compared to the thinner profiled membranes (Table 4.1). Considering the actual differences in membrane resistance (approximately 5 $\Omega \cdot cm^2$ higher for the cells with normal spacers compared to previous research), these results are in fair agreement with previous research [12]. In all cases, the stacks with spacers have a significant higher ohmic resistance than the stack with profiled membranes.

The stack with additional sub-corrugations has a slightly higher ohmic resistance than the stack with profiled membranes without sub-corrugations, although this difference is only significant for a few data points (Figure 4.5). The small differences in ohmic resistance of this stack with sub-corrugations re attributed to the slightly thicker profiled membranes with sub-corrugations, compared to the profiled membranes without sub-corrugations (Table 4.1).

4.3.3 Non-ohmic resistance

The non-ohmic resistance ($R_{non\text{-}ohmic}$) as function of Re_h is shown for all designs in Figure 4.6.

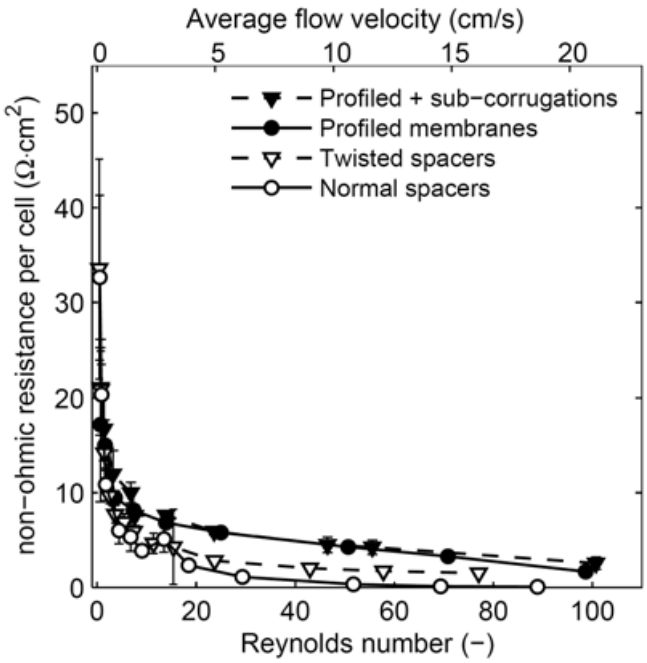

Figure 4.6: Non-ohmic resistance per cell for RED stacks with normal spacers, twisted spacers, profiled membranes and profiled membranes with additional sub-corrugations as function of the Reynolds number.

The ohmic resistance (Figure 4.5) dominates the non-ohmic resistance (Figure 4.6) for all Reynolds numbers and all cases. At a moderate flow rate corresponding to $Re_h = 10$, R_{ohmic} is approximately 3.5 times higher than $R_{non\text{-}ohmic}$ for designs with profiled membranes, and even 10 times higher for designs with spacers.

Furthermore, the non-ohmic resistance (Figure 4.6) decreases strongly with increasing Reynolds number. Since the non-ohmic resistance is due to concentration changes within the feedwater compartments, the non-ohmic resistance decreases when the residence time is lower, i.e., when the feedwater flow is higher. Moreover, higher Reynolds numbers imply higher velocity shears near the membrane-water interface, which decrease the concentration boundary layer (i.e., diffusive boundary layer) [23]. In other words, the concentration near the membrane-water interface is more similar to the inflow concentrations for higher flow rates, and consequently the non-ohmic resistance decreases for higher Reynolds numbers.

The non-ohmic resistances of the stacks with twisted spacers and sub-corrugations are similar or even higher than those for the comparable designs with normal spacers and profiled membranes without sub-corrugations. This result shows that the obtained power cannot be improved by adding these types of mixing promoters (twisted spacers and sub-corrugation) to reduce the non-ohmic resistance.

Previous research on (multilayer) spacers did show significant improvement in mass transfer using helical spacer structures [14, 15]. The absence of a decrease in $R_{non\text{-}ohmic}$ for the designs with twisted spacers and sub-corrugations in the present research can be explained by two factors. First of all, the distribution of the feedwater inflow dominates $R_{non\text{-}ohmic}$. The non-ohmic resistances for the stacks with normal spacers and profiled membranes (without sub-corrugations) are much lower in this research than in previous research with such stacks at similar residence time [12]; 27% lower for normal spacers and 44% lower for profiled membranes. This decrease is due to an improved flow design with a wide inflow and outflow manifold for the feedwater, whereas previous research used a single hole for the inflow of each feedwater type [12]. Wide manifolds ensure a more uniform feedwater distribution over the membrane area, while inflow and outflow from a single point as in previous research can create more preferential channelling and dead zones [24]. This effect is major, as demonstrated by the significant decrease in $R_{non\text{-}ohmic}$ in this research compared to previous research. In other words, the additional mixing that is generated due to the twisted spacers, for example, is insignificant compared to the effect of the feedwater distribution over the membrane.

A second reason why the twisted spacers and sub-corrugations do not reduce $R_{non\text{-}ohmic}$ is the low Reynolds numbers that are typically used in RED. Previous research on helical spacer structures [14, 15] was performed at $Re_h > 100$, while RED is typically operated at $Re_h < 100$ and preferably even $Re_h < 10$ [1, 10, 12]. At higher Reynolds numbers, unsteady vortices could be generated from disturbances such as spacer filaments or sub-corrugations [14, 25, 26]. Vortices at $Re_h < 100$ are reported in spacer-filled channels [14, 26], but are steady and limited to a small region near the spacer yarn only. Consequently, the effect is minor.

4.3.4 Flow visualization

To visualize the feedwater flow at the relatively low Reynolds numbers that are typical for RED, particle tracking velocimetry (PTV) was applied for the case with sub-corrugations. The experimentally obtained, time averaged, flow field of the design with sub-corrugations is shown in Figure 4.7 for the case with Re_h = 10 and Re_h = 100.

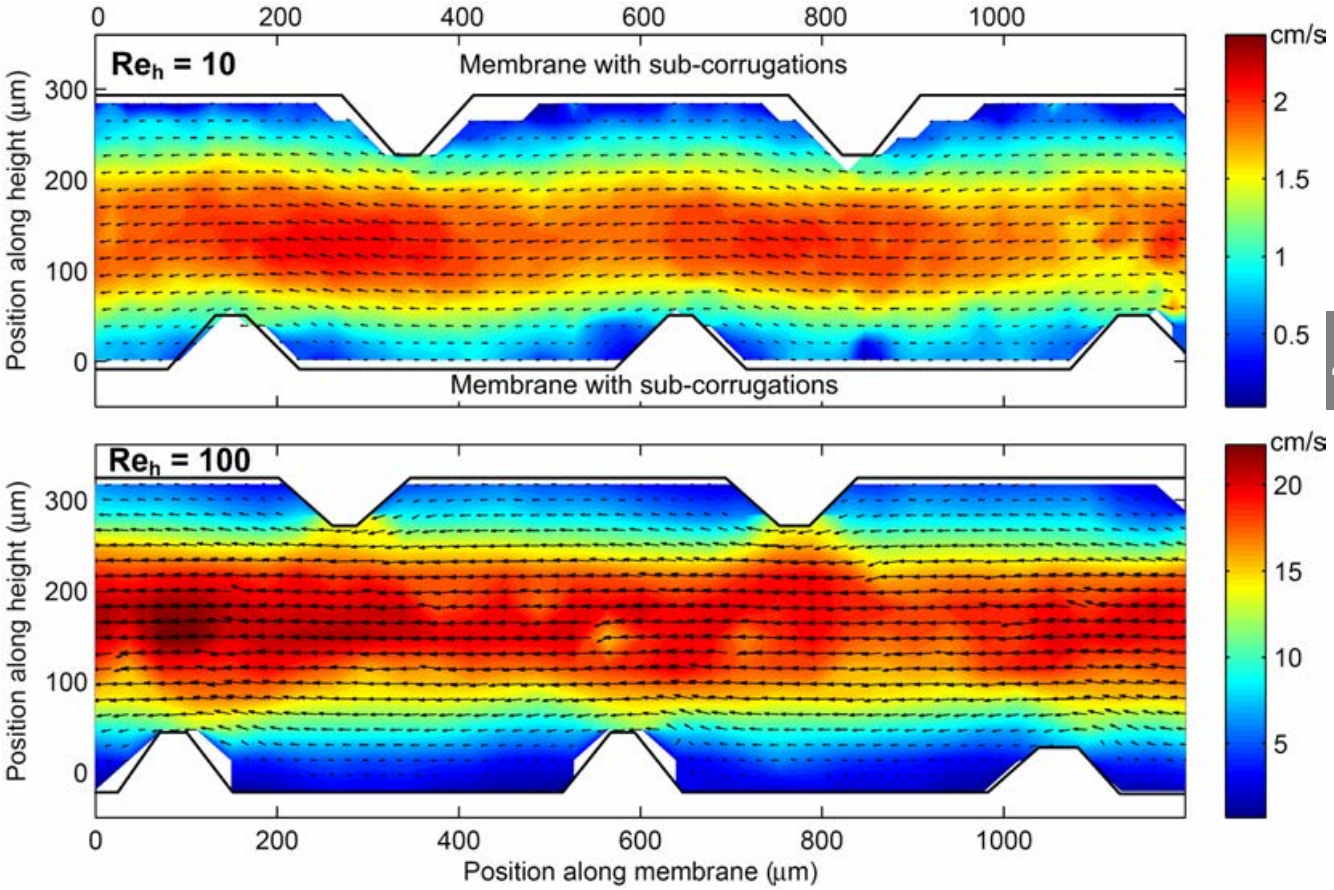

Figure 4.7: Experimentally obtained velocity field of flow between sub-corrugated membranes for Re_h = 10 and Re_h = 100. The colors indicate the velocity magnitude in cm/s, while the vectors indicate the flow direction and magnitude.

Figure 4.7 shows that the flow bends around the sub-corrugations at both Reynolds numbers. The flow velocity at the tips of the sub-corrugations is lower compared to that at positions in between two sub-corrugations at the same height for Re_h = 10, whereas at Re_h = 100 the velocity magnitude is even highest near the top of the sub-corrugations (indicated by the yellow color near the sub-corrugations at the top). At low flow rate (Re_h = 10), the water can follow the geometry of the sub-corrugated membranes, while at high flow rates the inertia of the water is larger and the flow is funneled near the sub-corrugations, which produces a

locally intensified flow velocity near the membrane surface. However, the flow is still fully laminar in both cases. The local minima and maxima in velocity magnitude near the centerline of the compartment are insignificant (due to particles out of focus). No vortices are observed behind the sub-corrugations, as shown in Figure 4.7, not for Re_h = 10 and neither for Re_h = 100. The sub-corrugations create a dead zone in front and behind the sub-corrugations, rather than introducing additional mixing due to vortices. Therefore, sub-corrugations are not suitable to promote mixing in the diffusive boundary layer in RED.

Higher Reynolds numbers could generate vortices in the diffusive boundary layer, but higher flow rates are unfavorable for application in RED due to the corresponding increase in power consumed for pumping [1]. Higher Reynolds numbers can be applied in electrodialysis (ED) applications, which is in general associated with larger intermembrane distances. As a consequence, these sub-corrugations may be useful to generate extra mixing for ED. Moreover, corrugated surfaces are known to enhance the onset for the overlimiting current (i.e., a lower voltage is required to start an overlimiting current) in cases of ED [27]. As RED always operates at underlimiting current, in absence of phenomena such as electro-convection [28], this effect does not benefit the obtained power in RED.

4.3.5 Net power density

The previous results showed that the feedwater distribution throughout each compartment, regulated by the inflow and outflow, mainly determines the non-ohmic resistance. The system for inflow and outflow also influences the pressure drop over the feedwater compartments, and thus the net power density (i.e., the obtained gross power density minus the power density consumed for pumping the feed waters). The pressure drop and the net power density for the four stacks investigated are shown in Figure 4.8 as a function of the Reynolds number.

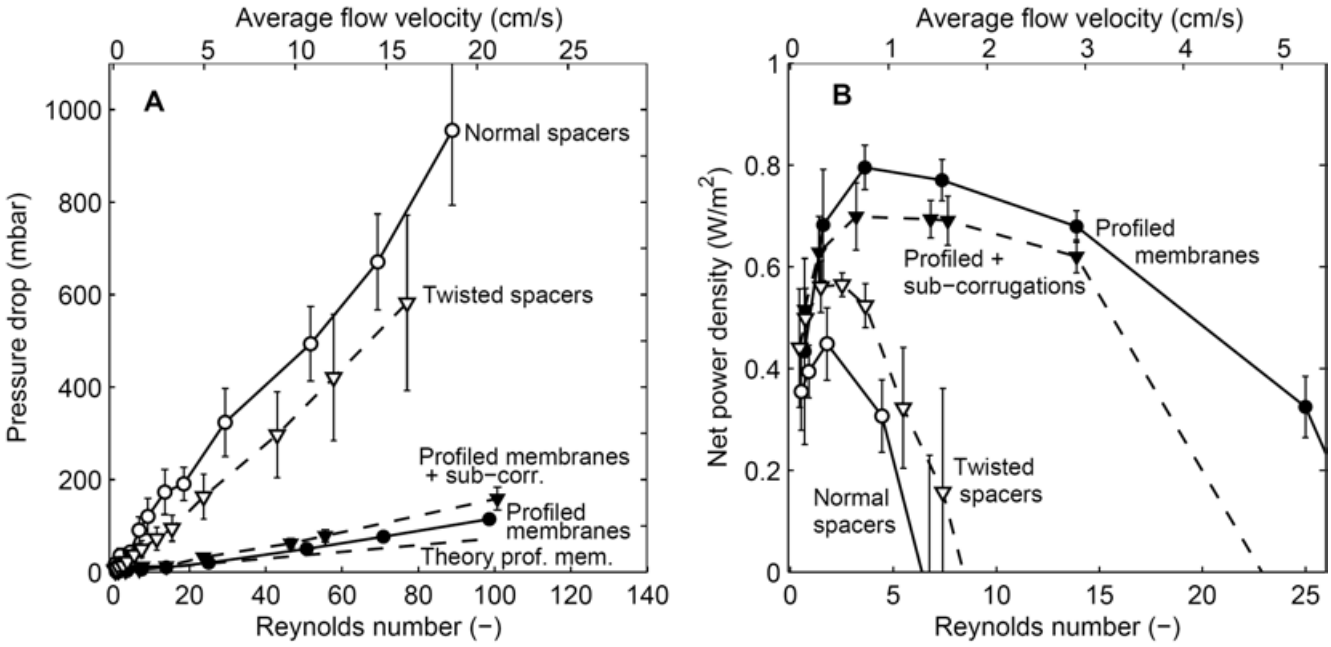

Figure 4.8: A) Pressure drop over feedwater compartment and B) net power density for all designs of this research as a function of the Reynolds number. The shown theoretical pressure drop in panel A corresponds to the case of profiled membranes.

Both designs with profiled membranes have a pressure drop which is close to the theoretical pressure drop for laminar flow in a (finite) rectangular channel, considering the porosity (ε) and the finite width [10, 29]. The small difference between the theoretical pressure drop and the experimentally obtained pressure drop can be due to slight pressure losses in the manifolds distributing the water [30], although this effect is much smaller in the wide manifolds used in this research compared to previous research [12].

The pressure drop, and thus the power consumed for pumping, is nearly an order of magnitude higher for both designs with spacers compared to both designs with profiled membranes (Figure 4.8A). The spacer yarns give substantial extra friction to the feedwater flow through the compartments, as was observed before [12, 31]. The large standard errors of the stacks with spacers, caused by the local (and unpredictable) imprint of the spacers in the membranes, do not allow to conclude which spacer corresponds to the lowest pressure drop. However, despite the slightly thinner spacers, the pressure drop for the twisted spacers can be considered rather lower than higher compared to the normal spacers. The high porosity and the corresponding large warp size seem to compensate for the slightly smaller thickness of the twisted spacers (Table 4.1).

The high pressure drops for the stacks with spacers (Figure 4.8A) are indirectly related to the low non-ohmic resistances for those stacks (Figure 4.6). The high pressure drop in the spacer filled compartment ensures a more uniform flow distribution, as the pressure drop in the manifolds becomes insignificant [30]. Therefore, the feedwater distributes more evenly over the full width of the feedwater compartments, which reduces the non-ohmic resistance. As a consequence, the stacks with the lowest pressure drops rank opposite for the non-ohmic resistance.

Due to the higher gross power and the relatively low pumping power consumption for stacks with profiled membranes, the net power density is significantly higher for stacks with profiled membranes than for stacks with spacers, as shown in Figure 4.8B. The net power densities for the stacks with profiled membranes are higher compared to previous research, due to the improved feedwater design in the present research. The net power density is maximum 0.8 W/m^2, which is almost twice the maximum net power density for the stack with normal spacers, and approximately 40% higher compared to the stack with (highly porous) twisted spacers. The addition of sub-corrugations results in general in a slightly lower net power density. Therefore, the use of sub-corrugations is considered not beneficial for RED.

4.4 Conclusions

This research investigates the power density obtained from mixing seawater and river water solutions in reverse electrodialysis (RED) using designs with and without mixing promoters in the feedwater to reduce the diffusive boundary layer. RED stacks with spacer yarns in a twisted structure outperform stacks with normal spacers, due to a higher open area and porosity of the twisted spacers. However, the non-ohmic resistance, which was expected to reduce due to additional mixing in the case of the twisted spacers, was similar to or even higher than that for stacks with normal spacers. For a spacerless design with profiled membranes, the addition of 50 μm sub-corrugations on the membrane surface as mixing promoters also did not show a decrease in non-ohmic resistance. Flow visualization of the profiled membrane with additional sub-corrugations showed that the corrugated surface does not create vortices at typical Reynolds numbers for RED applications ($Re_h \leq 100$). Moreover, the non-ohmic resistance is sensitive for the flow distribution of the feedwater. Ensuring a uniform feedwater flow by providing wide manifolds for the distribution of the feedwater makes the non-ohmic resistance inferior to the ohmic resistance in all cases.

Therefore, mixing promoters such as twisted spacers or sub-corrugations do not yield additional mixing that results in a significantly higher power density for RED. Overall, considering the net power density, stacks with profiled membranes without sub-corrugations perform slightly better than the design with additional sub-corrugations and outperform stacks with spacers with 40% or even more.

References

1. Vermaas, D. A.; Saakes, M.; Nijmeijer, K., Double Power Densities from Salinity Gradients at Reduced Intermembrane Distance. *Environmental Science & Technology* **2011,** *45*, (16), 7089-7095.
2. Długołęcki, P. E.; Gambier, A.; Nijmeijer, K.; Wessling, M., Practical Potential of Reverse Electrodialysis As Process for Sustainable Energy Generation. *Environmental Science & Technology* **2009,** *43*, (17), 6888-6894.
3. Post, J. W.; Goeting, C. H.; Valk, J.; Goinga, S.; Veerman, J.; Hack, P. J. F. M., Towards implementation of reverse electrodialysis for power generation from salinity gradients. *Desalination and water treatment* **2010,** *16*, 182-193.
4. Achilli, A.; Childress, A. E., Pressure retarded osmosis: From the vision of Sidney Loeb to the first prototype installation — Review. *Desalination* **2010,** *261*, 205-211.
5. Veerman, J.; Saakes, M.; Metz, S.; Harmsen, G., Reverse electrodialysis: evaluation of suitable electrode systems. *Journal of Applied Electrochemistry* **2010,** *40*, (8), 1461-1474.
6. Burheim, O. S.; Seland, F.; Pharoah, J. G.; Kjelstrup, S., Improved electrode systems for reverse electro-dialysis and electro-dialysis. *Desalination* **2012,** *285*, (0), 147–152.
7. Vermaas, D. A.; Bajracharya, S.; Sales, B. B.; Saakes, M.; Hamelers, B.; Nijmeijer, K., Clean energy generation using capacitive electrodes in reverse electrodialysis. *Energy & Environmental Science* **2013,** *6*, (2), 643-651.
8. Lacey, R. E., Energy by Reverse Electrodialysis. *Ocean Engineering* **1980,** *7*, (1), 1-47.
9. Długołęcki, P. E.; Dąbrowska, J.; Nijmeijer, K.; Wessling, M., Ion conductive spacers for increased power generation in reverse electrodialysis *Journal of Membrane Science* **2010,** *347*, (1-2), 101-107.
10. Vermaas, D. A.; Guler, E.; Saakes, M.; Nijmeijer, K., Theoretical power density from salinity gradients using reverse electrodialysis. *Energy Procedia* **2012,** *20*, 170-184.
11. Veerman, J.; Saakes, M.; Metz, S. J.; Harmsen, G. J., Reverse electrodialysis:A validated process model for design and optimization. *Chemical Engineering Journal* **2011,** *166*, (1), 256–268.
12. Vermaas, D. A.; Saakes, M.; Nijmeijer, K., Power generation using profiled membranes in reverse electrodialysis. *Journal of Membrane Science* **2011,** *385-386*, (0), 234-242.
13. Balster, J.; Stamatialis, D. F.; Wessling, M., Membrane with integrated spacer. *Journal of Membrane Science* **2010,** *360*, (1-2), 185-189.
14. Li, F.; Meindersma, G. W.; Haan, A. B. D.; Reith, T., Novel spacers for mass transfer enhancement in membrane separations. *Journal of Membrane Science* **2005,** *253*, (1-2), 1-12.
15. Balster, J.; Pünt, I.; Stamatialis, D. F.; Wessling, M., Multi-layer spacer geometries with improved mass transport. *Journal of Membrane Science* **2006,** *282*, 351–361.
16. Shrivastava, A.; Kumar, S.; Cussler, E. L., Predicting the effect of membrane spacers on mass transfer. *Journal of Membrane Science* **2008,** *323*, (2), 247-256.
17. Fritzmann, C.; Hausmann, M.; Wiese, M.; Wessling, M.; Melin, T., Microstructured spacers for submerged membrane filtration systems. *Journal of Membrane Science* **2013,** *446*, (0), 189-200.

18. Liu, J.; Iranshahi, A.; Lou, Y.; Lipscomb, G., Static mixing spacers for spiral wound modules. *Journal of Membrane Science* **2013,** *442*, (0), 140-148.

19. Stroock, A. D.; Dertinger, S. K. W.; Ajdari, A.; Mezic, I.; Stone, H. A.; Whitesides, G. M., Chaotic Mixer for Microchannels. *Science* **2002,** *295*, (5555), 647-651.

20. Kirtland, J. D.; McGraw, G. J.; Stroock, A. D., Mass transfer to reactive boundaries from steady three-dimensional flows in microchannels. *Physics of Fluids* **2006,** *18*, (073602), 1-13.

21. Post, J. W.; Hamelers, H. V. M.; Buisman, C. J. N., Energy Recovery from Controlled Mixing Salt and Fresh Water with a Reverse Electrodialysis System. *Environmental Science & Technology* **2008,** *42*, (15), 5785-5790.

22. Vermaas, D. A.; Veerman, J.; Yip, N. Y.; Elimelech, M.; Saakes, M.; Nijmeijer, K., High Efficiency in Energy Generation from Salinity Gradients with Reverse Electrodialysis. *Sustainable Chemistry & Engineering* **2013,** *1*, 1295−1302.

23. Długołęcki, P. E.; Ogonowski, P.; Metz, S. J.; Saakes, M.; Nijmeijer, K.; Wessling, M., On the resistances of membrane, diffusion boundary layer and double layer in ion exchange membrane transport. *Journal of Membrane Science* **2010,** *349*, (1-2), 369-379.

24. Hatzell, M. C.; Logan, B. E., Evaluation of Flow Fields on Bubble Removal and System Performance in an Ammonium Bicarbonate Reverse Electrodialysis Stack. *Journal of Membrane Science* **2013**, (in press).

25. Ahmad, A. L.; Lau, K. K.; Bakar, M. Z. A., Impact of different spacer filament geometries on concentration polarization control in narrow membrane channel. *Journal of Membrane Science* **2005,** *262*, 138–152.

26. Koutsou, C. P.; Yiantsios, S. G.; Karabelas, A. J., Numerical simulation of the flow in a plane-channel containing a periodic array of cylindrical turbulence promoters. *Journal of Membrane Science* **2004,** *231*, (1-2), 81-90.

27. Balster, J.; Yildirim, M. H.; Stamatialis, D. F.; Ibanez, R.; Lammertink, R. G. H.; Jordan, V.; Wessling, M., Morphology and Microtopology of Cation-Exchange Polymers and the Origin of the Overlimiting Current. *J. Phys. Chem. B* **2007,** *111*, (9), 2152-2165.

28. Druzgalski, C. L.; Andersen, M. B.; Mani, A., Direct numerical simulation of electroconvective instability and hydrodynamic chaos near an ion-selective surface. *Physics of Fluids* **2013,** *25*, 110804.

29. Bahrami, M.; Yovanovich, M. M.; Culham, J. R., Pressure drop of fully-developed, laminar flow in microchannels of arbitrary cross-section. *J. Fluids Engineering* **2006,** *128*, 1036-1044.

30. Gurreri, L.; Tamburini, A.; Cipollina, A.; Micale, G., CFD analysis of the fluid flow behavior in a reverse electrodialysis stack. *Desalination and Water Treatment* **2012,** *48*, (1-3), 390-403.

31. Da Costa, A. R.; Fane, A. G.; Wiley, D. E., Spacer characterization and pressure drop modelling in spacer-filled channels for ultrafiltration. *Journal of Membrane Science* **1994,** *87*, 79-98.

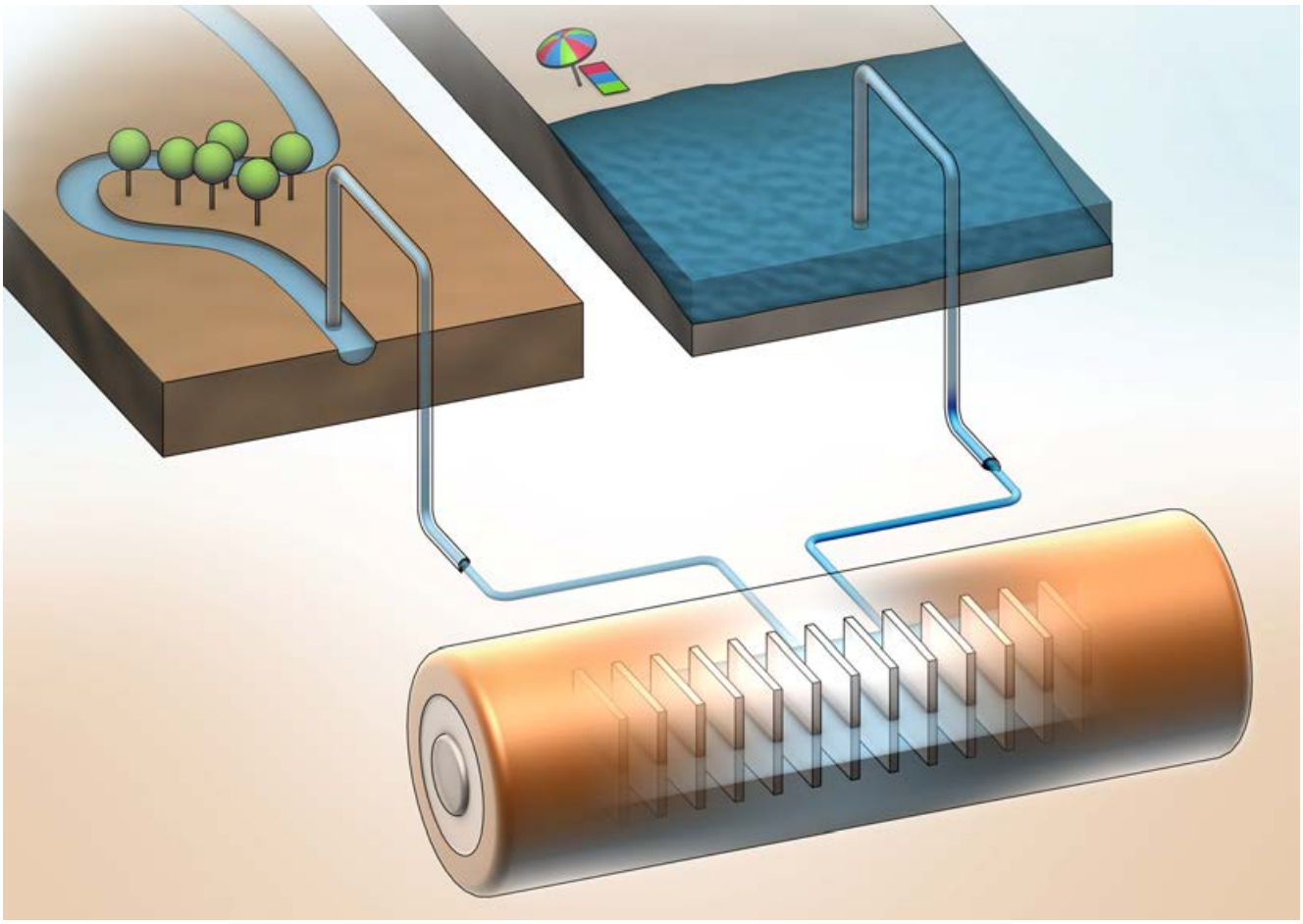

Chapter 5

High efficiency in energy generation with reverse electrodialysis

Abstract

Renewable energy can be captured from the mixing of salt and fresh water in reverse electrodialysis. This paper investigates the energy efficiency of this process for feed waters that pass a reverse electrodialysis cell once and waters that pass multiple cells or electrode segments. So far, the maximum theoretical energy efficiency was considered to be 50% when the feed waters pass a single cell once; significantly higher efficiencies could only be obtained when the waters were recirculated or passed multiple electrodes. In this study we show that the ion transport corresponding to the obtained energy and the electromotive force mutually influence each other, which enables to capture more than 50% (even up to 95%) of the theoretical energy, even when the feedwater streams pass a reverse electrodialysis cell only once.

This chapter has been published as

David A. Vermaas, Joost Veerman, Ngai Yin Yip, Menachem Elimelech, Michel Saakes, Kitty Nijmeijer, High Efficiency in Energy Generation from Salinity Gradients with Reverse Electrodialysis, *Sustainable Chemistry & Engineering*, **2013,** *1* (10), 1295-1302

5.1 Introduction

The increase in entropy upon mixing waters with different salinity gives the opportunity to capture renewable energy [1]. The potential for generating energy from salinity differences in natural waters is vast [2, 3]. Theoretically, mixing seawater and river water in equal quantities would provide as much energy as the potential energy when one of these waters has a level difference of more than 150 meters with respect to the other [2, 3]. Several technologies are proposed to capture this energy, amongst others pressure retarded osmosis (PRO) [4-6], reverse electrodialysis (RED) [7-9] and capacitive mixing (CAPMIX) [10-13].

Independent of the applied technology, a part of the theoretically available energy (i.e., exergy) is lost (even when perfect membranes are considered) if the energy is captured in a single step, i.e., when the feed flow is processed in a single stage in a continuous process. This is partly due to frictional losses (from water transport for PRO or ion transport for RED and CAPMIX) and partly due to unutilized available energy in the effluent. The latter is inevitable when a single pressure (PRO) or electrode voltage (RED and CAPMIX) is chosen to capture the energy. During operation, when the concentrations on either side of a selective membrane approach each other, to a level that the required pressure or voltage cannot be generated anymore, mixing stops and part of the available energy leaves the system unutilized.

For PRO, the energy efficiency was recently evaluated [6], concluding that theoretically up to 91% of the available energy could be obtained in a single step (constant pressure). Previous research on RED claimed that maximum 50% of the available energy can be captured using a single electrode segment [8, 9, 14-16], whereas the other 50% is dissipated due to the internal resistance of the RED cells. However, these previous calculations neglected the importance of local variations in electromotive force and electrical resistance.

In this study, we investigate the effect of local parameter variations on power generation, compared to the theoretically available energy. We present a model for RED stacks to simulate the energy capture with natural salinity gradients. The energy extraction efficiencies under different flow orientations along the membrane (co-flow, cross-flow and counter-flow) and with single or multiple electrodes pairs are compared and discussed, leading to new insights regarding the energy efficiency in RED.

5.2 Theory

5.2.1 Reverse Electrodialysis (RED)

A RED cell comprises membranes that are selective for cations (cation exchange membrane, CEM) or anions (anion exchange membrane, AEM) [1, 7], as illustrated in Figure 5.1. When waters with different salinity are present on either side of a CEM or AEM, a voltage is created due to the membrane selectivity for cations or anions. This voltage, known as the Donnan potential, can be accumulated when membranes are stacked alternately, with salt water and fresh water in between these membranes. Such a voltage can be used to power an electrical device when electrodes and a (reversible) redox reaction are introduced at both ends of the membrane stack [1, 7].

A RED cell can be operated in several modes. The flow of seawater and river water can be directed in the same way (co-flow, Figure 5.1a), in opposite direction (counter-flow, Figure 5.1b) or perpendicular to each other (cross-flow, Figure 5.1c). Some previous experimental designs for RED used co-flow [17] or counter-flow [18], but for practical reasons most designs were based on cross-flow [2, 8, 9]. Additionally, the electrodes can be composed of one single part (Figure 5.1a, 5.1b and 5.1c) or multiple segments (Figure 5.1d). Previous research indicated that multiple electrode segments increases the overall power density [15, 18]. This research will evaluate the maximum extractable energy for all cases.

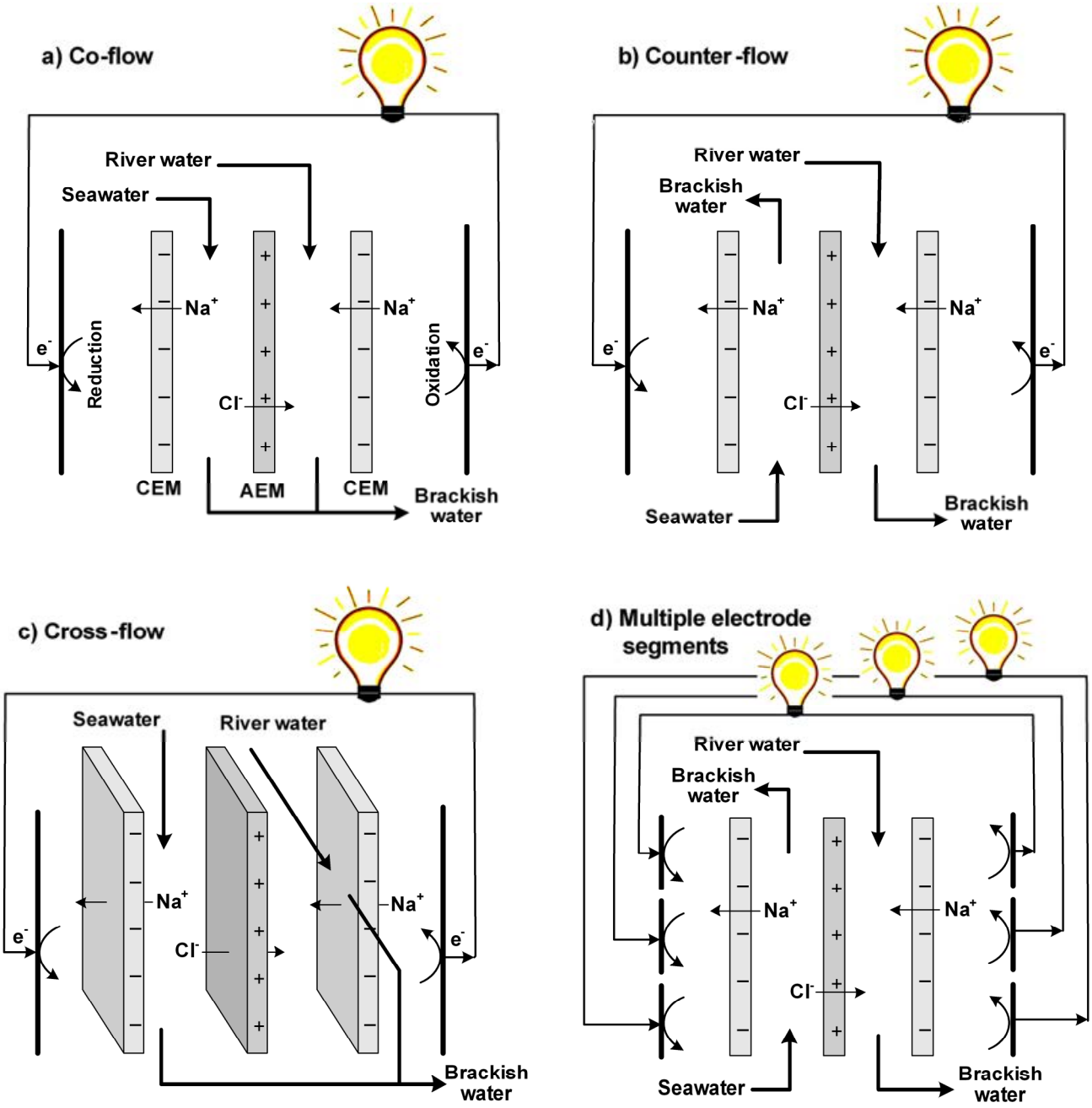

Figure 5.1: Principle of RED using a) co-flow, b) counter-flow, c) cross-flow and d) counter-flow with segmented electrodes. For simplicity, each setup is presented with one RED cell only, comprised of 2 membranes and 2 compartments. Multiple cells can be stacked between the electrodes. The final membrane serves to shield the electrode rinse solution from the feedwater.

5.2.2 Energy of Mixing

When two streams with different salinity are mixed until all available energy is released, both effluent streams attain the same salinity. In that case, the available energy is defined by the Gibbs free energy of mixing [2, 6]. Including the activity coefficients that account for the

non-ideality for concentrated solutions [2, 6], the theoretical obtainable energy, ΔG_{mix} (J), per mole of brackish water, n_b, is given by:

$$\frac{\Delta G_{mix}}{n_b} = -T \cdot \left(\Delta S_b - f \cdot \Delta S_s - (1-f) \cdot \Delta S_r\right) \qquad \text{(eq. 5.1)}$$

with $\Delta S = -R \cdot \sum_i x_i \cdot \ln\left(\gamma_i \cdot x_i\right)$

In these equations R is the universal gas constant (8.314 J/(mol·K)), T is the absolute temperature (K), f is the fraction of seawater relative to the total feed flow (-), x is the mole fraction of species i (-) and γ is the activity coefficient (-). The subscripts s, r and b indicate seawater, river water or brackish water, respectively. Similarly, the theoretical obtainable power $P_{\Delta G_{mix}}$ (W) is:

$$\frac{P_{\Delta G_{mix}} \cdot V_{mol,b}}{\Phi_b} = -T \cdot \left(\Delta S_b - f \cdot \Delta S_s - (1-f) \cdot \Delta S_r\right) \qquad \text{(eq. 5.2)}$$

Where Φ is the volumetric flow rate (m^3/s) and $V_{mol,b}$ is the molar volume of brackish water (m^3/mol).

Following eq. 5.2, mixing typical seawater (30 g/l NaCl) and river water (1 g/l NaCl), both at a flow rate of 1 m^3/s, would release 1.39 MW. Neglecting the mole fraction of H_2O has only a marginal effect on the released power (1.35 MW). Neglecting the activity coefficients has a slightly larger effect (1.45 MW).

5.2.3 Extractable Energy in RED

The actual obtained power depends on the voltage over the reverse electrodialysis cells and the electrical current through these cells. The voltage over a perfectly selective membrane (i.e., electromotive force), E (V), is given by the Nernst equation [19]:

$$E = \frac{R \cdot T}{z \cdot F} \cdot \ln\left(\frac{\gamma_s \cdot c_s}{\gamma_r \cdot c_r}\right) \qquad \text{(eq. 5.3)}$$

where z is the valence of the ions (-), F is the Faraday constant (96485 C/mol) and c is the salt concentration (mol/m^3). The voltage that is obtained over a cell, i.e., the electrode voltage U (V), equals the voltage over two perfectly selective membranes (one CEM and one AEM) minus the ohmic loss due to the cell resistance [7]:

$$U = 2 \cdot E - R_{cell} \cdot j \qquad \text{(eq. 5.4)}$$

where R_{cell} is the area resistance of a cell ($\Omega \cdot m^2$) and j is the electrical current density (A/m^2). The cell resistance is composed of the ohmic resistance of the membranes and the

feedwater. The resistance of the electrodes and the additional membrane to shield the electrode compartments is negligible for large numbers of cells [8].

The electrical current density corresponds to the local ion transport from seawater to river water. Because the feedwater compartments are elongated (i.e., the length of the flow channels is much larger than its thickness), diffusion and migration of ions can be assumed to be only perpendicular to the membrane. When further assuming a steady state and no leakage (perfect membranes), the concentration profile along the RED cell (in the direction of the flow) can be derived from two differential equations [15]. For co-flow, these equations are:

$$\frac{dc_s}{dy} = -\frac{j_{(y)} \cdot b}{\Phi_s \cdot F} \qquad \text{(eq. 5.5)}$$

$$\frac{dc_r}{dy} = \frac{j_{(y)} \cdot b}{\Phi_r \cdot F} \qquad \text{(eq. 5.6)}$$

where y is the distance from the feedwater inflow (m) and b is the width of the feedwater compartments (m). j is a function of y, as it represents the local current density. Because the electrical current density is dependent on the electromotive force, which is dependent on both the salt concentration in the seawater and the river water, these differential equations are coupled.

In case of counter-flow, the same equations are valid, but the sign in either eq. 5.5 or eq. 5.6 is reversed. For cross-flow, the derivative in eq. 5.5 is in perpendicular direction as in eq. 5.6, which makes eq. 5.5 and 5.6 partial differential equations in this case.

Because the concentrations are dependent on the location in the cell (y) and the electrical current through the cell, i.e., on the chosen electrode voltage (U), the electromotive force and the cell resistance are a function of y and U as well. We express that as E(y,U) and R_{cell}(y,U). The obtained power P (W) that is obtained at the electrodes of a RED cell is described by integration of the product of U and j and can be rewritten in terms of E(y,U) and R(y,U):

$$P = b \cdot \int_0^L U \cdot j \, dy = b \cdot \int_0^L \frac{2E_{(y,U)} \cdot U - U^2}{R_{cell\,(y,U)}} dy \qquad \text{(eq. 5.7)}$$

where L is the length of the cell from inflow to outflow (m).

When the outflow concentrations of the seawater stream and the river water stream are not equal, a part of the available power is unused. This unused power is calculated using the outflow concentrations for river water and seawater and eq. 5.2.

The energy efficiency η (-) is defined as the ratio of the actual obtained power P (W) versus the corresponding theoretical power according to the Gibbs equation ($P_{\Delta G_{mix}}$):

$$\eta = \frac{P}{P_{\Delta G_{mix}}} \cdot 100\% \qquad \text{(eq. 5.8)}$$

If the electromotive force E and the internal resistance R_{cell} are independent of the electrode voltage U, the power in eq. 5.7 would be at maximum when U equals the average of E. This implies that the electrode voltage is only 50% of the generated electromotive force while the other 50% is lost on internal ohmic losses [8, 9, 14-16], as given by:

$$P_{ohmic\ \ loss} = b\int_0^L j^2 \cdot R_{cell}\, dy \qquad \text{(eq. 5.9)}$$

If E equals U, the obtained power (eq. 5.7) will be equal to the power lost on ohmic losses. However, Because E and R_{cell} are (non-linearly) dependent on U, the relation between the power and electrode voltage U is more complex. If the electrode voltage decreases, the current density is increased, more ions will be transported from seawater to river water, and hence the electromotive force will decrease (i.e., $\partial E/\partial U > 0$) and the internal resistance will decrease (i.e., $\partial R_{cell}/\partial U > 0$). These feedback mechanisms imply that the maximum power can be obtained when U is different from the average of E, and the energy efficiency is not limited to 50% even for a single set of electrodes.

The ohmic losses can be reduced in any RED system by minimizing the electric currents, at the expense of slower ion transport, and consequently, more available energy will leave the system unused. To capture maximum energy at low current density, RED can be applied in multiple stages. This can be done by leading the feedwater through several RED cells in series [8], or divide the electrodes in multiple segments in series, each controlled individually [15] (Figure 5.1d). The current density in each stage can be kept low in such a system, as the unused energy can be captured in the next stages.

5.3 Modeling methodology

To calculate the energy efficiency for all these cases (co-flow, cross-flow or counter-flow, each with one single electrode pair or segmented electrode pairs), a model was designed to solve the differential eq. 5.5 and 5.6 and the corresponding maximum energy efficiency. The obtained energy was calculated by eq. 5.7, whereas the ohmic loss was calculated by eq. 5.9 and the unused energy was calculated based on the outflow concentrations for river water and seawater and eq. 5.2. As input parameters, a concentration of 30 g/l NaCl (0.513 M) was

chosen as seawater and 1 g/l NaCl (0.017 M) was chosen as river water inflow. The membranes were assumed perfect (i.e., 100% permselective and no membrane resistance), which resembles the practical case where the river water dominates the resistance R_{cell}. A cell length (distance between inflow and outflow) of 0.1 m and an intermembrane distance of 100 µm were chosen, as these values are typical for laboratory experiments [9, 20]. The total electrode area at each side of the membrane pile was 10 cm by 10 cm in all cases. When using segmented electrodes, only the electrodes are segmented, in equal parts, and the total electrode area remains 10 cm by 10 cm. The electrical current is assumed only perpendicular to the electrodes, which resembles a thin membrane pile relative to the length and width. The conductivity of the feedwater in the compartments was estimated using the concentration and a molar conductivity Λ of 0.01287 $S \cdot m^2/mol$ [21]. The activity coefficients were calculated based on the salt concentration and a modified three characteristic parameter correlation (TCPC) model [22]. Concentration changes in the boundary layer (referred to as concentration polarization) are assumed negligible. The residence time of the river water was fixed at 30 s, whereas the residence time for the seawater was varied to obtain different ratios between the feedwater flows.

The electrode voltage U was varied and optimized to obtain a maximum energy efficiency, using a Nelder-Mead simplex method [23]. In cases of segmented electrodes (Figure 5.1d), the voltage over each electrode segment, U, could be chosen individually. In the specific case of cross-flow with segmented electrodes, the electrodes were segmented in the direction of the river water flow, as the electromotive force is most sensitive to the concentration of the river water. The equations (eq. 5.1-5.7) were solved and optimized using Matlab (v7.7, The Mathworks). The concentration profile in the case with co-flow was solved using an ode45 solver, and the cases with counter-flow and cross-flow were solved using concentration profiles in matrices and a forward difference method. A resolution of 1000 grid points in each direction was used for the latter cases. The results were insensitive to further refinement of the step size and error tolerance.

5.4 Results

5.4.1 Influence of Flow Configuration

The energy efficiency for co-flow, cross-flow and counter-flow with a non-segmented electrode are shown in Figure 5.2A. Figure 5.2B-D show the theoretical available energy per m^3 river water for all theses cases split into obtained energy, energy lost as an ohmic loss and

unused energy in the effluent. Because the river water will be limited in most practical cases, all graphs are plotted as a function of the fraction of seawater (relative to the total feed flow).

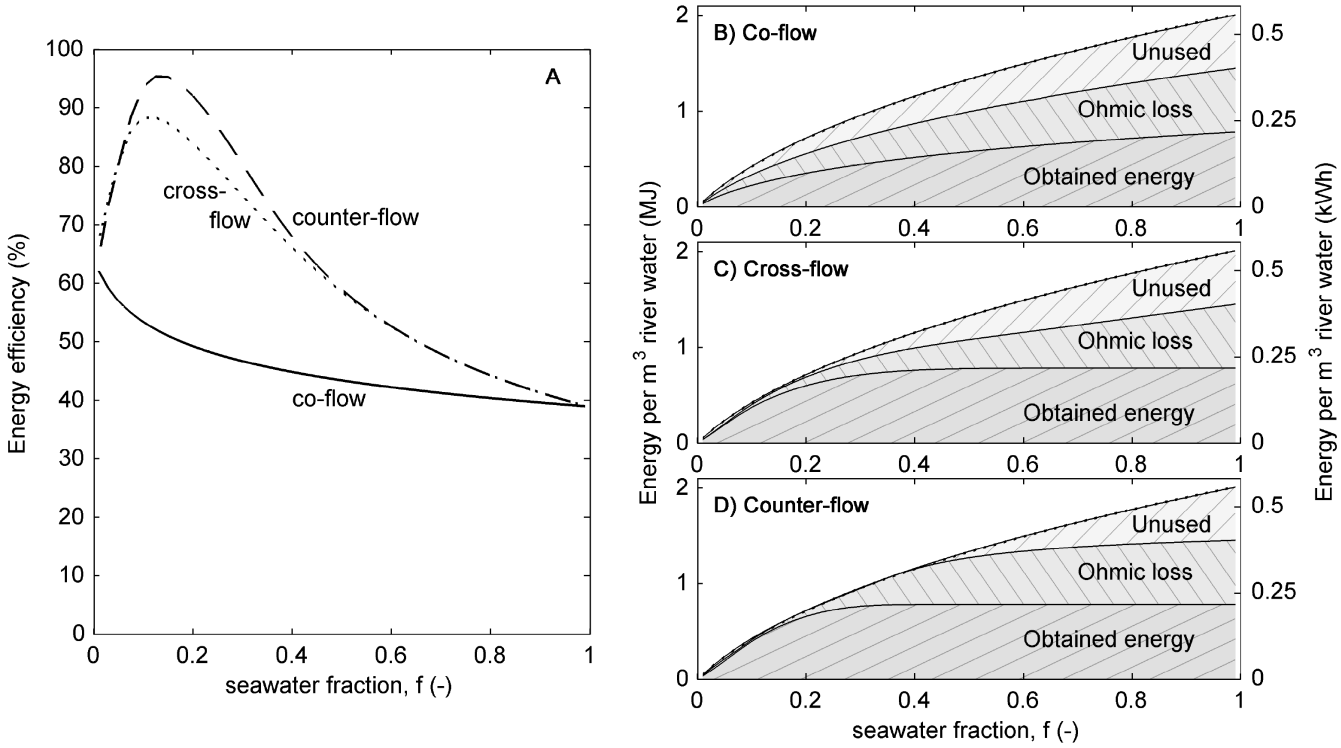

Figure 5.2: A) Energy efficiency as function of the seawater fraction, f = $\Phi_{sea}/(\Phi_{sea}+\Phi_{river})$, for co-flow, cross-flow and counter-flow. The theoretical available energy per m^3 river water is split into obtained energy, energy lost as an ohmic loss and unused energy, for B) co-flow, C) cross-flow and D) counter-flow, all as function of the fraction of seawater. All cases use non-segmented electrodes and a fixed residence time of the river water of 30 s. A seawater fraction of f = 0 implies that no seawater is used, while f = 1 implies that an infinite amount of seawater is used.

Figure 5.2A shows that even 95% of the theoretical available energy can be captured using only one electrode segment, for counter-flow at f = 0.13. This is clearly more than the previously claimed 50% [8, 9, 14-16], due to the interaction mechanism between electromotive force (E), electrode voltage (U) and cell resistance (R_{cell}) (eq. 5.7). The energy efficiency for the case with counter-flow is slightly higher than for the case with cross-flow and for some cases (f ≈ 0.15) almost twice the available energy is captured compared to the case with co-flow.

Although highest efficiencies are obtained at low seawater fractions f, Figure 5.2B-D show that the obtained energy (and thus the power density) increases when f increases. For cross-

flow and counter-flow, the obtained energy only slightly increases at f > 0.3, while for co-flow the obtained energy continues increasing for higher values of f. Figure 5.2B-D show that the ohmic loss as well as the unused energy is larger for co-flow at most values of f, compared to cross-flow and counter-flow. The ohmic loss and unused energy also increase in all cases when the seawater fraction increases. The additional energy that is available at increased seawater fraction cannot be used as efficiently as for low seawater fractions, as is observed in the lower efficiencies in Figure 5.2A with increasing f and the plateaus for cross-flow and counter-flow in Figure 5.2C and 5.2D. The unused energy and ohmic loss are discussed below in more detail.

5.4.2 Unused energy

The unused energy is largest in the case with co-flow. When co-flow is considered, ions cannot fully exchange to a level where the salt concentrations in both outflow streams are equal, because equal concentrations at either side of the membrane would correspond to a zero electromotive force close to the outflow of the cell. When a single electrode segment is used, the electromotive force needs to remain equal or larger than the electrode voltage. Therefore, part of the available energy is unused and remains in the effluent in a co-flow case. Using counter-flow, the local electromotive force will remain non-zero at all positions along the flow channels, even if the outflow concentrations of both streams are equal, Because the outflows are positioned opposite. As a consequence, the salinity difference can be fully utilized in a counter-flow case.

The unused energy for the cross-flow case (Figure 5.2C), and therefore the energy efficiency (Figure 5.2A), is in between the values for co-flow and for counter-flow. Considering cross-flow, the ion transfer in the water near the inlet of the other stream can continue along the flow channel until the concentration of the brackish mixture is reached, as for counter-flow. However, for the feedwater that is positioned near the outflow of the other stream, the local concentration difference between the water streams is smaller, such that the electromotive force is only slightly larger than the electrode voltage. Consequently, fewer ions are transferred here and the outflow concentration does not reach the concentration of the brackish mixture. This is reflected in the unused energy for the cross-flow case, which is higher than for the counter-flow case (Figure 5.2D), but lower than for the co-flow case (Figure 5.2B).

A small fraction of the unused energy of the cross-flow case is due to a varying concentration along the width of the river water outflow and the width of the seawater outflow. The feedwater that flows close to the inflow of the other feedwater has more ion exchange than the feedwater that flows close to the outflow of the other feedwater. As a consequence, the outflow concentrations within both feed streams vary along the width. When using a single manifold for each outflow stream, energy is lost due to irreversible mixing of the river water outflow and irreversible mixing of the seawater outflow. This effect is most pronounced close to equal flows for river water and seawater (f = 0.5), where it accounts for approximately 13% of the total available energy.

5.4.3 Ohmic loss

Although the ohmic loss is, for some seawater fractions, largest for counter-flow, the co-flow has the largest ohmic loss for all seawater fractions when normalized for the obtained energy (Figure 5.2B). The relatively large ohmic loss for co-flow can be explained when inspecting the local current density. Figure 5.3 shows the local current density for co-flow and counter-flow and for several seawater fractions. The cross-flow case is shown later separately, because the water streams flow in different dimensions in the cross-flow case.

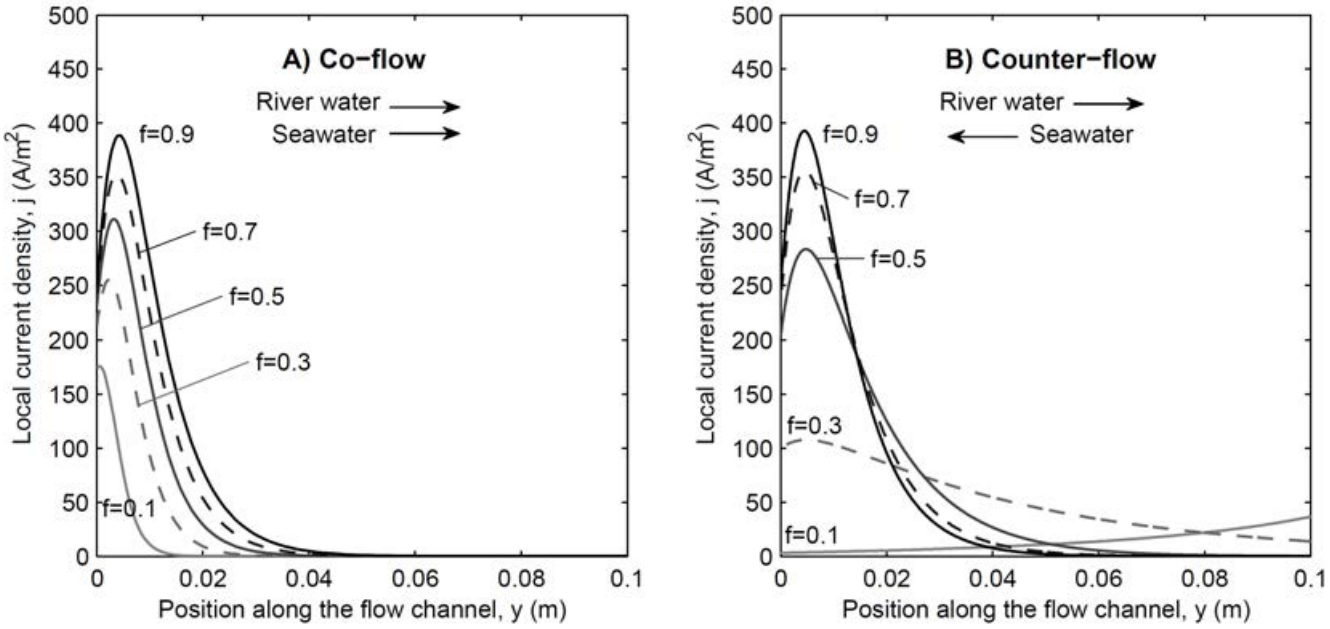

Figure 5.3: Local current density (j) as function of the position along the flow channels (y), for A) co-flow and B) counter-flow. Both panels show graphs for different seawater fractions (f). All cases use a fixed residence time of the river water of 30 s. The arrows show the flow direction for river water and seawater.

Figure 5.3 shows that the current density for large fractions of seawater ($f \geq 0.7$) peaks a few mm after the river water inflow ($y \approx 0.005$ m), both for co-flow and counter-flow, although the concentration difference between river water and seawater is even larger at $y = 0$. The reason is that the current density peaks slightly later, because the ohmic cell resistance (R_{cell}) is also largest at $y = 0$, due to the low conductivity of the river water. Previous research showed that the maximum local current density (and thus the highest local power density) is obtained when the river water concentration is increased to approximately 0.030 M [15].

For seawater fractions ≤ 0.5, the current density shows a distinct peak in the case of co-flow, whereas it is more equally distributed over the full channel for counter-flow. The high local current density for co-flow is a consequence of the rapidly decreasing concentration difference over the membrane as the waters flow along the channels. Because river water and seawater flow in the same direction, the (salt) enriched river water flows along the (salt) depleted seawater. This lowers the electromotive force and therefore limits the ion exchange in the case of co-flow. For counter-flow, the concentration difference over the membrane is more equally distributed, because the ions that are transferred from seawater to river water are discharged in opposite direction. The distinct peak in current density for co-flow explains the higher ohmic loss, as the ohmic loss is proportional to the local current density squared (eq. 5.9).

As the power density (i.e., power normalized for the membrane area) is proportional to the current density, Figure 5.3 implies that the power density also has a distinct peak near the river water inflow for most cases. A shorter residence time (i.e., faster flow rate or shorter flow channel) would significantly improve the power densities, which can result in a higher power density for co-flow compared to counter-flow [18]. The low current densities at $y > 0.04$ suggest that using half the residence time would significantly improve the power densities (roughly doubled), while the energy efficiency decreases less than 2%. The energy efficiency is only compromised seriously when the residence time would be more than 2.5 times smaller, which can be visualized by confining the y-axis to $y < 0.04$. In this range, a trade-off between high power densities and high efficiencies is required, as was observed in previous experiments [9, 18].

Cross-flow has an even smaller ohmic loss compared to the other cases (22% of the theoretical available energy, versus 32% and 37% for co-flow and counter-flow respectively), as demonstrated in Figure 5.2C. To show the current density in the two-dimensional cross-flow case, the local current density is plotted against the position on

the membrane in the feedwater flow channels in Figure 5.4 for the case of f = 0.5. This can be compared to the current density in the 1-dimensional cases with co-flow and counter-flow for f = 0.5 as presented in Figure 5.3.

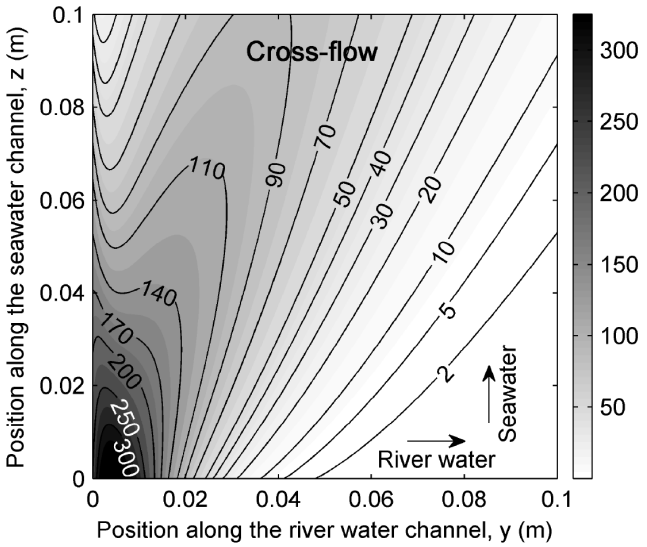

Figure 5.4. Local current density (j, in A/m^2) as function of the position on the membrane in the river water and seawater compartment (y and z), for cross-flow and f = 0.5. The arrows show the flow direction of river water and seawater.

Figure 5.4 shows, in comparison to the cases in Figure 5.3, that the current density is more equally distributed over the membrane area for the cross-flow case, which is most pronounced compared to the case with co-flow. In other words, the peak in current density in the case with cross-flow is less distinct and the area with a low current density is limited. This is indicated in Figure 5.4, for example, by a current density of approximately 15 A/m^2 near the outflow of river water and seawater, whereas the current densities near the river water outflow for the cases with co-flow and counter-flow are lower than 1 A/m^2. The reason is the larger variation (2-dimensional) in concentrations in case of cross-flow. Ion exchange can still occur even close to the outflows of both streams, because the feed waters did not have major ion exchange during their past route along the membranes. Therefore the high exchange in the area close to the outflows of both streams causes a more equal distribution of current density over the membrane area. Hence, the cross-flow case has the lowest ohmic loss at f = 0.5.

Considering the previous discussion, both ohmic loss and unused energy are dependent on the flow direction of the river water and seawater. Those losses are in general higher for

co-flow compared to cross-flow and counter-flow, due to a stronger decrease in electromotive force and therefore a more locally intensified current density in the case of co-flow.

5.4.4 Effect of seawater fraction

The same reasons for the lower energy efficiency in co-flow are applicable to the other cases when the seawater volumetric fraction (f) is increased. The energy efficiency in general decreases for increasing f (Figure 5.2A), which can be observed from the plateau value reached for the obtained energy for cross-flow (Figure 5.2C) and counter-flow (Figure 5.2D) at f > 0.5. At higher seawater fractions, the river water salinity increases faster along its path from inflow to outflow. Because the electromotive force depends on the salinity ratio (eq. 5.3), the electromotive force is sensitive to local changes in river water concentration along the feedwater channel. The corresponding low electromotive force decreases the ion transport rate and more energy will leave the system unused. Moreover, an excess in seawater creates a sharper peak in local current density close to the river water inlet (Figure 5.3) and hence increases the ohmic loss. Therefore, the excess of seawater is not used efficiently.

At extreme cases, for fractions of seawater nearly 0 or nearly 1, one of the feed flows fully limits the power production and ion transport is limited to a small area close to that inflow only. This situation disables the benefit of a more equal distribution of ion transfer for cross-flow and counter-flow. In these cases, the energy efficiency for situations with co-flow, cross-flow and counter-flow approach each other and the energy efficiency coincides at f = 0 and f = 1 for all cases presented in Figure 5.2A.

Although the highest efficiencies can be obtained for low seawater fractions, 1:1 mixing ratios or even an excess in seawater supply may be still favorable in practical situations where the river water supply is limited. The obtained energy per m^3 river water is largest for high seawater fractions. Moreover, the power density will increase even further for higher f, because the same electrical current can be obtained with a smaller membrane area, as demonstrated in Figure 5.3, which will reduce the membrane costs [24]. The exact optimum of the seawater fraction is dependent on amongst others the residence time, feedwater availability, membrane pricing and feedwater pretreatment. Therefore, the energy efficiency and obtained energy when using multiple electrode segments has been calculated for several seawater fractions.

5.4.5 Effect of Segmented Electrodes

o improve the obtained energy and the energy efficiency, segmented electrodes can be used. The energy efficiency is shown in Figure 5.5A as a function of the number of electrode segments. The obtained energy, ohmic loss and unused energy per m^3 river water as function of the seawater fraction when the electrodes are divided into four segments are presented in Figure 5.5B-D.

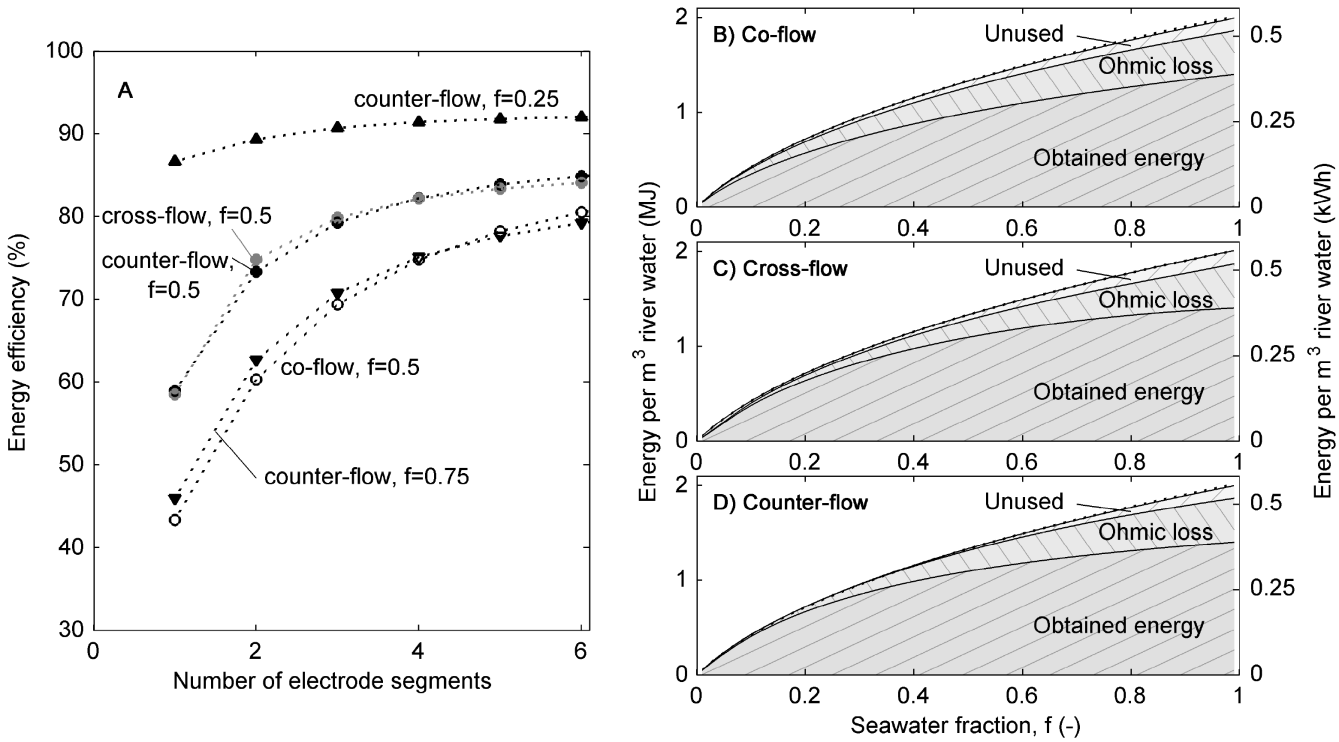

Figure 5.5: Energy efficiency (A) as function of the number of electrode segments, for co-flow and cross-flow with equal seawater and river water flow (f = 0.5) and for counter-flow, where the seawater fraction varies (f = 0.25, 0.5 and 0.75). The theoretical available energy per m^3 river water is split into obtained energy, energy lost as an ohmic loss and unused energy, for B) co-flow, C) cross-flow and D) counter-flow, all as function of the fraction of seawater and using four electrode segments. The residence time of river water was fixed to 30 s in all cases.

As expected, higher energy efficiencies can be achieved in all cases when multiple electrode segments (or multiple stacks in series) are used (Figure 5.5A). With multiple electrode segments, the system is divided in multiple steps, which is a basic condition for approaching a reversible process. Figure 5.5A shows that the case with co-flow and the case with counter-flow for f = 0.75 benefit most pronounced when using multiple electrode segments. In these cases, the effluent from the first electrode segment still contains a large fraction of unused

energy (Figure 5.2), because the electromotive force (E) quickly approaches the electrode voltage (U) in these cases, which limits the ion transport. With more electrode segments, the unused available energy after the first electrode segment(s) can be used for energy generation in the next segments. Each subsequent electrode segment can operate at a lower voltage, which enables to capture the available energy from the effluent of previous electrode segments. This is demonstrated in Figure 5.5B-D, which shows that the unused energy is reduced to only a few percent of the total available energy when the electrodes are divided into four segments.

Furthermore, the current density in the first segments can be lower than when using only one electrode segment, which reduces the ohmic losses. The first electrode segment, where the river water compartment is weakly conductive, operates at a high electrode voltage and low current density. At the subsequent voltages, the electrode voltage is lower while the current density is higher, due to a more conductive river water compartment as a result of the increased salt concentration. This strategy roughly halves the ohmic losses for a 1:1 mixture ($f = 0.5$) when using four electrode segments (Figure 5.5B-D) compared to using a single set of electrodes (Figure 5.2B-D). The ohmic loss is still lowest for the case with cross-flow (14% of the available energy for cross-flow versus 20% for co-flow and 16% for counter-flow at $f = 0.5$), due to the more uniform distribution of the current density, similar to the case with a single set of electrodes (Figure 5.3 and 5.4).

The cross-flow case has a similar energy efficiency as the counter-flow case at $f = 0.5$ using non-segmented electrodes as observed earlier (Figure 5.2A). The obtained energy is slightly higher for cross-flow than for counter-flow when using 2 and 3 electrode segments, and slightly lower for 5 or more electrode segments. The benefit of cross-flow when using 2 or 3 electrode segments stems from the fact that more unused energy remains when using one electrode segment for cross-flow than for counter-flow (Figure 5.2C-D). This energy can still be captured when using several electrode segments. The advantage for counter-flow for 5 or more electrode segments is explained from the arbitrary choice of segmenting the electrodes in the direction of the river water flow only. For a large number of electrode segments, cross-flow would benefit extra if the electrodes would be segmented in the direction of the seawater too.

At an infinite number of electrode segments and an infinite long residence time, the current density can be infinitely small and the ohmic loss can be neglected (i.e., reversible process). In that case, the obtained work can be derived from the integral of the electromotive force to

the transported charge, up to the point in which the effluent concentrations are equal. This yields an energy efficiency of 100%, which can be confirmed by this model, independent on the flow direction or the ratio between seawater and river water.

Even though the energy efficiency as calculated in this paper assumes ideal conditions, these results are still representative of actual (non-ideal) conditions. For example, when using a non-zero membrane resistance, the same energy efficiencies can be reached, although the residence time should be increased for this case. The extra resistance decelerates the process (i.e., lower power density), but does not cause irreversible losses. The same applies to the choice of the intermembrane distance; a larger intermembrane distance decelerates the process because of increased resistance but does not create irreversible losses. Only the transport of co-ions and water through the membranes (i.e., permselectivity <100%), which is neglected for ideal membranes as in this study, causes irreversible losses in the available energy from mixing seawater and river water. Such a loss is most pronounced for very low flow rates (e.g., an order of magnitude smaller as in this study) [20]. Nevertheless, experimental results using equal flows for seawater and river water (f = 0.5) and a design comparable with cross-flow, indicate that efficiencies as high as in this idealized study are realistic. Efficiencies of 53 ± 5% [9] for non-segmented electrodes and up to 80% when the feedwater passes the electrodes multiple cycles [2] are achieved experimentally, which indicates that this irreversible loss in available energy can be limited in practice.

5.5 Conclusions

The energy efficiency of mixing seawater and river water in RED can be derived from an analytical model. Assuming ideal membranes, the energy efficiency is dependent on the ratio between the seawater and river water flow, and the number of electrode segments. Energy efficiencies of 95% can be obtained when using seawater and river water flowing in opposite direction (counter-flow), even for a single electrode segment, whereas only 50% was predicted in previous studies. When seawater and river water flow in the same direction (co-flow), lower efficiencies are obtained, due to ohmic losses and more unused energy. Nevertheless, also in this case energy efficiencies much higher than 50% can be obtained. The efficiency in the more practical case of cross-flow, where the feed waters flow in a direction of 90º with respect to each other, is up to 88%, which is only slightly lower than the value obtained for counter-flow. This is based on using an excess amount of river water compared to the seawater volume. Equal flows of seawater and river water result in lower

theoretical efficiencies (45%-58%), but the obtained power strongly increases in these cases when multiple electrode segments are used. This implies that high efficiencies can be obtained in energy generation from RED.

References

1. Pattle, R. E., Production of Electric Power by mixing Fresh and Salt Water in the Hydroelectric Pile. *Nature* **1954,** *174*, (4431), 660-660.
2. Post, J. W.; Hamelers, H. V. M.; Buisman, C. J. N., Energy Recovery from Controlled Mixing Salt and Fresh Water with a Reverse Electrodialysis System. *Environmental Science & Technology* **2008,** *42*, (15), 5785-5790.
3. Logan, B. E.; Elimelech, M., Membrane-based processes for sustainable power generation using water. *Nature* **2012,** *488*, (7411), 313-319.
4. Achilli, A.; Cath, T. Y.; Childress, A. E., Power generation with pressure retarded osmosis: An experimental and theoretical investigation. *Journal of Membrane Science* **2009,** *343*, (1-2), 42-52.
5. Yip, N. Y.; Tiraferri, A.; Phillip, W. A.; Schiffman, J. D.; Hoover, L. A.; Kim, Y. C.; Elimelech, M., Thin-Film Composite Pressure Retarded Osmosis Membranes for Sustainable Power Generation from Salinity Gradients. *Environmental Science & Technology* **2011,** *45*, (10), 4360-4369.
6. Yip, N. Y.; Elimelech, M., Thermodynamic and Energy Efficiency Analysis of Power Generation from Natural Salinity Gradients by Pressure Retarded Osmosis. *Environmental Science & Technology* **2012,** *46*, (9), 5230-5239.
7. Lacey, R. E., Energy by Reverse Electrodialysis. *Ocean Engineering* **1980,** *7*, (1), 1-47.
8. Veerman, J.; Saakes, M.; Metz, S. J.; Harmsen, G. J., Reverse electrodialysis: Performance of a stack with 50 cells on the mixing of sea and river water. *Journal of Membrane Science* **2009,** *327*, (1-2), 136-144.
9. Vermaas, D. A.; Saakes, M.; Nijmeijer, K., Double Power Densities from Salinity Gradients at Reduced Intermembrane Distance. *Environmental Science & Technology* **2011,** *45*, (16), 7089-7095.
10. Brogioli, D., Extracting Renewable Energy from a Salinity Difference Using a Capacitor. *Physical Review Letters* **2009,** *058501*, 1-4.
11. Sales, B. B.; Saakes, M.; Post, J. W.; Buisman, C. J. N.; Biesheuvel, P. M.; Hamelers, H. V. M., Direct Power Production from a Water Salinity Difference in a Membrane-Modified Supercapacitor Flow Cell. *Environmental Science & Technology* **2010,** *44*, (14), 5661–5665.
12. Boon, N.; van Roij, R., 'Blue energy' from ion adsorption and electrode charging in sea and river water. *Molecular Physics* **2011,** *109*, (7-10), 1229-1241.
13. Vermaas, D. A.; Bajracharya, S.; Sales, B. B.; Saakes, M.; Hamelers, B.; Nijmeijer, K., Clean energy generation using capacitive electrodes in reverse electrodialysis. *Energy & Environmental Science* **2013,** *6*, (2), 643-651.
14. Veerman, J.; Post, J. W.; Saakes, M.; Metz, S. J.; Harmsen, G. J., Reducing power losses caused by ionic shortcut currents in reverse electrodialysis stacks by a validated model. *Journal of Membrane Science* **2008,** *310*, (1-2), 418-430.
15. Veerman, J.; Saakes, M.; Metz, S. J.; Harmsen, G. J., Reverse electrodialysis:A validated process model for design and optimization. *Chemical Engineering Journal* **2011,** *166*, (1), 256–268.
16. Kim, D.-K.; Duan, C.; Chen, Y.-F.; Majumdar, A., Power generation from concentration gradient by reverse electrodialysis in ion-selective nanochannels. *Microfluid Nanofluid* **2010,** *9*, (6).
17. Vermaas, D. A.; Saakes, M.; Nijmeijer, K., Power generation using profiled membranes in reverse electrodialysis. *Journal of Membrane Science* **2011,** *385-386*, (0), 234-242.

18. Veerman, J.; Saakes, M.; Metz, S. J.; Harmsen, G. J., Electrical Power from Sea and River Water by Reverse Electrodialysis: A First Step from the Laboratory to a Real Power Plant. *Environmental Science & Technology* **2010,** *44*, (23), 9207-9212.

19. Długołęcki, P. E.; Nijmeijer, K.; Metz, S. J.; Wessling, M., Current status of ion exchange membranes for power generation from salinity gradients. *Journal of Membrane Science* **2008,** *319*, (1-2), 214-222.

20. Veerman, J.; Jong, R. M. D.; Saakes, M.; Metz, S. J.; Harmsen, G. J., Reverse electrodialysis: Comparison of six commercial membrane pairs on the thermodynamic efficiency and power density. *Journal of Membrane Science* **2009,** *343*, (1-2), 7-15.

21. Moore, W. J., *Physical chemistry*. 5 ed.; Prentice-Hall: **1999**; 977 p.

22. Ge, X.; Wang, X.; Zhang, M.; Seetharaman, S., Correlation and Prediction of Activity and Osmotic Coefficients of Aqueous Electrolytes at 298.15 K by the Modified TCPC Model. *Journal of Chemical & Engineering Data* **2007,** *52*, (2), 538-547.

23. Lagarias, J., C. ; Reeds, J., A. ; Wright, M., H. ; Wright, P., E., Convergence Properties of the Nelder-Mead Simplex Method in Low Dimensions. *SIAM Journal of Optimization* **1998,** *9*, (1), 112-147.

24. Strathmann, H., Electrodialysis, a mature technology with a multitude of new applications. *Desalination* **2010,** *264*, (3), 268-288.

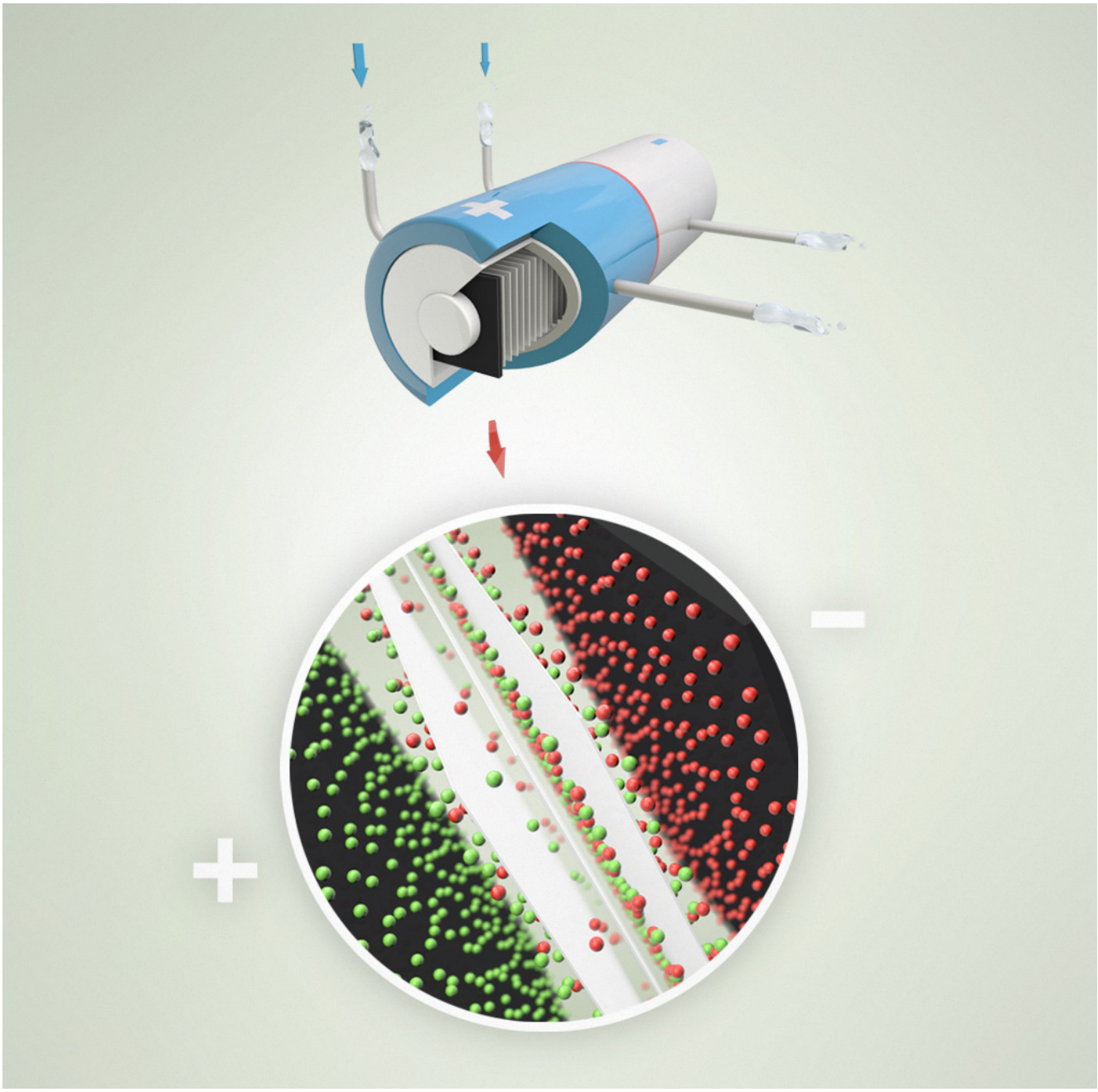

Chapter 6

Clean energy generation using capacitive electrodes: capacitive reverse electrodialysis (CRED)

Abstract

Capacitive reverse electrodialysis (CRED) is a newly proposed technology to generate electricity from mixing salt water and fresh water (salinity gradient energy), by using a membrane pile as in reverse electrodialysis (RED) and capacitive electrodes. The salinity difference between salt water and fresh water generates a potential difference over ion selective membranes, which can be used as a renewable power source. The strength and unique characteristic of CRED in comparison to the other technologies is that it allows multiple membrane cells between a single set of electrodes and at the same time avoid redox reactions using capacitive electrodes. The capacitive electrodes use activated carbon on a support of Ti/Pt mesh to store ions and their charge. A periodic switching of the feed waters, combined with a switching of the direction of the electric current, ensures that the capacitive electrodes do not get saturated. The large membrane pile enables to charge the electrodes more than in previous approaches for capacitive mixing. As a consequence, the energy cycle of CRED has a larger range in both voltage and accumulated charge compared to previous capacitive mixing technologies. The power density obtainable with CRED stacks with capacitive electrodes is an order of magnitude higher than in previous attempts for capacitive energy extraction and close to or even better than similar RED stacks with conventional redox based electrode systems. CRED is considered as a stable, safe, clean and high performing technology to obtain energy from mixing salt water and fresh water.

This chapter has been published as

David A. Vermaas, Suman Bajracharya, Bruno Bastos Sales, Michel Saakes, Bert Hamelers and Kitty Nijmeijer, Clean energy generation using capacitive electrodes in reverse electrodialysis, *Energy & Environmental Science*, **2013**, *6*, 643-651

6.1 Introduction

Energy can be obtained from the mixing of waters with different salinities, for example seawater and river water. The increase in entropy associated with mixing can be used to generate renewable energy. The potential power obtainable from mixing seawater and river water is large: approximately 2 TW is available from using the global discharge of river water and seawater [1, 2], which is close to the current global electricity consumption [3].

Several technologies are proposed to capture this energy, for example using the osmotic pressure difference (pressure retarded osmosis, PRO) [4-6], using ion selective membranes (reverse electrodialysis, RED) [1, 7, 8] or using capacitive mixing (CAPMIX) [9-13]. The latter technology (CAPMIX) uses the salinity gradients to charge and discharge capacitive electrodes, such as activated carbon. Seawater and river water flow subsequently through a compartment with capacitive electrodes on either side of the compartment. When seawater flows through the compartment, positively or negatively charged ions can be stored in the large pore area available in the activated carbon. When the seawater is subsequently replaced by river water, the electrodes are discharged. A net charge transport is created using ion exchange membranes or an electric field. The charge of the positive and negative ions in the electrodes is balanced with electrons from an external circuit. In other words, an electrical current is generated by the charge accumulation on the capacitive electrodes. These electrodes make the use of a redox reaction as in conventional RED obsolete.

Simplicity is an advantage of CAPMIX, as it does not require a turbine (as in PRO) or a redox reaction (as in RED) as an intermediate step to produce electricity. The absence of such an intermediate step does not only save the costs of auxiliary equipment, but also eliminates all possible risks associated with high pressures (for PRO) or potentially hazardous chemicals used or formed in the redox reactions (for RED).

Capacitive mixing systems can be equipped with ion exchange membranes [9, 12] or without any membranes [10, 11, 13]. The principle for capacitive mixing without membranes relies on the double layer expansion due to the salinity differences between the alternating feedwater. When the capacitive electrodes are covered with ion exchange membranes, the salinity difference creates a Donnan potential over the membranes that cause charging and discharging the electrodes. Although the addition of ion exchange membranes does imply extra costs, the salinity difference is used more efficiently and the power per electrode area is

several orders of magnitude higher when ion exchange membranes are used between the capacitive electrodes [12].

However, even when using capacitive mixing with ion exchange membranes, the power per electrode area, or the power per membrane area (i.e., power density) is still low compared to that obtainable in PRO and RED. The highest experimental power density from CAPMIX is 0.2 W/m^2 [9], while RED obtained an experimental power output of 2.2 W/m^2 [7] using the same concentrations, PRO even generated 3.5 W/m^2 [6] using slightly higher salinity gradients. Projected power densities are even higher for PRO and RED [2, 5, 14, 15]. To make salinity gradient energy financially attractive, the net gain should be at least 2 W per m^2 area of ion exchange membranes [16].

In this research we present a novel system to generate power from salinity gradients using RED technology and capacitive electrodes but with much higher power densities than obtained previously for capacitive electrode systems. This capacitive reverse electrodialysis (CRED) system synergistically combines previous developments in capacitive mixing and reverse electrodialysis. The principle and experimental setup of the CRED system are described, followed by the results. Results are expressed in terms of power density output and the influence of the number of membrane cells, current density, electrode rinse flow rate and switching interval time are evaluated. The results are compared to a conventional RED system using redox reactions as the electrode system and existing methods for capacitive energy extraction (CAPMIX). Our results show that capacitive reverse electrodialysis is a potentially safe, sustainable (no electrochemical reactions) and cheap option, able to generate power densities as high as the best performing existing RED system.

6.2 Concept

A schematic representation of the principle of capacitive reverse electrodialysis is shown in Figure 6.1. One or more membrane cells, each comprising a cation exchange membrane (CEM), a compartment for diluted salt water, an anion exchange membrane (AEM), and a compartment for concentrated salt water, generate a potential difference. This unit cell is similar to the cells used in a conventional RED system. Multiple membrane cells can be stacked between a single set of electrodes in CRED. The selective ion transport, driven by the salinity difference between the alternating seawater and river water, creates a potential difference over each membrane. This potential difference can be used as a power source when the ionic current is converted into an electric current at the electrodes.

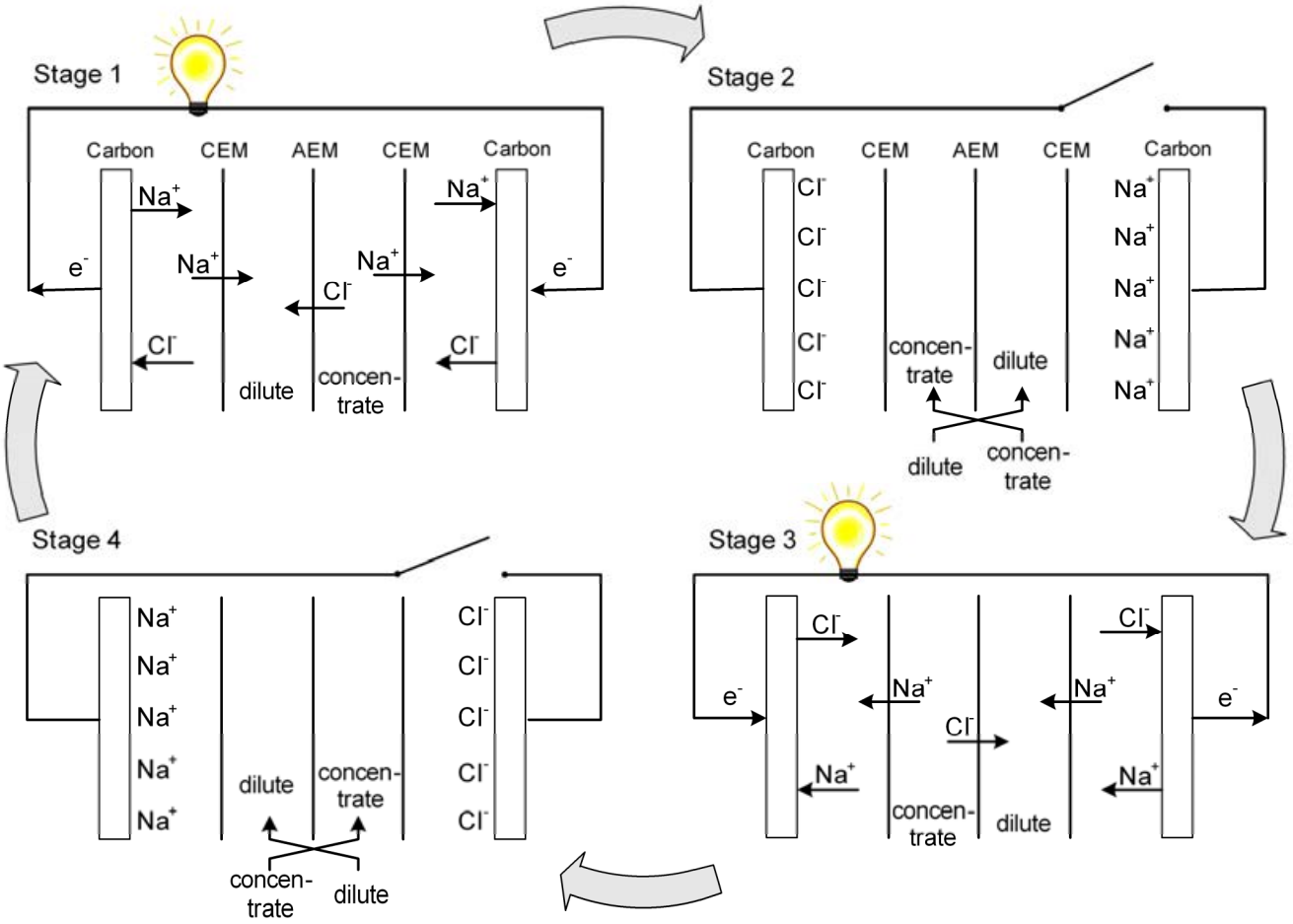

Figure 6.1: Principle of CRED in four stages, in this case for 1 cell (CEM, AEM, dilute, concentrate). Multiple membrane cells can be stacked between the electrodes.

Both outer ends of the total membrane stack are supplied with a compartment for the electrode rinse solution and, in contrast to a redox electrode as in a normal RED stack, with a capacitive electrode. Capacitive electrodes have been suggested for application in RED [8], although it was never applied before.

The capacitive electrode consists of a current collector (e.g., Ti/Pt mesh or glassy carbon) and a layer of activated carbon. The large pore surface area of the activated carbon allows the adsorption of ions and the conductive property of carbon allows electron transfer to neutralize the corresponding net ionic charge. When the ion storage capacity is saturated, the current direction is switched, to discharge the ions from the activated carbon.

The electrode rinse solution can be a NaCl solution, since the use of capacitive electrodes does not require redox reactions to convert the ionic current into an electrical current. The use of an electrode rinse compartment is not strictly necessary to obtain power from salinity

gradients, as shown in CAPMIX [12], but this electrode rinse compartment has several advantages for CRED. The concept of CRED, using multiple membrane cells in between the electrodes, enables to generate large voltages over the membrane pile. This provides the opportunity to prolong the electrode charging. The electrode rinse solution provides sufficient ions that accumulate as positive or negative charge on the capacitive electrodes. Furthermore, the presence of an electrode rinse solution has an experimental purpose; the electrode rinse solution can be controlled and monitored individually from the feed waters.

The cyclic operation of CRED can be described in four stages, as indicated in Figure 6.1. In stage 1 and 3, the potential generated by the membrane cells drives the ions in and out of the porous carbon. To obey electro-neutrality in the carbon, a current is forced through the external circuit and electricity is produced. At the end of stage 1 and 3, the carbon electrodes are saturated with ions. In stage 2 and 4 the feedwater streams are switched. After switching, the electrical current continues in opposite direction (stage 1 or 3) and the capacitive electrodes discharge. Charging the capacitive electrodes requires a potential difference, thus the obtainable power is temporary lower. However, that loss in power production is regained when the feed waters and electrical current are switched and the capacitive electrodes are discharged.

A RED system with conventional electrodes operates continuously in stage 1 (Figure 6.1) and switching of the feed waters does not take place, as the ionic current is continuously converted into electrical current using redox reactions at the electrodes.

Previous capacitive mixing technologies used a single compartment only for each electrode set, where the electrodes (with or without interference of an ion exchange membrane) face salt and fresh water subsequently. Using salt and fresh water at the same time in a membrane pile, as is the case in CRED, does not only reduce the number of electrodes per compartment, but the potential per membrane is also doubled because salt water and fresh water are used simultaneously. In CAPMIX, two membranes (CEM and AEM) are required for one compartment, while in CRED only one membrane is required per compartment that yields the same Donnan potential as two membranes in CAPMIX. Moreover, more membrane cells between a set of electrodes increase the voltage that is available for charging and discharging the capacitive electrodes, which increases the obtained power density [9].

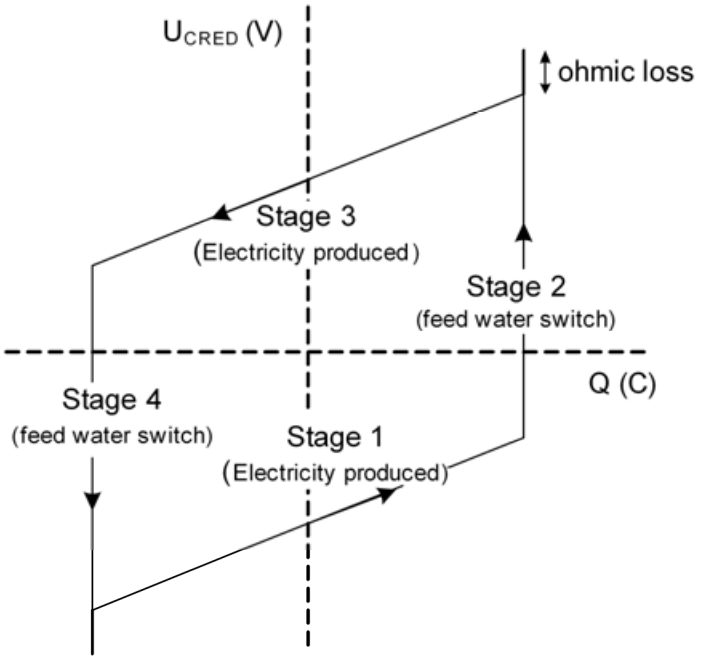

Figure 6.2: Energy cycle corresponding to the CRED principle. The voltage over the CRED stack U_{CRED} is plotted against the accumulated charge Q on the capacitive electrodes.

The cyclic process of CRED can be explained using the energy cycle [10, 11, 17] (Figure 6.2). The charge transport during stage 1 and 3 causes horizontal displacement in the energy cycle. During stage 2 and 4, the feed waters are switched and thus the membrane voltage is reversed. The slope of the line during stage 1 and 3 represents the inverse of the electrode capacity. Compared to the other technologies using capacitive electrodes [10-12, 17], the capacitive electrodes in this research can accumulate more charge (while using the same capacity), due to the larger voltage that is generated using multiple membrane cells between the electrodes. As a consequence, the energy cycle of CRED covers a broader range both in terms of voltage and accumulated charge, compared to the previous capacitive mixing technologies.

The total energy obtained from CRED for each cycle is determined by the area enclosed by the cycle of Figure 6.2. The obtained energy per cycle is maximized by applying a low current density (to minimize the ohmic loss) and maximum switching intervals, i.e., the duration of stage 1 and 3 (to maximize the charge transport). However, to obtain a high power density output, the time per cycle is also relevant. A high current density and small switching interval shorten the cycle time. Considering both aspects, an optimum current density and an optimum switching interval are expected to determine the maximum power density.

6.3 Experimental section

6.3.1 Stack setup

The capacitive electrodes were prepared using 90 wt% of activated carbon (AC) powder (DLC Super 30, Norit, The Netherlands) and 10 wt% polyvinylidene fluoride (PVDF) (KYNAR HSV 900, Arkema Inc., USA) as a binding substance [9]. Approximately 9 grams of the activated carbon / PVDF mixture was added to 81 ml of 1-methyl 2-pyrrolidone (NMP) (Merck Schuchardt, OHG, Germany) and placed in a ball mill grinder (PM 110, Retsch, Germany) for 30 minutes at 450 RPM to homogenize the mixture. Subsequently, the slurry was cast on and in the Ti mesh, with a Pt coating (50 g/m^2) at a size of 10 x 10 cm^2 (Magneto Special Anodes BV, The Netherlands), using a casting knife and dried for four days at room temperature. The Pt coating was used to ensure good contact between the current collector and the activated carbon and to prevent corrosion. A cheaper material (such as graphite) may work equally well or even better. An electrolyte of 0.25 M NaCl was flushed over the electrodes afterwards for one day to remove all solvent (NMP). The final layer of activated carbon and PVDF was approximately 3 gram per electrode.

The membrane cells to perform CRED were composed of Neosepta CMX / AMX membranes (Tokuyama inc, Japan). The spacers in between the membranes had a thickness of 200 μm (Sefar Nitex 03-500/51) and an open area of 51%. Gaskets of silicon film, also 200 μm thickness, were used to seal the compartments. The shape of the spacers and gaskets are described in previous research [18]. Stacks were built with 2, 5, 10, 20 and 30 membrane cells. All CRED stacks used the same set of electrodes.

Figure 6.3 shows the configuration of the setup. The membrane cells were fed with artificial seawater (0.508 M NaCl) and river water (0.017 M NaCl) at a flow rate of 20 ml/min per cell compartment. This corresponds to a constant Reynolds number of 9 and a residence time in the feedwater compartments of 6 s, when taking into account the spacer porosity and hydraulic diameter as well [14]. Two three-way switches were used before the stack inflow to enable a feedwater switch.

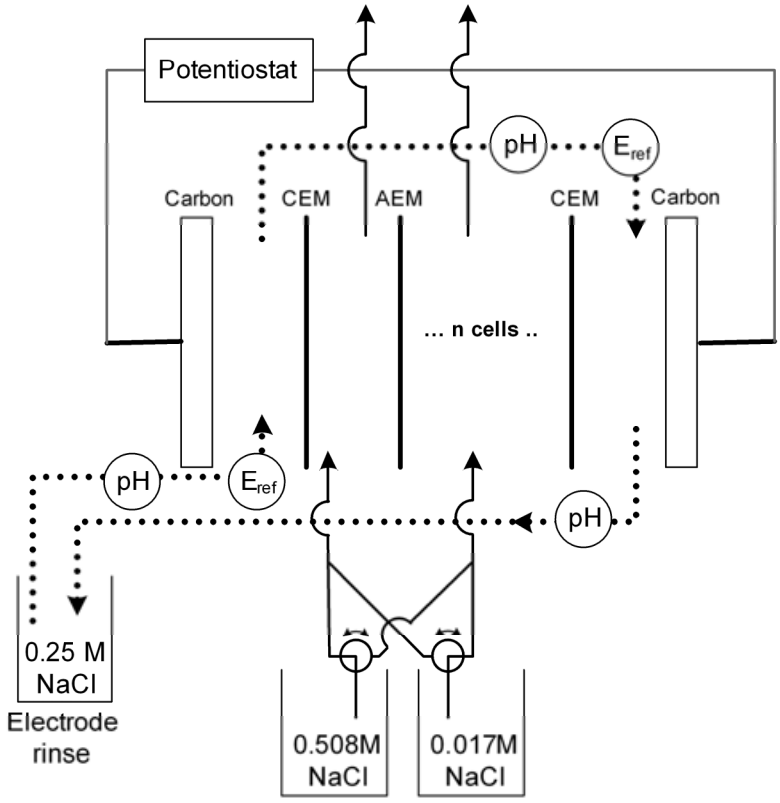

Figure 6.3: Illustration of the experimental CRED setup. The feed waters (0.508 M and 0.017 M NaCl) can be swapped using two switches. The electrode rinse solution (0.25 M NaCl) is circulated and passes 3 pH/temperature sensors and 2 reference electrodes (E_{ref}).

As electrolyte rinse solution, a 0.25 M NaCl solution was used by default. This solution was circulated along the electrodes at a flow rate of 200 ml/min, unless stated differently. The feedwater and electrolyte rinse solution were stored at a temperature of 25 (± 1) ºC. The pH and temperature were monitored (Endress+Hauser, Germany) in the electrode rinse solution before the first electrode, between the two electrodes and after the second electrode (see Figure 6.3). The concentration of chlorine was sampled frequently using chlorine sensitive test strips (Merck, Germany).

6.3.2 Electrochemical analysis

The obtained power density was measured during a galvanostatic cycle, imposed by a galvanostat (Ivium Technologies, The Netherlands). The current density during stage 1 and 3 was 20 A/m^2, unless stated otherwise. The duration of stages with open circuit (stage 2 and 4) was set at 60 s. The voltage over the total stack (U_{CRED}, in V) is the sum of the voltage

over the membrane cells (U_{mem}, in V) and the voltage at each electrode with respect to the corresponding reference electrode ($U_{electrode}$, in V):

$$U_{CRED} = U_{mem} + U_{electrode\ 1} - U_{electrode\ 2} \quad \text{(eq. 6.1)}$$

The four terms in eq. 6.1 were recorded individually. U_{CRED} was measured over the capacitive electrodes. To measure the latter three voltages of eq. 6.1, two reference electrodes (QIS, The Netherlands) were installed in the electrode rinse solution near the inlet of each electrode compartment (Figure 6.3) and a peripheral differential amplifier (Ivium Technologies, The Netherlands) was used to record the additional voltage series.

The average power density, P_{dens}, was calculated based on the total voltage over the total stack and the current density j (in A/m^2 of cross-sectional electrode area):

$$P_{dens} = \frac{1}{N_m} \cdot \frac{1}{t_2 - t_1} \sum_{t_1}^{t_2} U_{CRED} \cdot j \cdot \Delta t \quad \text{(eq. 6.2)}$$

In which N_m is the number of membranes (-) and t_1 and t_2 are the time (s) at the start and end of a full cycle (in s). The periods without power production (stage 2 and 4) are included as well for the calculation of the average power density.

All measurements at a current density of 20 A/m^2 or higher were repeated at least 4 cycles. Measurements at lower current densities were repeated at least 3 cycles. The first cycle was rejected for processing, to ensure a fully cyclic process. The average values of the remaining (usually 3) cycles are presented.

The performance of the CRED system was compared to that of the conventional RED system using two conventional redox electrode systems. Blank Ti/Pt mesh electrodes were used in both cases, i.e., one setup with 0.25 M NaCl rinse solution and one setup with 0.1 M $Fe(CN)_6^{3-/4-}$ and 0.25 M NaCl rinse solution. The system with only 0.25 M NaCl as an electrode rinse was equipped with 30 membrane cells, whereas the system with 0.25 M NaCl and 0.1 M $Fe(CN)_6^{3-/4-}$ was tested with 5 and with 30 membrane cells. The membrane cells had the same specifications as the CRED setup. The power density was measured setting a constant current density for at least 600 s. The feed waters for the conventional electrode systems were not switched, which benefits their power density (no switching interruptions).

6.4 Results

6.4.1 Typical cycle

Two typical cycles of the CRED system with 30 membrane cells between one set of capacitive electrodes, are shown in Figure 6.4. The voltages U_{CRED} (voltage over stack including electrodes) and U_{mem} (voltage over the membranes only, excluding electrodes) are shown, together with the change in pH over each electrode.

Figure 6.4 shows that the voltage over the membranes (U_{mem}) is almost constant within each stage, whereas the voltage over the whole stack (U_{CRED}) increases or decreases almost linearly when a constant current is applied, as expected for a constant capacitance. The voltage U_{mem} is generated by the salinity differences over each membrane and represents the voltage that can be measured when using an idealized conventional electrode system (i.e., a non-capacitive, reversible electrode system with no overpotentials). The difference between U_{mem} and U_{CRED} is mainly due to stored charge on the capacitive electrodes. The ohmic loss of the electrodes and electrode compartments has a minor effect for the case with 30 cells (3% of the total ohmic resistance), which is reflected in the reversible pattern of the voltage over the electrodes.

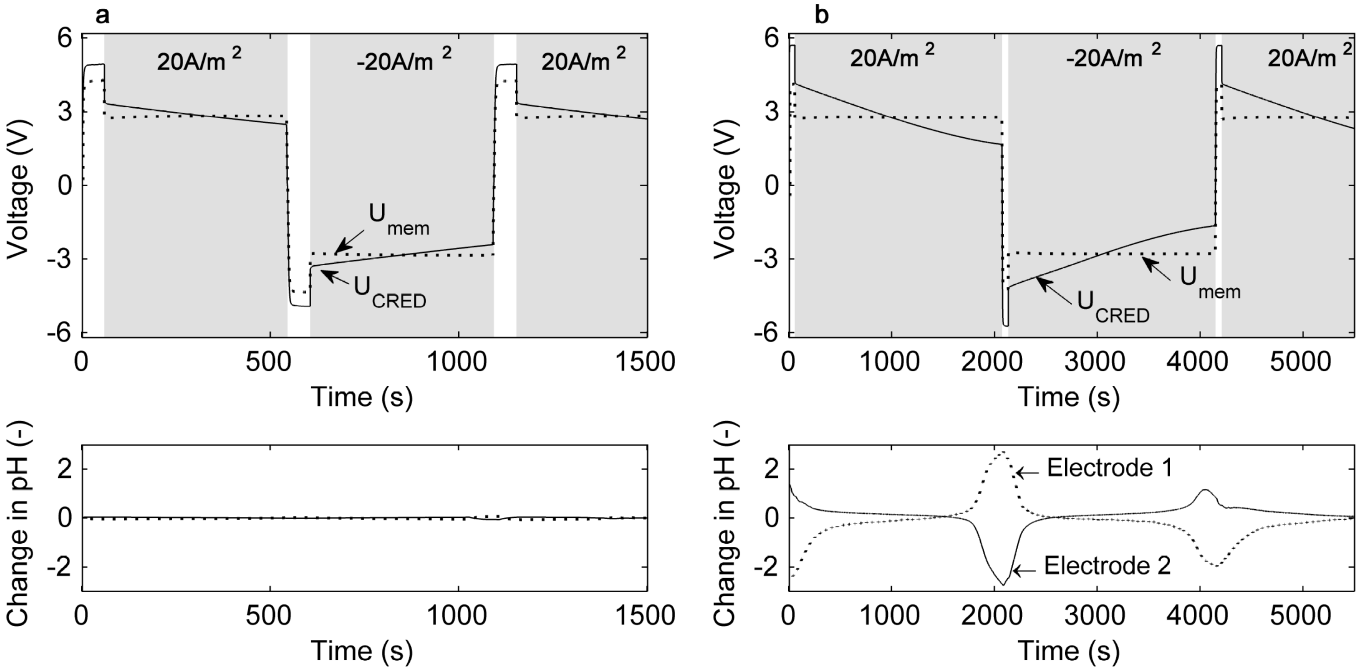

Figure 6.4: Typical cycles for CRED for a setup with 30 membrane cells between the capacitive electrodes, switching after a) 8 minutes and b) 33 minutes. The upper graphs show the voltage over the total stack (U_{CRED}) and that over the membranes only (U_{mem}). The shaded areas in the upper graphs indicate the periods where an electrical current was allowed. The lower graphs show the corresponding pH-change as derived from the pH measured before and after each electrode. The average pH was approximately 6.5.

In the beginning of each current stage, when U_{CRED} is higher than U_{mem}, the obtained power density is higher than when idealized conventional electrodes would have been used. At the end of each stage, the obtained power density is lower than what can be obtained when using idealized conventional electrodes. The average value of U_{CRED} is close to that of U_{mem} during each current stage, which indicates that the average power obtainable using CRED is similar to that of RED using idealized conventional electrodes.

When looking in more detail at the case in Figure 6.4b (switching after 33 minutes), the graph for U_{CRED} is slightly non-linear at the end of each current stage, for example around 2000 s. At this point the difference between U_{CRED} and U_{mem} exceeds 0.9 V and the pH over both electrodes changes (Figure 6.4b, bottom graph). These observations indicate that irreversible redox reactions occur at both electrodes, producing H^+ at one electrode and OH^- at the other. Several routes for such a redox reaction are possible, for example oxygen reduction at the cathode and carbon oxidation (reacting with water to carbon dioxide, H^+ and electrons) at the anode [19]. The exact reaction is beyond the scope of this paper.

When the feed waters are switched at smaller intervals, the occurrence of these redox reactions is avoided, as shown in Figure 6.4a. The absence of pH-change in this case shows that redox reactions can be avoided at the capacitive electrodes even when individual values of U_{CRED} and U_{mem} exceed the voltage required for water splitting. Redox reactions and the corresponding pH change only occur when the difference between U_{CRED} and U_{mem} (i.e., $U_{electrode1} - U_{electrode2}$) is exceeding 0.9V. Hence, a CRED stack with many cells can be operated without redox reactions as long as the switching interval time is limited.

6.4.2 Switching interval and current density

The effect of the switching interval and current density on the average power density is quantified in Figure 6.5. Figure 6.5a reveals a maximum power density when the feed waters are switched when 20 kC/m^2 is transferred, which corresponds in this case to a switching interval of 1000 s. In general, longer switching intervals benefit the average power density because the relative time of the periods without power production is reduced. However, when more than 20 kC/m^2 is transferred, redox reactions occur at the electrodes, as demonstrated in Figure 6.4b. These (irreversible) redox reactions consume energy, consequently reducing the obtained average power density.

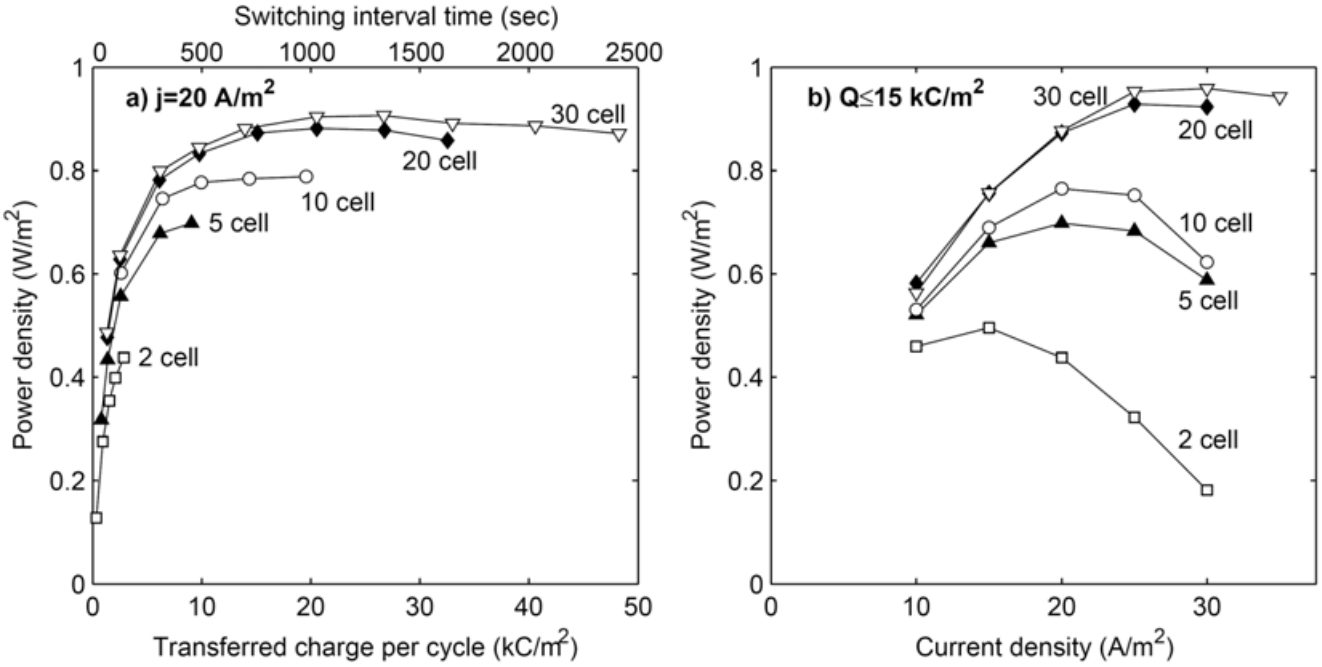

Figure 6.5: Average (gross) power density as function of a) transferred charge per cycle at a current density of 20 A/m^2 and b) current density (switched when 15 kC/m^2 was transferred or when the voltage reached 0 V), for stacks with 2, 5, 10, 20 and 30 membrane cells, all with capacitive electrodes. For clarity reasons, the standard deviations are not shown, but are typically less than 5% of the mean value.

Figure 6.5a also shows that stacks with more membranes, even at the same switching time, obtain a higher power density than stacks with less membranes. This is caused by the electrical resistance of the additional membrane that closes the final cell and the electrical resistance of the electrodes and their compartments. This resistance has a constant absolute value, which accounts for approximately 30% of the total stack resistance in case of the 2 cell stack and for only 3% in case of the 30 cell stack. The relatively lower resistance of the electrodes and their compartments increases the power density for stacks with more cells, at the same switching intervals.

The same effects on the power density can be observed when the current density is considered (Figure 6.5b). The optimum current density shifts towards higher values when the number of membrane cells increases. This shift is caused by three effects: 1) the relative resistance of the electrodes and electrode compartments decreases when the number of membrane cells is increased; 2) the ionic short-cut current [20] (i.e., the parasitic ionic current through the inflow and outflow manifolds) is reduced when the current density increases and the ionic short-cut current has most effect at higher numbers of membrane

cells [20]; and 3) smaller current densities increase the time between the switching and hence reduce the relative time of periods without power production. Because the stacks with 2 or 5 membrane cells are more limited in switching interval time than stacks with more cells because the voltage produced by the membrane cells is smaller, their optimum current density is lower.

In conclusion, the highest power densities, using these capacitive electrodes, can be found for a stack with (at least) 30 membrane cells, at a current density of approximately 30 A/m^2, using a cyclic charge transport of 20 kC/m^2 (i.e., 667 s).

6.4.3 Electrode stability

The capacitive electrodes appear to be stable on short and long term. The first experiment with the CRED stack (5 cells), was repeated again after 180, 460 and 600 CRED cycles. The power density for all these measurements was not significantly different (<4% difference). Consequently, errors due to aging of the capacitive electrodes and or to re-building stacks can be neglected in this research.

The performance loss due to self-discharge of the electrodes is also relatively small. The charge on loaded electrodes (~0.7 V) decreases exponentially with 12% in one hour under OCV conditions. In normal operation, the self-discharge is restricted to much lower values. When a current is applied, U_{CRED} decreases from the first minute on by the ohmic drop and discharge of the electrodes. Therefore, the self-discharge will be smaller than 12% per hour during normal operation.

6.4.4 Comparison CRED with RED and CAPMIX

Figure 6.6 compares the average power density obtained from CRED with the power density obtained from CAPMIX and RED with a conventional electrode systems (either $Fe(CN)_6^{3-/4-}$ or NaCl), as a function of the current density, for a) 5 cells and b) 30 cells.

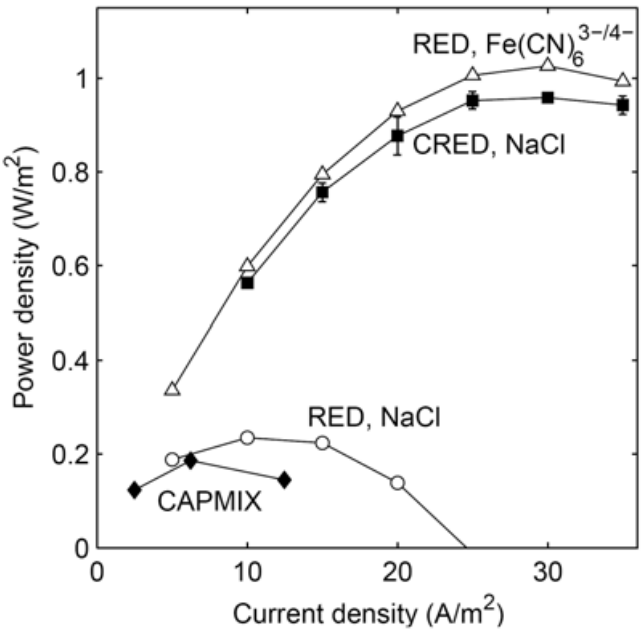

Figure 6.6: Average (gross) power density obtained with capacitive reverse electrodialysis (CRED) and RED stacks with conventional electrode systems, both with 30 membrane cells, and the average power density obtained from capacitive mixing reported in previous research (CAPMIX) [9]. For CRED stacks, the feedwater was switched when 15 kC/m^2 was transferred (to prevent redox reactions). The feedwater was not switched in the conventional electrode systems. The standard deviations are available for the CRED measurements only (some are smaller than the marker).

Figure 6.6 reveals that the CRED system obtains a much higher power density than when using previous CAPMIX technology or a conventional RED system with NaCl as an electrolyte or using capacitive mixing as reported in previous research [9]. The concept of CRED benefits on one hand from stacking multiple membrane cells (with corresponding prolonged charging and low self-discharge as shown in Figure 6.2) and on the other hand avoiding the use of redox reactions (with the corresponding overpotentials).

The power density of CRED is only slightly lower when compared to stacks with conventional Ti/Pt electrodes and $Fe(CN)_6^{3-/4-}$ electrode rinse system. The slightly higher power density for $Fe(CN)_6^{3-/4-}$ compared to the capacitive electrodes, is because the feed waters in the system with $Fe(CN)_6^{3-/4-}$ do not need to be switched periodically. Assuming the same switching interval times for the stack with conventional electrodes and that with the $Fe(CN)_6^{3-/4-}$ electrode rinse system, the power densities of the CRED system would be equal or even slightly higher than those obtained from conventional RED.

The energy efficiency (i.e., the obtained energy per liter feedwater, relative to the theoretical equivalents) is directly proportional to the obtained power density, considering equal flow

rate and equal membrane area. Therefore, the energy efficiency is similar as that for the conventional RED system with $Fe(CN)_6^{3-/4-}$ as electrode rinse. In this experiment, an energy efficiency of approximately 4.4% was achieved for the CRED system, obtained at a current density of 30 A/m^2. When the flow rate would be optimized, or when the feedwater would be recircurculated, energy efficiencies up to 80%, as obtained in conventional RED, are envisaged.

An important advantage of CRED with respect to conventional RED is the environmental benefit. When conventional electrodes are used with $Fe(CN)_6^{3-/4-}$ as an electrolyte, small leakages of the electrolyte to the feedwater compartments can pollute the environment via the brackish effluent and counterbalance the ion exchange groups present in the anion exchange membranes [8, 21]. Furthermore, hexacyanoferrate can precipitate with free Fe-ions (e.g., from sea water) [8]. When a RED stack with conventional electrodes and NaCl as an electrode rinse solution was used, chlorine was detected in the electrode rinse solution (>100 mg within 3 minutes at 20 A/m^2). In contrast, no free chlorine could be detected (<10 mg) in the stacks with capacitive electrodes; not even after several hours of (cyclic) operation and not even in cases where pH-changes did occur.

6.4.5 Future improvement

Now that the power density obtained in CRED with capacitive electrodes is similar to that of RED, the electrical resistance of the membrane cells becomes limiting. Even when using 5 membrane cells only, the electrical resistance of all membrane cells together is experimentally determined at approximately 140 Ω·cm^2, while the capacitive electrodes contribute for only 13 Ω·cm^2 to the electrical resistance. When very thin membranes and thin feedwater compartments would be applied, the power obtained in RED can be more than doubled compared to the values that are obtained in this research [7]. The same improvement can be obtained for CRED with such a membrane cell design.

Apart from the options to improve the membrane cells, several options are available to tweak the power density of a CRED stack. Such strategies include e.g. optimization of the current interrupt time (stage 2 and 4), alteration of the concentration or flow rate of the electrode rinse solution and optimization of the electrode properties.

In the present work, the current interrupt time was chosen as 60 s (to monitor the OCV), while the voltage is already high enough to enable a 20 A/m^2 current density in approximately 5 s after switching the feedwater. When current is applied 5 s after switching

the feedwater, the power density would increase approximately 10% in case of the 5 cell CRED stack. This would make the power density equal to the best performing systems with conventional electrodes.

Another strategy to improve the power output by increasing the concentration of the electrode rinse solution. As an example, an electrode rinse solution of 2 M NaCl was used. The concentration of the feed waters was the same in all cases (0.508 M and 0.017 M NaCl). As a consequence, the sum of electromotive forces will remain the same; the high salinity gradient between the electrode rinse and the first compartment is balanced by the high salinity gradient in opposite direction over the last membrane. The increase in concentration of the electrode rinse solution only influences the conductivity of the electrode compartments and possibly the electrode capacity. The effect of this higher concentration and the flow rate of the electrode rinse solution on the power density are shown in Figure 6.7a. Power densities are compared to those obtained from RED stacks (Figure 6.7b) using 0.1 M $Fe(CN)_6^{3-/4-}$ and 0.085 M NaCl or 1.84 M NaCl. NaCl was added in this case to obtain the same conductivity as that of the electrode rinse in the CRED stacks.

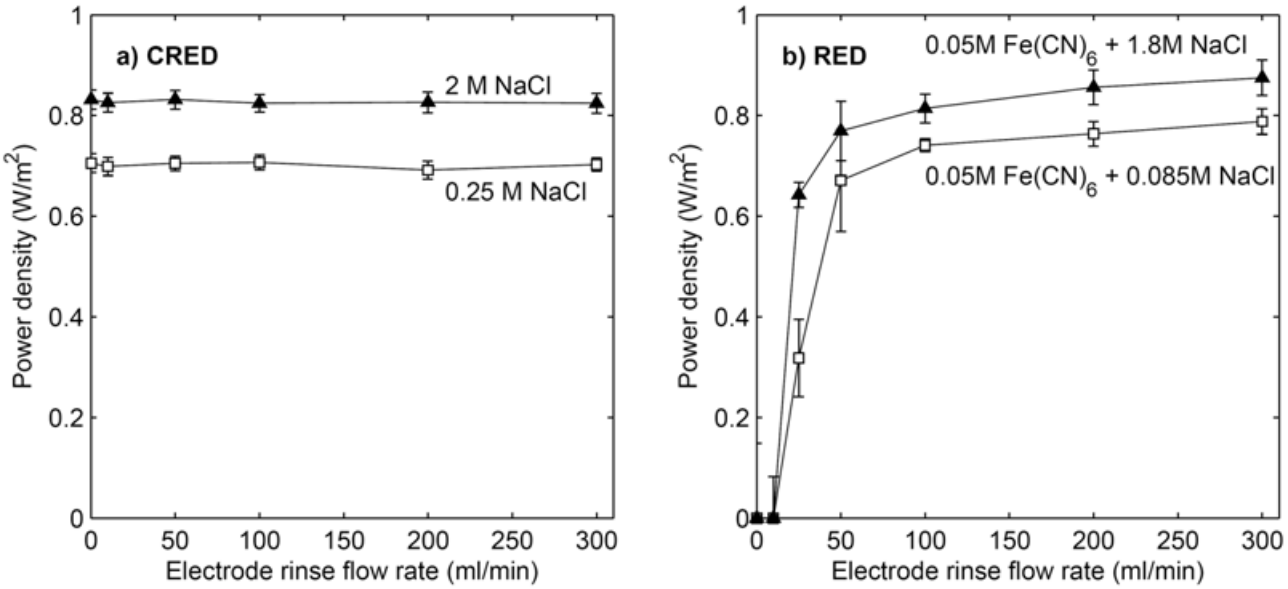

Figure 6.7: Average (gross) power density as a function of the electrode rinse flow rate measured for a) CRED stacks with an electrode rinse concentration of 0.25 M NaCl or 2 M NaCl, and b) RED stacks with 0.1 M $Fe(CN)_6^{3-/4-}$ *and either 0.085 M NaCl or 1.8 M NaCl. All stacks had 5 membrane pairs and were operated 20 A/m*^{2} *using a maximum switching interval.*

The data from Figure 6.7 show that the electrode rinse flow rate has no significant effect on the power density obtained with CRED. Even at no flow, the same power density was obtained as at high flow rate of electrode rinse solution. This indicates that the process of CRED is not limited by mass transfer in the electrode rinse compartments. These results show that a CRED system can be designed without the circulation of electrode rinse solution. This would simplify the design, as the pump and tubing infrastructure for the electrode rinse are no longer required.

The CRED system with 2 M NaCl has a clearly higher power density than the system with 0.25 M NaCl electrode rinse. The ohmic resistance of the setup is decreased by approximately 10%, which leads directly to an increase in power density of 10%. In addition, the capacitive electrodes benefit from another mechanism. The experimentally measured electrode capacitance also increases approximately 15% when the electrode rinse concentration was increased from 0.25 M to 2 M NaCl. This is in line with Gouy-Chapman-Stern (GCS) theory that predicts a higher capacitance at higher salt concentration [10]. Therefore the switching interval time can be larger when using 2 M NaCl as an electrode rinse solution, and the average power density is even more increased. The RED system with conventional electrodes is less sensitive to the concentration of NaCl in the electrode rinse solution compared to a CRED system. The increase in power density for RED stacks is only caused by the lower ohmic resistance.

A final strategy to improve the power density obtainable from CRED is to optimize the capacitive electrodes. Although the present capacitive electrodes are already high performing (a capacitance of 1.2 F/cm^2 of projected electrode area and an area resistance of only 13 $\Omega \cdot cm^2$) compared to previous research [12, 22], the thickness of the activated carbon layer and the material for the current collector can be tuned. Replacing the current collector material could reduce the electrical resistance of the contact between the current collector and the activated carbon. Replacing the Ti/Pt, for example by graphite, could reduce the contact resistance between the current collector and the activated carbon, but also reduce the costs of these electrodes drastically.

6.5 Conclusions

Capacitive reverse electrodialysis (CRED) is a newly proposed technology to generate electricity from mixing salt water and fresh water (salinity gradient energy). CRED makes use of RED technology and capacitive electrodes, to avoid the use of redox reactions at the

electrodes and obtain high power densities (i.e., power per membrane area). The obtained power density of a CRED stack is maximized when the number of cells is increased (at maximum 30 cells in this research), at current densities between 15 and 30 A/m^2. For a maximum power density, the feed waters should be switched periodically when approximately 20 kC/m^2 is transferred, which implies a switching interval time of more than 10 minutes. The obtained power densities are close to the best performing conventional electrode systems (using $Fe(CN)_6^{3-/4-}$) and yield a much higher power density compared to electrode systems that facilitate water splitting (production of H_2, O_2 and Cl_2). In addition, the electrode rinse solution does not have to be circulated in CRED, while it is required in a conventional electrode system. Our work shows that such capacitive electrodes are a high performing, clean and safe electrode system for reverse electrodialysis to generate power from the mixing of salt and fresh water.

References

1. Weinstein, J. N.; Leitz, F. B., Electric Power from Differences in Salinity: The Dialytic Battery. *Science* **1976,** *191*, (4227), 557-559.
2. Logan, B. E.; Elimelech, M., Membrane-based processes for sustainable power generation using water. *Nature* **2012,** *488*, (7411), 313-319.
3. EIA, *International energy outlook 2011*. U.S. Department of Energy: Washington D.C., **2011**; 301 p.
4. Loeb, S., Production of energy from concentrated brines by Pressure-Retarded Osmosis, I. Preliminary technical and economic correlations. *Journal of Membrane Science* **1976,** *1*, 49-63.
5. Yip, N. Y.; Tiraferri, A.; Phillip, W. A.; Schiffman, J. D.; Hoover, L. A.; Kim, Y. C.; Elimelech, M., Thin-Film Composite Pressure Retarded Osmosis Membranes for Sustainable Power Generation from Salinity Gradients. *Environmental Science & Technology* **2011,** *45*, (10), 4360-4369.
6. Gerstandt, K.; Peinemann, K. V.; Skilhagen, S. E.; Thorsen, T.; Holt, T., Membrane processes in energy supply for an osmotic power plant. *Desalination* **2008,** *224*, 64-70.
7. Vermaas, D. A.; Saakes, M.; Nijmeijer, K., Double Power Densities from Salinity Gradients at Reduced Intermembrane Distance. *Environmental Science & Technology* **2011,** *45*, (16), 7089-7095.
8. Veerman, J.; Saakes, M.; Metz, S.; Harmsen, G., Reverse electrodialysis: evaluation of suitable electrode systems. *Journal of Applied Electrochemistry* **2010,** *40*, (8), 1461-1474.
9. Liu, F.; Schaetzle, O.; Sales, B. B.; Saakes, M.; Buisman, C.; Hamelers, H. V. M., Effect of additional charging and current density on the performance of Capacitive energy extraction based on Donnan Potential. *Energy & Environmental Science* **2012,** *5*, 8642-8650.
10. Brogioli, D.; Zhao, R.; Biesheuvel, P. M., A prototype cell for extracting energy from a water salinity difference by means of double layer expansion in nanoporous carbon electrodes. *Energy & Environmental Science* **2011,** *4*, (3), 772-777.
11. Brogioli, D., Extracting Renewable Energy from a Salinity Difference Using a Capacitor. *Physical Review Letters* **2009,** *058501*, 1-4.
12. Sales, B. B.; Saakes, M.; Post, J. W.; Buisman, C. J. N.; Biesheuvel, P. M.; Hamelers, H. V. M., Direct Power Production from a Water Salinity Difference in a Membrane-Modified Supercapacitor Flow Cell. *Environmental Science & Technology* **2010,** *44*, (14), 5661–5665.

13. Boon, N.; van Roij, R., 'Blue energy' from ion adsorption and electrode charging in sea and river water. *Molecular Physics* **2011,** *109*, (7-10), 1229-1241.

14. Vermaas, D. A.; Guler, E.; Saakes, M.; Nijmeijer, K., Theoretical power density from salinity gradients using reverse electrodialysis. *Energy Procedia* **2012,** *20*, 170-184.

15. Ramon, G. Z.; Feinberg, B. J.; Hoek, E. M. V., Membrane-based production of salinity-gradient power. *Energy & Environmental Science* **2011,** *4*, (11), 4423-4434.

16. Post, J. W.; Goeting, C. H.; Valk, J.; Goinga, S.; Veerman, J.; Hack, P. J. F. M., Towards implementation of reverse electrodialysis for power generation from salinity gradients. *Desalination and water treatment* **2010,** *16*, 182-193.

17. Biesheuvel, P. M., Thermodynamic cycle analysis for capacitive deionization. *Journal of Colloid and Interface Science* **2009,** *332*, (1), 258-264.

18. Post, J. W.; Hamelers, H. V. M.; Buisman, C. J. N., Energy Recovery from Controlled Mixing Salt and Fresh Water with a Reverse Electrodialysis System. *Environmental Science & Technology* **2008,** *42*, (15), 5785-5790.

19. Lee, J.-H.; Bae, W.-S.; Choi, J.-H., Electrode reactions and adsorption/desorption performance related to the applied potential in a capacitive deionization process. *Desalination* **2010,** *258*, (1-3), 159-163.

20. Veerman, J.; Post, J. W.; Saakes, M.; Metz, S. J.; Harmsen, G. J., Reducing power losses caused by ionic shortcut currents in reverse electrodialysis stacks by a validated model. *Journal of Membrane Science* **2008,** *310*, (1-2), 418-430.

21. Burheim, O. S.; Seland, F.; Pharoah, J. G.; Kjelstrup, S., Improved electrode systems for reverse electro-dialysis and electro-dialysis. *Desalination* **2012,** *285*, (0), 147–152.

22. Simon, P.; Gogotsi, Y., Materials for electrochemical capacitors. *Nat Mater* **2008,** *7*, (11), 845-854.

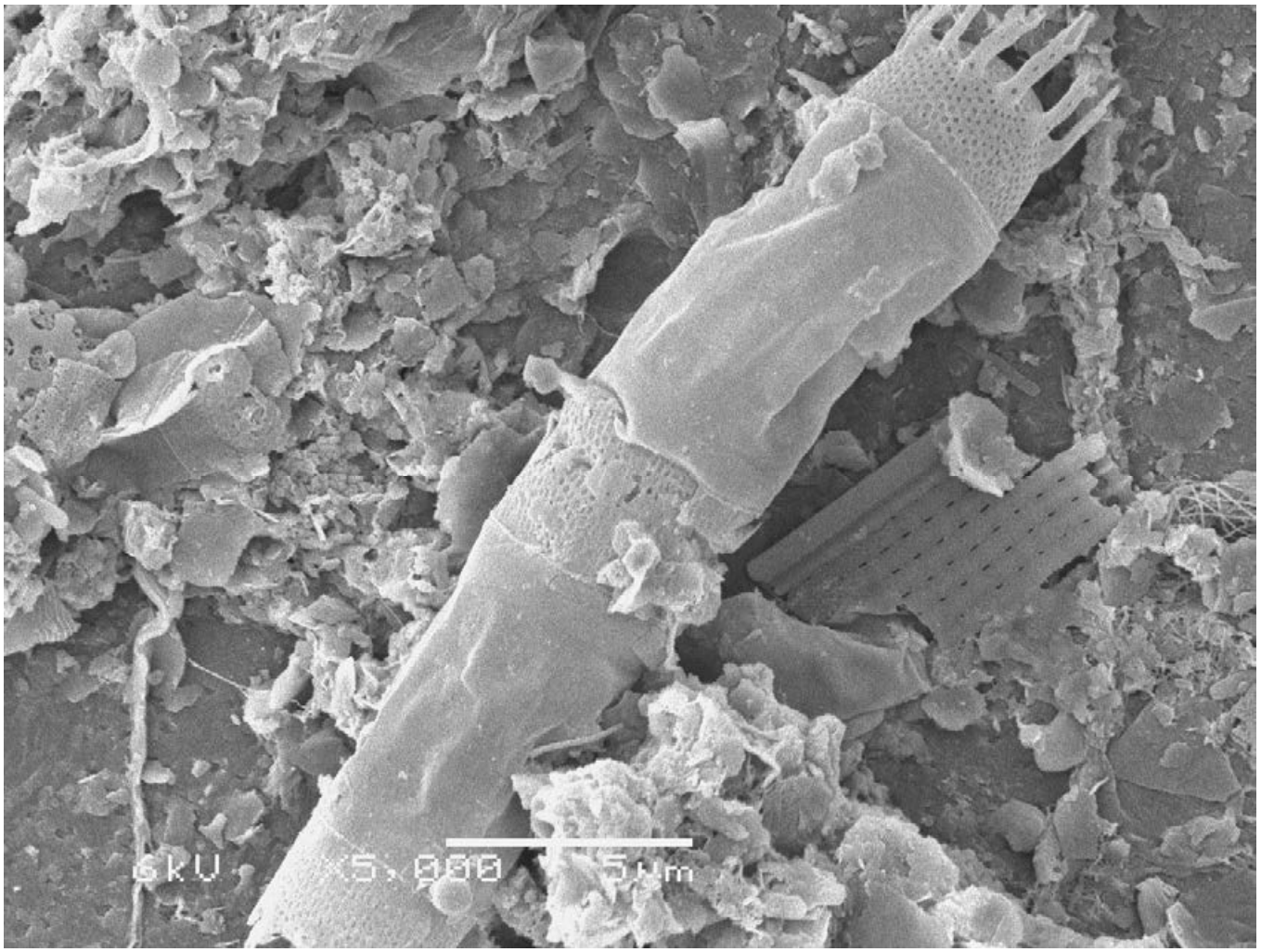
6kV X5,000 5μm

Chapter 7

Fouling in reverse electrodialysis under natural conditions

Abstract

Renewable energy can be generated from mixing salt water and fresh water in reverse electrodialysis. The potential for energy generation from mixing seawater and river water is enormous. To investigate the effect of fouling when such natural feed waters are used, the performance of three different setups for reverse electrodialysis was evaluated for 25 days using seawater and river water as feedwater, with no other (pre-)treatment than a 20 μm filter. Due to the absence of other anti-fouling treatments, a mixture of fouling is observed on the membranes, composed of remnants of diatoms, clay minerals, organic fouling and scaling. The fouling type was dependent on the different membrane types. The anion exchange membranes attract mainly diatoms and clay minerals, whereas scaling was only found on the cation exchange membranes. As a reference, plastic sheets without charge were used, which results in significant cleaner surfaces. Additionally, the setups without spacers in between the membranes (i.e., profiled membranes) appear significant less sensitive to fouling. This was quantified by the pressure drop over the feed waters and the power density obtained from the membrane piles. The pressure drop increases four times slower and the power density remains higher when profiled membranes are use instead of flat membranes with spacers. Although the obtained power density reduced with approximately 40% in the first day under these conditions, caused by organic fouling, several strategies are available to maintain a high power output using reverse electrodialysis.

This chapter has been published as

David A. Vermaas, Damnearn Kunteng, Michel Saakes and Kitty Nijmeijer, Fouling in reverse electrodialysis under natural conditions, *Water Research*, **2013,** *47* (3), 1289-1298

7.1 Introduction

Salinity gradient power is a potentially large source for electricity generation. Energy can be extracted from mixing (salt) sea water and (fresh) river water, due to the increase in entropy. Considering the total global discharge of rivers to the sea, a theoretical power production of 2.4 TW is estimated [1], which is even larger than the present electricity consumption [2].

A technology to capture the power from salinity gradients is reverse electrodialysis (RED) [3, 4]. In reverse electrodialysis, an electrical potential difference is created when waters with different salinity are on either side of a membrane that allows the passage of only anions (anion exchange membrane, AEM) or only cations (cation exchange membrane, CEM). The potential difference, as generated by the salinity difference, generates an electrical current using electrodes and a reversible redox reaction. The electrical current can be used to power an electrical device. This process is illustrated in Figure 7.1.

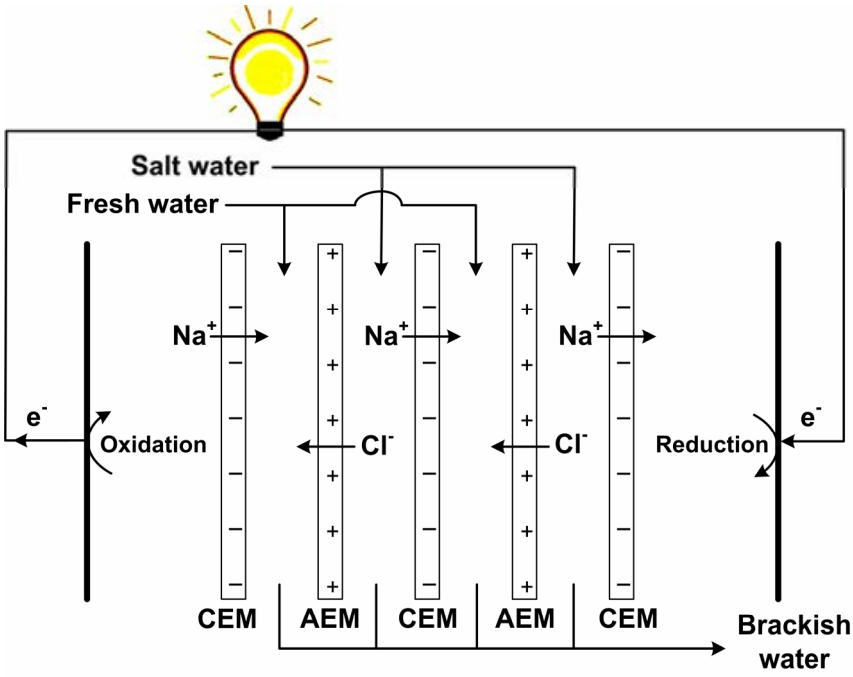

Figure 7.1: Principle of reverse electrodialysis (RED). The salt water and fresh water flow alternately along cation exchange membranes (CEM) and anion exchange membranes (AEM). A (reversible) redox reaction (in an electrolyte that can be circulated) converts the ionic current into an electrical current.

As an alternative technology, power from salinity gradients can be captured with pressure retarded osmosis (PRO) [5, 6]. Pressure retarded osmosis relies on water transport through semi-permeable membranes, which creates a pressure difference and generates a turbine.

Regarding the fouling tendency, RED is expected less sensitive to clogging or fouling than PRO [7-9], as in RED only ions pass the membranes, while water and additional colloids are retained the membrane and only flow along the membrane.

However, although the fouling issue in RED is expected to be less pronounced than in PRO, fouling may still be a problem. Previous research on fouling in RED is very limited. Post [10] studied biological fouling and the effect of different strategies to prevent fouling and a subsequent increase in pressure drop due to this biofouling (e.g., reversing flow direction and switching feed waters), under accelerated biofouling conditions in a laboratory experiment. He concluded that the biofouling process could be slowed down when the feedwater was interchanged and reversed in flow direction periodically, but fouling nevertheless occurred under the applied accelerated biofouling conditions. Only a setup without spacers did not show a significant pressure increase for 14 days under accelerated fouling conditions [10]. Also in other membrane technologies, such as reverse osmosis (RO), fouling is mostly concentrated on the feedwater spacers [11]. A RED setup using profiled membranes instead of a design with spacers was recently presented [12]. Such a spacerless setup is expected less sensitive to fouling.

The effects of other fouling types in RED, such as colloidal fouling and fouling with organic substances, were not studied before. The individual fouling types in electrodialysis are investigated in larger extent [13-18], especially for anion exchange membranes, as they are most sensitive for organic and colloidal fouling [13, 16-18]. These fouling types are generally composed of large negatively charged molecules, and therefore attracted by the surface charge of the anion exchange membranes. All common fouling types in ED (organic, colloidal, biofouling, scaling) can be reduced by switching the electrical current direction frequently, for example by applying short electrical pulses [16, 19] or by switching the feed waters [15, 20] (electrodialysis reversal, EDR). However, the fouling behavior in ED and EDR is expected to be different than that in RED. In ED and EDR, the process is opposite (concentrating the salt solution increases the risk of scaling), the typical intermembrane distance and current density are much larger in ED / EDR and only one feedwater type is used as inflow in that case.

Fouling studies for RED (but also for ED) under environmental conditions are sparse. Kjelstrup Ratjke *et al.* [21] studied the power density obtained from a RED stack with spacers for 180 days, fed with natural sea water and artificial river water. They concluded that the power density was decreased by 67% after 180 days of operation, due to biological

fouling [21]. The pressure drop between the inlet and outlet of the feedwater (which is a measure for the occurrence of fouling) was not reported. To our best knowledge, no research has been published so far, in which seawater and river water both from natural sources was used.

This research presents, for the first time, the fouling behavior of RED stacks that are operated for 25 days without cleaning and supplied by natural seawater and river water. The goal of this research is to characterize the typical fouling types in RED and the effect on the obtained power density and the pressure drop for pumping the feed waters. This research aims to indicate what fouling type limits the performance of RED, rather than focusing on a single controlled type of fouling. After a brief review of the expected influences of fouling in RED, an experiment is described and presented, where three different stack designs were fed by natural seawater and river water. One stack contained flat cation and anion exchange membranes with spacers in between, a second stack was spacerless using profiled cation and anion exchange membranes, and a third stack was spacerless using profiled (non-conductive and non-charged) plastic sheets, to show the effect of membrane charge. The differences in fouling behavior observed experimentally also show the directions for effective anti-fouling strategies.

7.2 Theory

To distinguish the effects of fouling and the effects that can be due to this specific location and this specific experimental setup (such as salinity, temperature, flow rate), the performance of the RED stacks is compared to theoretical values that would be expected when no fouling would occur. These expected theoretical equivalents can be deduced from laboratory experiments as published in previous research [4, 12]. Based on these experimental data, an analytical model was developed for realistic estimates of the open circuit voltage (OCV), resistance, power and pressure drop [22]. A brief description of this analytical model is given here.

7.2.1 Open circuit voltage

The theoretical voltage that is created by the salinity difference over an ion exchange membrane is given by the Nernst equation. Corrected for the apparent mean permselectivity α of the ion exchange membranes, the voltage over N_m membranes can be calculated as:

$$E_{OCV} = \alpha \cdot N_m \cdot \frac{R \cdot T}{z \cdot F} \cdot \ln\left(\frac{\gamma_{sea} \cdot c_{sea}}{\gamma_{river} \cdot c_{river}}\right) \quad \text{(eq. 7.1)}$$

In which R is the universal gas constant (8.314 J/(mol·K)), T is the absolute temperature (K), F is the Faraday constant (96485 C/mol), z is the valence of the ion species (-), γ is the activity coefficient of the salt species (-) and c is the concentration of the salt (mol/liter). The subscripts *sea* and *river* indicate seawater or river water, respectively.

Previous research showed that the apparent permselectivity is highest for membranes that have a high charge density (i.e., fixed charge in the membrane per volume of absorbed water) [23]. Dissolved charged foulants, such as organic fouling, can counterbalance the fixed charge groups in the membrane, and reduce the apparent membrane permselectivity, which is observed before in electrodialysis [24].

7.2.2 Electrical resistance

The electrical resistance of a RED stack is composed of the ohmic resistance (dependent on the conductivity of the membranes and feed waters) and a non-ohmic resistance. The non-ohmic resistance slowly develops when an electrical current is set and the ions are transferred from the seawater to the river water side. The ion transfer reduces the salinity difference and as a consequence reduces the electromotive force, which can be interpreted as a (non-ohmic) resistance when divided by the electrical current. The total electrical resistance of a RED stack is the sum of the described components (all in $\Omega \cdot cm^2$):

$$R_{total} = R_{ohmic} + R_{non-ohmic} \quad \text{(eq. 7.2)}$$

The experiments can reveal both R_{ohmic} (from the instantaneous voltage drop at a current interruption) and the sum of all components R_{total} (from the stationary voltages) directly [4]. The resistances in eq. 7.2 can also be estimated theoretically, based on the membrane specifications, water conductivity, water temperature, flow rate and cell dimensions [22].

The resistance increases when membranes are fouled, due to two mechanisms. First, dissolved charged foulants, such as organic fouling, can counterbalance charged groups in the membrane, and therefore increase the ohmic resistance of the membrane [17, 18, 24]. Anion exchange membranes (AEMs) are more sensitive for this type of fouling than cation exchange membranes (CEMs) [13, 17, 18] because organic salts are often composed of a large anion (‘poisoning’ the AEM) and a small cation (which can pass the CEM). Additionally, research in ED showed that colloids adhered to the membranes increase the

thickness of the concentration boundary layer, and therefore increase the non-ohmic resistance [13].

7.2.3 Power density

The power density that is generated by a RED stack equals the product of the voltage and the electrical current, divided by the membrane area. The current can be chosen, based on the external load that is connected. A small current yields a high voltage and vice versa. The maximum obtainable power density (W/m^2) can be calculated by [4]:

$$P = \frac{E_{OCV}{}^2}{4 \cdot N_m \cdot R_{total}} \qquad \text{(eq. 7.3)}$$

A part of the produced energy is consumed by pumping the feedwater through the stack. When this part is subtracted, the net power density is obtained, given by:

$$P_{net} = \frac{E_{OCV}{}^2}{4 \cdot N_m \cdot R_{total}} - \frac{\Delta p_{sea} \cdot \Phi_{sea} + \Delta p_{river} \cdot \Phi_{river}}{N_m \cdot A} \qquad \text{(eq. 7.4)}$$

in which Δp is the pressure drop (Pa) over the inlet and outlet of the feedwater, Φ is the flow rate (m^3/s) of the feedwater and A is the area of one membrane (m^2).

Obviously, the presence of colloidal fouling and biofouling will increase the pressure drop over the feedwater channels [10], and therefore reduce the net power density.

7.3 Experimental setup

Three stacks were built, each containing 11 membranes that create 5 compartments for seawater and 5 compartments for river water. The first stack was built with flat ion exchange membranes and spacers in between. The second stack was spacerless, using profiled ion exchange membranes [12]. The third stack was also spacerless, but used profiled plastic sheets that are not ion-conductive. This enables to test the effect of spacers on fouling, but also to test the effect of membrane surface charge on fouling. The specifications of these stacks are given in Table 7.1.

The electrode dimensions and the effective membrane area of each membrane was 10x10 cm^2. The profiled membranes and the profiled plastic sheets were created by thermal pressing for 10 minutes at 140ºC and 200 bar. The resulting profiled membranes and profiled plastics had ridge-structured corrugations of 200 μm wide in a parallel orientation at every 1 mm. More details, such as the geometry of the profiled membranes and the spacers, are described in previous research [12]. The stacks were assembled and the membranes were

brought in equilibrium for 24 hours in artificial seawater (0.5 M NaCl) and river water (0.017 M NaCl) before use.

Table 7.1: Specifications of the 3 RED stacks as used in this research.

	Stack 1	Stack 2	Stack 3
Membrane material	Ralex CMH/AMH	Ralex CMH/AMH	LD-PE
Membrane surface	Flat	Profiled	Profiled
Surface contact angle	n/a	58 ± 3 º	98 ± 12 º
Compartment support	Spacer (Sefar Nitex 07-300/46)	Membrane profile	Plastic profile
Intermembrane distance	240 ± 10 μm	240 ± 10 μm	200 ± 10 μm

All experiments were conducted at the Wetsalt demo site in Harlingen, The Netherlands, during summer, from August 9th to September 2nd 2011. All stacks were fed continuously with natural seawater and natural fresh water, at a flow rate of 100 ml/min (unless stated otherwise). Fresh water was obtained from a nearby canal (Van Harinxmakanaal) and salt water was obtained from the nearby harbor in the Wadden Sea. The water was pre-filtered through a series of microfilters, in which the final filter had a median diameter of 20 μm. No additional fouling prevention was applied. The feedwater was not switched, nor reversed.

The pressure difference over the inlet and outlet of each feedwater channel (for each stack) was measured with six differential pressure meters (Endress+Hauser, Deltabar S, Germany). The pressure differences were recorded every 30 s in a data logger (Endress+Hauser, Ecograph T, Germany).

The conductivity and temperature of the influent and effluent were monitored (ProMinent, Dulcometer, Germany) and recorded every 30 s (LabView 7.1, National Instruments, United States). Samples of the influent were taken three times during the experiment and the chemical composition of the water was analyzed using ion chromatography (IC) and inductively coupled plasma (ICP).

The OCV, the (ohmic and total) electrical resistance and the power density of the stack with spacers and the stack with profiled membranes was measured three times a week, each time in duplicate (or more), using chronopotentiometry (Iviumstat, Ivium Technologies, The Netherlands). To facilitate an electrical current, the electrodes (Ti mesh, coated with Ir/Ru)

were supplied with an electrode rinse solution of 0.25 M NaCl. Two reference electrodes were installed at each stack, one connected to each electrode compartment. Hence, the voltage over the membrane stack only was measured, excluding the overpotential of the electrodes.

At the end of the experiment, the stacks were opened and fouled membrane samples were analyzed using a scanning electron microscope (SEM), Energy Dispersive X-ray spectroscopy (EDX) and X-Ray diffraction (XRD).

7.4 Results

To show the effect of fouling in this experiment, the feedwater properties are shown first, followed by a visual and microscope inspection of the fouled samples. Later, the effect of the fouling on the performance during the experiments is shown, quantified by the pressure drop, obtained power density, apparent permselectivity and ohmic resistance of the reverse electrodialysis stacks.

7.4.1 Feedwater properties and effect of multivalent ions

The feedwater is characterized by the salinity, temperature, ion composition and total organic carbon (TOC) as given in Table 7.2. The standard deviations indicate the temporal variability of each parameter. The fluctuations in salinity and temperature emphasize that the actually measured power density must be normalized to theoretical equivalents (eq. 7.1 - 7.3) in order to distinguish the effects of fouling and the effects of changes in salinity and temperature. Although the relatively low salinity of the seawater (Wadden Sea) will yield low absolute values for the power density compared to most laboratory research [4, 8, 12], the normalized values will be representative for a wider range of feedwater concentrations.

Table 7.2: Salinity, temperature and composition of the natural seawater and river water that were used for this research.

	Salinity (mM)	Temperature (ºC)	Cations (mM)	Anions (mM)	Other (mg/L)
Seawater	280 ± 10	19 ± 2	Na^+: 202 ± 10 Ca^{2+}: 7 ± 1 Mg^{2+}: 28 ± 2	Cl^-: 242 ± 10 SO_4^{2-}: 11 ± 0	PO_4^{3-}: 2.8 ± 0.2 TOC: 10 ± 5
River water	38 ± 5	19 ± 3	Na^+: 38.7 ± 3.0 Ca^{2+}: 2.2 ± 0.9 Mg^{2+}: 3.3 ± 0.9	Cl^-: 43.9 ± 2.5 SO_4^{2-}: 2.3 ± 0.1	PO_4^{3-}: <0.5 ± 0.1 TOC: 18 ± 6

As typically for natural seawater and river water, the species Na^+ and Cl^- have the largest concentrations in both streams. Nevertheless, the presence of the multivalent ions (Ca^{2+}, Mg^{2+}, SO_4^{2-}), in approximately the same relative amount in both feed waters, will significantly reduce the produced voltage [25]. When comparing solutions with monovalent ions only to solutions with multivalent ions only, the salinity gradient in monovalent ions would produce twice the voltage that multivalent ions would generate (eq. 7.1). A mixture of monovalent and multivalent ions gives a more complex situation. Because the voltage generated by the salinity gradient of the monovalent ions is larger than the voltage that follows from the salinity gradient of the multivalent ions, two monovalent ions are exchanged for one multivalent ion to restore the inequality in the voltages that follows from the salinity gradients of monovalent and multivalent ions. In other words, a divalent ion can be drawn back to the saline compartment and exchanged for two monovalent ions [25], without a net electrical current. Consequently, the salinity gradient for monovalent ions will decrease and the produced voltage will decrease. Therefore, the addition of multivalent ions to a solution with monovalent ions works counterproductive for reverse electrodialysis. Based on the concentrations in Table 7.2, and assuming that multivalent ions exchange for monovalent ions until their corresponding voltages are balanced, the presence of multivalent ions decreases the produced voltage by approximately 7%. In addition, the membrane selectivity is lower for multivalent ions, but this effect is insignificant for the voltage when using homogeneous membranes.

In addition, the multivalent ions have a minor effect on the electrical resistance. The resistance of the water compartments is decreased by the presence of multivalent ions on one hand, but the electrical resistance of the membranes increases, compared to monovalent ions with the same concentration [25]. As a consequence, the total resistance can increase or decrease due to the presence of multivalent ions, dependent on the contributions of the feed waters and membranes in the total stack resistance.

7.4.2 Visual and microscopic inspection

After 25 days of operation, the membranes and spacers of all stacks are investigated visually and by SEM. The anion exchange membranes (AEMs) are colored brown-red (originally beige), while the cation exchange membranes (CEMs) and the profiled plastics preserve their original beige color. The brown-red color of the AEMs indicates that negatively charged molecules, such as humic acids, are absorbed on the AEMs.

In addition to the color of the membrane, a grey-brown material filled up a part of the porous spacers (both for seawater and river water) and the channels in the profiled AEMs. The distribution of this fouling is not equal, but concentrates at more or less random locations over the spacer or membrane. The profiled CEMs and the profiled plastics are covered with less of this grey-brown deposition, except for the part of the membranes close to the inlet and outlet of the feedwater. The profiled plastics in contact with the sea water are optically least fouled; more than 95% of the area of their sheets are visually clean.

The fouled membrane / plastic samples from all stacks are inspected with SEM and representative images are shown in Figure 7.2. These images show that all samples, except for the profiled plastic in seawater, are covered with a mixture of deposits. Remnants of diatoms are found, most densely present at the AEMs in river water samples. The river water is probably the largest source of these remnants of diatoms, and these diatoms are attracted to the AEMs because of the negative charge on the silica skeleton of the diatoms [26]. Apart from a few green algae and bacteria (at the profiled plastic in seawater), no intact organisms are observed.

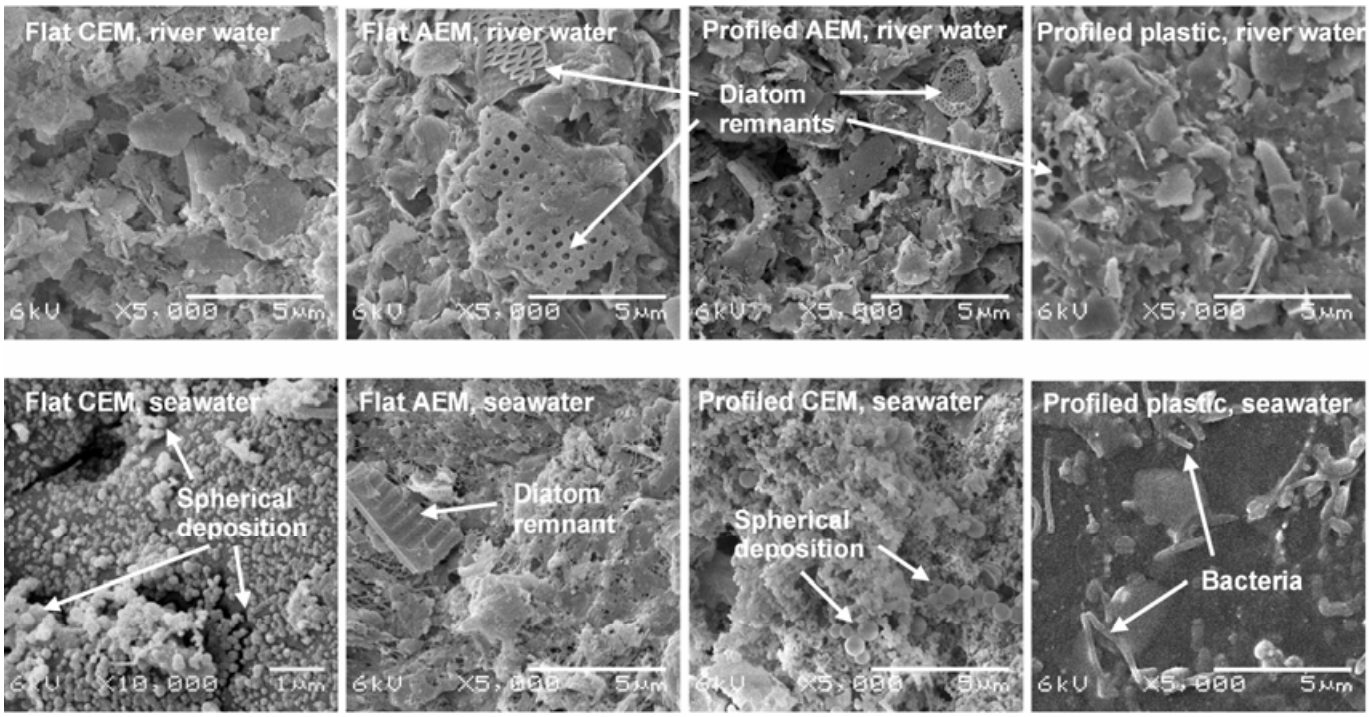

Figure 7.2: SEM images of cation and anion exchange membranes (CEMs and AEMs) and profiled plastics. The images in the upper row were in contact with river water, whereas the images in the lower row were in contact with seawater. The four images at the left side are obtained from flat membranes (stack 1, river water side and seawater side), the other images are obtained from profiled membranes (stack 2) and profiled plastics (stack 3). Most images were saved at a magnification of 5000x; only the flat CEM in contact with seawater was saved at 10000x, to see the spherical deposition. Remnants of diatoms, bacteria and spherical deposition are indicated by arrows.

The CEMs in seawater show spherical structures, most pronounced at the profiled CEM in seawater, possibly growing mineral crystals. The remaining part of the deposit comprises unorganized fragments of typically 1 μm size. This was observed for both the profiled membranes and the flat membranes. The composition of these fragments and crystals is investigated using Energy Dispersive X-ray spectroscopy (EDX) for all samples. The elements that appear in highest quantities in the samples from the flat membranes of stack 1 (both seawater and river water side) are listed in Table 7.3.

Table 7.3: EDX of CEM and AEM (seawater and river water side) from the stack with spacers (stack 1), in atom percentage. The composition of the fouling in stack 2 is similar. The EDX-results of the samples from stack 3 are dominated by the carbon content of the plastic, because the fouling layer was insufficient to cover the plastic polymer fully. The values with standard deviation are measured in triplicate, the other values are measured once.

	Flat CEM (stack 1), seawater side	Flat CEM (stack 1), river water side	Flat AEM (stack 1), seawater side	Flat AEM (stack 1), river water side
Carbon (%)	42 ± 28	22	45	51 ± 2
Oxygen (%)	36 ± 18	53	35	31 ± 1
Silicon (%)	4 ± 1	6	7	8 ± 1
Potassium (%)	0 ± 0	1	1	1 ± 0
Calcium (%)	6 ± 3	4	1	0 ± 0
Aluminum (%)	1 ± 0	4	2	3 ± 0
Phosphorus (%)	7 ± 4	5	2	1 ± 0

The relatively high carbon content in the EDX-results is the result of the polymer structure of the membrane, which contains significant amounts of carbon. The higher standard deviation in carbon content for the CEMs is because the fouling layer is thinner and sometimes does not cover the full area in case of CEMs. The concentration of calcium and phosphorus are typically higher according to the EDX-results (Table 7.3) on the cation exchange membranes at the seawater side, especially when the image was zoomed to the spherical deposition in this fouling layer (Figure 7.2, middle images at lower row). Calciumphosphates can be precipitated as a consequence of increased concentrations due to the exchange of multivalent ions for monovalent substitutes. This ion exchange causes a

higher concentration of multivalent ions (such as calcium and phosphate) in the seawater compartment. This may be more pronounced visible at the CEM than at the AEM, because the fouling in the AEM is dominated by other colloids. In electrodialysis, scaling is also observed more pronounced at CEMs than at AEMs [13].

The fouling layer at the anion exchange membranes shows higher contents of Si and O than at the cation exchange membranes (Table 7.3), indicating silica components. To distinguish whether this silica originates from the diatoms or from non-organic substances (e.g., clay minerals), XRD was performed. Some samples show hardly any peaks in the XRD-spectrum, while other samples show sharp peaks which are most pronounced at twice the diffraction angle (2θ) of 26.8, 31.8, 35.0, 45.6, and 56.6 degrees. The peaks at 26.8, 35.0 and 45.6 degrees correspond to the clay mineral muscovite, composed of $KAl_2(Si_3Al)O_{10}(OH)_2$ [27]. This corresponds to the EDX-results qualitatively, where the contents of aluminum and potassium are significantly higher at AEMs than at CEMs. However, the ratio between aluminum, silicon and oxygen from Table 7.3 does not match the ratio of the elements in muscovite. The content of silicon is relatively higher. Moreover, some samples did not show these peaks. In conclusion, the fouling layer can be considered as a mixture of clay minerals (e.g., muscovite) and amorphous silica from diatoms.

Although this specific clay mineral is dependent on the exact feedwater content, the accumulation of clay minerals and diatoms to the AEMs is expected in general, due to the net negative charge on these particles. Both the mineral muscovite and the silica shell of diatoms carry a net negative charge, which explains their presence at the AEMs and not at the CEMs. Similar observations are done in electrodialysis [13, 16].

The rather clean plastic sheets from stack 3 show that the charge of the membrane is important in attracting fouling. Moreover, the non-conductive plastic sheets from stack 3 disable ion exchange, and therefore the scaling as seen on the CEMs is not present on the plastic sheets.

7.4.3 Pressure drop

Time series for the pressure drop over the inlet and outlet of the feed waters, for all three stacks, are presented in Figure 7.3.

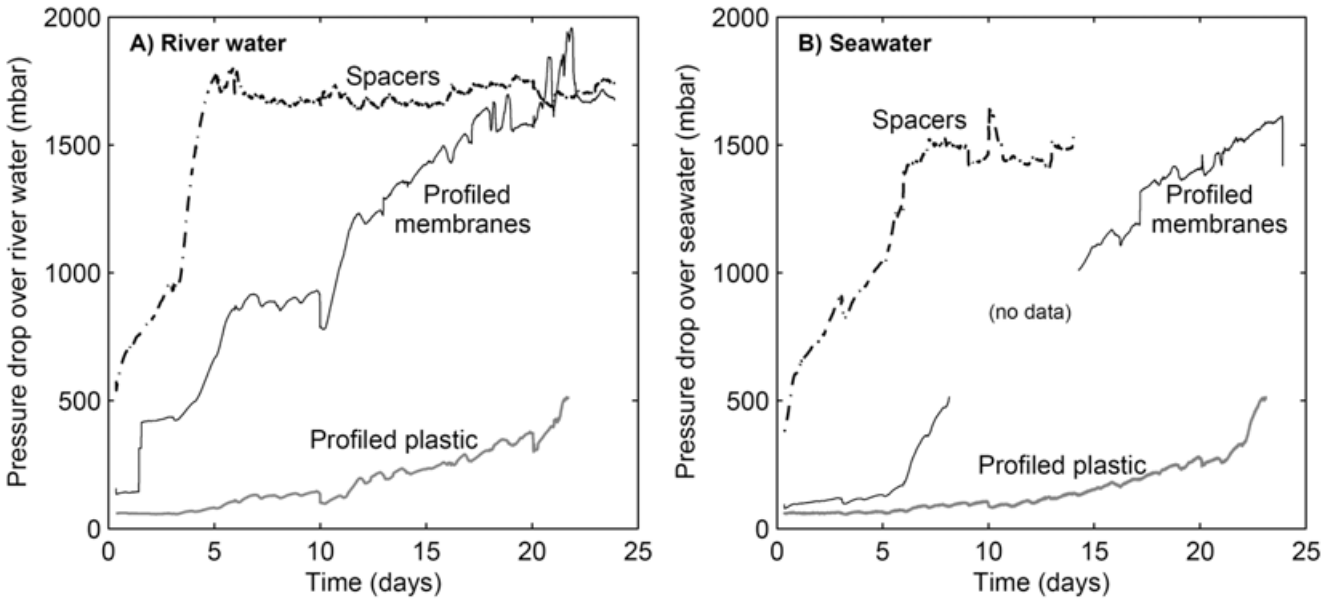

Figure 7.3: Pressure drop over the river water (A) and over the seawater (B) compartments, plotted against the time after the start of the experiment. A part of the series for the pressure drop over the seawater is not recorded, because the pressure meter that was used for profiled membranes was out of range. The pressure meter for the stack with spacers is used for the stack with profiled membranes from day 14 on.

The pressure drop in the stack with spacers increased rapidly to the maximum value that the feedwater pumps could produce (~ 1.5 bar). Because the pumps could not produce an even higher pressure on the feedwater, the pressure for the stack with spacers remained at its maximum value, but the flow rate for the stack with spacers slowly decreased after 5 days, to only 10% of its original value after 25 days.

For the stack with profiled membranes, the pressure drop increased much slower than for the stack with spacers. The pressure drop increased to 1.5 bar in approximately 20 days after the start of the experiment (Figure 7.3). The slower increase in pressure in the stack with profiled membranes, compared to the stack with spacers, can be explained by the absence of woven spacer structure. The woven spacer structure, with its crosswise filaments and knits, leaves only small openings for the feedwater flow and creates regions with wakes. Colloids are easily trapped in the small openings, which increase the pressure drop in the stack with spacers. The smooth, parallel channels that are created by the profiled membrane give less opportunity for colloids to attach, and consequently resulting in a less steep increase of the pressure drop.

The pressure drop over the feedwater in the stack with profiled plastic increased even slower; the pressure drop increased to 500 mbar after 23 days (Figure 7.3). As shown in Figure 7.2, the uncharged plastic sheets did not attract (charged) colloids and therefore the pressure drop remains lowest in the stack with profiled plastic.

The pressure drop in the stack with profiled plastic was also lowest from the start of the experiment, although the intermembrane distance was slightly smaller than for the other two stacks. The hydrophobic property (Table 7.1) of the uncharged plastic may cause a slip of the hydrodynamic boundary layer of the feedwater, whereas the water flow over the hydrophilic membranes has a no-slip boundary condition. Although the hydrophobic 'membrane' surface reduces the pressure drop, it may be unfavorable for ion transport. Since the profiled plastic is non-conductive, this could not be tested in this experiment.

The pressure drop does not increase monotonically, but decreases at some days, for example at day 10 and day 16 (Figure 7.3). At these days, the 20 μm filters were changed and the pumps were stopped shortly. Although the pumps were only stopped for approximately 5 minutes, the pressure drop of the profiled membranes remained at a lower value for about 1 day. The small pressure shock, that is created by stopping and starting the pumps, clears up the colloids that block a part of the compartment. This effect is most pronounced visible for the stack with profiled membranes (Figure 7.3), because the colloids are harder to remove from the knitted structure of the spacers. This suggests that a pulsating flow, which is used as anti-fouling strategy in other applications [28], is effective to reduce the pressure drop in a stack with profiled membranes even more.

7.4.4 Power density

The apparent permselectivity, resistance, and power density were normalized using eq. 7.1 - eq. 7.4 and the actual temperature, salinity and flow rate, to account for the changes in these parameters during the experiment. In addition, assumptions are made to obtain the normalized values. The average apparent permselectivity of the Ralex membranes, using monovalent ions, is assumed 92% [12]. The presence of multivalent ions reduces the open circuit voltage by another 7%, which yields 85% of the voltage that would be obtained with perfectly selective membranes and if monovalent ions only would be present. We assume that the response time and apparent membrane selectivity for multivalent ions is similar for the membranes in this research as for homogeneous membranes [25]. The average membrane resistance of all membranes is assumed 5.5 $\Omega \cdot cm^2$ [12]. The spacer shadow effect

is modeled using a spacer mask factor of 0.5 for spacers (50% open area) [22] and 0.2 for the profiled membranes (20% of the area covered by ridges [12]). The conductivity of the feedwater compartments is corrected for the (spacer) porosity [22], which is assumed 75% for spacers and 80% for the profiled membranes (20% occupied with ridges).

The normalized power density, as function of the number of days of operation, is shown in Figure 7.4.

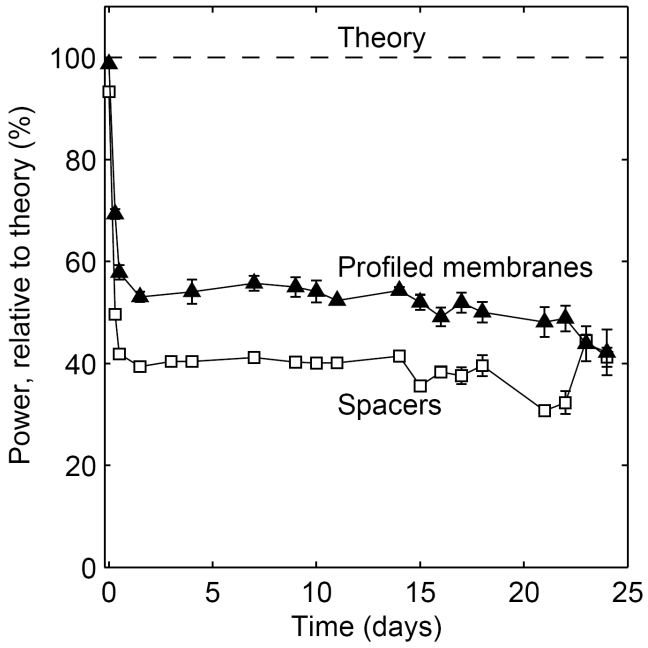

Figure 7.4: Obtained power density as function of the number of days after the start of the experiment, for a stack with spacers (open symbols) and a stack with profiled membranes (filled symbols).

The power density at the very beginning is close to the expected value (100%), but decreases by more than 40% in the first day and then remains more or less constant, with a slow decrease at the end of the experiment for the stack with profiled membranes. The stack with profiled membranes performs relatively better than the stack with spacers. In absolute values, the difference between the stacks is even larger (110-140 mW/m^2 for profiled membranes versus 50-80 mW/m^2 for the stack with spacers). The normalization of the power density, considering the lower flow rate in the stack with spacers after the fifth day, reduces the relative difference.

The decrease in power density is much faster than the increase in pressure drop (Figure 7.3), which suggests that the decrease in power density is caused by another mechanism than that for the increase in pressure drop. Also the presence of multivalent ions cannot explain the

decrease in power density, since the theoretical voltage includes the effect of multivalent ions. The decrease in power density could be caused by organic fouling, preferential channeling or a very thin layer of deposits that isolates the ion-conductive membranes. To distinguish these effects, the open circuit voltage (i.e., apparent permselectivity) and ohmic resistance are analyzed.

7.4.5 Permselectivity and resistance

The apparent permselectivity and normalized ohmic resistance, as derived from the stacks with spacers and the stack with profiled membranes, are shown in Figure 7.5.

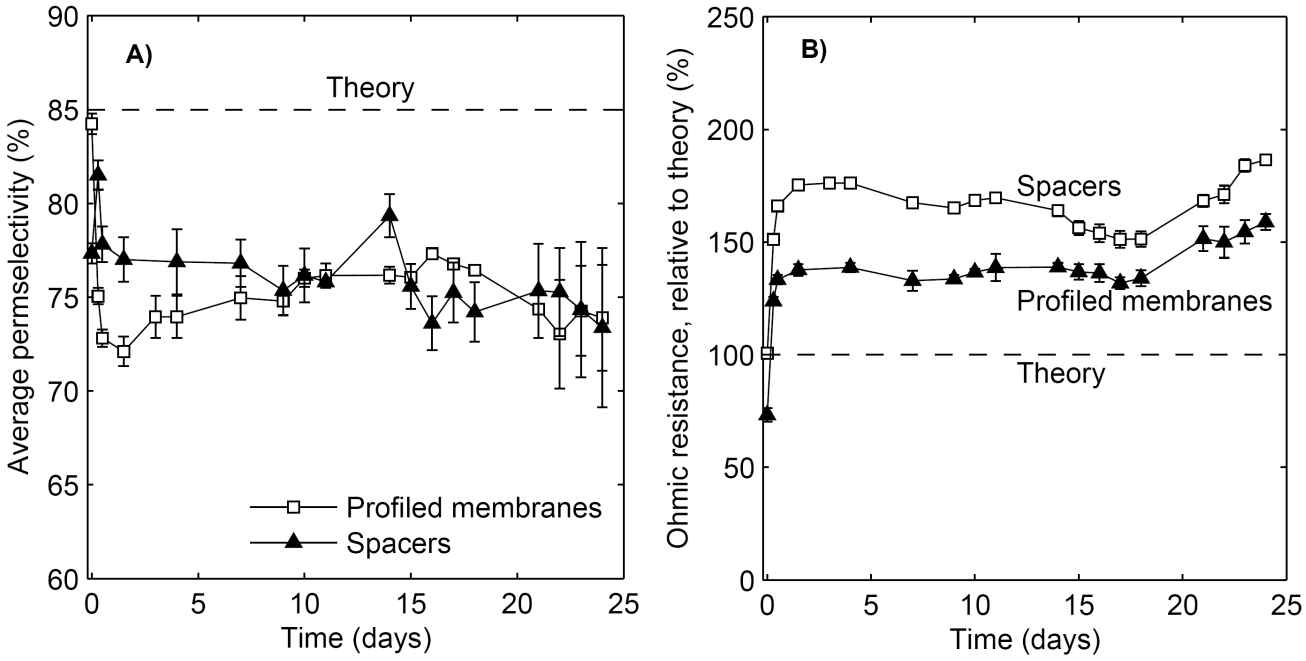

Figure 7.5: Apparent permselectivity (A) and ohmic resistance relative to the theoretical ohmic resistance (B) as function of the time after the start of the experiment.

The apparent permselectivity decreases sharply (by approximately 10%) and the electrical resistance increases rapidly (by 40% to 70%) during the first day of the experiment. Although the relative increase in the resistance is larger than the decrease in apparent permselectivity, both have a major effect on the power density, since the power density is dependent on the apparent permselectivity squared (eq. 7.3). The significant decrease in apparent permselectivity and increase in ohmic resistance suggests that organic fouling plays an important role. These charged molecules are large in comparison to ions and will be trapped in the surface layer of the ion exchange membranes where they counterbalance the effective surface charge of the membranes. As a consequence, the charge density that is

available for ion transport decreases. This causes the reduced apparent permselectivity [23, 24] and increased ohmic resistance [13, 17, 24]. Preferential channeling or a very thin layer of deposits on the membranes could show an increase in electrical resistance, but does not explain the decrease in permselectivity.

The changes in permselectivity and ohmic resistance are larger in the stack with spacers compared to the stack with profiled membranes, probably because organic fouling intensifies in the case with spacers, due to the relatively large membrane area that is covered by non-conductive spacers. The larger (local) current density increases the rate and the degree of organic fouling [18]. The same would apply for RED stacks that operate at a higher current density, for example when homogeneous membranes are used that have a lower electrical resistance than the membranes used in this research.

7.5 Possible anti-fouling strategies

The present research shows that fouling quickly reduces the power density if no anti-fouling strategies (other than a microfilter) are applied. However, several options to reduce fouling and maintain a sufficiently high power density are available. The decrease in power density occurs faster than the increase in pressure drop. This suggests that strategies against non-colloidal fouling are required to maintain a high power density. In electrodialysis, an effective strategy to reduce the effect of fouling is to periodically switch the electrical current direction, by means of switching the feed waters. For electrodialysis, this strategy is called electrodialysis reversal (EDR). This strategy appeared effective to reduce organic fouling, charged colloids [15, 20] and scaling [29] in EDR, as well as to reduce possible biofouling in RED [10]. This strategy will be most effective for a stack with profiled membranes, since this research indicated that disturbances are more effective in removing colloids for a stack with profiled membranes, compared to a stack with spacers.

Alternatively, short electrical pulses in the opposite direction reduce the effect of humate fouling in ED [16, 19], and may also be effective for maintaining a high power density is RED. As a third option, a chemically modified membrane surface, using for example high molecular mass surfactants, make the anion exchange membranes less sensitive for organic fouling [24]. These surfactants have a fixed negative charge, that repels large organic anions from the anion exchange membrane, while the selectivity and conductivity of the membrane where only slightly affected [24]. Adding a surfactant with a fixed charge opposite to the fixed charge in the membrane also creates selectivity for monovalent ions [25], in a way

similar to the commercial monovalent selective membrane Neosepta CMS, for example. The use of monovalent selective membranes reduces the exchange of multivalent ions for monovalent ions and the corresponding voltage decrease [25].

7.6 Conclusions

Reverse electrodialysis stacks are successfully used to generate electricity from mixing natural seawater and natural river water. When no anti-fouling strategies are applied (other than a 20 μm filter for the feedwater), a mixture of fouling on the membranes and spacers increases the pressure drop over the feedwater and reduces the obtained power density. When spacers are substituted for profiled membranes, the effects of fouling are reduced; the pressure drop increased four times slower and the power density remained relatively higher. Such spacerless stacks using profiled membranes are regarded less sensitive to fouling than stacks with spacers.

The charge of the membranes does strongly influence the rate and the type of fouling. At the anion exchange membranes, remnants of diatoms, clay minerals and organic fouling are observed. At cation exchange membranes, scaling of calciumphosphate is observed. Plastic sheets of non-conductive PE are least sensitive to fouling.

The decrease in obtained power density in the first day of the experiment is, most likely, caused by organic fouling. Several strategies are proposed to reduce this fouling, such as periodical switching of the current direction by means of switching the feed waters, to remain a high power density in RED.

References

1. Wick, G. L., Power from salinity gradients. *Energy* **1978,** *3*, (1), 95-100.
2. EIA, *International energy outlook 2010*. U.S. Department of Energy: Washington D.C., **2010**; 328 p.
3. Lacey, R. E., Energy by Reverse Electrodialysis. *Ocean Engineering* **1980,** *7*, (1), 1-47.
4. Vermaas, D. A.; Saakes, M.; Nijmeijer, K., Double Power Densities from Salinity Gradients at Reduced Intermembrane Distance. *Environmental Science & Technology* **2011,** *45*, (16), 7089-7095.
5. Norman, R. S., Water Salination: A Source of Energy. *Science* **1974,** *186*, (4161), 350-352.
6. Yip, N. Y.; Tiraferri, A.; Phillip, W. A.; Schiffman, J. D.; Hoover, L. A.; Kim, Y. C.; Elimelech, M., Thin-Film Composite Pressure Retarded Osmosis Membranes for Sustainable Power Generation from Salinity Gradients. *Environmental Science & Technology* **2011,** *45*, (10), 4360-4369.
7. Post, J. W.; Veerman, J.; Hamelers, H. V. M.; Euverink, G. J. W.; Metz, S. J.; Nijmeijer, K.; Buisman, C. J. N., Salinity-gradient power: Evaluation of pressure-retarded osmosis and reverse electrodialysis. *Journal of Membrane Science* **2007,** *288*, (1-2), 218-230.
8. Ramon, G. Z.; Feinberg, B. J.; Hoek, E. M. V., Membrane-based production of salinity-gradient power. *Energy & Environmental Science* **2011,** *4*, (11), 4423-4434.

9. She, Q.; Jin, X.; Li, Q.; Tang, C. Y., Relating reverse and forward solute diffusion to membrane fouling in osmotically driven membrane processes. *Water Research* **2012,** *46*, (7), 2478-2486.
10. Post, J. W. Blue Energy: electricity production from salinity gradients by reverse electrodialysis. PhD thesis Wageningen University, **2009**.
11. Vrouwenvelder, J. S.; Schulenburg, D. A. G. v. d.; Kruithof, J. C.; Johns, M. L.; Loosdrecht, M. C. M. v., Biofouling of spiral-wound nanofiltration and reverse osmosis membranes: A feed spacer problem. *Water Research* **2009,** *43*, (3), 583-594.
12. Vermaas, D. A.; Saakes, M.; Nijmeijer, K., Power generation using profiled membranes in reverse electrodialysis. *Journal of Membrane Science* **2011,** *385-386*, (0), 234-242.
13. Korngold, E.; de Körösy, F.; Rahav, R.; Taboch, M. F., Fouling of anionselective membranes in electrodialysis. *Desalination* **1970,** *8*, (2), 195-220.
14. Kim, T.; Kang, J.; Lee, J.-H.; Yoon, J., Influence of attached bacteria and biofilm on double-layer capacitance during biofilm monitoring by electrochemical impedance spectroscopy. *Water Research* **2011,** *45*, (15), 4615-4622.
15. Katz, W. E., The Electrodialysis Reversal (EDR) process. *Desalination* **1979,** *28*, 31-40.
16. Lee, H.-J.; Moon, S.-H.; Tsai, S.-P., Effects of pulsed electric fields on membrane fouling in electrodialysis of NaCl solution containing humate. *Separation and Purification Technology* **2002,** *27*, (2), 89-95.
17. Lindstrand, V.; Sundström, G.; Jönsson, A.-S., Fouling of electrodialysis membranes by organic substances. *Desalination* **2000,** *128*, (1), 91-102.
18. Lindstrand, V.; Jönsson, A.-S.; Sundström, G., Organic fouling of electrodialysis membranes with and without applied voltage. *Desalination* **2000,** *130*, (1), 73-84.
19. Cifuentes-Araya, N.; Pourcelly, G.; Bazinet, L., Impact of pulsed electric field on electrodialysis process performance and membrane fouling during consecutive demineralization of a model salt solution containing a high magnesium/calcium ratio. *Journal of Colloid and Interface Science* **2011,** *361*, (1), 79-89.
20. Allison, R. P., Electrodialysis reversal in water reuse applications. *Desalination* **1995,** *103*, (1-2), 11-18.
21. Kjelstrup Ratjke, S.; Fiksdal, L.; Holt, T. *Effect of biofilm formation on salinity power plant output on labarotory scale*; 121; University of Trondheim: Trondheim, **1984**; p 14.
22. Vermaas, D. A.; Guler, E.; Saakes, M.; Nijmeijer, K., Theoretical power density from salinity gradients using reverse electrodialysis. *Energy Procedia* **2012,** *20*, 170-184.
23. Długołęcki, P. E.; Nijmeijer, K.; Metz, S. J.; Wessling, M., Current status of ion exchange membranes for power generation from salinity gradients. *Journal of Membrane Science* **2008,** *319*, (1-2), 214-222.
24. Grebenyuk, V. D.; Chebotareva, R. D.; Peters, S.; Linkov, V., Surface modification of anion-exchange electrodialysis membranes to enhance anti-fouling characteristics. *Desalination* **1998,** *115*, (3), 313-329.
25. Post, J. W.; Hamelers, H. V. M.; Buisman, C. J. N., Influence of multivalent ions on power production from mixing salt and fresh water with a reverse electrodialysis system. *Journal of Membrane Science* **2009,** *330*, (1-2), 65-72.
26. Sumper, M., A Phase Separation Model for the Nanopatterning of Diatom Biosilica. *Science* **2002,** *295*, (5564), 2430-2433.
27. RRUFF Database of Raman spectra, X-ray diffraction and chemistry data for minerals. http://rruff.info/ **(29 June 2012**),
28. Blel, W.; Legentilhomme, P.; Bénézech, T.; Legrand, J.; Le Gentil-Lelièvre, C., Application of turbulent pulsating flows to the bacterial removal during a cleaning in place procedure. Part 2: Effects on cleaning efficiency. *Journal of Food Engineering* **2009,** *90*, (4), 433-440.
29. Grebenyuk, V. D.; Grebenyuk, O. V., Electrodialysis: From an Idea to Realization. *Russian Journal of Electrochemistry* **2002,** *38*, (8), 806-809.

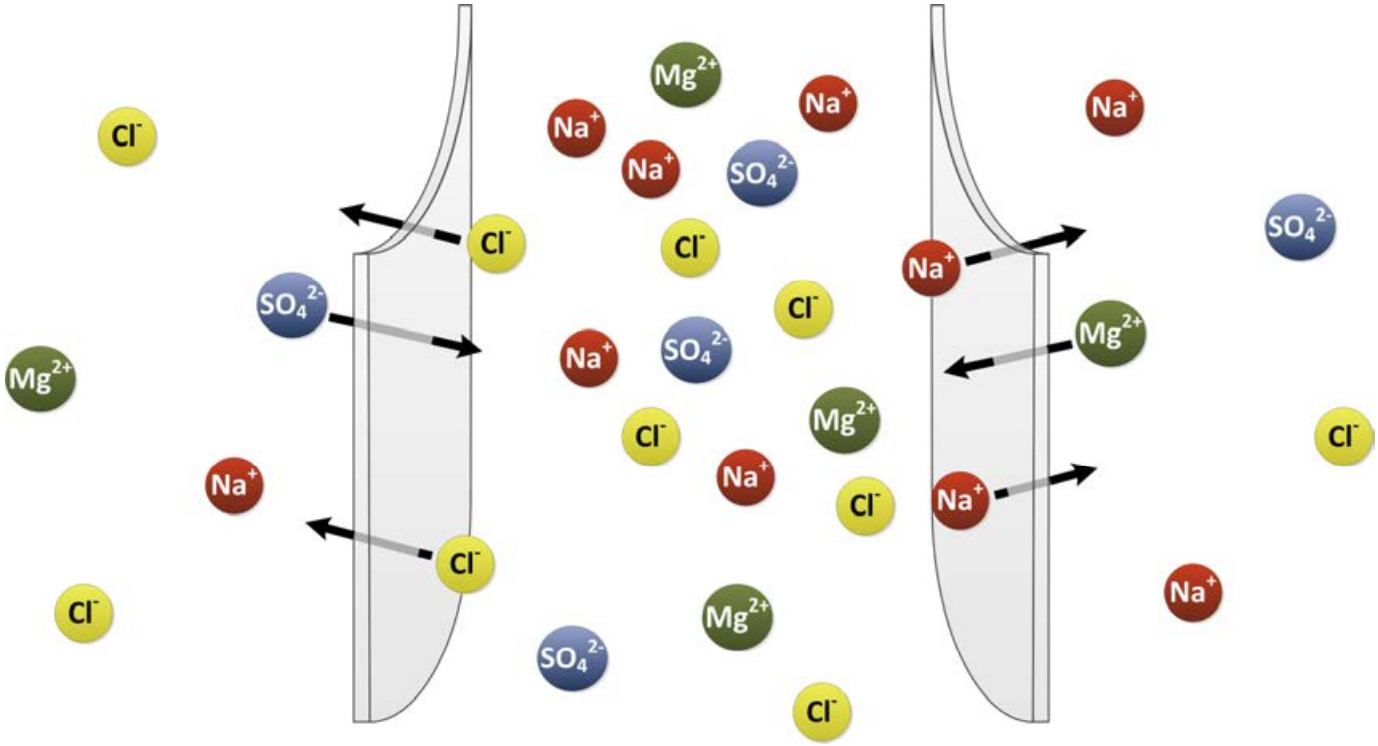
Mg2+
Na+
Na+
Na+
Cl-
SO4 2-
Na+
Cl-
Cl-
SO4 2-
SO4 2-
Na+
Mg2+
Mg2+
Cl-
Cl-
Na+
Na+
Cl-
Cl-
Cl-
Na+
Mg2+
SO4 2-
Cl-

Chapter 8

Ion transport and obtainable power density using mixtures of monovalent and multivalent ions

Abstract

Renewable energy can be generated when mixing seawater and river water. This energy is captured in reverse electrodialysis (RED) using ion exchange membranes. Although natural sources of seawater and river water are composed of a mixture of monovalent and multivalent ions, laboratory research on RED is generally performed with artificial solutions of sodium chloride. This research demonstrates that the presence of magnesium- and sulphate ions in feed solutions with NaCl has a major effect on the obtained open circuit voltage and power density for three different membranes types. When using a mixture with a molar fraction of 10% $MgSO_4$ and 90% of NaCl in both feed waters, the experimentally obtained power density in steady state decreases from 29% to 50% compared to the case where the feed solutions contain only NaCl as a salt. This effect is among others explained by the transport of Mg^{2+} and SO_4^{2-} against their concentration gradient, as is elaborated in a theoretical framework and which is justified by experimental data. Non-stationary cases, where feedwater is switched from a NaCl solution to a mixture of NaCl and $MgSO_4$, show that the voltage response time is in the order of tens of minutes up to several hours, due to ion exchange between the membranes and the feedwater. The knowledge gained from electrochemical measurements in stationary and non-stationary conditions and a novel technique to monitor the ion transport inside cation exchange membranes, can be used to improve the obtained power density in practical applications of RED using natural feed water.

This chapter has been submitted to *Energy & Environmental Science* as

David A. Vermaas, Joost Veerman, Michel Saakes and Kitty Nijmeijer, Influence of multivalent ions on renewable energy generation in reverse electrodialysis

8.1 Introduction

Renewable energy can be generated from mixing salt water, such as seawater, and fresh water, e.g., river water, using reverse electrodialysis (RED) [1-5]. This available energy from salinity differences can be captured using ion exchange membranes, which are selective for cations (cation exchange membranes, CEMs) or anions (anion exchange membranes, AEMs). The salinity difference induces a potential difference over the membranes when seawater is supplied at one side and river water is supplied at the other side of the membrane. Stacking the CEMs and AEMs alternately, with seawater and river water supplied in between, accumulates the voltage. When electrodes are introduced at the outer ends of the membrane pile, this voltage can be used to generate a redox reaction [6], or for capacitive storage [7, 8], which enables an electrical current when an external circuit is connected.

The potential to generate power from the mixing of seawater and river water is huge, as approximately 2 TW can be generated theoretically from the global river water runoff [9, 10]. This is close to the current worldwide electricity demand [11]. For artificial feedwater and laboratory conditions, high energy efficiencies (> 50%) [3, 12] and high gross power densities (> 2 W/m^2) [13] can be obtained. However, the obtained power and energy efficiency decrease rapidly when natural feedwater sources are used. A recent study on RED using natural feedwater for 25 days indicated that the power density decreased to approximately 50% of the initial power at a timescale of several hours [14]. This result implies that artificial feedwater composed of pure NaCl solutions in laboratory conditions is not representative for natural feedwater, although the dominant dissolved species in natural feedwater is NaCl.

The decrease in power density as observed in previous research when using natural feed waters was among others attributed to organic foulants [14]. Additionally, the presence of multivalent ions was identified as a limiting factor for the obtained power density [14]. Organic foulants, such as humic acids, are known to shield the charged groups of the ion exchange membranes and consequently lower the selectivity and increase the membrane resistance [15, 16]. The negative impact of multivalent ions on the obtained power density in RED is less well known.

Only very limited research is done on the effect of other salts than NaCl, such as $MgSO_4$, on the obtained power in RED [17, 18]. Post *et al.* [17] indicated that $MgSO_4$ in the feedwater reduces the stack voltage and increases the stack resistance compared to solutions with NaCl only [17]. Lacey *et al.* [19] indicated that multivalent ions such as iron, borates and silicates

may shield the membrane charge irreversibly, which would decrease the membrane permselectivity and increase the membrane resistance. Quantitative results on the obtained power density and the typical timescale of the effects of multivalent ions lack.

Previous research on multivalent ions in electrodialysis (ED) cannot be used *a priori* for RED, as some effects may work similar (e.g., effect on membrane resistance) but other effects work contrary in ED as in RED (e.g., direction of ion transport). In order to identify and understand the negative effect of multivalent ions on the power density in RED, the stationary and non-stationary effects of monovalent ions, multivalent ions and mixtures thereof need to be investigated systematically. Such research will explain the cause of the rapid decrease of approximately 50% in power density observed when using natural feed waters instead of artificial NaCl feed solutions [14].

This paper unravels the effect of the presence of $MgSO_4$ in feed waters on the RED performance and explains the underlying mechanisms. The concentration of $MgSO_4$ in the feedwater is systematically varied and the RED performance in terms of voltage, resistance and power density is analyzed. Additionally, the effect of the type of membrane and the distribution of $MgSO_4$ in the membranes using SEM-EDX is investigated. The results show how RED can be operated using feed mixtures of NaCl and $MgSO_4$, as representative for natural feed waters, while maintaining a high power density.

8.2 Theory

8.2.1 Electromotive force

The supply of waters with different salinity on either side of an ion exchange membrane creates a voltage over this membrane due to the Donnan potential at the membrane-water interface. This voltage is given by the Nernst equation, corrected for the activity of the feed waters and the apparent permselectivity of the non-perfect membrane [20]:

$$E = \alpha \frac{R \cdot T}{z_i \cdot F} \ln\left(\frac{a_{i,s}}{a_{i,r}}\right) \qquad \text{(eq. 8.1)}$$

In which E is the electromotive force over the membrane (V), α is the apparent membrane permselectivity of the membrane (-), R is the universal gas constant (8.314 J/(mol·K)), z_i is the valence of the ionic species i (-), F is the Faraday constant (96485 C/mol), and a_i is the activity of ionic species i in the feedwater (M). The subscripts s and r indicate seawater or

river water, respectively. Eq. 8.1 shows that the salinity ratio of monovalent ions (e.g., Na^+, Cl^-) creates twice the voltage created by the same salinity ratio of divalent ions (e.g., Mg^{2+}, SO_4^{2-}), assuming that the activities and apparent membrane permselectivity remain constant.

8.2.2 Uphill transport

However, transport is more complex when a mixture of monovalent and multivalent ions is present at both sides of an ion exchange membrane [21-24]. In that case, ions are exchanged through the membrane, in order to obtain equilibrium in chemical potential at both sides of the membrane [21]. This can be illustrated using an exemplary system with NaCl and $MgSO_4$ at both sides of a cation exchange membrane (CEM), in the same ratio but at different concentrations, as illustrated in Figure 8.1.

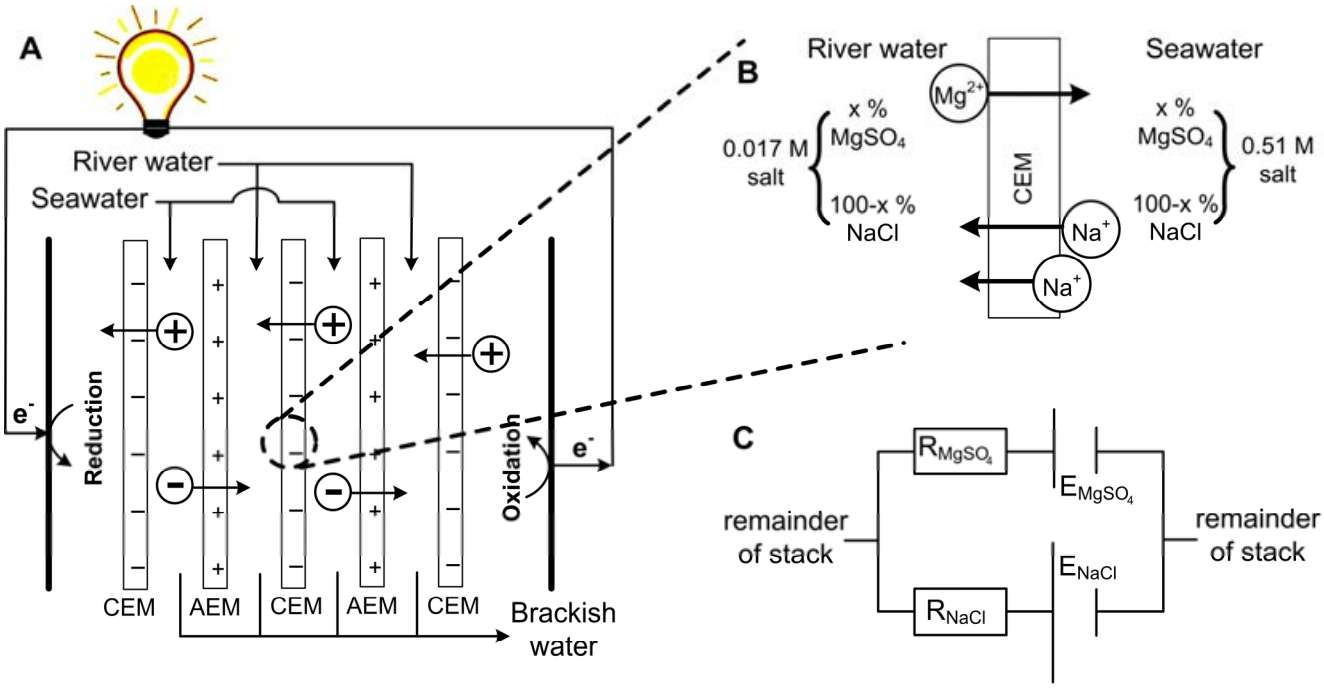

Figure 8.1: Principle of RED (A), with a zoomed section of a CEM showing the principle of uphill transport (B). The equivalent electrical circuit of this membrane is presented at the right bottom (C).

Because of the valence of the ion, the electromotive force related to the difference in $[Na^+]$ is larger than that of $[Mg^{2+}]$ (see eq. 8.1). Hence, Mg^{2+} is transported from the dilute solution to the concentrated solution in exchange for double the amount of Na^+ in opposite direction (Figure 8.1B). The transport of Mg^{2+} against the concentration gradient is described in

literature as uphill transport [17, 21]. This system can be illustrated in an electrical circuit, having two power sources with an unequal voltage (Figure 8.1C) in parallel. The source with the lowest voltage will be loaded, at cost of the source with the highest voltage. The membrane resistances for Mg^{2+} and Na^{+}-ions, which are illustrated in the electrical circuit as an electrical resistance, slow down the uphill transport of Mg^{2+}.

The uphill transport of Mg^{2+} sacrifices the salinity difference of the monovalent species, in this case Na^{+}, while at the same time no net charge transport is obtained. As a consequence, the presence of multivalent ions causes an irreversible loss in the available energy from monovalent ions [17]. A similar process occurs at the anion exchange membrane (AEM) for Cl^{-} and SO_4^{2-}.

The uphill transport stops when the salinity differences are such that the electromotive forces of both ionic species are equal. This can be best defined considering the case in which the feed waters are not refreshed (i.e., a batch process). Using eq. 8.1 and assuming that the apparent permselectivity is equal for both ionic species, this stationary situation is reached when the ion activities at either side of the membrane obey:

$$\alpha \cdot \frac{R \cdot T}{z_{Na^+} \cdot F} \ln\left(\frac{a_{Na^+,s}}{a_{Na^+,r}}\right) = \alpha \cdot \frac{R \cdot T}{z_{Mg^{2+}} \cdot F} \ln\left(\frac{a_{Mg^{2+},s}}{a_{Mg^{2+},r}}\right) \qquad \text{(eq. 8.2)}$$

$$\left(\frac{a_{Na^+,s}}{a_{Na^+,r}}\right) = \left(\frac{a_{Mg^{2+},s}}{a_{Mg^{2+},r}}\right)^{1/2} \qquad \text{(eq. 8.3)}$$

The molar transport of Mg^{2+}, in exchange for 2 Na^{+}, can then be calculated as function of the initial feedwater concentrations and the activity coefficients. When the changes in feedwater concentration are regarded small, the activity coefficients γ (-) can be assumed constant, and the molar transport of Mg^{2+} can be solved from:

$$\left(\frac{\gamma_{Na^+,s} \cdot \left(c_{Na^+,s} - 2J/V_s\right)}{\gamma_{Na^+,r} \cdot \left(c_{Na^+,r} + 2J/V_r\right)}\right) = \left(\frac{\gamma_{Mg^{2+},s} \cdot \left(c_{Mg^{2+},s} + J/V_s\right)}{\gamma_{Mg^{2+},r} \cdot \left(c_{Mg^{2+},r} - J/V_r\right)}\right)^{1/2} \qquad \text{(eq. 8.4)}$$

in which c is the salt concentration of Na^{+} or Mg^{2+} (M), J is the molar transport (mol) of Mg^{2+} towards the seawater compartment and V is the volume of the compartments (L). The uphill transport J can be calculated numerically from eq. 8.4. The initial concentrations plus or minus the uphill transport yield the final concentrations of Na^{+} and Mg^{2+} when uphill transport completes.

8.2.3 Theoretical energy and voltage

The available energy from mixing solutions with different concentrations can be derived from the Gibbs free energy of mixing [25]. When using mixtures of salts, the contribution of each ionic species to the available energy can be calculated individually considering the molar fraction of that specific salt only. Such calculation has been performed for mixtures of the monovalent salt NaCl and the multivalent salt $MgSO_4$, disregarding uphill transport. In addition, the available energy is calculated for the concentrations after uphill transport, as are derived from the equilibrium condition in eq. 8.3. These calculations of the available energy are shown in Figure 8.2A as a function of the molar salt fraction of $MgSO_4$ in both the seawater and river water feed. Correspondingly, Figure 8.2B considers the open circuit voltage over a perfectly selective membrane, when uphill transport is completed, as a function of the fraction of $MgSO_4$ in both feed waters. In addition, Figure 8.2B shows the cases in which $MgSO_4$ is only present in the seawater feed or river water feed.

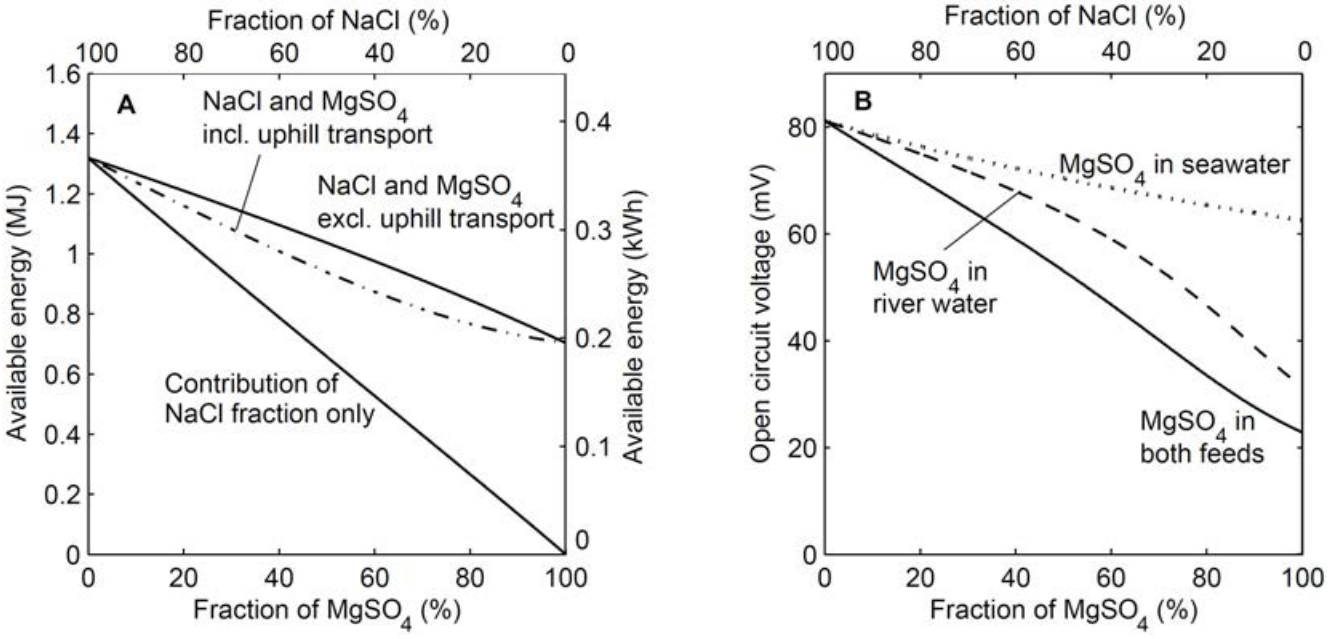

Figure 8.2: Theoretical available energy using 1 m^3 of both feed waters (A) and open circuit voltage over one membrane (B) as a function of the molar salt fraction $MgSO_4$ in the feedwater. The available energy (A) corresponds to the case when $MgSO_4$ is in both feed waters. The open circuit voltage (B) is also calculated for cases when $MgSO_4$ is only present in the river water or in the seawater. The total salt concentrations for the inflowing feedwater are 0.508 M and 0.017 M for all cases. The activity coefficients are derived from the modified three characteristic parameter correlation (TCPC) model [29].

Figure 8.2A shows that the available energy decreases when a larger fraction of NaCl is substituted for $MgSO_4$, even when disregarding the loss due to uphill transport. The contribution of NaCl decreases practically linearly, proportional to the molar fraction of NaCl, due to the lower concentrations of NaCl. However, the contribution of $MgSO_4$ cannot compensate for this decrease in available energy, due to the relatively low activity coefficients for $MgSO_4$, which effectively limit the increase in entropy when mixing the feed waters. Hence, the total available energy of a mixture of NaCl and $MgSO_4$ is lower than when using NaCl only. This effect is inevitably related to the use of $MgSO_4$ as a salt and hence will also be relevant for other salinity gradient power technologies such as pressure retarded osmosis (PRO) [25, 26] and capacitive mixing (CAPMIX) [8, 27, 28].

The uphill transport of $MgSO_4$, and the corresponding exchange for NaCl, further limits the available energy in RED. Because two moles of NaCl are exchanged for one mole of $MgSO_4$, available energy is lost when uphill transport of $MgSO_4$ occurs. This irreversible loss is largest for a fraction $MgSO_4$ of approximately 60%, where it accounts for approximately 10% of the available energy. The maximum is found at this particular fraction due to a combination of large uphill transport J (eq. 8.4) when both ionic species are present in significant fractions and the different contributions of NaCl and $MgSO_4$ to the available energy.

The open circuit voltage (OCV) over each ion exchange membrane decreases relatively much more than the total available energy when increasing the fraction of $MgSO_4$ in the feedwater (Figure 8.2B). When $MgSO_4$ is mixed in both feed waters, the OCV decreases from approximately 80 mV for feedwater without $MgSO_4$ to little more than 20 mV for feedwater with $MgSO_4$ only. This decrease is much larger than that for the available energy, mainly due to the fact that the valence (z_i) appears in the denominator in eq. 8.1. Hence, the voltage is halved for solutions with $MgSO_4$ only compared to NaCl only even when equal activities would be considered. Additionally, uphill transport plays a larger role in the OCV because the salinity ratio, which determines the OCV, is more sensitive to small changes in the river water concentrations than the available energy.

The isolated effect of the uphill transport is best visible when considering the cases in which a fraction of $MgSO_4$ is present in the seawater or in the river water only. The OCV decreases strongest for the case where $MgSO_4$ is present in the river water feed. This is due to enhanced uphill transport of $MgSO_4$, in order to create a concentration ratio for $MgSO_4$ that balances the Donnan potentials created by the NaCl system. When $MgSO_4$ is only present in

the seawater feed, this uphill transport of multivalent ions will not occur, as the concentration of $MgSO_4$ in seawater is already high enough to balance the potential corresponding to the salinity ratio of NaCl. The difference between these two cases visualizes the uphill transport effect on the open circuit voltage. In practical cases, the fraction of multivalent ions in seawater (typically 10% [14]) is often lower than that in river water.

8.2.4 Power density

The much lower open circuit voltage, but only slightly lower available energy, suggests that a larger membrane area is required to capture an equal portion of the available energy when a fraction of $MgSO_4$ is present in the feedwater. In other words, the power density is expected to be lower when the fraction of multivalent ions is increased. The obtainable power density of a RED stack can be derived from the open circuit voltage and the electrical resistance of the stack:

$$P_{dens} = \frac{OCV^2}{4 \cdot N_m \cdot R_{stack}} \qquad \text{(eq. 8.5)}$$

in which P_{dens} is the power density (W per m^2 membrane area), N_m is the number of membranes (-) and R_{stack} is the electrical area resistance of the RED stack ($\Omega \cdot m^2$ stack cross-sectional area). The electrical resistance is composed of an ohmic contribution, due to the membrane, feedwater and spacers, and a non-ohmic contribution, due to the concentration changes when ions are transported under influence of an electrical current.

Although this theoretical framework helps to understand the effect of $MgSO_4$, the actual open circuit voltage, electrical resistance and power density are more complex to calculate. For example, the equilibrium as described in eq. 8.4 assumes a batch mode and hence disregards the supply of new feedwater. Therefore, the actually generated voltage, electrical resistance and obtained power in RED need to be investigated experimentally, which is described in the next section.

8.3 Experimental setup

8.3.1 Stack

Three RED stacks were built, each with different ion exchange membranes. One stack was composed of heterogeneous membranes (Ralex CMH / AMH, MEGA AS, Czech Republic),

a second stack was composed of commercial homogeneous membranes (Neosepta CMX / AMX, Tokuyama, Japan) and a third stack was composed of a new type of homogeneous membranes (V1 CEM / V1 AEM, Fujifilm Europe, The Netherlands). The specifications of these membranes are listed in Table 8.1. These membranes are selected to observe the effect of $MgSO_4$ for different types of membranes (heterogeneous and homogeneous) and possible difference in (uphill) ion transport due to the differences in membrane thickness and membrane resistance.

Table 8.1: Membrane properties according to specifications of the suppliers.

Membrane name	Membrane type	Thickness (wet)	Charge density [30]	Apparent permselectivity (0.5 M – 0.1 M KCl)	Area resistance (in 0.5 M NaCl)
Ralex CMH / AMH	Heterogeneous	<725 μm	5.5 M	>91 %	< 8.8 Ω·cm^2
Neosepta CMX / AMX	Homogeneous	155 μm	8.4 M	98 %	2.7 Ω·cm^2
Fujifilm V1	Homogeneous	125 μm	-	93 %	1.6 Ω·cm^2

A woven net spacer of 200 μm thickness (Sefar 06-300/51, Switzerland) was used in between the ion exchange membranes to create alternately compartments for salt water and fresh water. The spacer geometry, gaskets and inflow geometry were described in previous research [3, 31]. All stacks were confined between two endplates with embedded Ti-Ru/Ir mesh electrodes (MAGNETO Special Anodes B.V., The Netherlands) with a dimension of 10 cm by 10 cm.

The electrode rinse solution, composed of 0.05 M $Fe(CN)_6^{3-/4-}$ and 0.25 M NaCl, was circulated in the electrode compartments at a flow rate of 150 ml/min and kept at a static overpressure of 0.5 bar to ensure that the membranes are closely packed.

The stack with Fujifilm membranes was equipped with additional buffer compartments similarly to previous research [32], created by a Neosepta CMX membrane between the membrane pile and the electrode compartment. This buffer compartment was circulated with 0.25 M NaCl. The buffer compartment was installed in this case to avoid leakage of electrode rinse solution towards the feedwater, which was no issue with the other membrane types.

To correct for the additional resistance of the electrode compartment and the possible buffer compartment, the resistance of an empty stack, composed of two electrodes, corresponding electrode compartments and possibly buffer compartments, was measured. The resistance of such blank was used to correct the resistance of the measurement series, and allowed comparison of the different stacks.

8.3.2 Feedwater

Salt and fresh water streams, composed of a mixture of dissolved NaCl (99.5% purity, ESCO, The Netherlands) and/or $MgSO_4$, $MgCl_2$ or Na_2SO_4 (at least 98% purity, VWR, The Netherlands), were fed to the RED stacks. The total salt concentration of the artificial seawater was 0.508 M in all cases, whereas the total salt concentration of the artificial river water was always 0.017 M. In other words, compared to artificial solutions with only NaCl, part of the NaCl was replaced with $MgSO_4$, $MgCl_2$ or Na_2SO_4, in order to maintain the molarity of the inflowing feed (and hence the conductivity, to a certain degree) constant.

When considering mixtures of NaCl and $MgSO_4$, a molar percentage of 0%, 5%, 10%, 25%, 50% or 100% of the total dissolved salt was accounted for by $MgSO_4$. This percentage was equal for both feedwater streams. The remaining amount of dissolved salt was NaCl. When considering the mixtures of NaCl and $MgCl_2$ or Na_2SO_4, 10% of the dissolved salts was $MgCl_2$ or Na_2SO_4 and the remaining 90% was NaCl.

All stacks were first fed with solutions containing of 0.508 M NaCl and 0.017 M NaCl, to equilibrate the membranes with NaCl solutions. After at least one hour of operation, the feedwater solutions were suddenly switched to one of the previously described mixtures. The stacks operated for at least four hours using these solutions before switching back to solutions with dissolved NaCl only.

The flow rate of the feedwater solutions was 60 ml/min in all cases, which is equivalent to a flow velocity of 1.3 cm/s and a Reynolds number of 5. The effluent was not re-cycled, i.e., new feedwater was supplied continuously. The temperature of the feed waters was maintained at 25 ± 1.5 ºC.

8.3.3 Electrochemical measurements

A chronopotentiometric series was applied (Ivium Technologies, The Netherlands), comprising a stage with no current (open circuit) and a stage with a current density of 10 A/m^2. Both stages were applied for 60 s and repeated continuously. The stack resistance

was calculated from the difference in voltage at these two stages, divided by the current density.

Some measurements were duplicated to check the reproducibility. The steady voltages of these duplicates were typically within 3% of the original series.

In addition, the open circuit voltage over a single membrane (CEM or AEM, 10 cm x 10 cm) was measured, using a single membrane enveloped with only two compartments for feedwater connected to an Ag/AgCl reference electrode (QIS, The Netherlands). The same feedwater solutions as for the stacks were used for these individual membrane setups and were supplied at a flow rate of 12 mL/min.

8.3.4 Membrane cross-sections

To study the ion transport through the membranes, the position of the ionic species in the membrane cross-sections was identified with energy dispersive X-ray spectra (EDX or EDS). Membrane cross-sections were made for all membranes, after 0, 2, 15, 30, 45 and 300 min of operation with feedwater solutions in which 10% of the salt concentration was $MgSO_4$ and 90% was NaCl.

After this specified duration, the stacks were opened, the membranes were rinsed in demineralized water and directly frozen in liquid nitrogen to conserve the position of the ions in the membranes. The process to stop the stack operation, dismantle the stack and freeze the membranes took approximately one minute. Subsequently, the frozen membranes were broken and freeze dried (Edwards, United Kingdom).

The EDX analysis (JEOL, JSM 6010LA, United States) was performed over at least two cross-sectional lines of each sample, each comprising at least 10 scan points. The average atomic percentages of the detected elements of Na, Cl, Mg and S were calculated.

8.4 Results

The results will first comprise the stationary RED performance with different NaCl-$MgSO_4$ mixtures, which is representative for large-scale operations with steady feedwater conditions. Subsequently, the transition from one feed to another feed is presented, which resembles the cases where e.g. tides cause fluctuating feedwater concentrations.

8.4.1 Stationary performance

The open circuit voltages (OCV) for steady operation are shown in Figure 8.3 for stacks with Ralex, Neosepta or Fujifilm membranes, as a function of the percentage of $MgSO_4$ to the total dissolved salt of both feedwater streams.

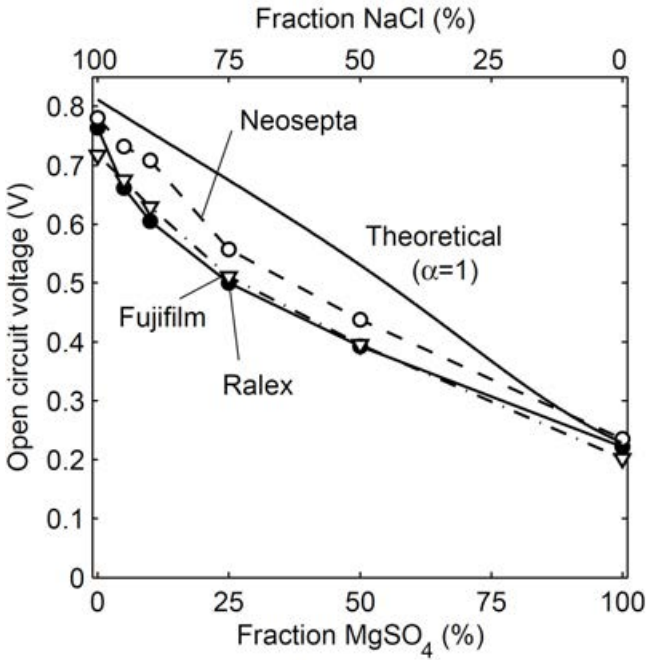

Figure 8.3: Open circuit voltage versus the molar fraction of $MgSO_4$ of the total amount of dissolved salt in the feedwater. The experimental results are obtained with Ralex, Neosepta or Fujifilm membranes. The presented values are averaged based on stationary data series of at least one hour. Error bars at twice the standard deviations of this series are too small to be visible.

The open circuit voltage decreases when more $MgSO_4$, relative to the total amount of dissolved salt, is present in the feedwater (Figure 8.3). This decreasing trend was expected, as demonstrated already in Figure 8.2B. The open circuit voltage is highest for the stack with Neosepta membranes, due to the high charge density of these membranes [30, 33] and the high permselectivity according to its specifications (Table 8.1).

The open circuit voltage is close to the theoretical voltage for perfectly selective membranes in the case of 0 or 100% $MgSO_4$, which indicates that the membranes are highly selective and co-ions are excluded in these cases. The exclusion of co-ions is dependent on the electrical force on these ions, which is proportional to the product of the Donnan potential and the ion charge. The relatively high OCV for 0% $MgSO_4$ is well known and originates from the high Donnan potentials that exclude the co-ions effectively from the double layer

when using monovalent ions only. On the other hand, when using multivalent ions only, the high ionic charges (2+ or 2−) exclude the co-ions from the double layer, which is visible as a good agreement between the theoretical and experimental values at 100% $MgSO_4$.

However, the experimental OCV is lower than the theoretical one when mixtures of monovalent and multivalent ions are used. This is explained from the combination of relatively low Donnan potentials (due to the presence of multivalent ions) and relatively low valence of the monovalent co-ions, which increases the permeation of co-ions through the ion exchange membranes [22]. In other words, the permeation of co-ions through the non-ideal membranes is an increasing issue when using a mixture of monovalent and multivalent ions. This co-ion transport is not taken into account for the theoretical curve, as the theory assumes a perfect 100% selective membrane at all conditions ($\alpha = 1$). The actual apparent permselectivity is lower when using mixtures of monovalent and multivalent ions, which results in a lower open circuit voltage than the theoretical equivalents.

The area resistance and obtained power density for steady operation are shown in Figure 8.4 for stacks with Ralex, Neosepta or Fujifilm membranes, as a function of the percentage of $MgSO_4$ to the total dissolved salt of both feedwater streams.

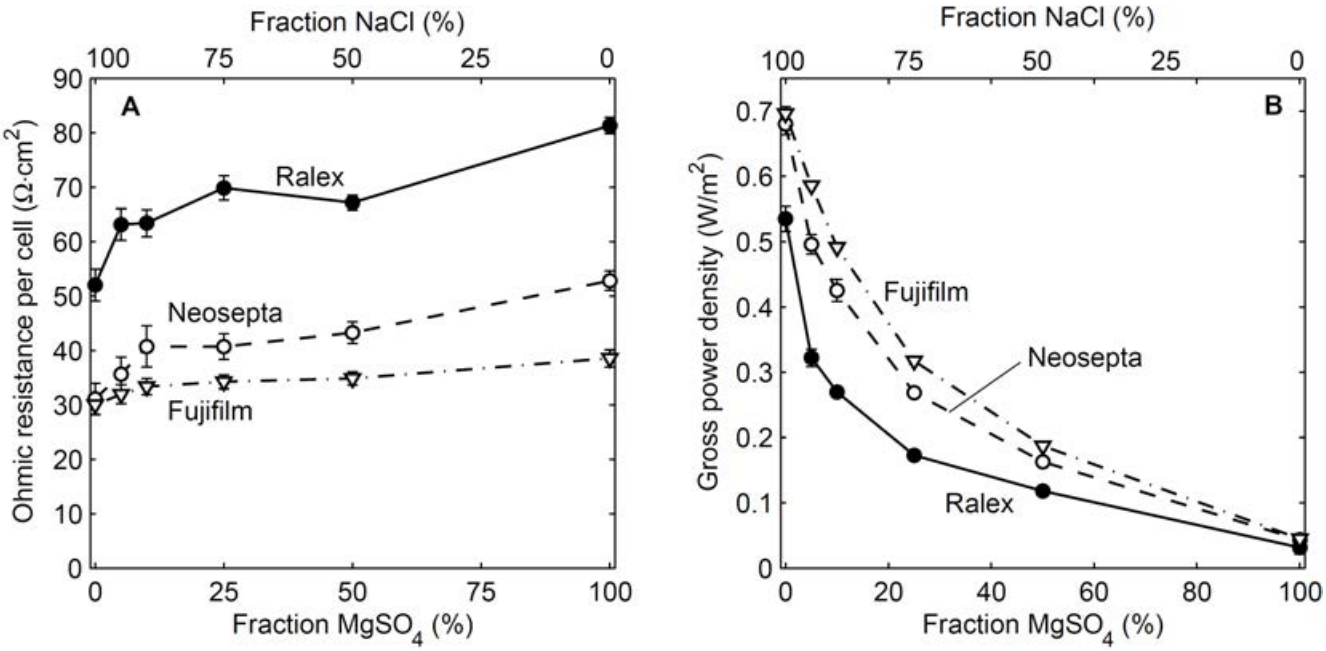

Figure 8.4: Ohmic resistance (A) and power density (B) versus the molar fraction of $MgSO_4$ of the total amount of dissolved salt in the feedwater. The experimental results are obtained with Ralex, Neosepta or Fujifilm membranes. The presented values are averaged based on stationary data series of at least one hour, and twice the standard deviation is shown as error bar. Most error bars are too small to be visible.

The ohmic resistance increases slightly with increasing $MgSO_4$ fraction for all membrane types (Figure 8.4A), due to higher membrane resistance as well as slightly lower conductivity of the feedwater. A higher electrical resistance in case of mixtures with $MgSO_4$ was observed before [17] and can be explained from the slightly lower diffusion coefficients of Mg^{2+} and SO_4^{2-} compared to Na^+ and Cl^-. Additionally, steric hindrance of the larger (hydrated) Mg^{2+} and SO_4^{2-} ions possibly plays a role [34]. Nevertheless, the increase in ohmic resistance is less pronounced than the decrease in open circuit voltage when increasing the fraction of $MgSO_4$. The non-ohmic resistance on the other hand does not change significantly (not shown), as this contribution is mainly dependent on the hydrodynamics of the feedwater [35-37].

The decreasing OCV and to a lesser extent the increasing ohmic resistance, are resembled in the obtained power density (Figure 8.4B). Because the power density is proportional to the OCV squared, the power density decreases rapidly when increasing the fraction of $MgSO_4$ in the feedwater. When the salt in the feedwater comprises only 10% $MgSO_4$, which is most representative for typical seawater and river water, the power density decreases with 29% (Fujifilm), 37% (Neosepta) and even 50% (Ralex) compared to pure NaCl as feed. This large decrease in power density emphasizes the importance of the open circuit voltage when using mixtures of NaCl and $MgSO_4$.

To further understand the behavior of NaCl-$MgSO_4$ mixtures, the individual effect of Mg^{2+} and SO_4^{2-} is investigated separately using mixtures with $MgCl_2$ or Na_2SO_4 next to NaCl. The obtained open circuit voltages using single membranes (CEM or AEM) are shown in Figure 8.5.

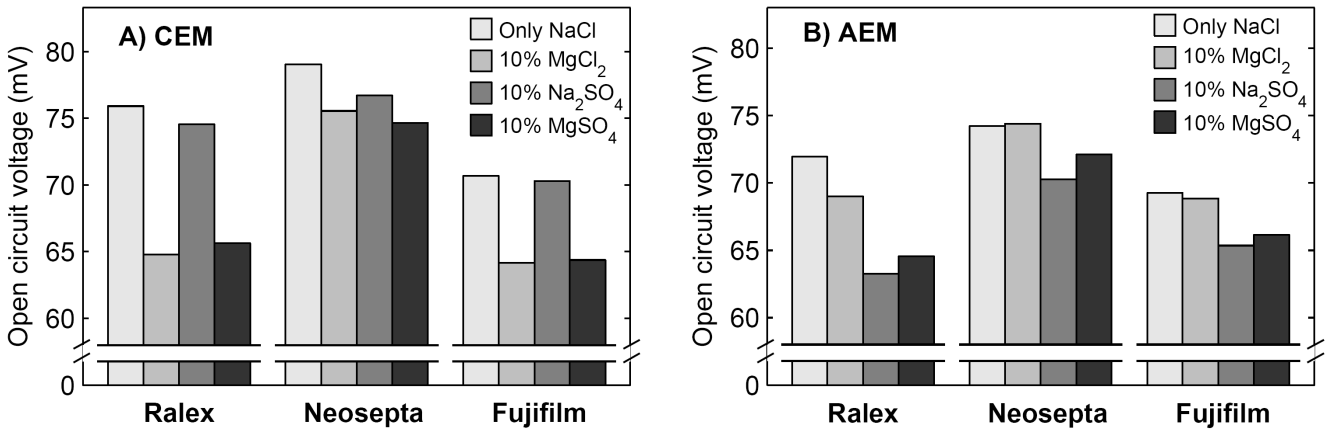

Figure 8.5: Open circuit voltage for single cation exchange membranes (A) and anion exchange membranes (B) when using feedwater composed of NaCl only or 10% $MgCl_2$, Na_2SO_4 or $MgSO_4$ and 90% NaCl. The values of the obtained voltages have typically a precision of 1 mV.

Figure 8.5 shows that the type of cation (Mg^{2+} or Na^{+}) only affects the voltage over the CEMs significantly, while the type of anion (SO_4^{2-} or Cl^{-}) only influences the voltages over the AEMs significantly. This is a direct effect of the charge selectivity of the ion exchange membranes.

Ralex membranes show the largest decrease in OCV when comparing 100% NaCl to 10% $MgSO_4$/90% NaCl, while these membranes feature the largest membrane resistance. Apparently, the uphill transport is not strongly influenced by the membrane resistance. This can be explained from the concept of the double layer at the membrane-water interface. A very small flux of ions through the membrane (due to uphill transport) is sufficient to bring the concentration in the thin double layer in equilibrium with the chemical potential and determine the voltage over the membrane. Therefore, the membrane resistance does not play a significant role for this ion transport in the stationary case.

The reason that Ralex membranes demonstrate even largest decreases in OCV when mixtures of monovalent and multivalent ions are present is that these membranes have a relatively low fixed charge density [30]. Therefore, these membranes feature a relatively low permselectivity, especially when mixtures of monovalent and multivalent ions are used. As explained before, the combination of relatively low Donnan potentials due to the presence of multivalent ions and monovalent co-ions increases the permeation of co-ions through the ion exchange membranes [22].

Both homogeneous membrane types (Neosepta en Fujifilm) show only a minor decrease in OCV due to the presence of multivalent counter-ions when compared to Ralex membranes (Figure 8.5). The Neosepta membranes have a higher fixed charge density than the Ralex membranes (Table 8.1) [30]. The charge density of Fujifilm membranes is not specified, but it is expected more or less similar to that of the homogeneous Neosepta membranes.

The presence of Mg^{2+} generally induces a larger decrease in membrane voltage for CEMs (Figure 8.5A) than the presence of SO_4^{2-} does for AEMs (Figure 8.5B). This may be due to the formation of ion pairs of sodium and sulphate, $NaSO_4^{-}$, which is effectively a monovalent ionic species [38]. Hence, the OCV for a stack with CEMs and AEMs will decrease less pronounced when SO_4^{2-} is present than when Mg^{2+} is present.

8.4.2 Mass transport

The effect of the uphill transport can be analyzed when considering the salinity ratio (seawater to river water) of individual ionic species in the effluent. In the influent, all ions

have a salinity ratio of 30:1 between the seawater and river water feed. The ratio of each ionic species in the effluent, when using 10% $MgSO_4$ in both feed waters, is shown in Figure 8.6 as a function of the current density.

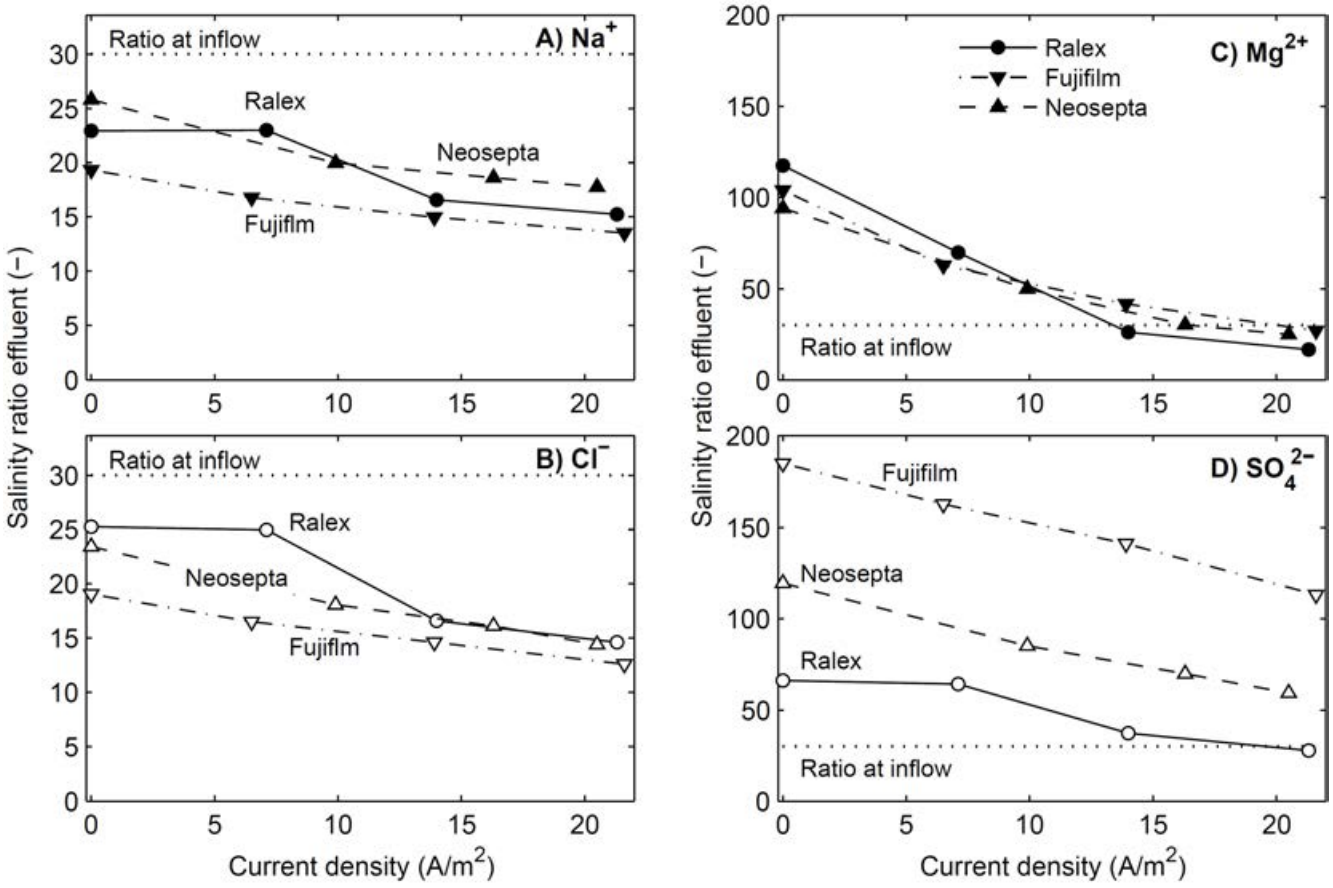

Figure 8.6: Ratio of Na^+ (A), Cl^- (B), Mg^{2+} (C) and SO_4^{2-} (D) between the seawater effluent and the river water effluent, as a function of the current density.

Figure 8.6A-B show that the ratio for Na^+ and Cl^- in the effluent decreases for increasing current density, as a higher ionic current directly implies a larger ionic flux from seawater to river water. In other words, a part of the available energy is used. However, also when no electrical current is generated, the concentration ratio for the monovalent ions in the effluent is already significantly lower than 30. This is explained from the uphill transport of multivalent ions, in exchange for monovalent ions.

This uphill transport of multivalent ions is proven in Figure 8.6C-D, which show a concentration ratio for Mg^{2+} and SO_4^{2-} significantly higher than 30 when no current density is generated. Although the concentration ratios of these multivalent ions clearly indicate

uphill transport, the concentration ratios for multivalent ions are expected even higher based on the theoretical framework (eq. 8.3). This discrepancy is also observed in previous research [17], and justifies the concept that the concentrations in the double layer (which determine the OCV) adapt quickly while the effluent concentrations are dominated by the concentrations in the bulk fluids. The continuous feedwater flow prevents that the concentrations in the bulk fluids equilibrate with these in the double layer.

The concentration ratios for multivalent ions decrease when the current density increases. This is caused by a decrease in voltage over each membrane, due to an ohmic voltage drop. Such decrease in voltage reduces the electromotive force for uphill transport of multivalent ions at higher current density. As a consequence, this effect shifts the optimum current density to a higher value for a system with a mixture of monovalent and multivalent ions.

Comparing the different membrane types, the transport of Mg^{2+} is similar for all membrane types (Figure 8.6C), while the transport of the SO_4^{2-} is significantly higher in Fujifilm membranes, followed by Neosepta and Ralex membranes (Figure 8.6D). The differences in transport rate of SO_4^{2-} are due to the differences in membrane resistance. A lower membrane resistance corresponds to more uphill transport, as indicated earlier by the electrical circuit (Figure 8.1C). The differences in membrane resistance are more pronounced for the AEMs than for the CEMs, and therefore the differences in the concentration ratios are more significant for SO_4^{2-} than for Mg^{2+}. Moreover, the diffusion of the used anionic species is faster than that of the cationic species [39] due to the smaller hydrated radii of monovalent species [34].

8.4.3 Non-stationary performance

The previous results discussed stationary performance, i.e., when feedwater with the same concentrations is fed for a long time. Non-stationary cases, for example when feedwater with monovalent ions only is suddenly replaced by feedwater with mono- and multivalent ions, allow to analyze the mass transport mechanisms in the membrane, double layer and feedwater bulk. The power density as a function of time after such feedwater change is shown for all stacks in Figure 8.7.

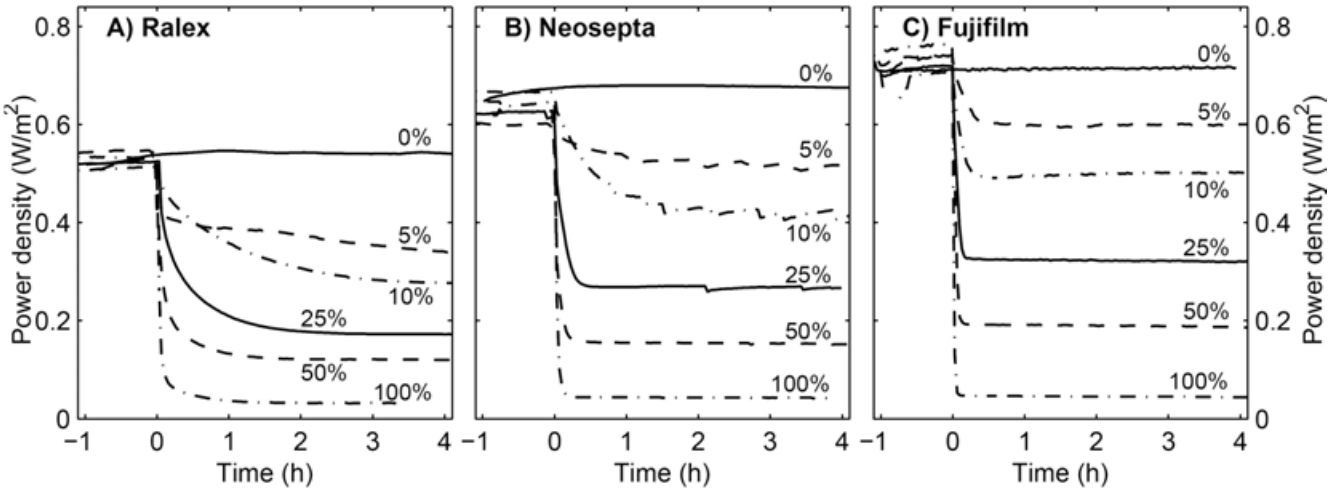

Figure 8.7: Power density as a function of time, for stacks with A) Ralex membranes, B) Neosepta membranes and C) Fujifilm membranes. At time = 0 h, the feedwater source is switched from NaCl solutions to salt solutions with a certain percentage of $MgSO_4$ (as indicated in the graphs) and the remaining percentage of NaCl. Small deviations in power density are observed for all stacks with 5% $MgSO_4$ and the Neosepta stack with 10% $MgSO_4$, which are due to temporarily entrapment of air in the feedwater.

In all cases, the steady power densities for the stack with heterogeneous Ralex membranes are lower than for the stacks with homogeneous membranes, especially when mixtures of NaCl and $MgSO_4$ are used, as already demonstrated in Figure 8.3. However, the non-stationary power density in Figure 8.7 reveals that the stack with Ralex membranes responds slower than the stack with Neosepta membranes and this is even more pronounced when compared to the stack with Fujifilm membranes. When using a mixture with 10% $MgSO_4$, the power density does not reach a constant value after 4 hours of operation in case of Ralex membranes, while for Fujifilm membranes the power density is rather constant after 0.5 h already. These differences in response time are also observed when the feedwater is switched back to feedwater with NaCl only (not shown).

The decrease in power density and the corresponding response time match qualitatively and quantitatively very well with previous experiments with real natural feedwater, in which approximately 10% of the ions is multivalent [14, 40]. Therefore, this artificial mixture of monovalent (90%) and multivalent (10%) ions is considered representative for at least the first hours of operation of RED with natural feeds.

The slow response of the power in case of mixtures with $MgSO_4$ is the consequence of the limitations in ion exchange between the membrane and the double layer and that between the

double layer and the diffusive boundary layer. The double layer, which is as thin as only a few nm, experiences hardly any ion transport from the bulk fluid by convection and hence is strongly influenced by the ionic composition of the membranes. The Ralex membranes are much thicker than the homogeneous membranes, and therefore have the largest NaCl buffer when switched to a solution with a fraction of $MgSO_4$. This process suggests a gradual change of the counter-ions within the membrane interior in time. Figure 8.8 shows the percentage of magnesium elements relative to the total counter-ions (magnesium + sodium) in cross-sections of the cation exchange membranes of Ralex, Neosepta and Fujifilm, for different durations of operation on feedwater with 10% $MgSO_4$/90% NaCl.

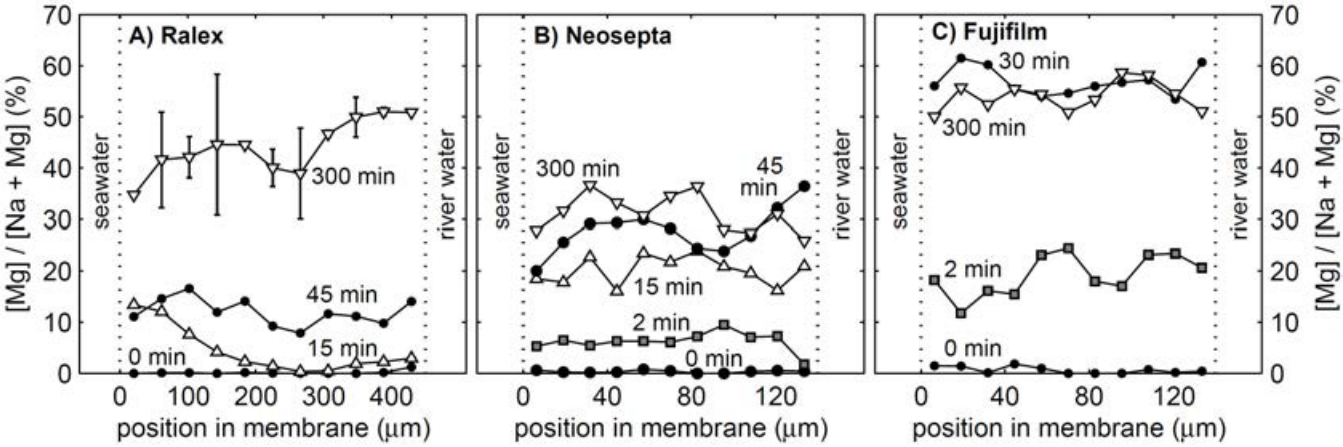

Figure 8.8: Relative contribution of magnesium as counter-ion in Ralex (A), Neosepta (B) and Fujifilm (C) cation exchange membranes, as a function of the position in the membrane cross-section. The elements are experimentally detected with EDX. The left sides of each graph correspond to the membrane side that faced the seawater compartment, while the right side faced the river water compartment. The standard error is indicated by the error bars for Ralex 300 min.

Figure 8.8 shows that the interior of the cation exchange membranes does not contain any magnesium before switching to feedwater with $MgSO_4$ (i.e., at 0 min) within the accuracy of the measurement. The contribution of magnesium strongly increased to 30% to 60% of the total amount of counter-ions after 300 minutes of operation with feedwater with 10% $MgSO_4$. The relatively large fraction of magnesium in the membrane material is explained from its high valence ($z = 2$ for Mg^{2+}) compared to Na^+ ($z = 1$). Therefore, Mg^{2+} binds stronger to the negative fixed membrane charges than Na^+ does. This results in a relatively large fraction of magnesium elements in the membrane after 300 min. The strong affinity for

Mg^{2+} of the CEMs explains why the ohmic resistance is most sensitive to only small fractions of $MgSO_4$, as observed already in Figure 8.3B.

When considering the Ralex membrane in more detail, the gradient in the relative concentration of magnesium is directed from the seawater compartment towards the river water compartment after 15 min, while it is opposite after 300 min of operation (Figure 8.8A). The exact shape of these curve cannot be determined due to the limited accuracy, but the contributions of $MgSO_4$ at the seawater side are significantly different than at the river water side. Both observations are expected based on the theoretical framework. Because the ionic current is directed from the seawater compartment towards the river water compartment, magnesium enters the membrane initially from the seawater side, which explains the profile at 15 min. When steady concentration profiles are established in the membrane (i.e., at 300 min), the concentration gradient of multivalent ions should be directed towards the highest concentration [22], in line with the uphill transport of multivalent ions. Such concentration profile was already predicted by Higa *et al.* [22], and is, to our best knowledge, for the first time experimentally observed, in this case in the Ralex membrane. These details in concentration profiles cannot be distinguished for the other membrane types, probably due to ion exchange in these thinner membranes when dismantling the stack and preparing the membrane samples for EDX analysis. The much larger thickness of the Ralex membranes better conserves the concentration gradients as representative during the experiment.

The relative concentration of Mg^{2+} increases much faster in Fujifilm CEMs and (in lesser degree) in Neosepta CEMs compared to Ralex CEMs. The contribution of magnesium more than doubles between 45 min and 300 min for Ralex membranes (Figure 8.8A), while it increases only slightly for Neosepta membranes in this period (Figure 8.8B). For Fujifilm membranes (Figure 8.8C), the relative concentration of magnesium does not even change significantly anymore after the first 30 min. The transition time to establish a steady concentration profile in the membrane is expected to be proportional to the ion exchange capacity and the membrane thickness. The Ralex membranes offer a slightly higher ion exchange capacity and are much thicker than Neosepta membranes [30] and therefore provide the largest source of Na^+, which is in agreement with Figure 8.8. Although the ion exchange capacity of Fujifilm membranes is not specified, the fast stabilization of the concentration profile predicts a low ion exchange capacity of these membranes. However, an

exact value cannot be inferred, as micro-heterogeneity in the membranes complicates the uniform release of monovalent ions from the membrane interior [41].

During the non-stationary period, the double layer is supplied with Na^+ ions transported out of the membrane in exchange for Mg^{2+} transported into the membrane, which effectively reduces the fraction of multivalent ions in the double layer. Hence, the voltage over the CEMs is temporarily higher compared to steady operation on feedwater with a fraction of $MgSO_4$. The same effect occurs for AEMs, where Cl^- is slowly released in exchange for SO_4^{2-} (not shown due to the less reliable detection of sulfur). This slow release of monovalent ions towards the double layer also explains the slow transition in power density as observed in Figure 8.7, in particular for Ralex membranes.

The slow response in power density (Figure 8.7) due to ion supply from the membrane interior predicts that the response can be accelerated at higher current density, and that the response can be decelerated when the current density is periodically reversed. The latter behavior is recently observed for RED stacks that operate using natural feedwater; a stack with periodic feedwater switch (which induces a switch of the current direction) showed a slower decrease in power density than a stack with continuous feedwater supply [40].

A fast response, which may occur at high current densities in the same direction, can be useful when applying a treatment with NaCl (brine) to flush the multivalent ions from the membranes. Such treatment should be applied as short as possible, to limit the volume of feedwater required for such cleaning. In this way, the gradual ion exchange between monovalent and multivalent ions in the membrane can be used beneficially. Hence, such operational strategy can be applied to improve the power density when RED is used for power production from natural feedwater streams.

8.5 Conclusions

Energy generation from mixing seawater and river water is mimicked representatively using artificial mixtures of salts with monovalent ions (e.g., NaCl) and salts with multivalent ions (e.g. $MgSO_4$). The global potential for salinity gradient power, as quantified by the available energy per water volume, decreases only slightly for increasing fractions of $MgSO_4$, while the obtained voltage and power density decrease drastically. For a mixture with a molar fraction of 10% $MgSO_4$ and 90% of NaCl in both feed waters, the experimentally obtained power density in steady state decreases between 29% and 50%, depending on the membrane type, compared to the case where the feed solutions contain only NaCl as a salt.

This decrease in power density is mainly due to a lower open circuit voltage and only slightly due to higher electrical resistance. This lower open circuit voltage is theoretically predicted due to the transport of Mg^{2+} and SO_4^{2-} against their concentration gradient. This uphill transport of multivalent ions is driven by the difference in voltage as generated by a monovalent species and a multivalent species. In addition, the permeation of co-ions through the non-ideal membranes is an increasing issue when using a mixture of monovalent and multivalent ions. This effect is more pronounced for heterogeneous membranes than for homogeneous membrane types.

Non-stationary cases, where feedwater is switched from NaCl solutions to mixtures of NaCl and $MgSO_4$, show that the voltage response time is in the order of tens of minutes up to several hours, due to ion exchange between the membranes and the feedwater. The voltage remains temporarily higher than in its steady state due to the gradual release of monovalent ions from the membrane interior in exchange for multivalent ions, as is visible in the concentration profiles in membrane cross-sections. This knowledge opens the possibility to improve the power density in practical applications of RED using varying concentrations of feedwater

References

1. Pattle, R. E., Production of Electric Power by mixing Fresh and Salt Water in the Hydroelectric Pile. *Nature* **1954,** *174*, (4431), 660-660.
2. Długołęcki, P. E.; Gambier, A.; Nijmeijer, K.; Wessling, M., Practical Potential of Reverse Electrodialysis As Process for Sustainable Energy Generation. *Environmental Science & Technology* **2009,** *43*, (17), 6888-6894.
3. Post, J. W.; Hamelers, H. V. M.; Buisman, C. J. N., Energy Recovery from Controlled Mixing Salt and Fresh Water with a Reverse Electrodialysis System. *Environmental Science & Technology* **2008,** *42*, (15), 5785-5790.
4. Logan, B. E.; Elimelech, M., Membrane-based processes for sustainable power generation using water. *Nature* **2012,** *488*, (7411), 313-319.
5. Ramon, G. Z.; Feinberg, B. J.; Hoek, E. M. V., Membrane-based production of salinity-gradient power. *Energy & Environmental Science* **2011,** *4*, (11), 4423-4434.
6. Veerman, J.; Saakes, M.; Metz, S.; Harmsen, G., Reverse electrodialysis: evaluation of suitable electrode systems. *Journal of Applied Electrochemistry* **2010,** *40*, (8), 1461-1474.
7. Vermaas, D. A.; Bajracharya, S.; Sales, B. B.; Saakes, M.; Hamelers, B.; Nijmeijer, K., Clean energy generation using capacitive electrodes in reverse electrodialysis. *Energy & Environmental Science* **2013,** *6*, (2), 643-651.
8. Burheim, O. S.; Liu, F.; Sales, B. B.; Schaetzle, O.; Buisman, C. J. N.; Hamelers, H. V. M., Faster Time Response by the Use of Wire Electrodes in Capacitive Salinity Gradient Energy Systems. *The Journal of Physical Chemistry C* **2012,** *116*, (36), 19203-19210.
9. Wick, G. L., Power from salinity gradients. *Energy* **1978,** *3*, (1), 95-100.

10. Isaacs, J. D.; Seymour, R. J., The ocean as a power resource. *International journal of Environmental Studies* **1973,** *4*, 201-205.
11. EIA, *International energy outlook 2011*. U.S. Department of Energy: Washington D.C., **2011**; 301 p.
12. Vermaas, D. A.; Veerman, J.; Yip, N. Y.; Elimelech, M.; Saakes, M.; Nijmeijer, K., High Efficiency in Energy Generation from Salinity Gradients with Reverse Electrodialysis. *Sustainable Chemistry & Engineering* **2013,** *1*, 1295−1302.
13. Vermaas, D. A.; Saakes, M.; Nijmeijer, K., Double Power Densities from Salinity Gradients at Reduced Intermembrane Distance. *Environmental Science & Technology* **2011,** *45*, (16), 7089-7095.
14. Vermaas, D. A.; Kunteng, D.; Saakes, M.; Nijmeijer, K., Fouling in reverse electrodialysis under natural conditions. *Water Research* **2013,** *47*, (3), 1289-1298.
15. Grebenyuk, V. D.; Chebotareva, R. D.; Peters, S.; Linkov, V., Surface modification of anion-exchange electrodialysis membranes to enhance anti-fouling characteristics. *Desalination* **1998,** *115*, (3), 313-329.
16. Lindstrand, V.; Jönsson, A.-S.; Sundström, G., Organic fouling of electrodialysis membranes with and without applied voltage. *Desalination* **2000,** *130*, (1), 73-84.
17. Post, J. W.; Hamelers, H. V. M.; Buisman, C. J. N., Influence of multivalent ions on power production from mixing salt and fresh water with a reverse electrodialysis system. *Journal of Membrane Science* **2009,** *330*, (1-2), 65-72.
18. Mehta, G. D., Performance of present-day ion-exchange membranes for power generation using a saturated solar pond. *Journal of Membrane Science* **1982,** *11*, 107-120.
19. Lacey, R. E., Energy by Reverse Electrodialysis. *Ocean Engineering* **1980,** *7*, (1), 1-47.
20. Veerman, J.; Saakes, M.; Metz, S. J.; Harmsen, G. J., Electrical Power from Sea and River Water by Reverse Electrodialysis: A First Step from the Laboratory to a Real Power Plant. *Environmental Science & Technology* **2010,** *44*, (23), 9207-9212.
21. Higa, M.; Tanioka, A.; Miyasaka, K., Simulation of the transport of ions against their concentration gradient across charged membranes. *Journal of Membrane Science* **1988,** *37*, (3), 251-266.
22. Higa, M.; Tanioka, A.; Miyasaka, K., A study of ion permeation across a charged membrane in multicomponent ion systems as a function of membrane charge density. *Journal of Membrane Science* **1990,** *49*, 145-169.
23. Tasaka, M.; Kiyono, R.; Yoo, D.-S., Membrane Potential across a High Water Content Anion-Exchange Membrane Separating Two Solutions with a Common Counterion but Two Different Co-ions. *The Journal of Physical Chemistry B* **1998,** *103*, (1), 173-177.
24. Higa, M.; Kira, A., Theory and simulation of ion transport in nonstationary states against concentration gradients across ion-exchange membranes. *The Journal of Physical Chemistry* **1992,** *96*, (23), 9518-9523.
25. Yip, N. Y.; Elimelech, M., Thermodynamic and Energy Efficiency Analysis of Power Generation from Natural Salinity Gradients by Pressure Retarded Osmosis. *Environmental Science & Technology* **2012,** *46*, (9), 5230-5239.
26. Chou, S.; Wang, R.; Fane, A. G., Robust and High performance hollow fiber membranes for energy harvesting from salinity gradients by pressure retarded osmosis. *Journal of Membrane Science* **2013,** *448*, (0), 44-54.
27. Brogioli, D., Extracting Renewable Energy from a Salinity Difference Using a Capacitor. *Physical Review Letters* **2009,** *058501*, 1-4.
28. Liu, F.; Schaetzle, O.; Sales, B. B.; Saakes, M.; Buisman, C.; Hamelers, H. V. M., Effect of additional charging and current density on the performance of Capacitive energy extraction based on Donnan Potential. *Energy & Environmental Science* **2012,** *5*, 8642-8650.
29. Ge, X.; Wang, X.; Zhang, M.; Seetharaman, S., Correlation and Prediction of Activity and Osmotic Coefficients of Aqueous Electrolytes at 298.15 K by the Modified TCPC Model. *Journal of Chemical & Engineering Data* **2007,** *52*, (2), 538-547.

30. Długołęcki, P. E.; Nijmeijer, K.; Metz, S. J.; Wessling, M., Current status of ion exchange membranes for power generation from salinity gradients. *Journal of Membrane Science* **2008,** *319*, (1-2), 214-222.

31. Veerman, J.; Saakes, M.; Metz, S. J.; Harmsen, G. J., Reverse electrodialysis: Performance of a stack with 50 cells on the mixing of sea and river water. *Journal of Membrane Science* **2009,** *327*, (1-2), 136-144.

32. Vermaas, D. A.; Saakes, M.; Nijmeijer, K., Power generation using profiled membranes in reverse electrodialysis. *Journal of Membrane Science* **2011,** *385-386*, (0), 234-242.

33. Galama, A. H.; Post, J. W.; Cohen Stuart, M. A.; Biesheuvel, P. M., Validity of the Boltzmann equation to describe Donnan equilibrium at the membrane-solution interface. *Journal of Membrane Science* **2013,** *442*, (0), 131-139.

34. Geise, G. M.; Paul, D. R.; Freeman, B. D., Fundamental water and salt transport properties of polymeric materials. *Progress in Polymer Science* **2013**.

35. Vermaas, D. A.; Saakes, M.; Nijmeijer, K., Enhanced mixing for energy generation in reverse electrodialysis. *Journal of Membrane Science (revisions submitted)* **2013**.

36. Vermaas, D. A.; Saakes, M.; Nijmeijer, K., Early detection of preferential channeling in reverse electrodialysis. *Electrochimica Acta (revisions submitted)* **2013**.

37. Hatzell, M. C.; Logan, B. E., Evaluation of Flow Fields on Bubble Removal and System Performance in an Ammonium Bicarbonate Reverse Electrodialysis Stack. *Journal of Membrane Science* **2013,** *446*, 449-455.

38. Daly, F. P.; Brown, C. W.; Kester, D. R., Sodium and magnesium sulfate ion pairing. Evidence from Raman spectroscopy. *The Journal of Physical Chemistry* **1972,** *76*, (24), 3664-3668.

39. Lide, D. R., ed., *CRC Handbook of Chemistry and Physics 2004-2005: A Ready-Reference Book of Chemical and Physical Data*. CRC press: **2004**; 2660 p.

40. Vermaas, D. A.; Kunteng, D.; Veerman, J.; Saakes, M.; Nijmeijer, K., Periodic feed water reversal and air sparging as anti fouling strategies in reverse electrodialysis. *Environmental Science & Technology (submitted)* **2013**.

41. Zabolotsky, V. I.; Nikonenko, V. V., Effect of structural membrane inhomogeneity on transport properties. *Journal of Membrane Science* **1993,** *79*, 181-198.

8

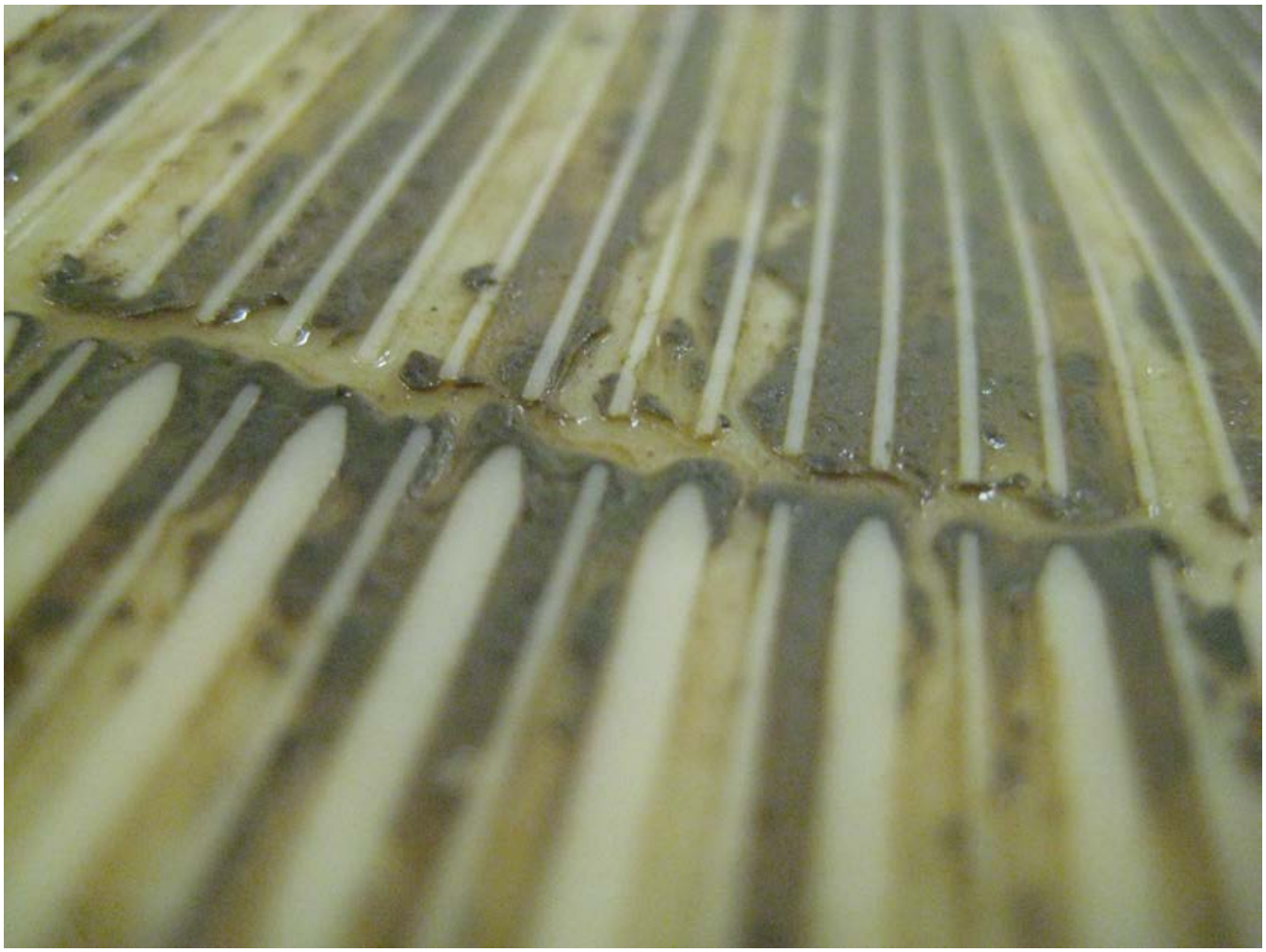

Chapter 9

Early detection of preferential channeling for effective fouling control

Abstract

Membrane applications often experience fouling, which prevent uniform flow distribution through the feedwater compartments, i.e., preferential channeling may occur. This research shows the effect of preferential channeling on energy generation from mixing salt water and fresh water using reverse electrodialysis (RED). The experimentally obtained power density, electrical resistance and pressure drop are evaluated for artificially controlled preferential channeling. The obtained power density decreases significantly when part of the feedwater compartment is inaccessible for flow; a blockage of only 10% of the feedwater compartments decreases the net power density by approximately 20%. When 80% of the feedwater channels is inaccessible, the net power densities are only marginally positive. This decrease in power density is due to an increase in non-ohmic resistance, which is related to the concentration changes in the feedwater compartments when ions are transported from the seawater to the river water side. Chronopotentiometric measurements show that the typical response time to establish a non-ohmic overpotential is an even more sensitive and easily scalable parameter to detect preferential channeling (and the presence of possible fouling) in an early stage. In practical applications, this response time can thus be used as an indicator for preferential channeling and serve to decide on and selectively apply cleaning in RED and other applications.

This chapter has been accepted for publication in *Electrochimica Acta* as

David A. Vermaas, Michel Saakes and Kitty Nijmeijer, Early detection of preferential channeling in reverse electrodialysis

9.1 Introduction

Renewable energy can be generated when waters with different salinity (e.g., river and seawater) mix. The theoretical potential of such a process is huge; considering the mixing of the global river discharge into the sea generates a decrease in Gibbs free energy in the order of 2 TW [1, 2]. The theoretical potential of this renewable energy source is comparable to the current global electricity consumption [3].

Reverse electrodialysis (RED) is one of the technologies that can capture the available energy when waters with different salinity mix. See Figure 9.1 for an illustration of the principle of RED. A RED module comprises ion exchange membranes selective for either cations (cation exchange membrane, CEM) or anions (anion exchange membrane, AEM). When waters with different salinity are supplied at either side of an ion exchange membrane, an electrical potential difference over the membrane (the Donnan potential) exists. When multiple cation and anion exchange membranes are stacked alternately, with fresh and salt water flowing in between, the voltage over these membranes accumulates. Electrodes and a reversible redox reaction [4, 5] or capacitive electrodes [6] can be used to transfer the ionic current into an electrical current.

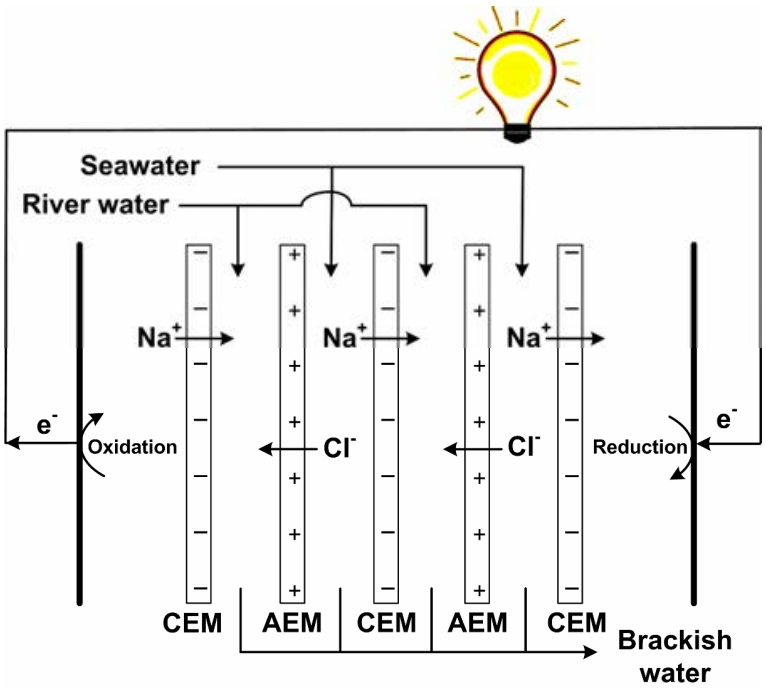

Figure 9.1: Principle of reverse electrodialysis (RED), in this case with 2 cells, each comprising an anion exchange membrane (AEM), a cation exchange membrane (CEM), seawater and river water. In this case, a (reversible) redox reaction is used to transfer the ionic current into an electrical current.

The obtained power per installed membrane area, i.e., the gross power density, was recently increased to more than 2 W/m^2 [7]. Improvements in power density have been obtained by reducing the intermembrane distance (i.e., thin feedwater compartments) and by removing the non-conductive spacers that serve to keep the membranes separated and provide a channel for the feedwater flow [8]. The use of profiled membranes, with ion conductive ridges on their surface, integrating the membrane and spacer functionality, makes the use of (non-conductive) spacers obsolete. A stack with such profiled membranes has a reduced ohmic resistance compared to a stack with non-conductive spacers. Additionally, it has a lower power consumption to pump the feed waters, overall resulting in a higher net power density [9].

These improvements significantly increased the obtained net power density for a RED module at laboratory conditions. However, in practical cases when natural feed waters are used, fouling occurs [10]. In that case, membrane stacks are subject to a non-uniform flow due to colloidal, chemical (i.e., scaling) or biological fouling [11]. Although stacks with profiled membranes are less sensitive to fouling compared to stacks with spacers, fouling was also observed in stacks with profiled membranes [10]. Fouling accumulates at positions with a locally lower velocity (such as spacer knits [10, 12-15] or irregularities of the membrane surface) thereby locally blocking the flow and further decreasing the local velocity in these regions. Hence, the non-uniformity of the feedwater distribution intensifies, such that in the end all feedwater flows over a very limited membrane area only, which limits the membrane area that is available for ion transport. In other applications, this is known as preferential channeling [12, 13].

As preferential channeling reduces the effective membrane area, the performance of the stack decreases (e.g., lower power density or higher pressure drop). Even at laboratory conditions without fouling, the uniformity of feedwater flow has a significant effect on the obtained power density in RED [9, 16]. Previous research showed that a uniform distribution of the feedwater in a RED stack due to improved inflows for the feed waters increased the net power density by more than 50% compared to a system with less uniform feedwater inflow [9, 16]. The non-ohmic resistance, due to the diffusive boundary layer near the membrane surface (also referred to as concentration polarization [17]) is only significant for a non-uniform distribution of the feedwater [16], as the diffusive boundary layers grow especially at zones with low velocity or even no flow (i.e., dead zones) [18]. The observed decrease in power density can thus indicate the occurrence of preferential channeling.

However, the power density is influenced by many other fluctuating factors as well, such as the feedwater salinities [19, 20], concentrations of multivalent ions [21] and possibly organic foulants [10], which camouflages the effects of preferential channeling at an early stage. Nevertheless, it is desired to detect preferential channeling at an early stage and distinguish this phenomenon from other factors. In that way, effective cleaning can be scheduled and performed before the performance is significantly reduced.

We present a method for early detection of preferential channeling in reverse electrodialysis, justified by laboratory experiments. First, a theoretical framework is given to describe the non-ohmic resistance. Then, chronopotentiometric experiments on RED stacks with artificially induced preferential channeling are presented, indicating the effects of preferential channeling. This research reveals what is the most sensitive and scale-independent method for an early detection of preferential channeling. This approach can be used to prevent preferential channeling in practical applications.

9.2 Theory

9.2.1 Generated voltage

At open circuit, the voltage over a RED stack is given by the Nernst equation, adapted for the number of membranes and corrected for the apparent permselectivity of the membranes, α (-):

$$E_{OCV} = N_m \cdot \alpha \frac{R \cdot T}{z \cdot F} \ln\left(\frac{\gamma_s \cdot c_s}{\gamma_r \cdot c_r}\right) \qquad \text{(eq. 9.1)}$$

In which E_{OCV} is the open circuit voltage (V), N_m is the number of membranes (-), R is the universal gas constant (8.314 J/(mol·K)), z is the valence of the ions (-), F is the Faraday constant (96485 C/mol), γ is the molar activity coefficient (-) and c is the salt concentration (M). The subscripts s and r indicate seawater and river water, respectively.

9.2.2 Resistance

When the electrical circuit is closed and the RED system can supply an electrical current, the voltage over the stack will decrease, caused by the electrical resistance of the stack. This stack resistance is composed of an ohmic resistance, due to the membrane resistance and the limited conductivity of the feed waters, and a non-ohmic resistance, which is due to the

change in concentrations when an electrical current is produced. The electrical current implies ion transport from the seawater side to the river water side. This ion transport results in a decrease in salinity difference over the membrane and as such the generated voltage decreases, as can be deduced from eq. 9.1. The corresponding decrease in electromotive force is defined as $\eta_{non\text{-}ohmic}$ (in V), similar to a concentration overpotential in other applications [4, 22]. The voltage over the stack, U (in V), can be described as:

$$U = E_{OCV} - \eta_{non-ohmic} - R_{ohmic} \cdot j \qquad \text{(eq. 9.2)}$$

Or, when $\eta_{non\text{-}ohmic}$ is normalized with respect to j:

$$U = E_{OCV} - \left(R_{ohmic} + R_{non-ohmic}\right) \cdot j \qquad \text{(eq. 9.3)}$$

In which R_{ohmic} is the ohmic area resistance and $R_{non\text{-}ohmic}$ is the non-ohmic area resistance (both in $\Omega \cdot m^2$) and j is the current density (A/m^2).

The ohmic and non-ohmic resistances can be distinguished in several ways, e.g., using impedance spectroscopy [23, 24], comparing AC- and DC-resistances [25] or using chronopotentiometry [1, 7, 9], which is used in the present research. The ohmic and non-ohmic resistances can be identified separately when a sudden change in electrical current is induced; the ohmic resistance causes a prompt change in stack voltage, while the response of the non-ohmic resistance is much slower and induces a gradual, time-dependent, change in stack voltage. A typical chronopotentiometric series for the electrode voltage (in time) is given in Figure 9.2, indicating the E_{OCV}, $\eta_{non\text{-}ohmic}$, R_{ohmic} and the typical time scale for establishing a steady voltage, τ (in s).

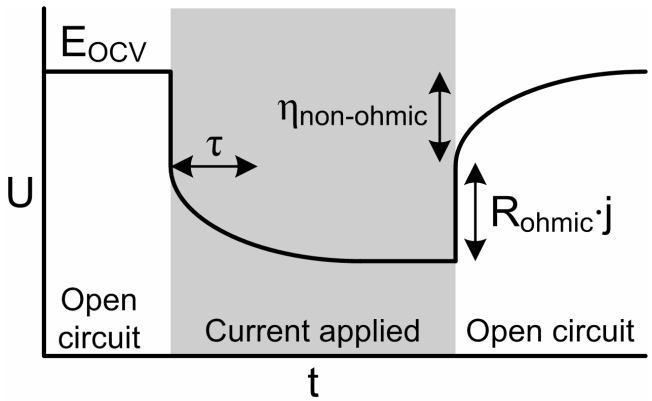

Figure 9.2: Example of chronopotentiometric series, in which the stack voltage is plotted versus time, revealing the ohmic and non-ohmic resistance.

In theory, the ohmic and non-ohmic resistances can be measured at the sudden start or at the sudden stop of each electrical current. However, the resistances are slightly dependent on the current density itself [9], due to the change in feed water concentrations (and the corresponding conductivity) as induced by the ion transport. Therefore, the resistances are most representative for the obtained power density when measured after a stage with electrical current i.e. at the sudden stop of the electrical current j, as indicated in Figure 9.2.

9.2.3 Typical time scales

A typical chronopotentiometric curve as shown in Figure 9.2 reaches a constant voltage when a current is applied for a longer time. The typical time scale for the voltage response, defined as the response time τ (in s), is dependent on the ionic transport in the RED stack. When the feedwater distributes uniform, convective transport of ions is dominant and τ can be assumed proportional to the average residence time of the feedwater. This assumes linearization of the relation between the salinity changes and voltage changes, which is acceptable for relatively small changes in concentration. The average residence time is derived from the compartment volume divided by the volumetric feedwater flow rate.

On the other hand, when part of the feedwater compartment is blocked and hence inaccessible for feedwater flow, the diffusion time scale t_D is considered as the typical time scale for the membrane area where the feedwater compartments at one or both sides have no flow. As the diffusion coefficients for Na^+ and Cl^- are unequal [26], and the diffusion length scale is not well defined, t_D can only be estimated roughly As a first approximation, the diffusion time scale can be estimated based on the thickness of both feed water compartments (d) squared divided by the average diffusion coefficient of the ionic species in water (D), i.e., $t_D = \frac{(2d)^2}{D}$. This diffusion time scale neglects the diffusion inside the membranes, which is acceptable because the ionic concentration inside the membrane is much higher than that in the feedwater due to the fixed membrane charge [27].Theoretically, diffusive transport to and from the feed water compartments without convective flow can also occur in lateral direction, i.e., parallel to the membranes. However, this transport is expected minor compared to the transport through the membranes, as the width of the feed water compartments is typically much larger than its thickness.

As shown in the previous paragraphs, physically based time scales can be derived for the channels that experience convective flow (i.e., residence time) and for channels that are

inaccessible (i.e., diffusion time scale). However, the overall time scale when feed water compartments are partly accessible and partly inaccessible is less well defined. Because the ion transport at the membrane area with flow and the membrane area without flow interact continuously, a common arithmetic average does not suffice. As a first proposal, the typical response time τ is assumed proportional to the weighted geometrical average of the residence time and the diffusion time scale. This can be expressed as:

$$\tau \propto t_{res}^{\,1-A} \cdot t_D^{\,A} \qquad \text{(eq. 9.4)}$$

In which t_{res} is the average residence time (s), t_D is the diffusion time scale (s) and A is the membrane area fraction that has no feed water flow at one or either side of the membrane (-). Although the use of a geometrical average is not proven for this situation, the individual time scales and the weighing factor A are physically grounded. When the degree of preferential channeling is similar in both the seawater compartment and the river water compartment, A can be approximated by:

$$A = 1 - (1 - \xi)^2 \qquad \text{(eq. 9.5)}$$

in which ξ is the fraction of the compartment volume that is inaccessible for feedwater flow (-).

9.2.4 Power density

The (gross) power density of a RED stack, P_{dens} (in W/m^2), is defined as the product of U and j, normalized for the total membrane area:

$$P_{dens} = \frac{U \cdot j}{N_m} \qquad \text{(eq. 9.6)}$$

The power density (eq. 9.6) and the stack voltage U (eq. 9.3) are both a function of the current density j. A maximum power density can be found when optimizing the current density. When substituting eq. 9.3 in eq. 9.6, this maximum gross power density (in W/m^2) is given by:

$$P_{dens,\max} = \frac{E_{OCV}^{\,2}}{4\left(R_{ohmic} + R_{non-ohmic}\right)N_m} \qquad \text{(eq. 9.7)}$$

The obtained gross power density is partly consumed to pump the feedwater through the feedwater compartments. The maximum gross power density minus the power consumed for pumping yields the net power density.

9.2.5 Pressure drop

In addition to the chronopotentiometric series, preferential channeling can be detected by an increased pressure drop over the feedwater compartments. For laminar flow in channels without spacers, the pressure drop over a feedwater compartment is directly proportional to the flow velocity, thus inversely proportional to the cross-sectional area that is available for water flow. When part of the feedwater compartments is inaccessible for feedwater flow, and when laminar flow between parallel membranes is assumed [28], the pressure drop over the feedwater compartments (Δp, in Pa) can be described by:

$$\Delta p = \frac{12\mu \cdot L \cdot \Phi}{(1-\xi) \cdot A_{cross} \cdot D_h{}^2} \qquad \text{(eq. 9.8)}$$

In which μ is the viscosity of feedwater (Pa·s), L is the length of the feedwater compartments (m), Φ is the feedwater flow rate (m^3/s), A_{cross} is the cross-sectional area in the feedwater compartments (m^2) and D_h is the hydraulic diameter of the feedwater compartments (m).

9.3. Experimental setup

9.3.1 Stack design

RED stacks were composed of 5 cells, each consisting of a CEM and an AEM (Ralex CMH/AMH, MEGA AS, Czech Republic), as illustrated in Figure 9.3. The compartments for feedwater were created by ridges on the membrane surface with dimensions of approximately 200 μm high and 300 μm wide. The feedwater channels created in this way are in dry form 200 μm in height and 1900 μm in width. In wet shape, the channels are approximately 240 μm in height, as measured with a digital thickness gauge (Mitutoyo 547-401, Japan). The profiled geometry on the membrane was created by hot pressing of a flat membrane into a mould for 10 minutes at 140 ºC and 200 bar [9]. The ridges in compartments for one type of feedwater are perpendicular to the ridges of the other feedwater type, to allow cross-flow of both feed waters (see Figure 9.3A).

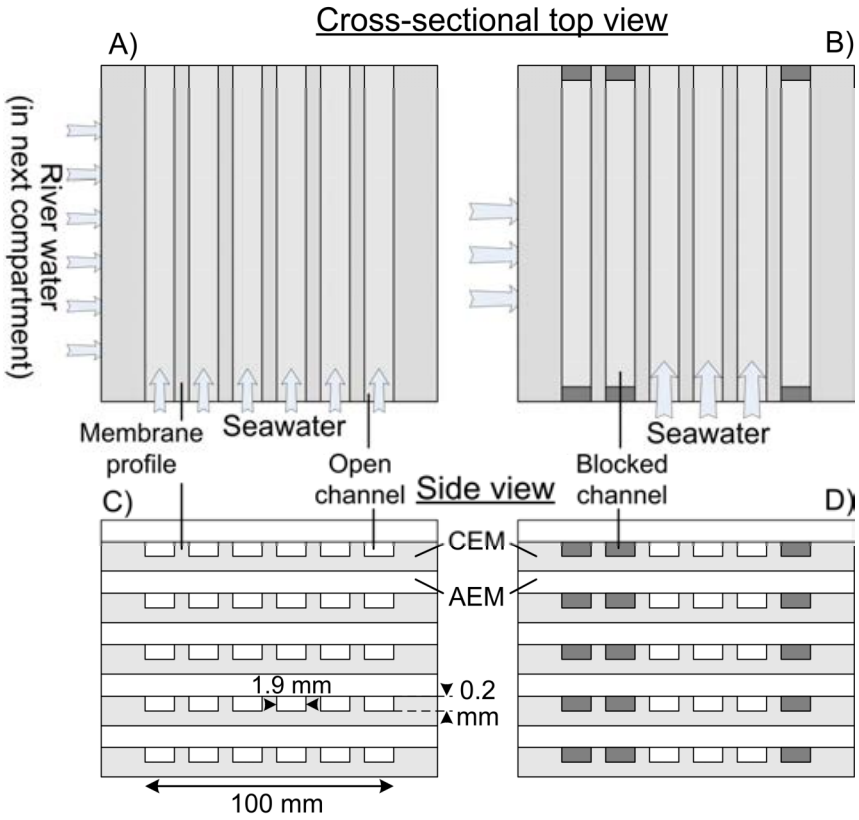

Figure 9.3: Illustration of feedwater compartment geometry in which all channels are open (A and C) and in which 50% of the feedwater channels are inaccessible (B and D). The membrane stack and profiles are not on scale. The upper illustrations (A and B) show a seawater compartment in a cross-sectional top view of the membrane stack, i.e., perpendicular to the membrane surface. At the other side of the membrane, river water is flowing perpendicular to the seawater flow. The lower illustrations (C and D) show a side view of the membrane stack.

The five membrane pairs were stacked between two endplates with a Ti/Pt mesh electrode (MAGNETO special anodes B.V., The Netherlands) with an area of 10 cm by 10 cm. The resistance of the electrodes and the corresponding electrode compartments was subtracted from the resistance of the total stack, as the electrodes would not contribute significantly to the stack resistance for large scale applications. Each feedwater compartment was open for one feedwater type (artificial river water or seawater) and sealed for the other type by means of an extra wide profile ridge at the sides of the profiled membrane (Figure 9.3A-B).

The feed waters were inserted into the feedwater compartment using a feedwater chamber, 1 mm thick, that acts as a manifold (i.e., feedwater distribution chamber) attached to each side of the membrane stack (REDstack B.V., The Netherlands). These manifolds allow the feed waters to distribute evenly over the full width of the feedwater compartments, and hence create a uniform feedwater flow covering the full membrane area.

Preferential channeling (i.e., non-uniform feedwater flow) was induced by covering part of the inflow and outflow of the channels created by the membrane profiles (Figure 9.3B and 9.3D). 0%, 10%, 30%, 50% or 80% of the feedwater channels was covered (Toupret, white putty, France). The stack was brought under (brackish, 0.25 M NaCl) water when covering the channels and only the inflow and outflow of these channels were closed with putty (Figure 9.3B), such that the interior of the covered feedwater channels was still filled with feedwater, to be representative for stacks in practical applications with preferential channeling. As the straight profiled channels confine the feedwater without rebuilding the membrane pile, the stack performance (e.g., power density) before and after blocking part of the feedwater channels can be directly compared.

For seawater, an artificial solution of 0.508 M NaCl (ESCO, The Netherlands, 99.5% pure NaCl) was used and river water was represented by an artificial solution of 0.017 M NaCl. Feed waters were pumped at flow rates of 10, 25, 50, 80, 120, 180 and 250 ml/min, independent of the percentage of feedwater channels that were covered. In case all feed water channels are accessible for flow, this corresponds to average flow velocities between 0.2 and 4.1 cm/s. The pressure difference over the feedwater channels was measured (Endress+Hauser, Deltabar S, Germany). A solution of 0.25 M NaCl and 0.05 M $Fe(CN)_6^{3-/4-}$ at a constant flow rate of 150 ml/min was used as electrode rinse solution and kept at a constant overpressure of 300 mbar (which is always beyond the pressure in the RED cells) to ensure that all membranes are closely packed together.

9.3.2 Electrochemical measurements

A chronopotentiometric measurement series, with current densities of 5, 10, 15 and 20 A/m^2 was applied for at least 50 times the average residence time of the feedwater. For example, at a flow rate of 50 ml/min, the residence time of the feedwater is approximately 12 s and consequently each current density was applied for 600 s. In between all current densities, a period without current (OCV) was applied for the same duration as for the steps with electrical current.

Chronopotentiometry was conducted using a galvanostat (Ivium technologies, The Netherlands) at a sample rate of 20 Hz. Data was post-processed with Matlab (Mathworks, v7.7). All measurements were duplicated, using two different stacks, to verify the reproducibility. Average values of these two measurement series and corresponding standard errors are presented.

9.4 Results

9.4.1 Chronopotentiometry

Typical experimentally measured chronopotentiometric series, for cases when all feedwater channels are open and cases when part of the feedwater channels is inaccessible are shown in Figure 9.4.

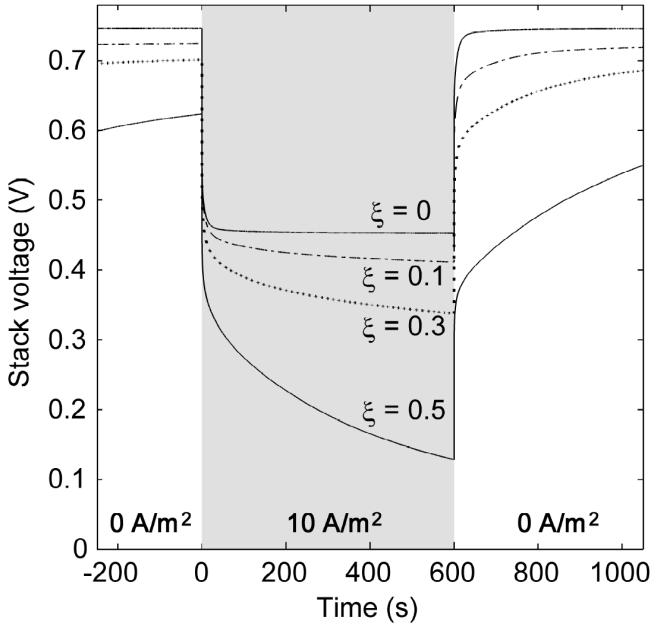

Figure 9.4: Chronopotentiometric series for stacks in which all feedwater channels were open (ξ = 0) or a part of the feedwater channels were artificially blocked (ξ = 0.1, 0.3 and 0.5), all with a feedwater flow rate of 50 ml/min. The time is set to t = 0 at the start of the electrical current.

Figure 9.4 shows that the voltage decreases when an electrical current is applied, due to the electrical resistance of the stack. The sudden decrease in voltage is due to the ohmic resistance, while the remaining gradual decrease is due to the non-ohmic resistance, as indicated earlier in Figure 9.2. Figure 9.4 indicates that a lower voltage is obtained when part of the feedwater compartment is inaccessible, i.e., when preferential channeling occurs. Moreover, the voltage does not stabilize within 600 s in these cases (i.e., $\xi \geq 0.1$), while the voltage reaches a constant value within 100 s when all channels are open (ξ = 0). Even at much longer sample times (4000 s per step) the voltage does not reach a constant value for $\xi \geq 0.1$ (results not shown).

The extremely slow response of the produced stack voltage disables to derive the (non-ohmic) resistance and thus the power density within a reasonable time interval in cases with

$\xi \geq 0.1$. To be able to compare and quantify the ohmic resistance, non-ohmic resistance and power density, the experimental data were fitted and extrapolated using an analytical equation. The experimentally obtained chronopotentiometry curves as shown in Figure 9.4 are non-linearly dependent on the current density, the flow velocity and distribution thereof, the absolute concentrations and the concentration gradients in 3 dimensions. Non-stationary concentration profiles are already highly complicated in simplified one-dimensional cases without feedwater flow [29-32]. Using additionally non-uniform flow distributions, the complexity of such functions thus disables to describe the voltage series in a theoretically derived analytical equation. Therefore, the experimental data are fitted using an empirical function. As presented in Appendix A, a hyperbolic function fits better than an exponential function. Each step of the chronopotentiometric series can be best described by:

$$U = \beta_1 \cdot \left(\frac{1}{t/\tau + 1} \right) + \beta_2 \qquad \text{(eq. 9.9)}$$

In which β_1, β_2 and τ are parameters to fit each stage of the experimental series and t is the time after the start or stop of the electrical current (s). The parameter β_1 acts as the (extrapolated) amplitude of the non-ohmic overpotential (V), β_2 acts as the voltage at the start or stop of the electrical current (V) and τ is the response time (s). For a perfect fit of a series where an electrical current is instantaneously applied, these parameters are:

$\beta_1 = - \eta$

$\beta_2 = E_{OCV} - R_{ohmic} \cdot j$

At $t = \tau$, 50% of the non-ohmic overpotential is achieved, i.e., $U = E_{OCV} - 0.5 \cdot \eta - R_{ohmic} \cdot j$. In other words, τ can be interpreted as the half-life to establish a steady voltage.

The response time τ is larger when an electrical current is interrupted than when an electrical current is applied. In other words, the voltage response is faster for the transition from OCV to electrical current than for the opposite case. This is demonstrated and explained in Appendix B. Moreover, τ appears to be dependent on the current density when a current is interrupted (OCV), while it to less extent dependent on the current density when a current is applied, as also elaborated on in appendix B. Because this research focuses on the effect of preferential channeling rather than on the current density, this research only uses the response time τ derived from the steps when a current is applied.

9.4.2 Resistance

Using the hyperbolic fits, the ohmic and non-ohmic resistances of each voltage curve can be distinguished, as presented in Figure 9.5 as a function of the feedwater flow rate. Graphs are created for cases with 0%, 10%, 30%, 50% and 80% of the feedwater channels blocked.

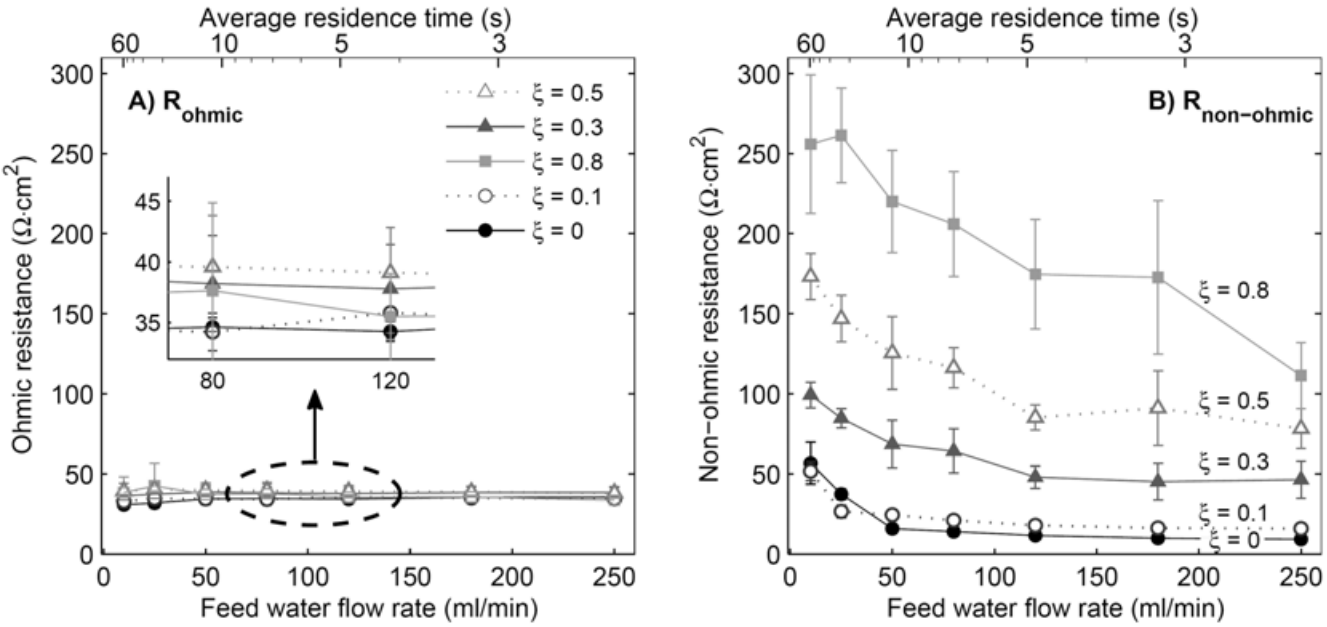

Figure 9.5: Ohmic resistance (A) and non-ohmic resistance (B) as a function of the feedwater flow rate for stacks in which all feedwater channels are open (ξ = 0) or part of the feedwater channels is inaccessible (ξ = 0.1, 0.3, 0.5 and 0.8). A zoomed section is inserted in Figure 9.5A. The average residence time is based on the total (accessible+ inaccessible) compartment volume.

Figure 9.5 shows that the ohmic resistance is rather independent of the feedwater flow rate, while the non-ohmic resistance decreases significantly for increasing flow rate, in agreement with previous research [7, 9, 16, 25]. The non-ohmic resistance decreases with increasing flow rates because the salinity difference between the seawater compartment and the river water compartment has less time to decrease and the larger velocity shear decreases the diffusive boundary layer thickness [16, 23, 32]. As a consequence, the electromotive force remains higher at higher flow rates, and therefore the non-ohmic resistance is lower.

This does not play a role for the ohmic resistance, which is determined by the membrane resistance and conductivity of the feedwater. The ohmic resistance is also independent of the feedwater blockage, as the slight differences in ohmic resistance are insignificant (Figure 9.5A). Although the river water in the channels that are blocked is more conductive (due to accumulated ion transport) compared to the case without preferential channeling (ξ = 0), this

does not have a significant effect on the ohmic resistance. Modeling already showed that the ion transport intensifies in only a small part of the membrane area, where the salinity difference over the membrane is highest, even when the feedwater compartments are accessible [33, 34]. This part of the membrane area with highest current density contributes most to the ohmic voltage loss. Consequently, the observed ohmic resistance is mainly determined by the membrane area where feedwater flow is apparent at both sides of the membrane. Therefore, the ohmic resistance is independent of (the degree of) preferential channeling, even though the feedwater concentrations can be different in the inaccessible part of the feedwater compartments. When the preferential channeling would increase even further, i.e., $0.8 < \xi < 1$, the current density will intensify even more, which will create a larger ohmic voltage loss, and the observed ohmic resistance is expected to increase significantly.

The non-ohmic resistance, however, increases rapidly when part of the feedwater channels is inaccessible ($\xi > 0$), as demonstrated in Figure 9.5B. The effect is even more amplified when the Reynolds number (or linear flow velocity) is used instead of the flow rate, as the feedwater is confined to a smaller cross sectional area when part of the feedwater channels is inaccessible. Also, when considering the residence time based on the open compartment volume only, the differences between the graphs in Figure 9.5B would be even larger. The increase of the non-ohmic resistance due to preferential channeling is clear when considering the case with $\xi = 0.3$; the non-ohmic resistance is approximately 4 times higher in this case compared to the case when all feedwater channels are open. For comparison, the non-ohmic resistance is even larger than the ohmic resistance for all flow rates when considering preferential channeling with $\xi \geq 0.3$. This emphasizes that a relatively small dead zone has a major impact on the non-ohmic resistance and total stack resistance in RED. This increase in non-ohmic resistance is due to the decreasing salinity difference over the membranes at the dead zones. As the water is not supplied at these dead zones, the salinity difference decreases, which decreases the electromotive force. This is observed as a non-ohmic resistance.

9.4.3 Power density

The strong increase in non-ohmic resistance in cases with preferential channeling is visible in the obtained power density as well. These maximum gross and net power densities are shown in Figure 9.6, as a function of the flow rate for several degrees of preferential channeling.

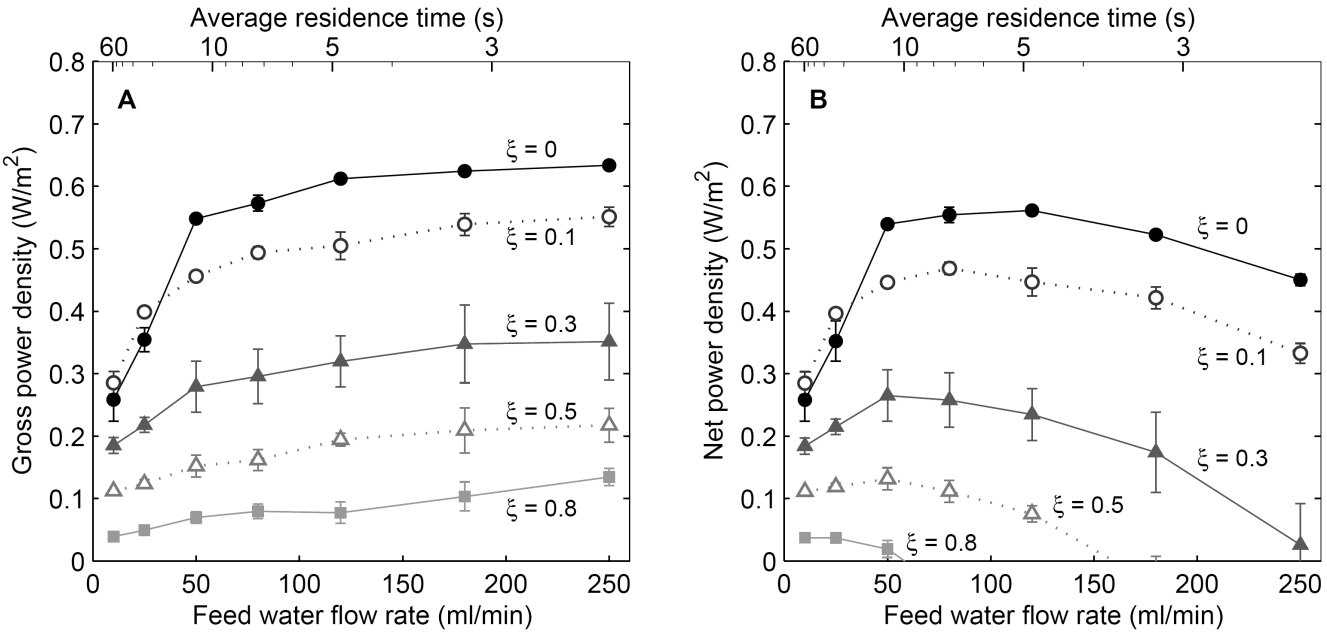

Figure 9.6: Gross power density (A) and net power density (B) as a function of the feedwater flow rate for stacks in which all feedwater channels are open (ξ = 0) or part of the feedwater channels is inaccessible (ξ = 0.1, 0.3, 0.5 and 0.8).

Figure 9.6A shows that the gross power density increases with increasing flow rate, which is in agreement with the decreasing (non-ohmic) resistance and previous experiments [7, 9, 25]. Furthermore, the power density decreases when preferential channeling occurs. Because the ohmic resistance (Figure 9.5A) and the open circuit voltage (not shown) are rather independent of the occurrence of preferential channeling, this decrease in power density is only due to the increase in non-ohmic resistance (Figure 9.5B). The effect of preferential channeling is significant because the gross power density almost halves when only 30% of the feedwater compartments is inaccessible.

When taking into account the power consumed to pump the feed waters (Figure 9.6B), the effect of preferential channeling is even more pronounced. The pumping power increases when preferential channeling occurs, which results in a lower net power density. Also, the maximum obtainable net power density shifts towards lower flow rates when larger part of the feedwater compartment is inaccessible. When 80% of the feedwater compartment is inaccessible, the net power density remains only positive at very low flow rates (Φ < 60 ml/min), while at higher flow rates the system would consume energy to operate.

9.4.4 Indicators for preferential channeling

These results show the significant effect of preferential channeling on the obtained power density. However, the power density is not a useful indicator for preferential channeling, as many other factors influence the power density as well. Besides that fixed properties such as membrane properties [35-37], compartment thickness [7] and the spacer shadow effect [8] have a major impact on the power density, also fluctuating properties such as salinity differences [19, 20], salt composition [21] temperature [25] and possibly organic fouling [10] influence the power density and therefore mask an early stage of preferential channeling.

Three options are considered as indicator for preferential channeling:

1. The increase in pressure difference over a feedwater channel is considered, because this parameter is often used to monitor fouling or preferential channeling in other technologies [12, 13, 38].
2. The non-ohmic resistance showed to be sensitive to preferential channeling (Figure 9.5B) and is therefore also considered as an indicator for preferential channeling.
3. The response time, τ, is considered as an indicator for preferential channeling.

The pressure drop, non-ohmic resistance and response time τ are plotted as function of the degree of blockage of the feedwater channels (ξ) in Figure 9.7.

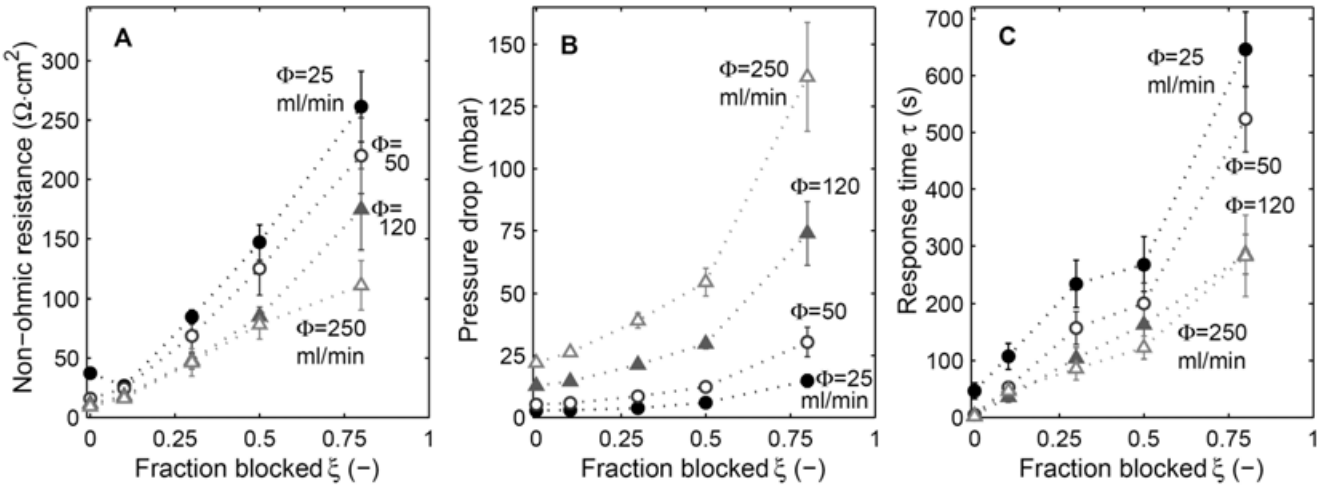

Figure 9.7: Non-ohmic resistance (A), pressure drop (B), and response time (C) as a function of the fraction of the feedwater compartments that is inaccessible for different feedwater flows (25, 50, 120 and 250 ml/min).

Figure 9.7 shows that the non-ohmic resistance, pressure drop and τ all increase when the fraction of inaccessible channels increases. These three parameters will be discussed individually.

The non-ohmic resistance shows relatively large increases when a small part of the feedwater compartment is inaccessible (38% increase on average at $\xi = 0.1$ compared to $\xi = 0$) as demonstrated in Figure 9.7A. Hence, a large non-ohmic resistance discloses preferential channeling, except for some data at the lowest flow rates (25 ml/min or less). Therefore, the non-ohmic resistance can be used as indicator for preferential channeling, especially when using sufficient high flow rates.

The pressure drop increases when a part of the feedwater compartments are inaccessible due to confinement of the cross-sectional area available for the feedwater (Figure 9.7B). The experimentally obtained pressure drop is inversely proportional to $(1 - \xi)$, which is in agreement with the theoretical pressure drop as given in eq. 9.8. Although the pressure drop can be monitored easily, the pressure drop is not very accurate as an early warning for preferential channeling, because this parameter is rather insensitive when ξ is small. When the pressure drop starts to increase significantly, a high degree of preferential channeling has been reached already. Moreover, the pressure drop would also increase in cases with an evenly distributed fouling layer. Hence, the increase in pressure drop can detect fouling, but does not distinguish between preferential channeling and evenly distributed fouling.

The values of τ increase most pronounced of all parameters and τ is sensitive to only small changes in preferential channeling over the full range of ξ (Figure 9.7C). Blockage of only 10% of the feedwater channels increases τ tenfold on average. The increase is best visible at flow rates higher than 25 ml/min. The increase in response time would be even more spectacular when τ would be plotted against the actual flow velocity in the open channels only (which is higher as part of the channels is blocked) instead of the total flow rate. The large response time for stacks with preferential channeling, i.e., the slow response of the non-ohmic overpotential, is explained by the slow diffusive transport at the dead zones in the feedwater compartment and the feedback mechanism with the other part of the feedwater compartment. In the channels that are inaccessible for feed water flow, convection is absent and a thick diffusive boundary layer will slowly develop. In other words, the seawater compartments will desalinate most pronounced at the dead zones, and the salinity will increase most at the river water compartments of the dead zones. As a consequence, the electromotive force over the membrane at the dead zones will decrease and the electrical

current will redistribute such that the current density is intensified at areas where feed waters are rinsed, maintaining a larger electromotive force.

This redistribution of current density implies a low current density in the channels that are inaccessible for feed water. The ion transport within a feed water compartment can be facilitated by convection (i.e., water flow), migration (due to an electric field) or diffusion (due to concentration changes). The dead zones experience no convective flow and only small electrical current, which disables ion transport by convection and strongly limits the transport by migration. Hence, only diffusive transport can establish the concentrations in these dead zones that match the stack voltage as generated by the rest of the stack. The voltage can only be stationary at those dead zones when the diffusive boundary layer covers the full compartment thickness. Because diffusive ion transport is very slow, the typical time scale to establishing a steady state voltage (i.e., τ) strongly increases when preferential channeling occurs.

Although the transport in the inaccessible part of the feed water compartment is much slower than in the part with feed water flow, a high residence time (equivalent to low flow rate) does increase the response time even further (Figure 9.7C). Because the current density is intensified in the part of the compartment where feed water is supplied, the ohmic and non-ohmic loss are larger in this area of the stack. The stack voltage is only stationary when the concentration within each channel is such that the corresponding locally generated voltage over the membrane minus the local ohmic loss is in dynamic equilibrium for all positions on the membrane. Hence, the feedback between the inaccessible and the accessible part of the feed water compartment further increases the response time.

9.4.5 Response time

Although all three parameters in Figure 9.7 increase when part of the feedwater compartment is inaccessible, the response time τ is the most sensitive parameter to monitor early stages of preferential channeling (i.e., at low ξ). Moreover, the response time can be expressed in a residence time, diffusion time scale and ξ only, which simplifies the use of τ at different scales and different stack modes (e.g., with spacers or profiled membranes).

The relation between the experimentally obtained response time τ and the typical physical time scales, $t_{res}^{1-A} \cdot t_D^{A}$, is shown in Figure 9.8 for all data (i.e., all flow rates ranging from 10 – 250 ml/min and all degrees of preferential channeling). A diffusion time scale of 177 s was used, based on twice the wet compartment thickness squared divided by the average

diffusion coefficient of Na^+ and Cl^- [26]. Because the inaccessible feed water channels are much wider (in the order of cm) than its thickness (240 μm), lateral diffusive transport can be neglected.

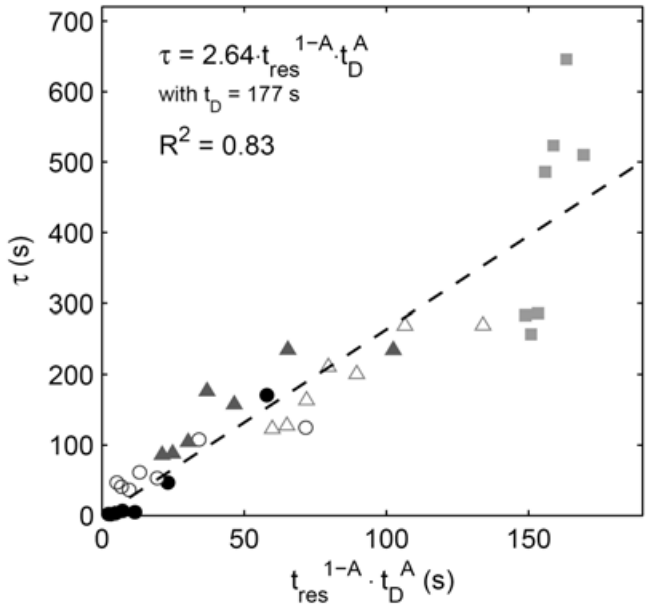

Figure 9.8: Experimentally obtained response time τ versus weighted time scale $t_{res}^{1-A}\cdot t_D^A$, for all data obtained for different flow rates (ranging from 10 to 250 ml/min) and different degrees of preferential channeling. The symbols indicate ●: ξ = 0; o: ξ = 0.1; ▲: ξ = 0.3; Δ: ξ = 0.5 and ■: ξ = 0.8. The dashed line represents the best fit, corresponding to $2.64\cdot t_{res}^{1-A}\cdot t_D^A$, using t_D = 177 s.

Figure 9.8 shows that the response time τ reasonably fits when plotted as function of $t_{res}^{1-A}\cdot t_D^A$, as predicted in eq. 9.4. The scatter around the trendline is mostly because the data presented are measured over a wide range of residence times (between 2 and 58 s) and over a wide range of preferential channeling (between 0% and 80%), while the relation in eq. 9.4 simplifies the effects of flow rate and preferential channeling. The scatter is most pronounced for ξ = 0.8, as the response time is very large for this severe preferential channeling and hence other temporal fluctuations (e.g., in temperature) weaken the fit of the chronopotentiometric curve. Despite this scatter, the coefficient of determination (R^2 = 0.83) is reasonable high, considering the fact that the used residence times and the diffusion time scale of 177 s are physically grounded. The correlation is slightly better when a somewhat higher diffusion time scale of 240 s (R^2 = 0.84) is used, but this time scale is not physically justified.

9.5 Outlook

As the residence time includes the stack dimensions and the diffusion time scale involves the intermembrane distance and compartment type, we infer that the given relation between the response time τ and $t_{res}^{1-A} \cdot t_D^{A}$ is also valid for RED stacks with different dimensions or different feedwater compartments (e.g., spacers). Therefore, the response time τ, as obtained with chronopotentiometry, can be used as a sensitive tool for early detection of preferential channeling in RED stacks on laboratory scale as well as on larger scale. For large scale operation, the response time can be derived when switching from one current density to another current density, instead of using current interrupts, to prevent a stop in power production. Consequently, preferential channeling can be detected on line and cleaning treatments can be applied selectively, which results in a high power density with a minimum cleaning effort. Using the present mechanism for early detection of preferential channeling, future research can be directed towards methods that specifically clean colloidal fouling and hence solve preferential channeling.

Although this paper focused on the occurrence of preferential channeling using seawater and river water feeds, the same approach will be useful for preferential channeling for RED stacks with other feed types. For example, the use of the response time may be useful to detect non-uniform flow due to stagnant air bubbles e.g. when using salinity gradients in thermolytic solutions of ammonium bicarbonate, to generated energy from waste heat [18].

Other applications, especially applications using ion exchange membranes such as electrodialysis and microbial fuel cells, may experience the same effect on the response time when preferential channeling occurs. These applications experience scaling [39] and biofouling [40] that can alter the flow field, i.e., create preferential channeling. Future research to the response time in these applications may also distinguish preferential channeling from other factors that influence the performance. Hence, a selective cleaning measure (e.g., reverse polarization or cleaning agents) can be applied to solve this type of fouling in practical applications.

9.6 Conclusions

Preferential channeling is often observed when fouling in membrane applications occurs, where part of the feedwater compartments is blocked due to colloidal fouling or scaling. This research shows that the experimentally obtained power density in reverse electrodialysis (RED) decreases significantly when (artificial) preferential channeling occurs. The net

power decreases with approximately 20% when only 10% of the feedwater channels is inaccessible for flow. When 80% of the feedwater channels is inaccessible, the net power densities are only marginally positive. This decrease in power density is mainly caused by an increase in non-ohmic resistance, which is related to the concentration changes in the feedwater compartments when ions are transported from the seawater to the river water side. In the present design, where we used profiled membranes instead of non-conductive spacers, the non-ohmic resistance even dominates the ohmic resistance when at least 30% of the feedwater channels is inaccessible. The large increase in non-ohmic resistance can be used as an indicator for the occurrence of preferential channeling in practical cases. However, the time scale to establish a steady non-ohmic overpotential increases even more pronounced and therefore this typical time scale is an even more sensitive parameter to detect preferential channeling in early stages. To quantify this typical time scale to establish a steady state non-ohmic overpotential, we introduce the response time τ, which can be derived from a chronopotentiometric series. This research shows that the response time τ can be related to the degree of preferential channeling, normalized for flow rates and stack dimensions. Therefore, this method can be used in practice as an early detection for preferential channeling in RED stacks, which helps to use cleaning treatments more effectively and hence maintain a high power density.

References

1. Post, J. W.; Hamelers, H. V. M.; Buisman, C. J. N., Energy Recovery from Controlled Mixing Salt and Fresh Water with a Reverse Electrodialysis System. *Environmental Science & Technology* **2008,** *42*, (15), 5785-5790.
2. Wick, G. L., Power from salinity gradients. *Energy* **1978,** *3*, (1), 95-100.
3. EIA, *International energy outlook 2010*. U.S. Department of Energy: Washington D.C., **2010**; 328 p.
4. Burheim, O. S.; Seland, F.; Pharoah, J. G.; Kjelstrup, S., Improved electrode systems for reverse electro-dialysis and electro-dialysis. *Desalination* **2012,** *285*, (0), 147–152.
5. Veerman, J.; Saakes, M.; Metz, S.; Harmsen, G., Reverse electrodialysis: evaluation of suitable electrode systems. *Journal of Applied Electrochemistry* **2010,** *40*, (8), 1461-1474.
6. Vermaas, D. A.; Bajracharya, S.; Sales, B. B.; Saakes, M.; Hamelers, B.; Nijmeijer, K., Clean energy generation using capacitive electrodes in reverse electrodialysis. *Energy & Environmental Science* **2013,** *6*, (2), 643-651.
7. Vermaas, D. A.; Saakes, M.; Nijmeijer, K., Double Power Densities from Salinity Gradients at Reduced Intermembrane Distance. *Environmental Science & Technology* **2011,** *45*, (16), 7089-7095.
8. Długołęcki, P. E.; Dąbrowska, J.; Nijmeijer, K.; Wessling, M., Ion conductive spacers for increased power generation in reverse electrodialysis *Journal of Membrane Science* **2010,** *347*, (1-2), 101-107.
9. Vermaas, D. A.; Saakes, M.; Nijmeijer, K., Power generation using profiled membranes in reverse electrodialysis. *Journal of Membrane Science* **2011,** *385-386*, (0), 234-242.

10. Vermaas, D. A.; Kunteng, D.; Saakes, M.; Nijmeijer, K., Fouling in reverse electrodialysis under natural conditions. *Water Research* **2013,** *47*, (3), 1289-1298.
11. Post, J. W. Blue Energy: electricity production from salinity gradients by reverse electrodialysis. PhD thesis Wageningen University, **2009**.
12. Vrouwenvelder, J. S.; Schulenburg, D. A. G. v. d.; Kruithof, J. C.; Johns, M. L.; Loosdrecht, M. C. M. v., Biofouling of spiral-wound nanofiltration and reverse osmosis membranes: A feed spacer problem. *Water Research* **2009,** *43*, (3), 583-594.
13. Picioreanu, C.; Vrouwenvelder, J. S.; Loosdrecht, M. C. M. v., Three-dimensional modeling of biofouling and fluid dynamics in feed spacer channels of membrane devices. *Journal of Membrane Science* **2009,** *345*, (1-2), 340–354.
14. Vrijenhoek, E. M.; Hong, S.; Elimelech, M., Influence of membrane surface properties on initial rate of colloidal fouling of reverse osmosis and nanofiltration membranes. *Journal of Membrane Science* **2001,** *188*, (1), 115-128.
15. Graf von der Schulenburg, D. A.; Vrouwenvelder, J. S.; Creber, S. A.; van Loosdrecht, M. C. M.; Johns, M. L., Nuclear magnetic resonance microscopy studies of membrane biofouling. *Journal of Membrane Science* **2008,** *323*, (1), 37-44.
16. Vermaas, D. A.; Saakes, M.; Nijmeijer, K., Enhanced mixing for energy generation in reverse electrodialysis. *Journal of Membrane Science (submitted)* **2013**.
17. Tanaka, Y., Concentration polarization. In *Ion exchange membranes: Fundamentals and Applications*, **2007**; pp 97-137.
18. Hatzell, M. C.; Logan, B. E., Evaluation of Flow Fields on Bubble Removal and System Performance in an Ammonium Bicarbonate Reverse Electrodialysis Stack. *Journal of Membrane Science* **2013,** *446*, 449-455.
19. Daniilidis, A.; Vermaas, D. A.; Herber, R.; Nijmeijer, K., Effect of salinity gradient on power output in reverse electrodialysis. *Renewable energy* **2013**, (submitted).
20. Tedesco, M.; Cipollina, A.; Tamburini, A.; van Baak, W.; Micale, G., Modelling the Reverse ElectroDialysis process with seawater and concentrated brines. *Desalination and Water Treatment* **2012,** *49*, (1-3), 404-424.
21. Post, J. W.; Hamelers, H. V. M.; Buisman, C. J. N., Influence of multivalent ions on power production from mixing salt and fresh water with a reverse electrodialysis system. *Journal of Membrane Science* **2009,** *330*, (1-2), 65-72.
22. Cooke, B. A., Concentration polarization in electrodialysis I. The electrometric measurement of interfacial concentration. *Electrochimica Acta* **1961,** *3*, (4), 307-317.
23. Długołęcki, P. E.; Ogonowski, P.; Metz, S. J.; Saakes, M.; Nijmeijer, K.; Wessling, M., On the resistances of membrane, diffusion boundary layer and double layer in ion exchange membrane transport. *Journal of Membrane Science* **2010,** *349*, (1-2), 369-379.
24. Sistat, P.; Kozmai, A.; Pismenskaya, N.; Larchet, C.; Pourcelly, G.; Nikonenko, V., Low-frequency impedance of an ion-exchange membrane system. *Electrochimica Acta* **2008,** *53*, (22), 6380-6390.
25. Długołęcki, P. E.; Gambier, A.; Nijmeijer, K.; Wessling, M., Practical Potential of Reverse Electrodialysis As Process for Sustainable Energy Generation. *Environmental Science & Technology* **2009,** *43*, (17), 6888-6894.
26. Lide, D. R., ed., *CRC Handbook of Chemistry and Physics 2004-2005: A Ready-Reference Book of Chemical and Physical Data*. CRC press: **2004**; 2660 p.
27. Galama, A. H.; Post, J. W.; Cohen Stuart, M. A.; Biesheuvel, P. M., Validity of the Boltzmann equation to describe Donnan equilibrium at the membrane-solution interface. *Journal of Membrane Science* **2013,** *442*, (0), 131-139.
28. Gurreri, L.; Tamburini, A.; Cipollina, A.; Micale, G., CFD analysis of the fluid flow behavior in a reverse electrodialysis stack. *Desalination and Water Treatment* **2012,** *48*, (1-3), 390-403.

29. Moya, A. A.; Sistat, P., Chronoamperometric response of ion-exchange membrane systems. *Journal of Membrane Science* **2013,** *444*, (0), 412-419.

30. Dworecki, K.; Wasik, S.; Slezak, A., Temporal and spatial structure of the concentration boundary layers in a membrane system. *Physica A: Statistical Mechanics and its Applications* **2003,** *326*, (3-4), 360-369.

31. Sistat, P.; Pourcelly, G., Chronopotentiometric response of an ion-exchange membrane in the underlimiting current-range. Transport phenomena within the diffusion layers. *Journal of Membrane Science* **1997,** *123*, (1), 121-131.

32. Spiegler, K. S., Polarization at ion exchange membrane-solution interfaces. *Desalination* **1971,** *9*, (4), 367-385.

33. Vermaas, D. A.; Veerman, J.; Yip, N. Y.; Elimelech, M.; Saakes, M.; Nijmeijer, K., High Efficiency in Energy Generation from Salinity Gradients with Reverse Electrodialysis. *Sustainable Chemistry & Engineering* **2013,** *1*, 1295−1302.

34. Veerman, J.; Saakes, M.; Metz, S. J.; Harmsen, G. J., Reverse electrodialysis:A validated process model for design and optimization. *Chemical Engineering Journal* **2011,** *166*, (1), 256–268.

35. Długołęcki, P. E.; Nijmeijer, K.; Metz, S. J.; Wessling, M., Current status of ion exchange membranes for power generation from salinity gradients. *Journal of Membrane Science* **2008,** *319*, (1-2), 214-222.

36. Guler, E.; Zhang, Y.; Saakes, M.; Nijmeijer, K., Tailor-Made Anion-Exchange Membranes for Salinity Gradient Power Generation Using Reverse Electrodialysis. *ChemSusChem* **2012,** *5*, (11), 2262-2270.

37. Guler, E.; Elizen, R.; Vermaas, D.; Saakes, M.; Nijmeijer, K., Performance-determining membrane properties in reverse electrodialysis. *Journal of Membrane Science* **2013,** *446*, 266–276.

38. Vrouwenvelder, J. S.; van Paassen, J. A. M.; Wessels, L. P.; van Dam, A. F.; Bakker, S. M., The Membrane Fouling Simulator: A practical tool for fouling prediction and control. *Journal of Membrane Science* **2006,** *281*, (1â€“2), 316-324.

39. Strathmann, H., Electrodialysis, a mature technology with a multitude of new applications. *Desalination* **2010,** *264*, (3), 268-288.

40. Logan, B., Scaling up microbial fuel cells and other bioelectrochemical systems. *Applied Microbiology and Biotechnology* **2010,** *85*, (6), 1665-1671.

Supporting information

Appendix A: Fit curve for chronopotentiometry

To compare the chronopotentiometric series quantitatively with each other, the chronopotentiometric series can be fitted with a theoretical function. Using such a universal function, the chronopotentiometric series can be described using the ohmic resistance (derived from the initial jump in voltage when a current starts or stops), the non-ohmic resistance (derived from the latter stationary voltage) and the time scale thereof. As indicated in the main text, the chronopotentiometric series are too complicated for an analytical solution. An empirical function is used to fit the experimental data. As the chronopotentiometric series approach asymptotically an equilibrium value for each current, an exponential or hyperbolic function is most probable.

Such an exponential function is given by:

$$U = \beta_1 \cdot e^{-t/\tau} + \beta_2 \qquad \text{(eq. S9.1)}$$

And a suitable hyperbolic function is given by:

$$U = \beta_1 \cdot \left(\frac{1}{t/\tau + 1} \right) + \beta_2 \qquad \text{(eq. S9.2)}$$

In which U is the electrode voltage (V) is the time after the start or stop of the electrical current (s) and β_1, β_2, and τ are parameters to fit each stage of the experimental series. The parameter β_1 acts as the amplitude of the non-ohmic overpotential (V), β_2 acts as the voltage at the start or stop of the electrical current (V) and τ is the time scale for the non-ohmic resistance (s).

An example of (part of) a chronopotentiometric series is given Figure S9.1, together with two possible fitted functions according to eq. S9.1 and S9.2.

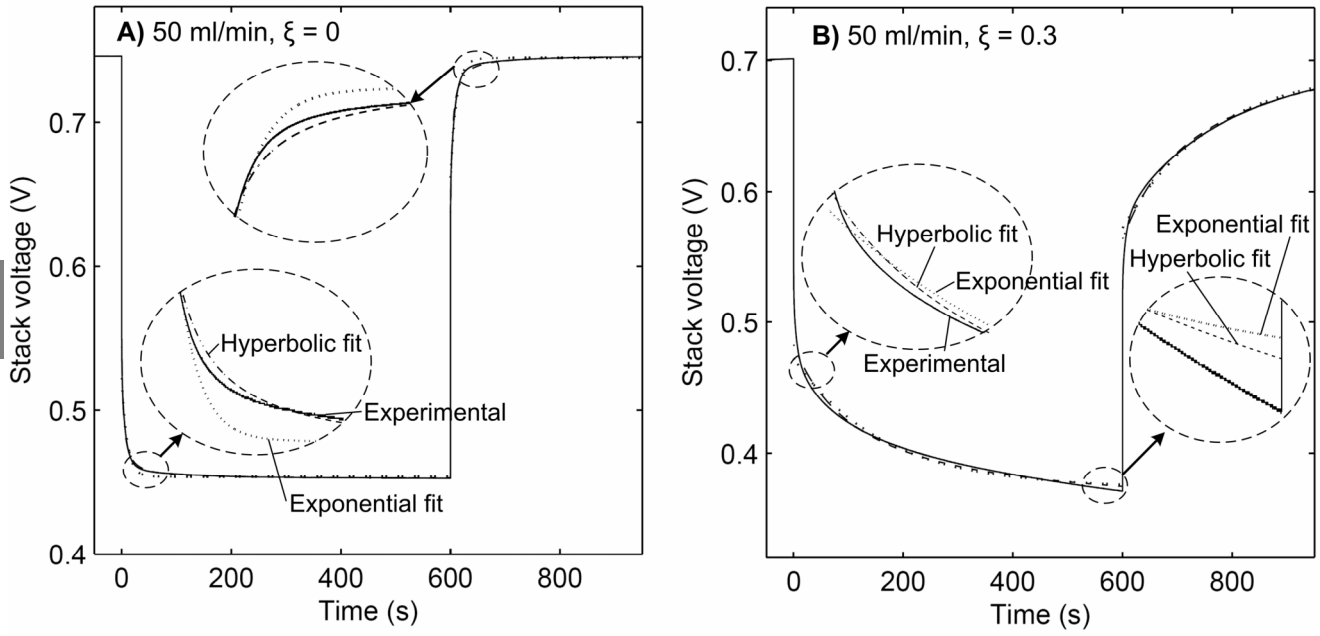

Figure S9.1: Chronopotentiometric series for a stack with a feedwater flow rate of 50 ml/min, in case none of the channels is blocked (A) and in case 30% of the channels is blocked (B). The solid line

represents experimental data, the dotted line indicates the exponential fit (eq. S9.1) and the dashed line indicates the hyperbolic fit (eq. S9.2). A current density of 10 A/m^2 was applied between 0 and 600 s, while open circuit was applied at the other time. The sections near t = 0 s and t = 600 s are zoomed.

As demonstrated in Figure S9.1, the hyperbolic fit describes the experimental data better than the exponential fit. The difference is most pronounced in the case where no preferential channeling occurs (Figure S9.1A), but also the case with preferential channeling fits better to a hyperbolic function than to an exponential function (Figure S9.1B). Therefore, we use a hyperbolic function to fit the experimental data and calculate the parameters β_1, β_2, and τ for each stage.

Appendix B: Effect of current density on response time τ

The response time τ can be calculated for the stage where an electrical current is suddenly applied and when an electrical current is suddenly stopped (i.e., transition to OCV). In this appendix, we will show that the time scale for the voltage response, τ, is not equal in these two cases. Figure S9.2 shows an example of the response time τ as a function of the current density j, for chronopotentiometric stages when a current density is suddenly applied or when a current density is suddenly stopped.

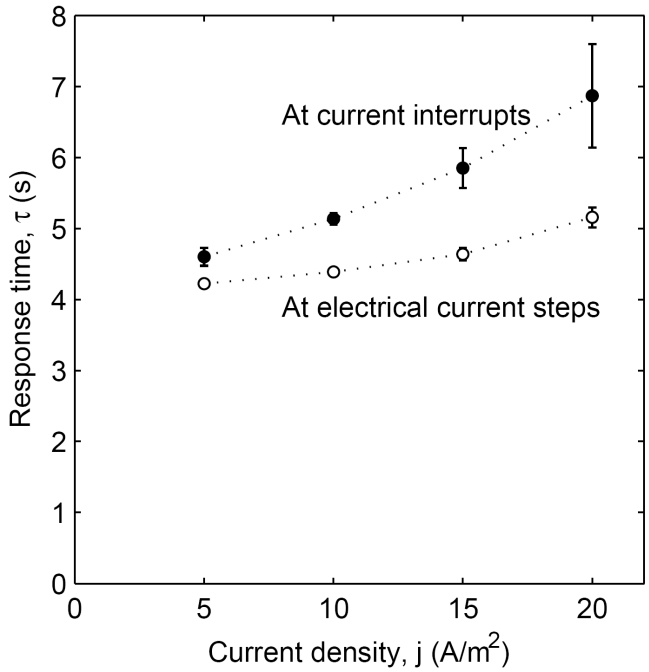

Figure S9.2: Experimentally derived time scale τ versus current density j, for chronopotentiometric stages when a current density is suddenly applied or when a current density is suddenly stopped, for a flow rate of 50 ml/min.

Figure S9.2 shows that τ increases with increasing current density for stages when the current is interrupted, while τ is less dependent on the current density for stages when the current is suddenly applied. Moreover, the response time τ is in general larger for stages when the current is interrupted compared to stages when the current is applied, as also demonstrated for the example in Figure S9.2. Both effects can be explained when analyzing the derivative of the electromotive force as generated by each membrane, and regarding the local concentrations at the membrane-water interface. The electromotive force is given by the Nernst equation, corrected for activity coefficients and average permselectivity:

$$E = \alpha \frac{R \cdot T}{z \cdot F} \cdot \ln\left(\frac{\gamma_{c,m} \cdot c_{c,m}}{\gamma_{d,m} \cdot c_{d,m}}\right) \quad \text{(eq. S9.3)}$$

In which E is the electromotive force (V), α is the permselectivity (-), R is the universal gas constant (8.314 J/(mol·K), z is the valence of the ions (-), F is the Faraday constant (96485 C/mol), $c_{s,m}$ is the concentration at the interface between the seawater and the membrane (M) and $c_{r,m}$ is the concentration at the interface between the river water and the membrane (M). γ are the corresponding molar activity coefficients.

The derivate for the transient series of E to time t (in s) is:

$$\frac{\partial E}{\partial t} = \alpha \frac{RT}{zF} \frac{\partial \ln\left(\frac{\gamma_{c,m} \cdot c_{c,m}}{\gamma_{d,m} \cdot c_{d,m}}\right)}{\partial t} \quad \text{(eq. S9.4)}$$

The temporal changes in activity coefficients are an order of magnitude smaller than that of the concentrations. Therefore, the activity coefficients are assumed steady. In other words, the activity coefficients are not neglected for the calculation of E, but assumed stationary for each individual compartment. This yields:

$$\frac{\partial E}{\partial t} \approx \alpha \frac{RT}{zF} \frac{\partial \ln\left(\frac{c_{c,m}}{c_{d,m}}\right)}{\partial t} \quad \text{(eq. S9.5)}$$

Applying the chain rule and quotient rule for differentiating yields:

$$\frac{\partial E}{\partial t} \approx \alpha \frac{RT}{zF} \frac{c_{d,m}}{c_{c,m}} \frac{\partial\left(\frac{c_{c,m}}{c_{d,m}}\right)}{\partial t} \quad \text{(eq. S9.6)}$$

$$\frac{\partial E}{\partial t} \approx \alpha \frac{RT}{zF} \frac{c_{d,m}}{c_{c,m}} \left(\frac{c_{d,m} \frac{\partial c_{c,m}}{\partial t} - c_c \frac{\partial c_{d,m}}{\partial t}}{{c_{d,m}}^2}\right) \quad \text{(eq. S9.7)}$$

$$\frac{\partial E}{\partial t} \approx \alpha \frac{RT}{zF} \frac{1}{c_{c,m} \cdot c_{d,m}} \left(c_{d,m} \frac{\partial c_{c,m}}{\partial t} - c_c \frac{\partial c_{d,m}}{\partial t}\right) \quad \text{(eq. S9.8)}$$

In practical cases, the derivative of the concentrations in the concentrated stream has an opposite sign to that in the diluted stream. Hence, this equation is easier to interpret as:

$$\frac{\partial E}{\partial t} \approx \alpha \frac{RT}{zF} \frac{1}{c_{c,m} \cdot c_{d,m}} \left(c_{d,m} \frac{\partial c_{c,m}}{\partial t} + c_{c,m} \frac{-\partial c_{d,m}}{\partial t} \right) \qquad \text{(eq. S9.9)}$$

Furthermore, the mixing conditions (i.e., flow rate and compartment geometry) in the concentrated and diluted compartment can be assumed equal. In that case, the concentration profile in the diffusive boundary layer of the concentrated stream is symmetrical to that in the diluted stream, and therefore the ionic transport (both by diffusion and due to the electrical field) is equal in magnitude. In other words, $\partial c_{c,m}/\partial t = -\partial c_{d,m}/\partial t = \partial c/\partial t$. That simplifies eq. S9.9 to:

$$\frac{\partial E}{\partial t} \approx \alpha \frac{RT}{zF} \frac{1}{c_{c,m} \cdot c_{d,m}} \left(c_{d,m} + c_{c,m} \right) \frac{\partial c}{\partial t} \qquad \text{(eq. S9.10)}$$

Because the sum of the diluted and concentrated solutions is constant (because equal mixing conditions were assumed), the only terms of interest are:

$$\frac{\partial E}{\partial t} \propto \frac{1}{c_{c,m} \cdot c_{d,m}} \frac{\partial c}{\partial t} \qquad \text{(eq. S9.11)}$$

This shows that the voltage response, after a sudden change in electrical current, is inversely proportional to the product of the diluted and concentrated concentrations. As a consequence, $\partial E/\partial t$ is largest when the diluted concentration (c_d) becomes very small, which occurs in practical cases when no electrical current is allowed for a while (OCV). In other words, the electromotive force E is more sensitive for the same change in concentration during the transition to OCV than during the transition towards a stage with an electrical current. This explains why τ is larger when the electrical current is interrupted, compared to the τ when an electrical current is suddenly applied.

A larger change in current density increases the concentration change that is induced near the membrane-water interface. Therefore, τ increases for increasing current density at stages when the current is interrupted. The larger current density implies a larger ion transport, and therefore the concentrations near the membrane-water interface do have a larger change over time. In other words, the factor $\partial c/\partial t$ in eq. S9.11 is larger when the current density increases. However, when the current density suddenly starts, the response time τ is not strongly affected. This is caused by two counteracting effects. The factor $\partial c/\partial t$ increases for larger current densities, but the larger ion transport rate decreases the factor $\frac{1}{c_{c,m} \cdot c_{d,m}}$ in eq. S9.11 for larger current densities. As these factors have a counteracting effect, the time scale τ is rather independent of the current density for stages when an electrical current is suddenly applied.

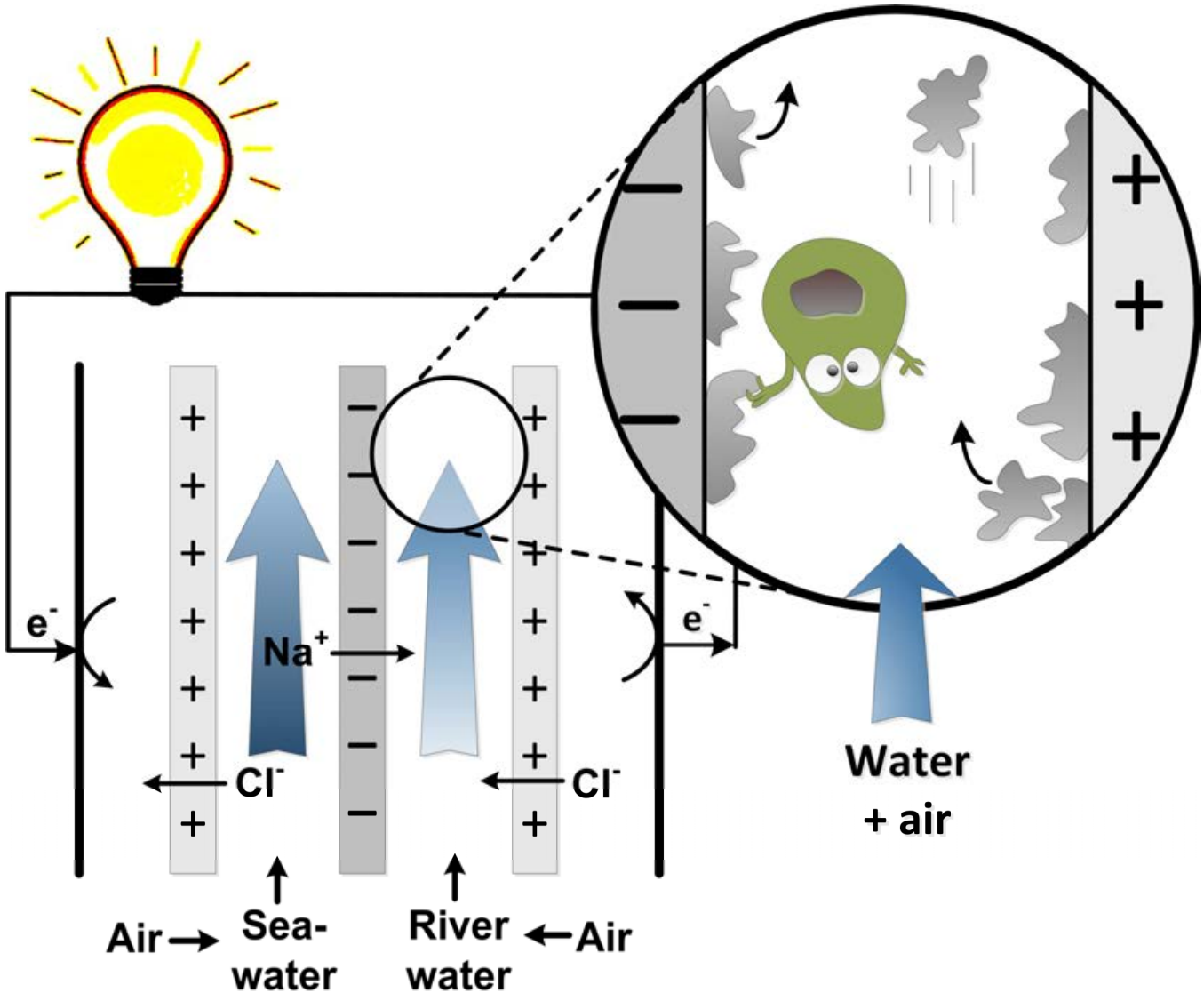
e-
Na+
Cl-
Cl-
e-
Water
+ air
Air
Sea-
water
River
water
Air

Chapter 10

Periodic feedwater reversal and air sparging as anti fouling strategies

Abstract

Renewable energy can be generated using natural streams of seawater and river water in reverse electrodialysis (RED). The potential for electricity production of this technology is huge, but fouling of the membranes and the membrane stack reduces the potential for large scale applications. This research shows that, without any specific anti fouling strategies, the power density decreases in the first 4 hours of operation to 40% of the originally obtained power density. It slowly decreases further in the remaining months. Using anti fouling strategies, a significantly higher power density can be maintained. Periodically switching the feed waters (i.e., changing seawater for river water and vice versa) generates the highest power density in the first hours of operation, probably due to a removal of multivalent ions and organic foulants from the membrane when the electrical current reverses. In the long term, colloidal fouling is observed in the stack without treatment and the stack with periodic feedwater switching, and preferential channeling is observed in the latter. This decreases the power density further. This decrease in power density is partly reversible. Only a stack with periodic air sparging has a minimum of colloidal fouling, resulting in a higher power density in the long term. A combination of the discussed anti fouling strategies, together with the use of monovalent selective membranes, is recommended to maintain a high power density in RED in short term and long term operation.

This chapter has been submitted to *Environmental Science & Technology* as

David A. Vermaas, Damnearn Kunteng, Joost Veerman, Michel Saakes and Kitty Nijmeijer, Periodic feedwater reversal and air sparging as anti fouling strategies in reverse electrodialysis.

10.1 Introduction

Renewable energy can be generated from mixing seawater and river water. The potential in this application is huge, as the theoretically obtained power from mixing the global river water runoff with seawater is well over 2 TW [1-3], i.e., close to the present worldwide electricity demand [4]. The energy that is required to separate fresh water and ions when seawater evaporates can be captured when fresh and salt water mix again. This power source is sustainable and predictable, as seawater evaporates continuously and river water continuously runs into the sea.

This electrical power can be captured in reverse electrodialysis using ion exchange membranes. A RED module (i.e., RED stack) is composed of a series of alternating cation exchange membranes (CEMs) and anion exchange membranes (AEMs), with flows of seawater and river water supplied in the compartments between these membranes [5]. Due to the salinity gradient over the membranes, the ions are transported from the seawater compartment towards the river water compartment. As the membranes are selective for either cations (CEM) or anions (AEM), each membrane creates an electrical potential. This potential can be used to drive an electrical current, when electrodes with a (reversible) redox reaction [6] are connected to an electrical consumer. Alternatively, capacitive electrodes can be used to transfer the ionic current into an electrical current without the necessity of a redox reaction [7]. This requires periodic switching of the feed waters to reverse the direction of the electrical current

The performance of a RED stack is well investigated under laboratory conditions [2, 8-14] or in idealized models [15-19]. Hence, the obtained gross power density, expressed in W per m^2 of membrane area, is increased to 2.2 W/m^2 for mixing seawater and river water [13] and up to 7.5 W/m^2 for increased salinity gradients [20]. The latter results suggest that practical applications are close to a positive net present value (NPV) during the lifetime of a RED power plant, especially when membrane prices would decrease [21].

However, research on RED under practical conditions, using natural streams of seawater and river water, is sparse. A recent fouling study [22] without any specific anti fouling strategies showed that fouling in RED decreases the power density by approximately 50% during the first day, followed by a slow further decrease in power density in the next 3 weeks. Moreover, the pressure drop over the feedwater inlet and outlet increased rapidly, to a maximum of approximately 2 bar [22]. For a stack with spacers in between the membranes, this maximum pressure drop was reached within 5 days. For a stack with profiled

membranes, which integrate the membrane and spacer, the maximum pressure drop was reached after 20 days. Although these profiled membranes reduced the effects of fouling, a thick layer of fouling was found in both designs, dominated by colloids such as clay minerals and remnants of diatom shells, and to a lesser degree scaling of calciumphosphate and biofouling [22].

Anti fouling strategies are required to reduce fouling and to maintain a sustainable high power density and a low pressure drop. However, regular anti fouling strategies are too expensive (e.g., pretreatment with ultrafiltration) or environmentally undesired (e.g., disinfectants or coagulatants) considering the large quantities of feedwater involved in a future commercial RED power plant. Therefore, only cheap and environmentally friendly anti fouling treatments can be considered. Previous research showed that periodic switching of feed waters (i.e., swapping seawater for river water and vice versa) significantly reduced the biofouling rate under artificial accelerated biofouling conditions [3]. Such an osmotic shock not only prevents biofouling, but also induces a reversal of the electrical field, which can reduce fouling of organic acids and charged colloids [23]. Moreover, a periodic feedwater switch enables the use of capacitive electrodes [7].

Alternatively, fouling may be reduced using disturbances in the flow conditions. Using natural feed waters, the pressure drop temporarily decreased for approximately one day when the feedwater flow rate was disturbed for a short time (e.g., 5 minutes) [22]. This observation gives reason to assume that artificial disturbances, for example introduced by air bubbles in the feedwater compartments, offer a possibility to reduce fouling.

This research investigates experimentally the performance of RED stacks using natural feed waters using two anti fouling strategies; namely 1) periodic switching of the feed waters, and 2) periodic injection of pressurized air (i.e., air sparging). The performance of these systems is compared to that of a stack without any anti fouling strategy. The results indicate that both anti fouling strategies significantly influence the degree and type of the fouling in a RED stack and as such generally increase the corresponding performance. Furthermore, the results give directions for additional new anti fouling strategies in order to maintain a high power density in RED.

10.2 Experimental setup

10.2.1 RED stacks

Three identical RED stacks were built according to Figure 10.1. The housings of these stacks were supplied by REDstack B.V. (The Netherlands). Profiled membranes were used to make the use of spacers obsolete. Each stack comprised 10 cells is composed of a CEM, an AEM (Ralex CMH / AMH, MEGA AS, Czech republic), a compartment for seawater and a compartment for river water. All membranes had an area of 10 cm by 10 cm available for ion exchange. The profiled membranes were hot pressed into an aluminum mould, such that the membrane surface contained profiles (i.e., ridges) of 230 μm in height and 300 μm in width. The created feedwater channels were 230 μm in height and 1.9 mm in width. The hot pressing was performed at a temperature of 140 ºC and a pressure of 200 bar, for 10 min, according to the previously explained procedure [24].

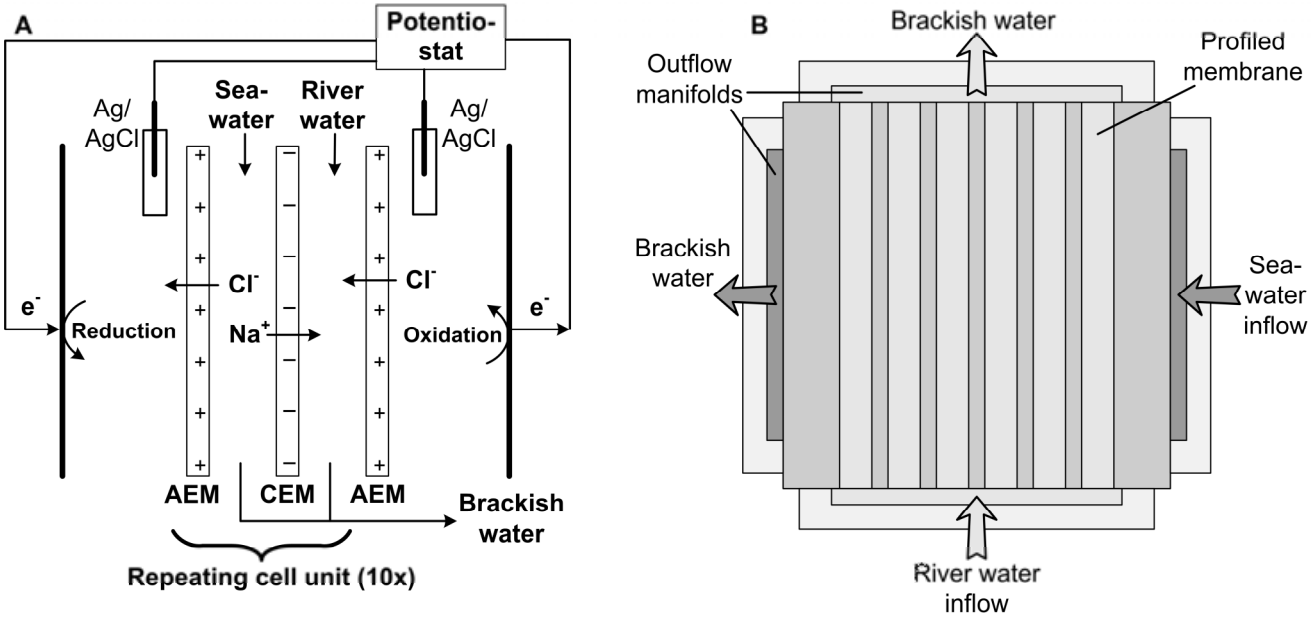

Figure 10.1: Schematic illustration of RED stack setup in a plane perpendicular to the membranes (A) and in a plane parallel to the membranes (B), which shows the cross-wise flow orientation as used for the experiments. The profiled ridges on the profiled membrane are only illustrated in panel B, using darker shading, and are not on scale. The lighter grey area indicates the area available for water flow, in this case river water. The seawater compartment faces the other side of this membrane.

The stack contains 10 CEMs and 11 AEMs, as the last compartment was closed with an AEM to shield the electrode rinse solution. The membrane pile was fixed between two endplates with an inserted working electrode made of Ti-Ru/Ir mesh and a dimension of 10 cm by 10 cm (MAGNETO Special Anodes B.V., The Netherlands). The electrode compartments were rinsed with 0.25 M NaCl solution. The potential over the RED cells was measured using an Ag/AgCl reference electrode (QIS, The Netherlands) connected to the middle of each electrode compartment. More details on the electrode system are described in Appendix A.

Feedwater was supplied to the stack via distribution chambers at all sides of the membrane pile and hence creating manifolds to distribute the feedwater uniformly over all feedwater channels (Figure 10.1B). The river water feed was oriented 90º with respect to the seawater feed, i.e., cross-flow is applied. After assembling of the stacks, the membranes were brought in equilibrium with artificial seawater (0.5 M NaCl) and river water (0.017 M NaCl) for at least one week, after which natural feed waters were supplied.

10.2.2 Feedwater

Natural feedwater was supplied to all stacks; fresh water was obtained from a nearby canal (Van Harinxmakanaal, The Netherlands) and salt water was obtained from the nearby harbor in the Wadden Sea (Harlingen harbor, The Netherlands). These sources are referred as river water and seawater in this paper, respectively. The river water was stored in a buffer tank (33 hour capacity during the first month of the experiment, 400 hour capacity for the later part of the experiment) to prevent a stop in the less reliable river water supply line. Both feed waters were filtered through microfilters with a median diameter of 10 μm. The water quality of the feedwater and pressure drop over the stack was monitored, as described in Appendix A. Both feedwater streams had a constant flow rate of 200 ml/min for each stack, which is equivalent to a superficial velocity of 1.7 cm/s and a Reynolds number of 8.

10.2.3 Anti fouling strategies

Two anti fouling strategies were evaluated, i.e., periodic feedwater switching and periodic air sparging. Therefore, one stack was supplied with 3-way valves in the feedwater line, such that every 30 minutes the supply of seawater to that stack was switched for river water and vice versa. A second stack was equipped with a T-joint and a valve, to which an air compressor was connected. The air was injected every 30 min for 30 s, at a pressure

difference over the stack of approximately 1 bar. Although the water flow was not stopped when air was injected, the volumetric air flow dominated the water flow rate during this 30 s period. A third stack was used as a reference, where no anti fouling strategy was applied.

Both anti fouling strategies consume some power to apply them or reduce the power output compared to clean stacks. In case of feedwater switching, the concentration difference is smaller during a short period, which results in a temporarily lower power density. Switching the feeds each 30 minutes reduced the average power density by approximately 2%. Based on the pressure drop during air sparging and assuming a volumetric flow rate of 2 L/min, approximately 50% of the obtained energy from the RED stack without fouling was consumed for air sparging. Although this is a significant consumption of power, the conditions for air sparging in this research were chosen to demonstrate its effect. The duration and frequency of air sparging can be optimized for the most efficient anti fouling treatment at large scale applications. Therefore, the power losses due to feedwater switching or air sparging are not included in the (gross) power density.

The fouling experiments were conducted at the Wetsalt demo site in Harlingen, The Netherlands, during autumn 2012 (from September 17th to November 23rd). After dismantling, two membrane pairs from the middle of each stack were used for autopsy. The remaining eight membrane pairs from each stack were cleaned manually with a brush and stored in demineralized water or 5 M NaCl (brine). After that treatment, these membranes were re-used in RED stacks to operate again from December 13th to December 17th, 2012.

10.2.4 Electrical measurements

To measure the open circuit voltage, stack resistance and power density, chronopotentiometry was applied, using individual potentiostats (Ivium technologies, The Netherlands) for all stacks, as described in Figure S10.1. For most of the time during the 30-minute chronopotentiometric cycles, a current density of 5 A/m^2 was generated by the stacks. The open circuit voltage (OCV, in V) was derived from a 90 s stage without electrical current. The stack area resistance was derived from the steady voltages during open circuit and during the stages with electrical current (2.5 A/m^2, 5 A/m^2 and 10 A/m^2), in combination with Ohm's law. The power density was derived from the OCV, the stack area resistance and the total membrane area, according to:

$$P_{dens} = \frac{OCV^2}{4R_{stack} \cdot N_m} \qquad \text{(eq. 10.1)}$$

in which P_{dens} is the power density (W/m^2), R_{stack} is the stack area resistance ($\Omega \cdot m^2$) and N_m is the number of membranes in the stack (-). The final membrane, between the last feedwater compartment and the electrode compartment, is not considered here because this last membrane would be insignificant in large scale applications with many membrane pairs [25].

10.2.5 Power density normalization

As the open circuit voltage (OCV) and stack resistance are dependent on the feedwater concentrations and temperature [8, 20] and these parameters fluctuate in time, the power density is normalized using a theoretical power density based on the actual feedwater concentrations and temperature. This theoretical power has been calculated using the Nernst equation for determining the OCV, corrected for the apparent membrane permselectivity α (-) and the activity coefficient γ (-):

$$OCV = \alpha \cdot \frac{N_m \cdot R \cdot T}{F \cdot z} \cdot \ln\left(\frac{\gamma_s \cdot c_s}{\gamma_r \cdot c_r}\right) \qquad \text{(eq. 10.2)}$$

In which R is the universal gas constant (8.314 J/(mol·K)), T is the absolute temperature (K), F is the Faraday constant (96485 C/mol), z is the valence of the transported ions, and c is the feedwater concentration (M). The subscripts s and r indicate seawater and river water, respectively.

As the valence of the ions (e.g., z = ± 1 for Na^+ and Cl^- and z = ± 2 for Mg^{2+} and SO_4^{2-}) influences the OCV, and a mixture of these ions is present in natural feedwater, the valence of the dominant species was used for calculations in this research, i.e., z = ± 1. Multivalent ions, which are present as minor species in the natural feed waters, actually reduce the OCV [26, 27]. To correct for these multivalent ions, a relatively low value of 0.85 is used for the theoretical apparent permselectivity [22].

The stack resistance is estimated based on the ohmic resistance, which is dependent on the membrane resistance and feedwater conductivity, and the non-ohmic resistance, which is due to the decrease in potential as ions are transported from seawater to river water in the stack [18].

Although the non-ohmic resistance is also influenced by preferential channeling [28], i.e., the non-uniform feedwater distribution, which can occur due to fouling, the non-ohmic resistance is initially estimated assuming uniform flow. Hence, the theoretical power density

should be considered as the power density that could be obtained when no (colloidal) fouling would occur. The response time to establish a steady voltage is used to indicate preferential channeling [28].

10.3 Results

10.3.1 Feedwater conditions

The salinity, temperature and feedwater composition of the natural feedwater sources as used in the present research are presented in Table 10.1.

Table 10.1: Ion concentrations, temperature, dissolved organic carbon (DOC) and humic substances (HS), which is the sum of humic acids and fulvic acids. The presented values are average values and standard deviations considering all samples.

	Cations (mEq/L)	Anions (mEq/L)	Temperature (ºC)	Organic compounds (mg-C/l)
River water	Na^+: 37 ± 25 Mg^{2+}: 9 ± 5 Ca^{2+}: 7 ± 1 Total: 55 ± 30	Cl^-: 43 ± 28 SO_4^{2-}: 5 ± 3 Total: 46 ± 29	16 ± 4	DOC: 28 ± 8 HS: 19 ± 9
Seawater	Na^+: 199 ± 32 Mg^{2+}: 43 ± 7 Ca^{2+}: 13 ± 2 Total: 264 ± 41	Cl^-: 254 ± 40 SO_4^{2-}: 27 ± 4 Total: 268 ± 42	12 ± 3	DOC: 12 ± 1 HS: 10 ± 3

The large standard deviations in the measured concentrations (Table 10.1) demonstrate that the salinity strongly fluctuates, which is due to the fact that the inlet of the seawater and that of the river water are located relatively close together. Therefore, the sources for seawater and river water partly mix near the river mouth, dependent on the tide and the river water discharge. The fluctuations in salinity and temperature result in a fluctuating theoretical and practical power production, as a higher salinity ratio and a higher temperature promote the power density in RED [8, 20]. The actual salinities corresponding to each electrical measurement are used to calculate the theoretical power density.

The concentrations of organic matter and humic substances are relatively high compared to typical concentrations of natural waters [29], which motivates to consider humics acids as a possible foulant for AEMs [30, 31].

10.3.2 Prevention of colloid fouling

Previous research showed that visible, colloidal fouling develops in RED stacks at a time scale of several days or weeks [22]. The time series for the average pressure drop over the feedwater channels, indicating clogging of feedwater channels with colloidal fouling, is shown in Figure 10.2A for the full duration of the present experiment. Figure 10.2B-G show autopsy photos of the fouled profiled membranes after the experiment.

All stacks experience a much lower pressure drop than stacks with spacer filled channels under practical conditions [22], because of the use of profiled membranes and the design with wide inflow manifolds. Nevertheless, the pressure drop increases significantly from day 10 for the stack without anti fouling strategy (Figure 10.2A) due to colloidal fouling. The pressure drop in the stack with feedwater switching started to rise later, most pronounced from day 22 on. The feedwater switching creates disturbances in the feedwater flow, which reduce colloidal fouling. However, this anti fouling strategy is apparently not sufficient to avoid fouling in the longer term.

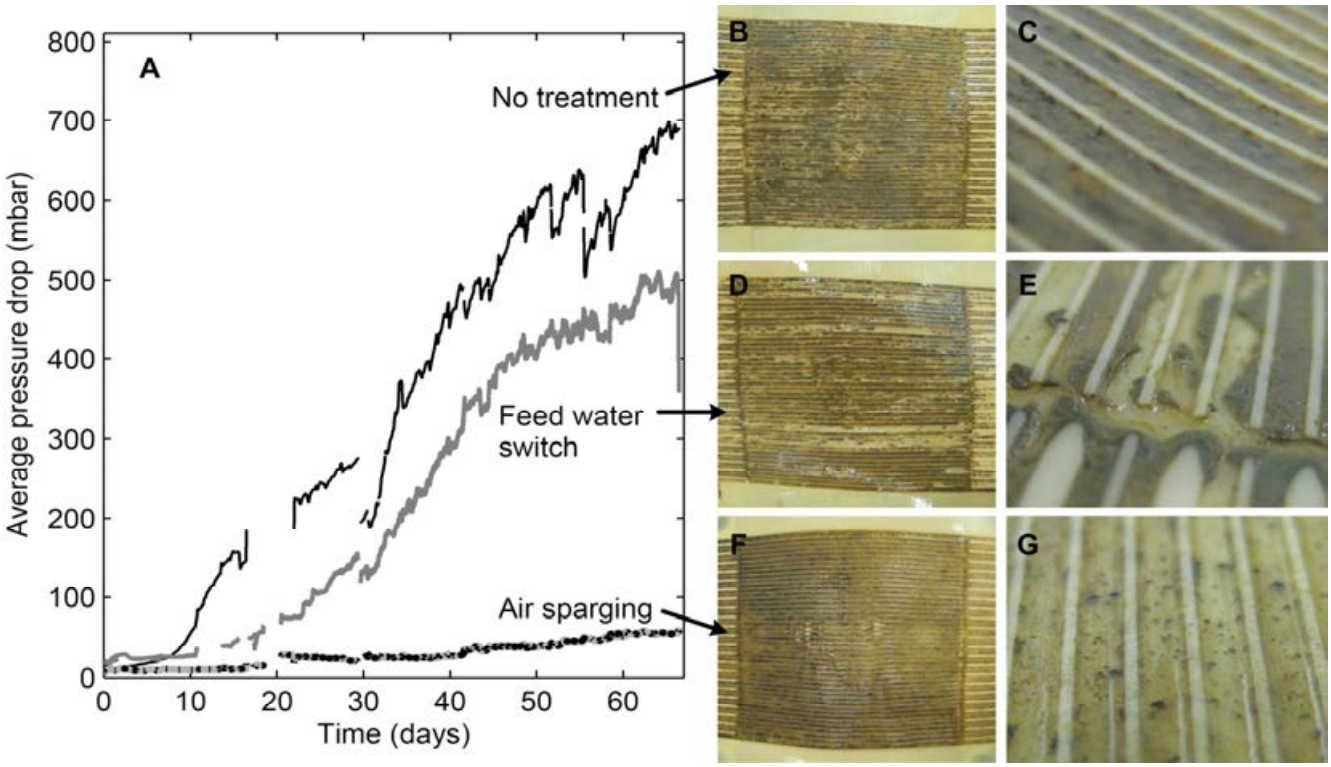

Figure 10.2: Average pressure drop as function of the time (A) and photos of profiled cation exchange membranes from the fouled stacks at the end of the experiment (B-G). Photos B, D and F show the full area of 10x10 cm^2, while the right photos (C, E and G) show images of approximately 1x1 cm^2, zoomed close to the inflow of the feedwater compartments. The original membrane color is beige.

In contrast, the stack with air sparging keeps a remarkably low pressure drop over the full duration of the experiment (Figure 10.2A), indicating that periodic air sparging prevents or removes colloidal fouling. The pressure drop increases very slowly, to a maximum of only 62 mbar after more than 2 months.

Photos of the membranes after dismantling the stacks support the observed pressure drops. The membranes in the stack without any treatment are almost completely covered with a thick layer of colloids (Figure 10.2B-C), whereas in the stack with feedwater switch a few channels are still relatively clean (Figure 10.2D-E). These open channels explain the slightly lower pressure drop for the stack with feedwater switching. This non-uniform distribution of fouling forces a non-uniform distribution of feedwater, which is known as preferential channeling [32]. Such preferential channeling is known to induce a large non-ohmic resistance and will decrease the power density in RED [28]. Preferential channeling starts at spots that are vulnerable to fouling, such as spacer knits in spacer filled channels [32] or arbitrary rough spots in profiled membranes. The lower local velocity due to an initial adhered colloid intensifies the fouling at these spots, leading to preferential channeling.

The membranes from the stack with air sparging also contain fouled colloids (Figure 10.2F), but in a much thinner layer and smaller fractions compared to the other stacks (Figure 10.2G). Therefore, fouling is not completely prevented using air sparging, but distributed such that the feedwater can still flow through the stack at a relatively low pressure drop. The periodically applied high pressure during air sparging and the water-air interfaces scour the feedwater channels, such that all channels remain open for feedwater flow.

Analysis of the colloidal fouling of these two stacks with scanning electron microscopy (SEM) revealed that the fouled surfaces mainly contain clay particles and diatom remnants (not shown), which is similar as found in previous research [22]. Additionally, the stack with air sparging showed small fractions of micro-organisms. This is probably due to the abundant supply of air (and hence oxygen) and the absence of a soft, partly moving colloidal bed. Nevertheless, this marginal amount of biofouling is not considered as a limiting issue for power generation in the stack with air sparging.

Preferential channeling can be electrochemically deduced *in situ* from the response time of the system to establish a steady voltage of the stack when the electrical circuit is suddenly opened or closed [28]. This response time is presented in Figure 10.3 as a function of time.

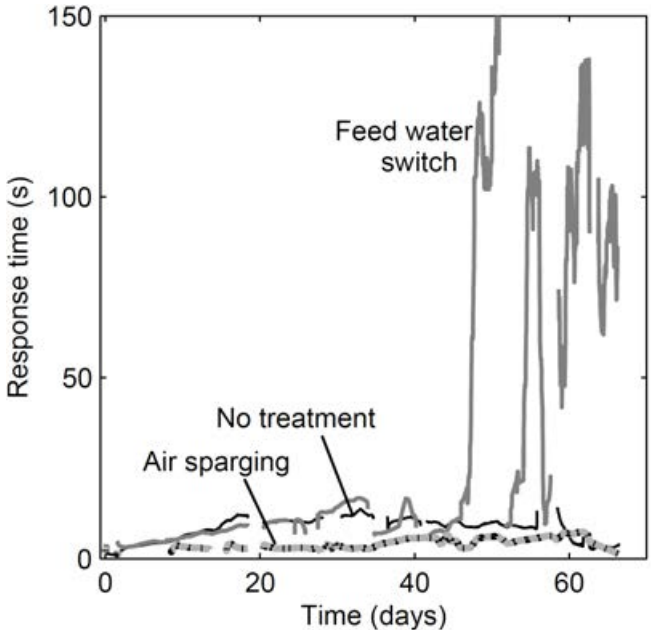

Figure 10.3: Response time, which is the typical time scale to establish a steady voltage after a sudden change in electrical current, as a function of the time of operation. A moving average with a span of 4 hours was applied.

The small response time at the start of the experiment (response time < 4 s) indicates that all stacks had a rather uniform flow distribution when no colloidal fouling was present. The response time fluctuates for all stacks to some extend but suddenly increases an order of magnitude at day 46 for the stack in which the feed waters are switched periodically (Figure 10.3). This is in agreement with the occurrence of preferential channeling as observed in the stack autopsy (Figure 10.2D-E). The increase in response time is remarkably rapid, which suggests that a few large colloids clogged the feedwater channels in this stack suddenly, rather than that a slow accumulation of a colloid layer occurs. For example, this can occur when clay particles that pass the prefiltration as individual particles agglomerate in the feedwater line or manifolds. As the response time is very sensitive when a small membrane area is inaccessible for feedwater [28], the response time increases rapidly when such non-uniform colloidal fouling occurs.

The response time does not increase above 20 s for the stack without treatment. This is partly due to the high pressure drop in the stack without treatment, as the high pressure drop pushes the large colloids harder. Therefore, this reduces the chance that a feedwater channel is fully blocked suddenly. For the same reason, the stack with air sparging has in general the lowest response time, as the high pressure during air sparging removes even large colloids from the feedwater channels. However, the prompt increase at day 46 for the stack with feedwater switch as compared to hardly any increase in the stack without treatment indicates that preferential channeling is unpredictable and partly coincidental. The increase at this particular day, and the absence of preferential channeling for the stack without treatment, cannot be predicted for a future experiment. Only the stack with air sparging has a very low chance to develop preferential channeling.

The occurrence of preferential channeling as indicated by the large response time is resembled in the non-ohmic resistance, which resembles the concentration changes in the bulk and diffusive boundary layer, as shown in Figure S10.2. The non-ohmic resistance increases in particular for the stack with feedwater switching, to approximately 500% of the theoretical value. This effect is included in the power density, which we will show later.

10.3.3 Obtained power density

For the obtained voltage and power, the short term effects (when no significant colloidal fouling occurs) are separated from the long term effects. The short term effects on the obtained voltage and power are discussed first.

The normalized open circuit voltage, i.e., the apparent permselectivity when considering monovalent ions only, and the normalized power density are shown in Figure 10.4 as a function of time for the first 4.5 hours of operation.

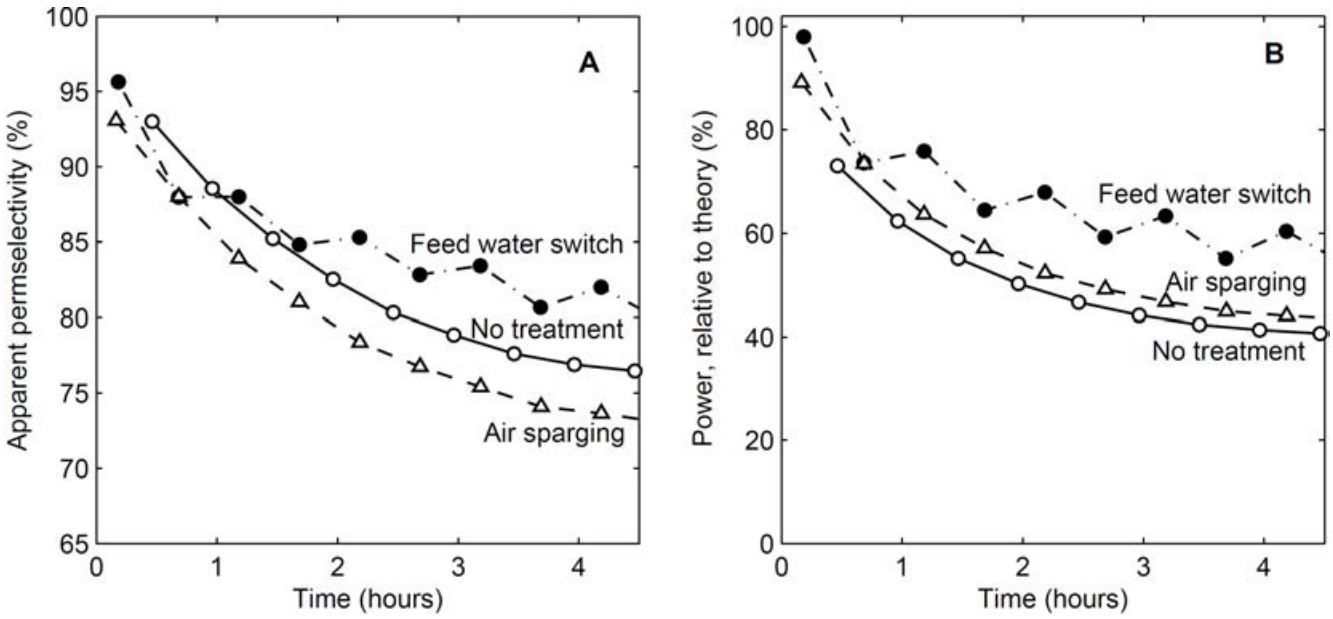

Figure 10.4: Experimentally derived apparent permselectivity (A) and normalized power (B) as a function of time, for the first 4.5 hours of the experiment. The apparent permselectivity was deduced from eq. 10.2 considering the actual open circuit voltage, salinities and temperature. The power density was normalized according to theoretical equivalents using eq. 10.1 and 10.2.

For all cases, the apparent permselectivity decreases from approximately 95% at the start of the experiment to 74 – 81% after 4 hours. The fluctuations visible at this small time scale for the stack with feedwater switch stem from the voltage reversal after every feedwater switch and a slight bias in the reference electrodes that measure the voltage.

The rapid decrease in apparent permselectivity in the first hours (Figure 10.4A) was also observed in previous research, although in less detail, and attributed to the presence of multivalent ions and organic substances such as humic acids [22]. At the start of the experiment, when the membranes are equilibrated with NaCl solutions, the apparent permselectivity is relatively high; even higher than the expected 85%. This indicates that the membranes are not yet in equilibrium with the actual feedwater, which is composed of a mixture of monovalent en multivalent ions. The presence of multivalent ions in the natural feedwater reduces the open circuit voltage, as can be deduced from the role of the valence z in eq. 10.2 [26, 27]. Organic substances such as humic acids may statically stick to the ion exchange membranes, specifically AEMs due to the negative charge and large molecular size, and hence shield charged moieties in the membrane. The lower available fixed membrane charge reduces the apparent permselectivity [30]. The exact role of multivalent

ions or humic acids cannot be deduced from these results, but further investigation of this effect is beyond the scope of this research.

The stack with feedwater switch has the highest apparent permselectivity after 4 hours, followed by the stack without any anti fouling treatment and the stack with air sparging (Figure 10.4A). These differences decrease slowly in time beyond the shown 4 hours; the differences in apparent permselectivity are less than 4% after 1 day of operation. The slower decrease in apparent permselectivity of the stack with feedwater switching may be attributed to the periodic reversal of the electrical current, which delays the penetration of $MgSO_4$ and possibly organic substances into the membranes. These substances are known to reduce the apparent permselectivity. As such, feedwater switching delays the unfavorable effect of fouling in the short term.

Switching the feedwater at other frequencies may be even more favorable. A higher switching frequency will be more effective to remove foulants, but is compromised with a period of lower power density when the feed waters just switched and the salinity difference over the membranes has to restore. Alternatively, the current direction can be reversed for a short time, i.e., an electrical pulse in opposite direction of the passive current can be applied, to remove fouling. This has been applied in other applications to remove humic substances [31, 33], proteins (BSA) [34] or minerals [35] from ion exchange membranes. Removing biofouling with e-pulses has also been investigated, but for electric fields that are outside the scope of RED (in the order of kV/cm) [36].

The obtained power density (Figure 10.4B) resembles the trends as observed for the apparent permselectivity, as the stack resistance did only change slightly (<15%) in this short time scale. The overall power density for the stack without treatment is slightly lower than that for the stack with air sparging. This small change is probably due to small differences in stack properties, e.g., a slightly higher membrane resistance or a slightly thicker compartment thickness. In the short term, the obtained power density is highest for the stack with feedwater switching, due to the superior apparent permselectivity of this stack.

The long term effect of fouling and the applied anti fouling strategies on electrochemical performance is demonstrated in Figure 10.5, where the apparent permselectivity and the normalized power density are plotted for the total duration of the experiment.

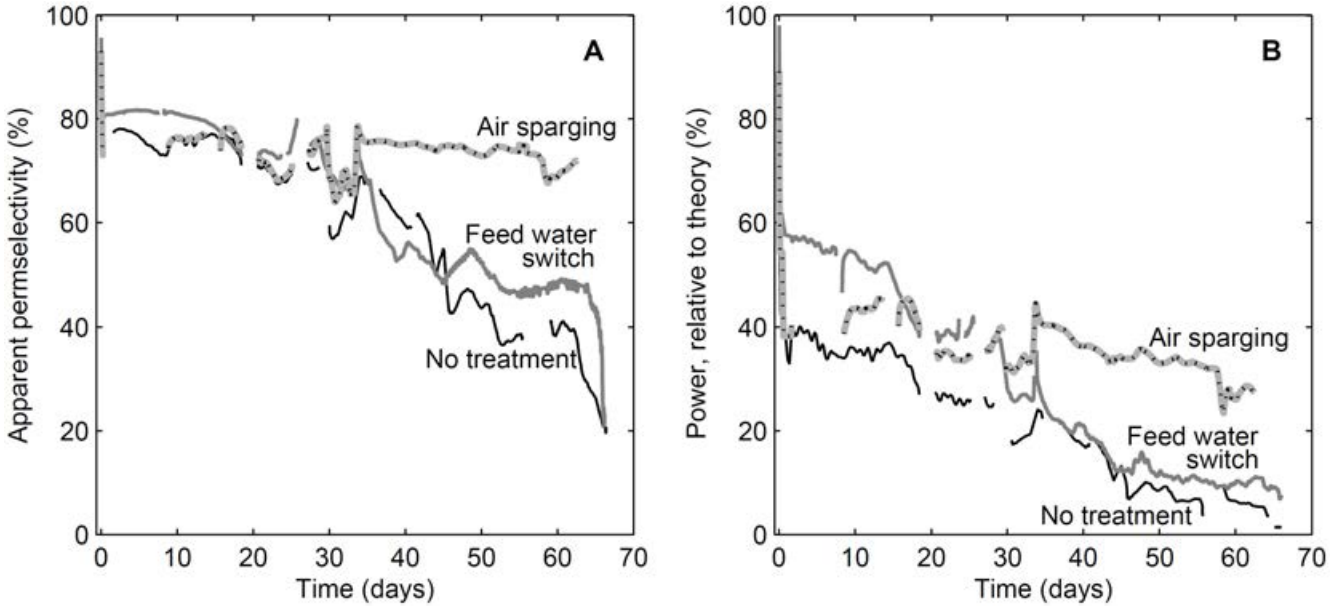

Figure 10.5: Experimentally derived apparent permselectivity (A) and power density (B) as a function of time, for the full span of the experiment. All series have small interruptions due to software failures or small air bubbles blocking the reference electrodes. Fluctuations with respect to these trends are mainly due to temporal changes in feedwater composition (e.g., relatively more multivalent ions). A moving average with a span of 24 hours was applied to remove short term noise.

Figure 10.5 shows a distinctively different behavior for the long term than when the short term (Figure 10.4) is considered only. The apparent permselectivity decreases further, especially after 30 days, except for the case with air sparging. The general decrease in apparent permselectivity after 20 days for the stacks without treatment or feedwater switch is due to colloidal fouling in these stacks (Figure 10.2). These colloids are often charged and therefore adhere to the membrane surface [22], which shields the membrane charge, disturbs the double layer of the membranes and hence reduces the apparent permselectivity of the membranes. Moreover, a layer of colloidal fouling on the membrane reduces the water flow near the membrane surface, which reduces the transport from the diffusive boundary layer towards the bulk solution. This reduced transport concerns both ions (co-ions and counter-ions) and water molecules that diffuse through the non-ideal membranes. As a consequence, the salinity difference over the membrane is lower than the salinity difference between the bulks of the feedwater compartments, even when no electrical current is applied. This is observed as a lower apparent permselectivity.

The power density decreases even more distinct than the apparent permselectivity in the long term (Figure 10.5B). Whereas the stack with feedwater switch performs clearly best in the

short term, the power density of this stack decreases gradually in the longer term, such that the power density is equal to that of the stack with air sparging after 15 days. After 33 days, the normalized power density for the stack with feedwater switching and that without treatment further decreases, even to values below 20% of the theoretical power density. The power density in the stack with air sparging also generally decreases, but remains at more than 25% of the theoretical power density during the full duration of the experiment.

The decrease in power density in the long term is most pronounced for the stacks without treatment or feedwater switch. This is partly due to the decreasing apparent permselectivity and partly due to an increasing resistance. The ohmic resistance increases slowly from 100% of the theoretical equivalents at the start of the experiment to 150% - 200% at the end of the experiments for all stacks (Figure S10.2). The non-ohmic resistance increases much more for the stack without treatment and the one with feedwater switching, due to preferential channeling (Figure 10.3), while this effect is less in the stack with air sparging.

The stack with air sparging is most effective to avoid colloidal fouling (Figure 10.2A) and therefore does not show a large decrease in power density on the long term (Figure 10.5B). Consequently, this anti fouling strategy is suitable to maintain the highest power density for long term operation with natural feed waters.

10.3.4 Effect of brine cleaning

Although switching the feedwater improves the power density in the short term and air sparging maintains the highest power density in the long term, both anti fouling strategies cannot prevent a decrease in obtained power density. Therefore, further understanding of the mechanisms that decrease the power density under practical conditions is required.

To investigate the reversibility of the decrease in power density, the stacks were opened after 67 days, colloidal fouling was manually removed as good as possible with a brush. A minor area of the membranes was slightly damaged, as the PES reinforcement was visible at the membrane surface for some spots. The membranes of the stack without anti fouling treatment were stored in demineralized water. The membranes from the other stacks were brought into brine (5M NaCl) instead of demineralized water. The demineralized water and brine solutions were refreshed 3 times with at least 24 hours in between. After 10 days in these solutions, the stacks were rebuilt with 8 membrane pairs and operated again using the same natural sources of seawater and river water. No anti fouling treatments were applied for

this new series of experiments. The power density after this cleaning procedure is shown in Figure 10.6 as a function of the time after the restart of the experiment.

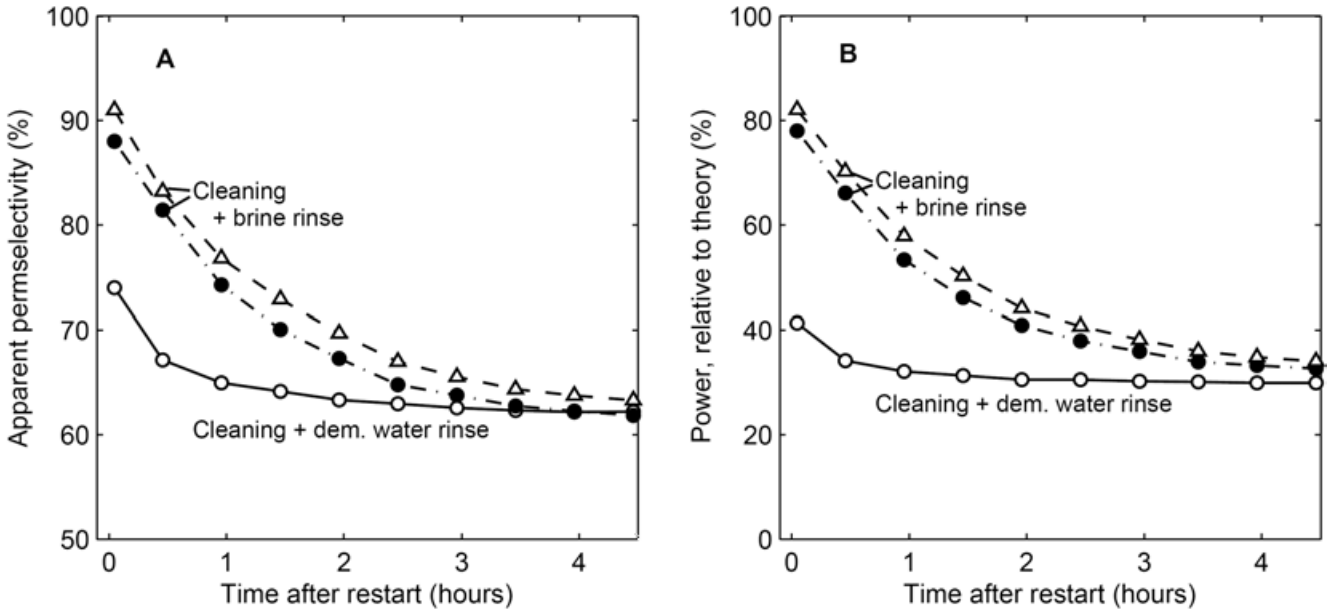

Figure 10.6: Experimentally derived apparent permselectivity (A) and power density (B) as a function of time after restarting the experiment with cleaned membranes. The apparent permselectivity was deduced from eq. 10.2 considering the actual open circuit voltage, salinities and temperature. The power density was normalized according to theoretical equivalents using eq. 10.1 and 10.2.

Figure 10.6 shows that the stacks that were cleaned with brine started with a high apparent permselectivity and power density, whereas the stack cleaned with demineralized water showed a much less significant recovery of the obtained voltage and power density. We hypothesize that the brine treatment exchanges the multivalent ions for Na^+ and Cl^- and removes (at least partly) humic substances as indicated by the brown color of the brine afterwards. This shows that the effect of non-colloidal foulants (probably multivalent ions such as Mg^{2+}, Ca^{2+} and SO_4^{2-} and humic substances), is reversible when using brine rinse, which also explains the initially high power density for these stacks. This increase in power after applying brine rinse suggests that brine flushing can be even applied as a clean-in-place (CIP) technique for RED, dependent on the availability of brine and the effect of a short brine flush.

At 4 hours after this restart, the apparent permselectivity and the normalized power density of all three stacks are similar again. These values, approximately 64% for apparent

permselectivity and 35% for normalized power density, are higher than those observed at the end of the first series of experiments (Figure 10.5, at 67 days), but significantly lower than those obtained at 4 hours after the start of the first experiments (Figure 10.4). This indicates that, although some fouling effects are reversible, some other effects are not fully reversible with the applied cleaning techniques.

We can only speculate about the cause of the irreversible fouling effects. The lower apparent permselectivity and power density suggest that the fixed membrane charge has been reduced, for example due to persistent charged colloids, organic substances or irreversible binding (sometimes referred as membrane poisoning) with multivalent ions such as iron, silicates and borates [9]. In addition or alternatively, the membranes may be damaged from a combination of stress during the corrugation procedure (hot pressing), long term operation and intensive cleaning with a brush. Only small punctures in the membrane can already result in reduced membrane selectivity [37].

10.4 Outlook

The possible irreversible effect of charged colloids and large charged molecules emphasizes the need for ion exchange membranes that are insensitive to these foulants. Ion exchange membranes coated with a thin layer that has an opposite charge are used for this purpose [30]. The need for such an AEM is most urgent, as most large charged molecules or charged colloids (such as clay) are negatively charged. An additional benefit is that these membranes are monovalent selective, which improves the power density when natural feed waters, containing monovalent as well as multivalent salts, are used [26]. Overall, such membranes, combined with the anti fouling strategies presented to prevent effects of fouling in the short term (feedwater switch) and that in the long term (air sparging) can maintain a high power density in RED using natural feedwater.

References

1. Wick, G. L., Power from salinity gradients. *Energy* **1978,** *3*, (1), 95-100.
2. Weinstein, J. N.; Leitz, F. B., Electric Power from Differences in Salinity: The Dialytic Battery. *Science* **1976,** *191*, (4227), 557-559.
3. Post, J. W. Blue Energy: electricity production from salinity gradients by reverse electrodialysis. PhD thesis Wageningen University, **2009**.
4. EIA, *International energy outlook 2011*. U.S. Department of Energy: Washington D.C., **2011**; 301 p.

5. Post, J. W.; Veerman, J.; Hamelers, H. V. M.; Euverink, G. J. W.; Metz, S. J.; Nijmeijer, K.; Buisman, C. J. N., Salinity-gradient power: Evaluation of pressure-retarded osmosis and reverse electrodialysis. *Journal of Membrane Science* **2007,** *288*, (1-2), 218-230.
6. Veerman, J.; Saakes, M.; Metz, S.; Harmsen, G., Reverse electrodialysis: evaluation of suitable electrode systems. *Journal of Applied Electrochemistry* **2010,** *40*, (8), 1461-1474.
7. Vermaas, D. A.; Bajracharya, S.; Sales, B. B.; Saakes, M.; Hamelers, B.; Nijmeijer, K., Clean energy generation using capacitive electrodes in reverse electrodialysis. *Energy & Environmental Science* **2013,** *6*, (2), 643-651.
8. Długołęcki, P. E.; Gambier, A.; Nijmeijer, K.; Wessling, M., Practical Potential of Reverse Electrodialysis As Process for Sustainable Energy Generation. *Environmental Science & Technology* **2009,** *43*, (17), 6888-6894.
9. Lacey, R. E., Energy by Reverse Electrodialysis. *Ocean Engineering* **1980,** *7*, (1), 1-47.
10. Pattle, R. E., Electricity from fresh and salt water - without fuel. *Chemical and process engineering* **1955,** *35*, 351-354.
11. Post, J. W.; Hamelers, H. V. M.; Buisman, C. J. N., Energy Recovery from Controlled Mixing Salt and Fresh Water with a Reverse Electrodialysis System. *Environmental Science & Technology* **2008,** *42*, (15), 5785-5790.
12. Veerman, J.; Saakes, M.; Metz, S. J.; Harmsen, G. J., Reverse electrodialysis: Performance of a stack with 50 cells on the mixing of sea and river water. *Journal of Membrane Science* **2009,** *327*, (1-2), 136-144.
13. Vermaas, D. A.; Saakes, M.; Nijmeijer, K., Double Power Densities from Salinity Gradients at Reduced Intermembrane Distance. *Environmental Science & Technology* **2011,** *45*, (16), 7089-7095.
14. Scialdone, O.; Guarisco, C.; Grispo, S.; Angelo, A. D.; Galia, A., Investigation of electrode material - Redox couple systems for reverse electrodialysis processes. Part I: Iron redox couples. *Journal of Electroanalytical Chemistry* **2012,** *681*, (0), 66-75.
15. Gurreri, L.; Tamburini, A.; Cipollina, A.; Micale, G., CFD analysis of the fluid flow behavior in a reverse electrodialysis stack. *Desalination and Water Treatment* **2012,** *48*, (1-3), 390-403.
16. Brauns, E., Salinity gradient power by reverse electrodialysis: effect of model parameters on electrical power output. *Desalination* **2009,** *237*, 378–391.
17. Veerman, J.; Saakes, M.; Metz, S. J.; Harmsen, G. J., Reverse electrodialysis:A validated process model for design and optimization. *Chemical Engineering Journal* **2011,** *166*, (1), 256–268.
18. Vermaas, D. A.; Guler, E.; Saakes, M.; Nijmeijer, K., Theoretical power density from salinity gradients using reverse electrodialysis. *Energy Procedia* **2012,** *20*, 170-184.
19. Ramon, G. Z.; Feinberg, B. J.; Hoek, E. M. V., Membrane-based production of salinity-gradient power. *Energy & Environmental Science* **2011,** *4*, (11), 4423-4434.
20. Daniilidis, A.; Vermaas, D. A.; Herber, R.; Nijmeijer, K., Effect of salinity gradient on power output in reverse electrodialysis. *Renewable energy* **2013**, (submitted).
21. Daniilidis, A.; Herber, R.; Vermaas, D. A., Upscale potential and financial feasibility of a reverse electrodialysis (RED) power plant. *Applied Energy* **2013**, (submitted).
22. Vermaas, D. A.; Kunteng, D.; Saakes, M.; Nijmeijer, K., Fouling in reverse electrodialysis under natural conditions. *Water Research* **2013,** *47*, (3), 1289-1298.
23. Allison, R. P., Electrodialysis reversal in water reuse applications. *Desalination* **1995,** *103*, (1-2), 11-18.
24. Vermaas, D. A.; Saakes, M.; Nijmeijer, K., Power generation using profiled membranes in reverse electrodialysis. *Journal of Membrane Science* **2011,** *385-386*, 234-242.
25. Logan, B. E.; Elimelech, M., Membrane-based processes for sustainable power generation using water. *Nature* **2012,** *488*, (7411), 313-319.

26. Post, J. W.; Hamelers, H. V. M.; Buisman, C. J. N., Influence of multivalent ions on power production from mixing salt and fresh water with a reverse electrodialysis system. *Journal of Membrane Science* **2009,** *330*, (1-2), 65-72.

27. Higa, M.; Tanioka, A.; Miyasaka, K., A study of ion permeation across a charged membrane in multicomponent ion systems as a function of membrane charge density. *Journal of Membrane Science* **1990,** *49*, 145-169.

28. Vermaas, D. A.; Saakes, M.; Nijmeijer, K., Early detection of preferential channeling in reverse electrodialysis. *Electrochimica Acta (submitted)* **2013**.

29. Oliver, B. G.; Thurman, E. M.; Malcolm, R. L., The contribution of humic substances to the acidity of colored natural waters. *Geochimica et Cosmochimica Acta* **1983,** *47*, (11), 2031-2035.

30. Grebenyuk, V. D.; Chebotareva, R. D.; Peters, S.; Linkov, V., Surface modification of anion-exchange electrodialysis membranes to enhance anti-fouling characteristics. *Desalination* **1998,** *115*, (3), 313-329.

31. Lee, H.-J.; Moon, S.-H.; Tsai, S.-P., Effects of pulsed electric fields on membrane fouling in electrodialysis of NaCl solution containing humate. *Separation and Purification Technology* **2002,** *27*, (2), 89-95.

32. Vrouwenvelder, J. S.; Schulenburg, D. A. G. v. d.; Kruithof, J. C.; Johns, M. L.; Loosdrecht, M. C. M. v., Biofouling of spiral-wound nanofiltration and reverse osmosis membranes: A feed spacer problem. *Water Research* **2009,** *43*, (3), 583-594.

33. Lee, H.-J.; Moon, S.-H., Enhancement of electrodialysis performances using pulsing electric fields during extended period operation. *Journal of Colloid and Interface Science* **2005,** *287*, 597-603.

34. Lee, H.-J.; Park, J.-S.; Moon, S.-H., A study on fouling mitigation using pulsing electric fields in electrodialysis of lactate containing BSA. *Korean Journal of Chemical Engineering* **2002,** *19*, (5), 880-887.

35. Cifuentes-Araya, N.; Pourcelly, G.; Bazinet, L., Impact of pulsed electric field on electrodialysis process performance and membrane fouling during consecutive demineralization of a model salt solution containing a high magnesium/calcium ratio. *Journal of Colloid and Interface Science* **2011,** *361*, (1), 79-89.

36. Amr, A. G.; Schoenbach, K. H., Biofouling prevention with pulsed electric fields. *Plasma Science, IEEE Transactions on* **2000,** *28*, (1), 115-121.

37. Zabolotsky, V. I.; Loza, S. A.; Sharafan, M. V., Physicochemical Properties of Profiled Heterogeneous Ion-Exchange Membranes. *Russian Journal of Electrochemistry* **2005,** *41*, (10), 1053–1060.

Supporting information

Appendix A: Experimental setup

Electrode system

The electrode compartments were rinsed with 0.25 M NaCl solution. Hence, when an electrical current is generated by the RED stack, hydrogen gas is formed at the cathode and a mixture of oxygen and chlorine gas is created at the anode. These redox reactions are irreversible and require a significant electrical overpotential. As the performance of the RED cells is of more interest than that of the electrodes, the potential over the RED cells was measured using an Ag/AgCl reference electrode (QIS, The Netherlands) connected to the middle of each electrode compartment. The electrode rinse solution was circulated at 100 ml/min and kept at a pressure of 500 mbar to prevent bulging of the membrane pairs towards the electrolyte compartment.

Feedwater monitoring

The conductivity and temperature of the feedwater streams were monitored continuously (ProMinent, Dulcometer, Germany) and water samples were taken regularly for an analysis of the ionic composition and organic components (total organic carbon (TOC) and liquid chromatography – organic carbon detection (LC-OCD)). The pressure drop between the inlet and the outlet of the feedwater streams was measured with a differential pressure meter (Endress+Hauser, Deltabar S, Germany) or as the difference between two individual pressure meters (Endress+Hauser, Cerabar T, Germany). The conductivities, temperatures and pressures were recorded every 30 s in a data logger (Endress+Hauser, Ecograph T, Germany).

Electrochemical cycles

The cycles for electrical current generation are illustrated in Figure S10.1. These 30-minute cycles were repeated continuously, except for some small interruptions when replacing the feedwater filters or during incidental software failures.

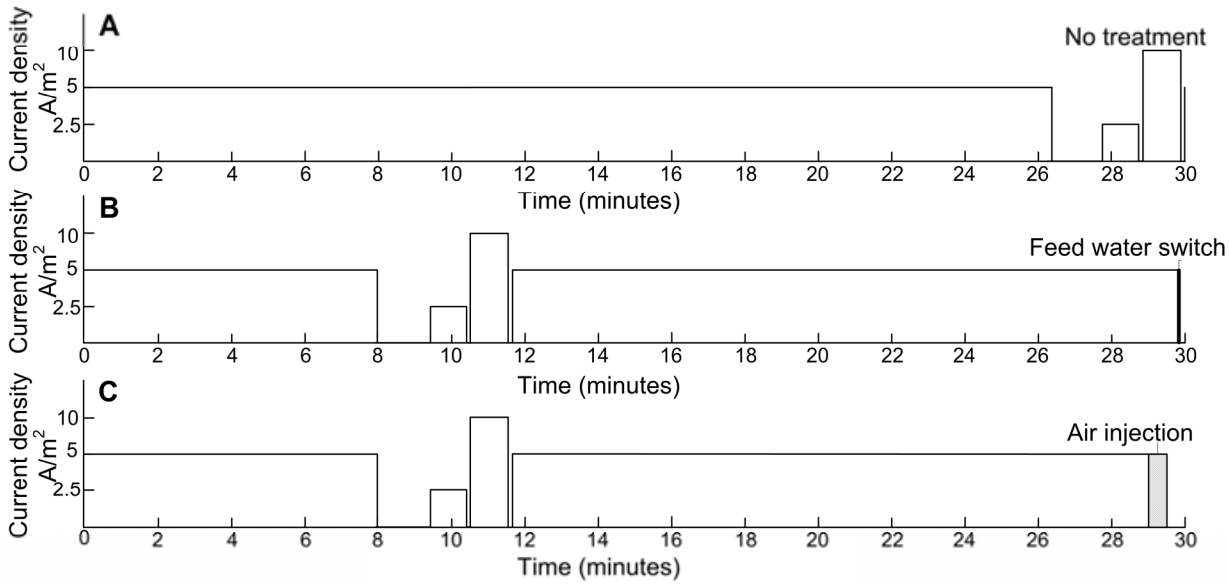

Figure S10.1: Chronopotentiometric cycles for three RED stacks. The first stack was used as reference and no anti fouling strategy was applied (A), the second stack was operated with periodic switching of the feedwater as anti fouling strategy (B) and the third stack was applied with periodic air sparging as an anti fouling strategy (C). For the stack with feedwater switch, the direction of the electrical current reverses after each feedwater switch as well.

For most of the time during the 30-minute chronopotentiometric cycles as illustrated in Figure S10.1 a current density of 5 A/m^2 was generated by the stacks. The open circuit voltage (OCV, in V) was derived from a 90 s stage without electrical current. The other stages for OCV are applied to recover after a feedwater switch (10 s OCV), after air sparging (15 s OCV) or to determine the ohmic resistance after a stage of electrical current (1 s OCV).

Appendix B: Stack resistance

Figure S10.2 shows the ohmic and non-ohmic resistance, as a function of time.

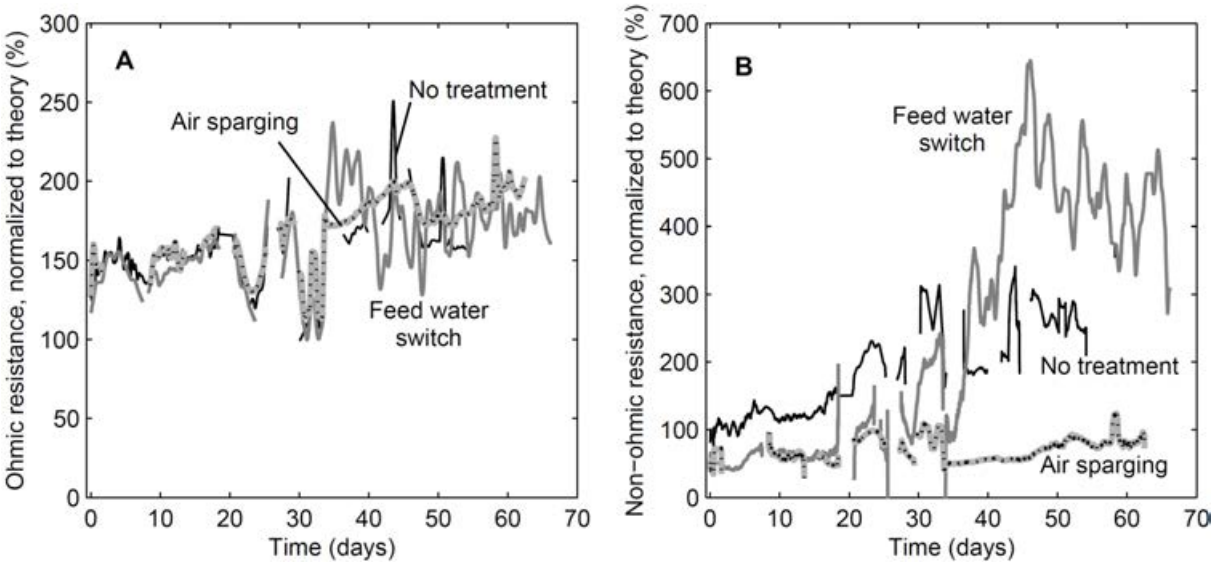

Figure S10.2: Normalized ohmic (A) and non-ohmic (B) resistance, as a function of time, for the full span of the experiment. All series have small interruptions due to software failures or small air bubbles blocking the reference electrodes. Fluctuations are due to temporal changes in feedwater composition (e.g., relatively more multivalent ions) and a slow response time as the fouling intensifies, which complicates distinguishing the ohmic and non-ohmic resistance. A moving average with a span of 24 hours was applied to remove short term noise.

As indicated in Figure S10.2A, the ohmic resistance increases only moderately for all stacks, to approximately twice the theoretical equivalents after 67 days. Fluctuations on this trend are due to temporal changes in feedwater composition (e.g., relatively more multivalent ions) and a slow response time as the fouling intensifies, which complicates distinguishing the ohmic and non-ohmic resistance. The non-ohmic resistance (Figure S10.2A) increases only significant for the stacks without treatment and with feedwater switching. The stack with feedwater switching has the highest non-ohmic resistance from approximately day 35, due to preferential channelling.

Photo: Rik Siebers, REDstack B.V.

Chapter 11

General discussion and outlook

11.1 Introduction

The previous chapters of this thesis offered scientific insight in the developments that improve the performance of RED on a laboratory scale. As RED starts to operate at larger scale (several kW to MW), implementation of these scientific developments is required. In the previous chapters, recommendations on the specific topics are already discussed. This chapter offers a general discussion considering the trade-off between several parameters in RED, possible directions for future RED designs, such as microdesigns, and the economic perspective of RED.

11.2 Trade-offs

As RED develops towards commercial application, the need for optimization grows. Before optimizing individual, sometimes counteracting operational parameters, a suitable response parameter (i.e., the parameter to be maximized) must be defined. This section will discuss the possible response parameters and how they are influenced by operational parameters.

Most of the research on RED focuses on the power density [1-7], as this parameter is believed to be most important for the economic potential of large scale operation of RED. Although the major contribution of the membranes to the total costs of a RED power plant [8, 9] justifies indeed maximizing the power density, optimizing the power density only would not lead to a realistic case for practical applications. For example, when optimizing the obtained gross power density only, the optimum would imply an infinite flow velocity, which is obviously not realistic. Therefore, a trade-off with other parameters is required to obtain useful set points for operating conditions in practical applications.

The first trade-off is related to the pumping power. The net power density (i.e., obtained gross power density minus power density consumed for pumping) accounts for the power consumed for pumping the feedwater through the stack. In fact, the maximum net power density resembles the optimum in the trade-off between the obtained power density and the pumping power. Such an optimum can be found easily, as the units for the obtained power density and the pumping power density are equal.

However, the net power density cannot be the only concern because the volumes of feedwater are usually limited. Hence, the energy efficiency (i.e., the actually obtained energy divided by the theoretically available energy per volume feedwater) should be involved too. When considering the trade-off between power density and energy efficiency, an optimum is more arbitrary. In cases where the feedwater is limiting, or where extensive feedwater pretreatment is required, the need for a high energy efficiency increases. In general, a larger residence time of the feedwater, e.g., using a lower flow rate, corresponds to higher energy efficiency, sacrificing gross power density, as for example demonstrated in Figure 2.3 in chapter 2 [6].

Also when considering the net power density instead of the gross power density, there is no flow rate at which both the net power density and energy efficiency parameters are maximized. The trade-off between net power density and energy efficiency was recognized before [10], and an equivalent of the product of these two parameters was proposed to obtain a single response parameter. Although such a parameter is arbitrary, it can be used to compare stacks and flow rates. For each specific case, feedwater limitations and pretreatments should be considered to make a trade-off between energy efficiency and net power density.

An example of the essential trade-off between net power density and energy efficiency is demonstrated in Figure 11.1, which shows the net power density as a function of the energy efficiency and the product of the net power density and the energy efficiency as a function of the Reynolds number. The shown experimental data is derived from four different stacks, each with a different spacer thickness.

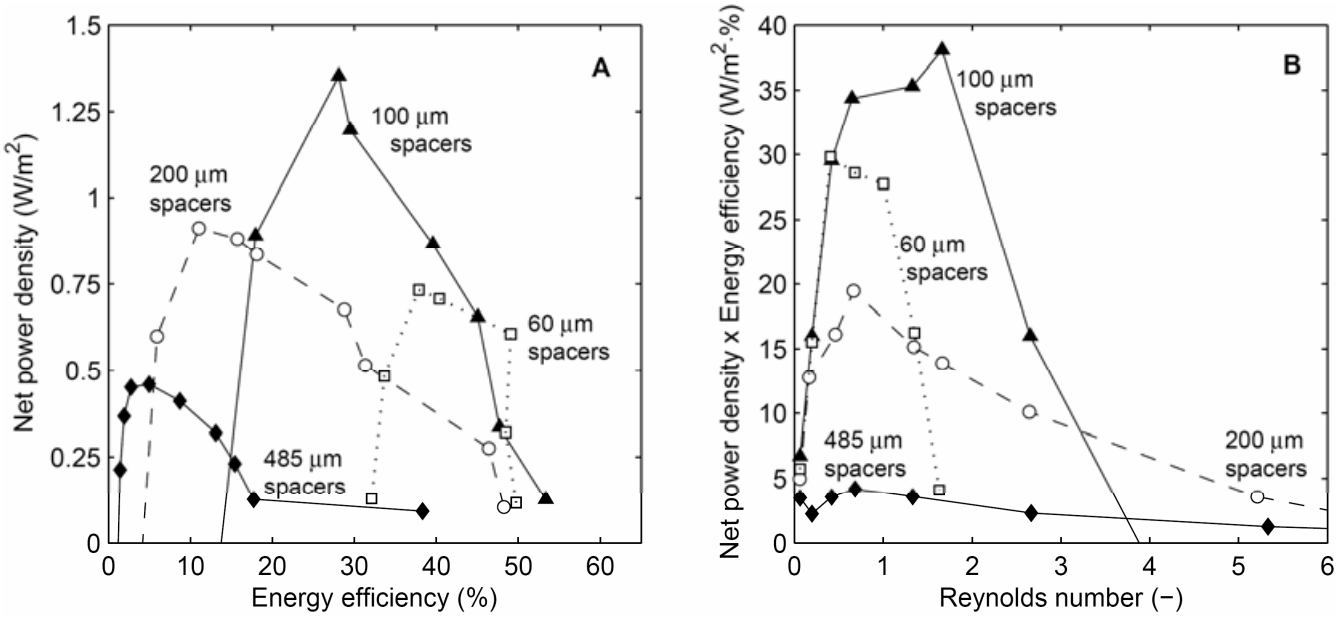

Figure 11.1: A) Net power density as a function of the energy efficiency, and B) net power density multiplied with energy efficiency for different spacer thicknesses. Data obtained from Vermaas et al.*, 2011 [6]. The data measured at the lowest feedwater flow rates can be found at the right side of panel A, while higher flow rates correspond to the data at the left side in panel A; which is opposite to panel B, where higher Reynolds numbers represent higher flow rates.*

As demonstrated in Figure 11.1A, the net power density increases as the energy efficiency increases at the left hand side of the maximum. There, the flow rate is high, corresponding to a short residence time. The short residence time prevents capturing a large fraction of the available energy, which results in a low energy efficiency. At the same time, the power required for pumping is high and the net power density is sub-optimal.

At higher energy efficiencies, at the right side of the maximum, the net power density can be sacrificed for energy efficiency. A longer residence time enables more ion exchange, which increases the energy efficiency, but also increases the non-ohmic resistance, which decreases the net power density. These operational conditions can be chosen in cases where the feedwater supply is limiting rather than the membrane price.

Adopting the product of the net power density and energy efficiency as a response parameter, the optimum intermembrane distance and Reynolds number are revealed. Figure 11.1B shows that a spacer thickness of 100 µm and a Reynolds number of approximately 1.5 (corresponding to a residence time of 9 s) is optimal when using spacers and corresponding stack designs. For larger intermembrane distances, the ohmic resistance

of the river water compartment limits the performance, while at smaller intermembrane distances the power consumed for pumping the feedwater dominates.

Although an intermembrane distance of 100 μm is optimal in the current design, even smaller intermembrane distances are promising for further improvement, as the pumping power can be strongly reduced, using e.g. profiled membranes [11] or a different feedwater inflow [7, 12]. Although such small intermembrane distances are challenging when considering fouling prevention, the large difference in performance justifies aiming for small intermembrane distances. This potential increase in performance can be illustrated when tuning the dimensions of a future RED stack, as is demonstrated in the next section.

11.3 Microdesigns

As an outlook for possible microdesigns in RED that obtain high power densities, the influence of stack dimensions (i.e., channel length and intermembrane distance) on the RED performance is evaluated using an empirical model. Systems with spacers as well as with profiled membranes (i.e., integrated membrane and spacer) are considered. A uniform feedwater distribution is assumed and the intermembrane distance and flow rate are optimized, to be representative for the maximum power density and energy efficiency using the present state-of-the-art technology. For such an idealized but realistic system, membranes with an area resistance of 1 $\Omega \cdot cm^2$ and an apparent permselectivity of 97% are considered, assuming an open area of 50% for spacers or 10% coverage of ridges for profiled membranes. Seawater is represented by 0.51 M NaCl and river water is represented with 0.017 M NaCl. The length of the feedwater channels is varied from 1 mm to 1 m. The intermembrane distance, residence time and current density are optimized to obtain a maximum product of the net power density and the energy efficiency for each individual calculation. More details on this empirical model are described in previous work [13].

Figure 11.2A-B shows the resulting net power density and the energy efficiency, as a function of the length of the feedwater channels (i.e., distance between inflow and outflow of the feedwater), for stacks with spacers and profiled membranes. The corresponding intermembrane distance and residence time of the feed waters are shown in Figure 11.2C-D.

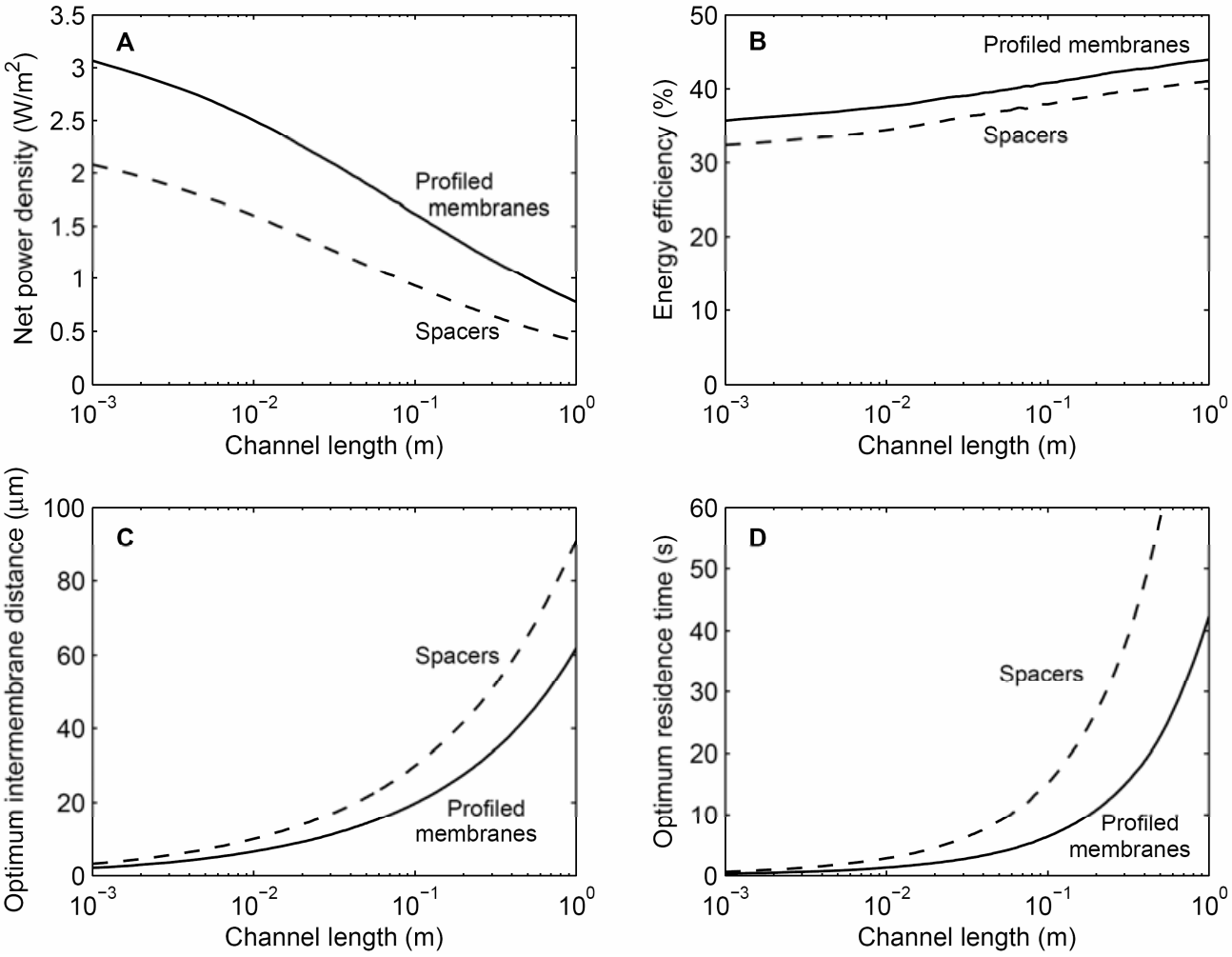

Figure 11.2: Modeled net power density (A), energy efficiency (B), and corresponding intermembrane distance (C) and residence time (D), as a function of the channel length, for RED stacks with spacers or profiled membranes. The results are obtained using the product of the net power density and the energy efficiency as a response parameter. A logarithmic scale is used for the channel length.

Figure 11.2 shows that the highest performance in terms of net power density is obtained at minimum channel length, very small intermembrane distances and short residence times. A net power density of more than 3 W/m^2 with an energy efficiency of 36% is envisaged for a stack with profiled membranes at a channel length of 1 mm. When longer feedwater channels are used, the net power density decreases significantly, while the energy efficiency increases only slightly. The high net power density for short channels is due to the relatively low power consumed for pumping of the feed waters. The low pumping power allows very small intermembrane distances (Figure 11.2C) and low residence times (Figure 11.2D) and hence minimized electrical resistance of the feedwater compartments, especially that of the

river water compartment. The increase in net power density for short channels is even more pronounced when membranes with lower area resistance are used for these calculations (not shown). Hence, the advantage of short feedwater channels (microchannels) is evident.

The use of profiled membranes eases the production of microchannel systems as it integrates the membrane, spacer and gasket functionality. However, systems with a channel length of 1 mm and a few μm intermembrane distance are two orders of magnitude smaller than the typical currently developed RED systems. Hence, the current design may not be suitable in terms of fabrication accuracy and membrane area required for sealing, because the current designs use several mm of membrane around each compartment for sealing. Therefore, different designs have to be considered. Microfluidic designs, also known as lab-on-a-chip, are well known in other research fields, e.g., biomimetics [14-16], and have proven to be successful creating accurately microchannels as small as outlined for an optimal micro-RED design. A draft for a similar micro-design for RED was proposed by Veerman *et al.* [10].

An ongoing challenge for microdesigns is to prevent clogging of foulants. Colloid fouling as observed in RED [17] can clog easier when the channel dimensions decrease. On the other hand, microfluidic designs offer a wide range of possibilities to reduce fouling. For example, nano-corrugated surfaces can reduce fouling [18], reduce the pressure drop over feedwater channels and improve mixing at the same time [19, 20]. In addition, micro-manifolds can inject small air bubbles to the feedwater flow to remove fouling (similar to air injection [21]) and enhance mixing of the fluid in the flow channels, due to a circulation within each fluid droplet [22]. Future research can be dedicated to develop suitable microdesigns for RED and control fouling in such devices.

11.4 Feedwater distribution

Besides fabrication and fouling issues, the main challenge of RED cells with small channel length is the uniform distribution of the feedwater, i.e., designing the manifolds. A system with feedwater channels of only 1 mm and small intermembrane distances (Figure 11.2C) corresponds to very low flow rates even though the residence time is low (Figure 11.2D). Hence, such system requires an ingenious feedwater distribution to process all feedwater in large scale applications. For a possible salinity gradient power plant at the Afsluitdijk a typical flow of 500 m^3/s is envisaged, which would correspond to 4 trillion feedwater channels of 1 cm wide and 1 mm length. Even when 1000 cells would be stacked, this would

correspond to a total width of approximately 40000 km of RED stacks, which is similar to the Earth's circumference.

The feedwater distribution in manifolds similar to the present state-of-the-art designs would probably be too costly for a financial feasible RED operation. Moreover, the gaskets to seal the feedwater compartments would occupy relatively larger membrane area when the area of each feedwater compartment decreases. For these two reasons, it is a future challenge to develop novel RED designs that efficiently distribute the feedwater over small compartments with a minimum of gaskets.

Current designs for heat exchangers [23, 24] can be an example for this challenge, as these systems also require fast exchange (of heat, in this case) and deal with large fluidic flow rates. For example, the use of radial flow designs in heat exchangers can be transferred to RED for at least one of the feedwater types. An exemplary design is demonstrated in Figure 11.3.

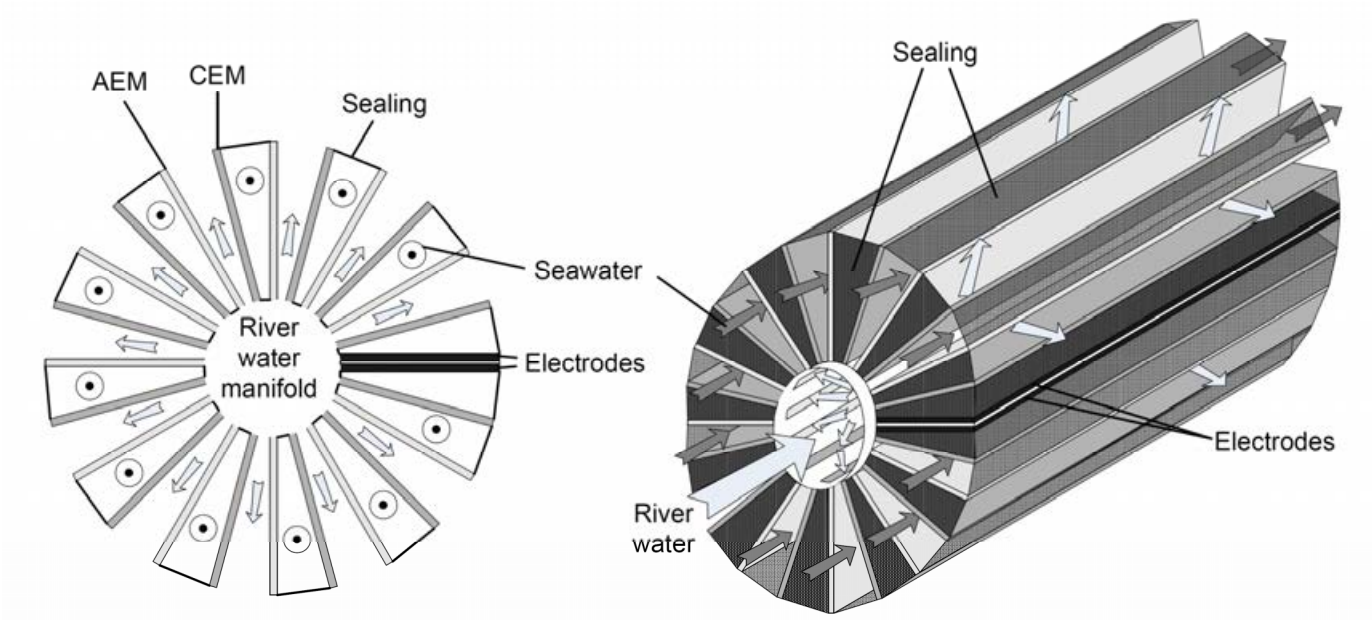

Figure 11.3: System with radial river water flow and axial seawater flow, in cross-sectional view (left) and three dimensional view (right). The ion exchange is in tangential direction.

The design in Figure 11.3 provides a radial flow of river water and an axial flow of seawater. The radial flow enables a relatively small inflow manifold for river water, as it connects to the feedwater compartments in all directions. Moreover, flow in round pipes is subject to a minimum hydraulic friction compared to its cross-sectional area [25]. Therefore short and

thin feedwater channels for river water can be supplied with relatively small manifolds. As the river water compartments have a major contribution to the electrical resistance, the small intermembrane distance for river water increases the power density. The channels for the well conductive seawater flow are longer in this case, and may feature a larger intermembrane distance to save power spent on pumping the feedwater.

In more detail, the feedwater compartments as proposed in Figure 11.3 are wedged, i.e., the intermembrane distance increases for the river water from inflow to outflow. Such variable intermembrane distance benefits the net power density, as the intermembrane distance is smallest where the river water is least conductive, while the pumping power is reduced for the larger intermembrane distance at the end of the flow channels. Similar designs using a variable intermembrane distance are filed in a patent [26].

In conclusion, the asymmetrical flow design and the radial manifold for river water saves volume (and probably costs) for the manifolds distributing feedwater. Hence, smaller and shorter channels are possible, especially for the river water compartments. Future research may be dedicated to designing and experimental testing some of the numerous possible systems inspired on existing designs in the field of heat exchangers and microfluidic systems.

11.5 Economic perspective

The future possibilities for RED mainly depend on the economic perspective. This paragraph roughly estimates the economic perspective for RED, and compares that to other electricity sources. To compare the corresponding estimated price for energy generation by RED to other (sustainable and non-sustainable) electrical power sources, the levelized cost of electricity (LCOE) can be used, expressed in €/kWh.

The improvements in the performance of RED, from this thesis and other research, favor the financial feasibility of a RED power plant. The maximum gross power density obtained with 100 μm spacers, combined with the pressure drop for profiled membranes, would result in a net power density of approximately 2.2 W/m^2 and 35% energy efficiency. These results are assumed representative for the present state-of-the-art performance of RED, adopting feedwater concentrations of 0.5 M NaCl and 0.017 M NaCl. Other assumptions are a capacity factor (i.e., ratio of actual output to its potential output) of 84%, a membrane lifetime of 7 years and 2% inflation per year [27]. The costs for feedwater pretreatment are

derived from previous cost estimations [8]. Other estimated values are described by Daniilidis *et al.*, 2013 [28].

The membrane price is a crucial factor that is hard to estimate accurately. Two scenarios are considered, one for a membrane price of 50 €/m^2 (as an educated guess for the current membrane price) and another for a membrane price of 4.3 €/m^2, which resembles the break-even point when considering a project time of 30 years [28]. These cases are presented in Table 11.1.

A third case is added to the calculation considering further improvement in power density and a decrease in membrane prices. Optimization of the intermembrane distance and flow rate [13] for profiled membranes [11] make it possible to achieve a net power density of 2.7 W/m^2 with the present stack design. This value is used in combination with a membrane price of 4 €/m^2, which is the approximate price of the cheapest currently available ion exchange membranes [29]. In this case, it is assumed that also high performance membranes (e.g., associated with low resistance) can be produced for this price in the future. The LCOE of these RED cases (Table 11.1) are compared to other power sources in Figure 11.4, using discount rates (i.e., the rate of return that could be earned with other investments) of 5% and 10%.

Table 11.1: Net power density and membrane price to estimate the economic perspective for three cases of RED. The membrane price is constant in time for all cases.

	Net power density	Membrane price
RED, case 1	2.2 W/m^2	50 €/m^2
RED, case 2	2.2 W/m^2	4.3 €/m^2
RED, case 3	2.7 W/m^2	4 €/m^2

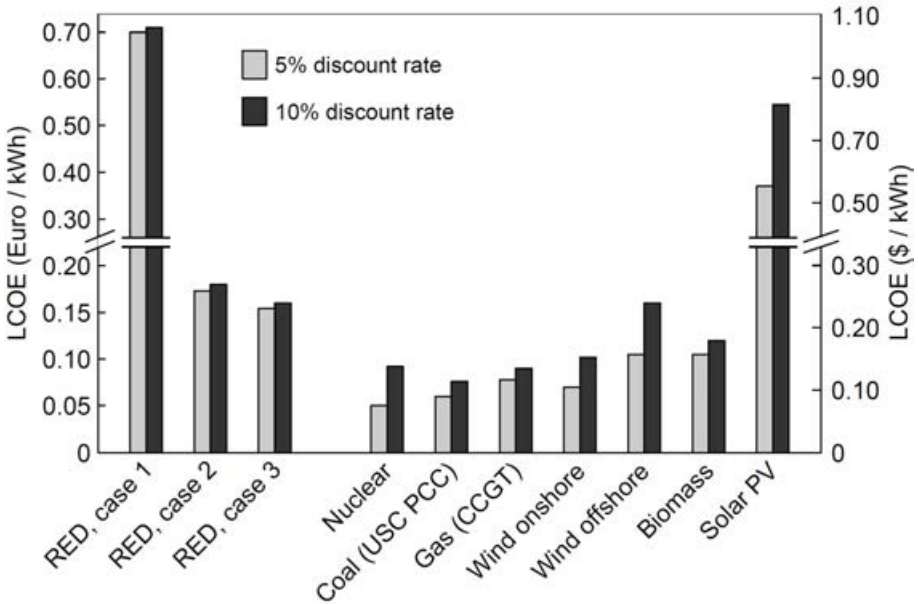

Figure 11.4: Levelised cost of electricity (LCOE) for different electrical power sources in The Netherlands, using 5% or 10% discount rate (i.e., the rate of return that could be earned with other investments). Data obtained from Daniilidis et al.*, 2013 [28]. The vertical axis is divided into 2 sections, from which the upper section uses larger steps than the lower section*

Figure 11.4 shows that a constant membrane price of 50 €/m^2 (case 1) makes RED more expensive than other energy sources [28]. When the membrane price is reduced to 4.3 €/m^2 (case 2), the levelised cost of electricity (LCOE) is reduced to approximately 0.18 €/kWh, which is significantly cheaper than using solar power from photovoltaic (PV) cells in The Netherlands and slightly more expensive than wind power [28]. When an increase in performance and a decrease in membrane price are envisaged (case 3), the LCOE would decrease to approximately 0.16 €/kWh. Such price for RED is close to that for offshore wind energy [28]. Although the price for onshore wind energy is significantly lower, RED can still be competitive to this renewable energy source because RED can be considered as a base load power source while the power generation from wind fluctuates much more.

A nuance is essential for this economic perspective, as numerous factors regarding the financial feasibility of RED are still highly uncertain, e.g., the costs for fouling prevention and investments for feedwater distribution. These factors cannot be extrapolated from the present experimental data, nor realistically modeled. Only experiments on larger scale under practical (natural) conditions yield representative information for these estimations. The RED pilot plant that is currently built on the Afsluitdijk (The Netherlands) by REDstack B.V. is crucial for a more realistic estimation of the requirements and costs for fouling

prevention and feedwater distribution. Having those values accurately established, the financial feasibility of RED can be better compared to other conventional and renewable energy sources.

The uncertain factors in the economic perspective of RED are not only a risk, but also an opportunity. A higher net power density is theoretically possible with e.g. microdesigns, and the costs for controlling the fouling can higher as well as lower than the currently expected costs. In the end, when issues such as stack dimensioning and fouling control are successfully solved, RED is promising as a large scale base load renewable energy source.

References

1. Długołęcki, P. E.; Gambier, A.; Nijmeijer, K.; Wessling, M., Practical Potential of Reverse Electrodialysis As Process for Sustainable Energy Generation. *Environmental Science & Technology* **2009,** *43*, (17), 6888-6894.
2. Guler, E.; Elizen, R.; Vermaas, D.; Saakes, M.; Nijmeijer, K., Performance-determining membrane properties in reverse electrodialysis. *Journal of Membrane Science* **2013,** *446*, 266–276.
3. Lacey, R. E., Energy by Reverse Electrodialysis. *Ocean Engineering* **1980,** *7*, (1), 1-47.
4. Veerman, J.; Jong, R. M. D.; Saakes, M.; Metz, S. J.; Harmsen, G. J., Reverse electrodialysis: Comparison of six commercial membrane pairs on the thermodynamic efficiency and power density. *Journal of Membrane Science* **2009,** *343*, (1-2), 7-15.
5. Veerman, J.; Saakes, M.; Metz, S. J.; Harmsen, G. J., Electrical Power from Sea and River Water by Reverse Electrodialysis: A First Step from the Laboratory to a Real Power Plant. *Environmental Science & Technology* **2010,** *44*, (23), 9207-9212.
6. Vermaas, D. A.; Saakes, M.; Nijmeijer, K., Double Power Densities from Salinity Gradients at Reduced Intermembrane Distance. *Environmental Science & Technology* **2011,** *45*, (16), 7089-7095.
7. Vermaas, D. A.; Saakes, M.; Nijmeijer, K., Enhanced mixing for energy generation in reverse electrodialysis. *Journal of Membrane Science (submitted)* **2013**.
8. Post, J. W.; Goeting, C. H.; Valk, J.; Goinga, S.; Veerman, J.; Hack, P. J. F. M., Towards implementation of reverse electrodialysis for power generation from salinity gradients. *Desalination and water treatment* **2010,** *16*, 182-193.
9. Turek, M.; Bandura, B., Renewable energy by reverse electrodialysis. *Desalination* **2007,** *205*, 67-74.
10. Veerman, J.; Saakes, M.; Metz, S. J.; Harmsen, G. J., Reverse electrodialysis:A validated process model for design and optimization. *Chemical Engineering Journal* **2011,** *166*, (1), 256–268.
11. Vermaas, D. A.; Saakes, M.; Nijmeijer, K., Power generation using profiled membranes in reverse electrodialysis. *Journal of Membrane Science* **2011,** *385-386*, (0), 234-242.
12. Vermaas, D. A.; Saakes, M.; Nijmeijer, K., Early detection of preferential channeling in reverse electrodialysis. *Electrochimica Acta (submitted)* **2013**.
13. Vermaas, D. A.; Guler, E.; Saakes, M.; Nijmeijer, K., Theoretical power density from salinity gradients using reverse electrodialysis. *Energy Procedia* **2012,** *20*, 170-184.
14. Eijkel, J. C.; Van Den Berg, A., Nanofluidics: what is it and what can we expect from it? *Microfluidics and Nanofluidics* **2005,** *1*, (3), 249-267.
15. Domachuk, P.; Tsioris, K.; Omenetto, F. G.; Kaplan, D. L., Bio-microfluidics: Biomaterials and Biomimetic Designs. *Advanced Materials* **2010,** *22*, (2), 249-260.

16. Emerson, D. R.; Cieslicki, K.; Gu, X.; Barber, R. W., Biomimetic design of microfluidic manifolds based on a generalised Murray's law. *Lab on a Chip* **2006,** *6*, (3), 447-454.

17. Vermaas, D. A.; Kunteng, D.; Saakes, M.; Nijmeijer, K., Fouling in reverse electrodialysis under natural conditions. *Water Research* **2013,** *47*, (3), 1289-1298.

18. Bhushan, B.; Jung, Y. C., Natural and biomimetic artificial surfaces for superhydrophobicity, self-cleaning, low adhesion, and drag reduction. *Progress in Materials Science* **2011,** *56*, (1), 1-108.

19. Haase, A. S.; Karatay, E.; Tsai, P. A.; Lammertink, R. G. H., Momentum and mass transport over a bubble mattress: the influence of interface geometry. *Soft Matter* **2013**.

20. Jung, Y. C.; Bhushan, B., Biomimetic structures for fluid drag reduction in laminar and turbulent flows. *Journal of Physics: Condensed Matter* **2010,** *22*, (3), 035104.

21. Vermaas, D. A.; Kunteng, D.; Veerman, J.; Saakes, M.; Nijmeijer, K., Periodic feed water reversal and air sparging as anti fouling strategies in reverse electrodialysis. *Environmental Science & Technology (submitted)* **2013**.

22. Shui, L.; Eijkel, J. C. T.; van den Berg, A., Multiphase flow in microfluidic systems - Control and applications of droplets and interfaces. *Advances in Colloid and Interface Science* **2007,** *133*, (1), 35-49.

23. Fan, Y.; Luo, L., Recent Applications of Advances in Microchannel Heat Exchangers and Multi-Scale Design Optimization. *Heat Transfer Engineering* **2008,** *29*, (5), 461-474.

24. Rebrov, E. V.; Schouten, J. C.; de Croon, M. H. J. M., Single-phase fluid flow distribution and heat transfer in microstructured reactors. *Chemical Engineering Science* **2011,** *66*, (7), 1374-1393.

25. Batchelor, G. K., *An introduction to fluid dynamics*. Cambridge University Press: New York, **2000**; 615 p.

26. Vermaas, D. A.; Hitsov, I.; Schaetzle, O.; Galama, O.; Saakes, M. Device and method for performing an ion-exchange process. NL 2011331, **2013**.

27. Daniilidis, A.; Vermaas, D. A.; Herber, R.; Nijmeijer, K., Effect of salinity gradient on power output in reverse electrodialysis. *Renewable energy* **2013**, (submitted).

28. Daniilidis, A.; Herber, R.; Vermaas, D. A., Upscale potential and financial feasibility of a reverse electrodialysis (RED) power plant. *Applied Energy* **2013**, (submitted).

29. Guler, E.; Zhang, Y.; Saakes, M.; Nijmeijer, K., Tailor-Made Anion-Exchange Membranes for Salinity Gradient Power Generation Using Reverse Electrodialysis. *ChemSusChem* **2012,** *5*, (11), 2262-2270.

List of publications

Publications in this thesis

David A. Vermaas, Saakes, Kitty Nijmeijer, Double Power Densities from Salinity Gradients at Reduced Intermembrane Distance. *Environmental Science & Technology* **2011,** *45*, (16), 7089-7095

David A. Vermaas, Michel Saakes, Kitty Nijmeijer, Power generation using profiled membranes in reverse electrodialysis. *Journal of Membrane Science* **2011,** *385-386*, (0), 234-242

David A. Vermaas, Damnearn Kunteng, Michel Saakes, Kitty Nijmeijer, Fouling in reverse electrodialysis under natural conditions. *Water Research* **2013,** *47*, (3), 1289-1298

David A. Vermaas, Suman Bajracharya, Bruno Bastos Sales, Michel Saakes, Bert Hamelers, Kitty Nijmeijer, Clean energy generation using capacitive electrodes in reverse electrodialysis. *Energy & Environmental Science* **2013,** *6*, (2), 643-651

David A. Vermaas, Joost Veerman, Ngai Yin Yip, Menachem Elimelech, Michel Saakes, Kitty Nijmeijer, High Efficiency in Energy Generation from Salinity Gradients with Reverse Electrodialysis. *Sustainable Chemistry & Engineering* **2013,** *1*, 1295−1302

David A. Vermaas, Michel Saakes, Kitty Nijmeijer, Enhanced mixing for energy generation in reverse electrodialysis. *Journal of Membrane Science,* **2014,** *453*, 312-319

David A. Vermaas, Michel Saakes, Kitty Nijmeijer, Early detection of preferential channeling in reverse electrodialysis. *Electrochimica Acta (in press, DOI 10.1016/j.electacta.2013.11.094)*

David A. Vermaas, Damnearn Kunteng, Joost Veerman, Michel Saakes, Kitty Nijmeijer, Periodic feed water reversal and air sparging as anti fouling strategies in reverse electrodialysis. *Environmental Science & Technology (submitted)*

David A. Vermaas, Joost Veerman, Michel Saakes, Kitty Nijmeijer, Influence of multivalent ions on renewable energy generation in reverse electrodialysis. *Energy & Environmental Science (submitted)*

Publications beyond this thesis

David A. Vermaas, Wim S.J. Uijttewaal, Ton J.F. Hoitink, Lateral transfer of streamwise momentum caused by a roughness transition across a shallow channel. *Water Resources Research* **2011,** *47*, (2), W02530

David A. Vermaas, Enver Güler, Michel Saakes, Kitty Nijmeijer, Theoretical power density from salinity gradients using reverse electrodialysis. *Energy Procedia* **2012,** *20*, 170-184

Enver Güler, Rianne Elizen, David A. Vermaas, Michel Saakes, Kitty Nijmeijer, Performance-determining membrane properties in reverse electrodialysis. *Journal of Membrane Science* **2013**, *446*, 266-276

Alexandros Daniilidis, David A. Vermaas, Rien Herber, Kitty Nijmeijer, Effect of salinity gradient on power output in reverse electrodialysis. *Renewable energy* **2014,** 64, 123-131

Alexandros Daniilidis, Rien Herber, David A. Vermaas, Upscale potential and financial feasibility of a reverse electrodialysis (RED) power plant. *Applied Energy (revisions submitted)*

Odne S. Burheim, Jon G. Pharoah, David Vermaas, B.B. Sales, K. Nijmeijer, H.V.M. Hamelers, *Reverse electrodialysis,* book chapter in *Encyclopedia of Membrane Science and Technology* (E.M.V. Hoek and V.V. Tarabara, eds), **2013,** ISBN 978-0-470-90687-3

Patents

David A. Vermaas, Joost Veerman, Machiel Saakes, Reverse electrodialysis energy generating system using capacitive electrodes and method there for, *NL 2008538,* **2012** and *WO 2013/147593 (A1),* **2013**

David A. Vermaas, Ivaylo Hitsov, Olivier Schaetzle, Anne H. Galama, Machiel Saakes, Device and method for performing an ion-exchange process, *NL 2011331*, **2013**

Awards

Oral presentation award, International Congress on Membranes and Membrane Processes 2011 (ICOM), Amsterdam, 23-29 July 2011

Marcel Mulder Award, 2012, awarded annually to a Wetsus researcher that combines scientific excellence with technological innovation and practical relevance.

Dankwoord / Acknowledgments

Na ruim 4 jaar met plezier te hebben gewerkt aan *Reverse Electrodialysis* nadert het einde van mijn werk als promovendus. Dat betekent niet alleen het afronden van een stuk werk, maar vooral ook het kunnen terugkijken op een leuke tijd bij Wetsus en in Leeuwarden. Veel mensen hebben daaraan bijgedragen, inhoudelijk of louter motiverend, en soms zonder hun eigen medeweten, en ik wil hen allen hiervoor graag bedanken.

Allereerst dank aan mijn promotor, Kitty, voor het vertrouwen en de vrijheid die je me hebt gegeven tijdens het hele onderzoek. Je bent altijd positief en constructief geweest, soms zo dat ik begon te twijfelen of je dat ook echt vond. Naast jouw inhoudelijke en tekstuele inbreng die heeft geleid tot een mooi aantal publicaties, was je advies altijd enorm motiverend en heb ik met veel plezier gewerkt. Mijn begeleider bij Wetsus, Michel, hartelijk bedankt voor je grenzeloze enthousiasme en ideeën voor de wildste uitvindingen. Voor de mensen die Michel nog niet kennen: stel hem twee vragen over batterijen en hij geeft je ideeën voor de rest van je promotietraject. Verder was Bert van grote waarde voor mij; het lijkt vaak alsof je overal veel vanaf weet en dan de juiste vragen op het juiste moment weet te stellen. Het is inspirerend hoe gemakkelijk je belangeloos tijd besteed aan het adviseren van promovendi; je hebt een goed luisterend oor voor wetenschappelijke vraagstukken en andere zaken die spelen bij veel promovendi in Wetsus. Bedankt daarvoor.

I would like to thank the colleagues and companies that participate in the Blue Energy theme. The participants of this theme have always been very helpful and constructive. Bruno, thank you for pushing me to write my first publication. Fei and Enver, thanks for the discussions we had about RED or about CAPMIX. Many thanks for Joost, Don, Simon, Kristan, Jan V., Rik, Piet and Inge from REDstack. It was very valuable that we could merge our forces in performing experiments, in the lab and in Harlingen, and merge our knowledge, which gave a major boost in the work to this thesis. Special thanks for Don, who is definitely world leader in building RED stacks and has the right karma for successful experiments. And I would like to acknowledge Joost in particular. Joost, your knowledge, modesty, enthusiasm and your energy to continue working are inspiring.

The office mates in our office, Hw1.06, have contributed definitely for a great part to the fun during my time at Wetsus. First with Marco, Elsemiek, Kamuran, Urania and Luciaan, and later with Jordi, Joeri, Pedro, João and Monir; I always had the feeling that this was the best office there was. Thanks to all of you. The 'office conferences', small talks, silly jokes and breaks (although I skipped quite some) were relaxing. I'm glad that the work on RED will be continued by one of these office mates, Jordi. And I think you will be a great team together with Timon.

Thank you to the other colleagues in Wetsus that helped during the past four years. It was great to have a very helpful technical team, from which in particular Wim, Jan, Jelmer and Foppe were always available for support. Thanks for Oane, who often shared his knowledge and equipment. And thanks for Jan, who provided wise advise as a RED-expert and who came at the right moment with the initiative of Better Bettery, our new company. Also many thanks for Sam, Doekle, Camiel, Bob, Slawek, Natalia, Johannes, Odne, Henk, Zlatica, Anna and Arie for providing assistance, inspiration or for other reasons.

Many students have assisted in the work in this thesis during their internship. Thanks for all of them because they worked highly dedicated on RED: Dovile, Ina, Roeland, Suman, Don, Alex, Alexandra, Kamil, Ivo, Karst, Leon and Steven. Your assistance in experiments was helpful and stimulated me to have a fresh look upon the topics. Also thanks for Petra, you're doing a great job in student acquisition and structuring the large amount of students, and still keep flexible to others in your job.

Verder ben ik de mensen van het Talent team (o.a. Jan Jurjen en Jos) dankbaar voor het uitdagen van de creatieve geesten binnen Wetsus, bijvoorbeeld met de proefjesborrels, en het verspreiden van Blue Energy over heel Nederland; in ieder geval de kennis erover. Daarbij ook dank voor Hester, die mij vaak in de gelegenheid heeft gesteld om te mogen vertellen over Blue Energy voor de (lokale) TV, krant of bezoekende delegaties.

De collega's van de Membrane Science & Technology groep in Twente wil ik ook hartelijk bedanken. Ondanks dat ik niet vaak aanwezig ben geweest op de vakgroep heb ik me er altijd welkom gevoeld en ik was dan ook verrast door de grote hulpvaardigheid. Met name dank voor Harmen, omdat je altijd wel wilde meedenken over processen in RED, en Greet,

die er altijd voor zorgt dat alles op rolletjes loopt zonder dat iemand het doorheeft. Een groot respect daarvoor.

Buiten Wetsus heb ik een super leuke tijd gehad met - en door - de huisgenoten van de Haniahof: José, Sibe Jan, Evelyn, Jos B., Koen, Heidi, Fokje, Benthe, Vera, Nynke, Henny, Ineke, Hielke, Sjoerd, Grytsje, Marco R., Tsjeard, Eva en Afke. Ik ben door de Hania mijn plek in Leeuwarden erg gaan waarderen en met enige pijn in het hart verhuisd uit de Haniahof. Bedankt voor leuke tijd, met gezellige avonden, Aan Tafels, huiskamerconcerten en andere gezelligheid. In het bijzonder dank aan Jos Blomsma, voor het maken van mooie illustraties voor dit proefschrift en leuke discussies over entomologie en uitvindingen. Verder bedank ik Mitica, voor zijn hulp, zijn enthousiasme en vooral door mij 'meneer de ingenieur!' te noemen.

Veel dank aan mijn grote liefde, Anne. Na 4 jaar lang heen en weer te hebben gereisd van en naar Leeuwarden zijn we nu eindelijk dagelijks samen. Dank je voor het controleren van het hele boekje (behalve dit hoofdstuk), maar vooral voor de liefde die je me de afgelopen 4 jaar hebt gegeven. En Adriaan, bedankt voor de grote hoeveelheid mogelijkheden voor connecties waar je mee op de proppen kwam.

Als laatste, minder concreet, maar zeker zo belangrijk, ben ik mijn ouders dankbaar voor de vrijheid en uitdagingen die ze me hebben gegeven. Je weet nooit hoe het anders zou lopen, maar ik ben met name mijn vader, Ad, en opa, Arie, dankbaar voor de interesse en waardering die ze hebben overgedragen om dingen te onderzoeken.
Met veel plezier heb ik aan dit onderzoek gewerkt, met trots presenteer ik hier dit boekje en ik hoop dat iedereen die me hierbij heeft geholpen ook een beetje trots zal zijn op dit werk.

David Vermaas
November 2013

About the author

David Arie Vermaas was born on October 6, 1983 in Hoogeveen, The Netherlands. After finishing his high school degree (R.S.G. Wolfsbos, Hoogeveen) in 2002, he started studying '*Soil, Water & Atmosphere*' at the Wageningen University. This BSc study was completed with a thesis on induced flow changes in lake *De Nieuwe Meer* due to cooling water extraction.

David started a subsequent MSc study, Hydrology and Water Quality, at the Wageningen University. This study was completed with two theses; one on boundary layer flow around coral reefs, in cooperation with the Utrecht University, and a second thesis about open channel flow over beds with heterogeneous roughness, in cooperation with the Delft University of Technology. This thesis was shortly followed by a research occupation on the same topic.

In September 2009, David started as a PhD student in the Membrane Science & Technology group at the University of Twente, performing his research in the laboratory of Wetsus in Leeuwarden. The research focused on feed water flows, diffusive boundary layers, fouling and electrodes for reverse electrodialysis. The results are presented in this thesis.

David started together with Jan Post the spin-off company 'Better Battery' (www.betterbattery.nl) for energy storage in salinity gradients.

This work was performed in the cooperation framework of Wetsus, centre of excellence for sustainable water technology (www.wetsus.nl). Wetsus is co-funded by the Dutch Ministry of Economic Affairs and Ministry of Infrastructure and Environment, the European Union Regional Development Fund, the Province of Fryslân and the Northern Netherlands Provinces. The authors like to thank the participants of the research theme “Blue Energy” for the fruitful discussions and their financial support.

Stellingen

behorende bij het proefschrift getiteld
Energy generation from mixing salt water and fresh water
Smart flow strategies for reverse electrodialysis
David A. Vermaas, 17 januari 2014, Enschede

1) De eenvoudigste methode om een hoge (netto) vermogensdichtheid te verkrijgen is door de compartimenten, en dus de hele RED stack, te miniaturiseren (dit proefschrift).

2) Het beheersen van colloïdale vervuiling, scaling en biofouling is eenvoudiger te bereiken dan het voorkomen van het nadelige effect op de vermogensdichtheid als gevolg van multivalente ionen in het gebruikte water (dit proefschrift).

3) De beste vergelijking met betrekking tot het toekomstperspectief van RED, PRO, CAPMIX en nano-RED geschiedt op basis van de prijs voor de geproduceerde energie (in €/kWh). Zo lang deze prijs nog zeer onzeker is, valt niet te zeggen welke technologie het meest succesvol wordt op grote schaal (dit proefschrift).

4) De uitdrukking in W per m^2 membraanoppervlak is vertekenend en kan bij leken het beeld opwekken van een zeer grote installatie. Een uitdrukking in W per m^3 installatie zou beter zijn.

5) Wiskundig gezien snijdt het geen hout om gelijke kansen voor mannen en vrouwen af te meten aan het aantal zittende vrouwen in topposities ten opzichte van het aantal mannen in die posities. Het is logischer om kansen af te meten aan de verhouding van het aantal potentiële kandidaten en het daadwerkelijk aangenomen aantal kandidaten per geslacht.

6) Een goed gemeten dataset behoeft nauwelijks uitleg; een slechte dataset uitwerken kost vele malen meer tijd dan het meten zelf.

7) Ondanks dat vrijwel iedere onderzoeker les heeft gehad over nauwkeurigheid, precisie, standaardafwijking, standaardfouten en de onderlinge verschillen, heeft de meerderheid deze kennis niet paraat. Een verplichte foutenanalyse voor artikelen met experimenteel onderzoek zou bijdragen aan de kwaliteit van het wetenschappelijk onderzoek.

8) Het meest schokkende van de ontdekte fraude van Diederik Stapel is dat er promovendi in de sociale wetenschappen zijn die data voor hun proefschrift niet zelf verzamelen noch controleren.

9) Consequent zijn is geen deugd; het is alleen prettig voor anderen dat je voorspelbaar bent.

10) De uitspraak van Einstein dat '*If we knew what it was we were doing, it would not be called research*' kan worden geïnterpreteerd dat onderzoeksopstellingen zo flexibel mogelijk moeten zijn. Dat rechtvaardigt ook een rommelig uiterlijk van een goed werkende onderzoeksopstelling.

Propositions

belonging to the thesis entitled
Energy generation from mixing salt water and fresh water
Smart flow strategies for reverse electrodialysis
David A. Vermaas, January 17, 2014, Enschede

1) The simplest strategy to increase the (net) power density is to miniaturize the compartments, and hence the whole RED stack (this thesis).

2) The control of colloidal fouling, scaling and biofouling is easier accomplished than the prevention of the limitation in power density due to the presence of multivalent ions in the feedwater (this thesis).

3) A fair comparison of RED, PRO, CAPMIX and nano-RED for future perspectives should be performed in terms of costs of the generated energy (in €/kWh). As long as this number is highly uncertain, it cannot be concluded which of these technologies will be most successful in large-scale application (this thesis).

4) The performance as expressed in W per m^2 of membrane area creates a distorted view for non-scientists; it may suggest a very spacious RED installation. An expression in W per m^3 of installed volume would be more visual.

5) From a mathematical point of view, it is irrelevant to consider the number of men and women in top positions as an indicator for gender equality. It would be more logical to use the ratio of the number of applications and approvals for women in comparison to that of men.

6) A proper data set hardly requires any explanatory text, while a poorly measured data set requires much more time to process and explain than it takes to perform the measurements.

7) Although virtually all researchers have attended lessons about accuracy, precision, standard deviation, standard errors and the differences between them, most researchers lack active knowledge about these statistical parameters. A compulsory error analysis for papers with experimental research will improve the quality of research.

8) The most shocking about the fraud case of scientist Diederik Stapel is that some of the PhD students in social sciences do not collect nor check the data in their own theses.

9) Consistency is not a virtue; it is only useful for others that one is predictable.

10) Einsteins expression '*If we knew what it was we were doing, it would not be called research*' can be interpreted to emphasize the importance of flexibility in research setups. This justifies the unorganized appearance of a well working research setup.